REPUBLIC OF TURKEY
YILDIZ TECHNICAL UNIVERSITY
GRADUATE SCHOOL OF NATURAL AND APPLIED SCIENCES

INFLUENCE OF POTENTIAL MODIFIERS ON SODIUM CARBONATE ACTIVATED SLAG: EARLY AGE CHARACTERIZATION, MICROSTRUCTURAL EVOLUTION AND PERFORMANCE

Büşra AKTÜRK

DOCTOR OF PHILOSOPHY THESIS
Department of Civil Engineering
Structural Engineering Program

Advisor
Assist. Prof. Dr. Ahmet B. KIZILKANAT

December, 2019

REPUBLIC OF TURKEY
YILDIZ TECHNICAL UNIVERSITY
GRADUATE SCHOOL OF NATURAL AND APPLIED SCIENCES

INFLUENCE OF POTENTIAL MODIFIERS ON SODIUM CARBONATE ACTIVATED SLAG: EARLY AGE CHARACTERIZATION, MICROSTRUCTURAL EVOLUTION AND PERFORMANCE

A thesis submitted by Büşra AKTÜRK in partial fulfillment of the requirements for the degree of **DOCTOR OF PHILOSOPHY** is approved by the committee on 26.12.2019 in Department of Civil Engineering, Structural Engineering Program.

Assist. Prof. Dr. Ahmet B. KIZILKANAT
Yildiz Technical University
Advisor

Approved By the Examining Committee

Assist. Prof. Dr. Ahmet B. KIZILKANAT, Advisor
Yildiz Technical University _____

Assoc. Prof. Dr. Nihat KABAY, Member
Yildiz Technical University _____

Prof. Dr. Nilüfer ÖZYURT ZİHNİOĞLU, Member
Bogaziçi University _____

Assoc. Prof. Dr. Orhan CANPOLAT, Member
Yildiz Technical University _____

Prof. Dr. Hakan N. ATAHAN, Member
Istanbul Technical University _____

I hereby declare that I have obtained the required legal permissions during data collection and exploitation procedures, that I have made the in-text citations and cited the references properly, that I haven't falsified and/or fabricated research data and results of the study and that I have abided by the principles of the scientific research and ethics during my Thesis Study under the title of Influence of Potential Modifiers on Sodium Carbonate Activated Slag: Early Age Characterization, Microstructural Evolution and Performance supervised by my supervisor, Assist. Prof. Dr. Ahmet B. KIZILKANAT. In the case of a discovery of false statement, I am to acknowledge any legal consequence.

Büşra AKTÜRK

Signature

This study was supported by the research grant of Yildiz Technical University Research Foundation (Project No.: 2016-05-01-DOP03).

Dedicated to my mother
Without her love, understanding and great support
this incredible journey would not have been possible

ACKNOWLEDGEMENTS

Firstly, I would like to express my sincere gratitude to my advisor Assist. Prof. Dr. Ahmet B. Kızılkanat for his guidance, support, encouragement, patience, and motivation throughout my research, without whom this dissertation surely would not have been possible. I've learned a lot from him during this period, not only the knowledge of carrying out scientific research, but also the way of thinking, and the ability to deal with difficult situations for research and also for life. I could not have imagined having a better advisor and mentor for my PhD study. I'll always be grateful him for everything we shared.

I would also like to thank the rest of my thesis committee: Dr. Nihat Kabay and Dr. Nilüfer Özyurt Zihnioğlu, for their insightful comments. A special thanks to Dr. Özyurt Zihnioğlu for her encouragement, valuable comments, and the opportunity she gave me to work at the BOUN Construction Materials Laboratory. I'd also like to thank whole YTU Construction Materials staff, I've learned a lot from all of them. Many thanks to Prof. Dr. Nabi Yüzer for managing my thesis for the first two years. I thank Dr. Sumanta Das and Dr. M.Timur Cihan for their contributions.

Many thanks to my friends and colleagues Dr. Serhan Ulukaya, Dr. Didem Oktay, and Dr. Abdullah H. Akca for their friendship and encouragement. Dr. Ulukaya always shared his knowledge from the first day of my beginning. Besides, the dinners we shared at the end of my tough and long laboratory days, and the conversations we made always motivated me. Dr. Oktay always supported me and was the best roommate during the 9 years we've spent together. A special thanks to Dr. Gökçe Aydın, for being the best friend, and never made me feel that he is far away for the last three years.

I also would like to thank my husband, Engin, for always believe me and caring for our child Tibet, especially for the last year. I'll always be grateful. One of my deepest thanks to my lovely son, Tibet for being such a good little boy. He always made me smile, full of life, and hopeful. Surely, before anything else, I should say a heartfelt thank you to my mother, Türkan Yücedağ, for encouraging me to follow my dreams.

Büşra AKTÜRK

TABLE OF CONTENTS

LIST OF SYMBOLS

a	Area of the disc specimen exposed to water
a_0	Initial notch depth
a_{eff}	Effective crack length
A_{lig}	Ligament area of the beam specimen
A_s	Area fraction of unhydrated slag
β	Brittleness index
b	Width of the beam specimen
c_0	Chloride concentration of the catholyte solution
c_d	Chloride concentration at which the colour changes
c_i	Initial compliance of load-CMOD curves
$CTOD_c$	Critical crack tip opening displacement
D	Pore diameter
d	Height of the beam specimen
d_{flow}	Flow spread diameter
d_{ini}	Initial flow spread diameter
d_{final}	Final flow spread diameter
d_{50}	Median diameter
Δ_{flow}	Flow loss
Δm	Mass loss
δ_{max}	Maximum displacement under the maximum load
D_{nssm}	Non-steady state chloride migration coefficient
ϵ	Ultimate drying shrinkage
E	Modulus of elasticity

F	Faraday constant
$f_{compressive}$	Compressive strength
$f_{c,3}$	3-days compressive strength
$f_{c,28}$	28-days compressive strength
$f_{flexural}$	Flexural strength
G_F	Fracture energy
g	Gravitational acceleration
γ	Surface tension of mercury
$\dot{\gamma}$	Shear rate
H_0	Thickness of the knife edges
I	Normalized absorbed fluid volume
I_{ini}	Initial absorption
I_{sec}	Secondary absorption
k	Primary sorptivity absorption
k_{sec}	Secondary absorption
K_{Ic}^{ini}	Initiation toughness
K_{Ic}^{un}	Unstable fracture toughness
L	Thickness of the disc specimen
m	Weight of the beam specimen
m_t	Mass change of specimen at time t
M_s	Silicate modulus
pH	Potential of hydrogen
P	Applied pressure
P_{ini}	Initial cracking load
P_{max}	The peak load of load-CMOD curve
R	Molar gas content
ρ	Density of water
S	Span length
T	Average temperature in anolyte solution

θ	Contact angle of mercury
τ	Shear stress
t	Test duration
t_{ini}	Initial setting time
t_{final}	Final setting time
U	Absolute voltage
W_0	Area under the load-CMOD curve
X_d	Penetration depths
z	Valance of chloride ion

LIST OF ABBREVIATIONS

AAM	Alkali-activated Material
AFm	Al_2O_3–Fe_2O_3-mono
ANOVA	Analysis of Variance
ASTM	American Society for Testing and Materials
BI	Brittleness Index
BSE	Backscattered Electron
CEN	Committee for European Norms
CH	Calcium Hydroxide
CLDH	Calcined Layered Double Hydroxide
CMOD	Crack Mouth Opening Displacement
CV	Coefficient of Variation
DTG	Derived Thermogravimetric Analysis
FTIR	Fourier Transform Infrared Spectroscopy
GLH	Grey Level Histogram
LNC	CH-substituted Mixes
LOI	Loss of Ignition
LVDT	Linear Variable Differential Tranducers
MIP	Mercury Intrusion Porosimetry
MOE	Modulus of Elasticity
NC	Sodium Carbonate
NCAS	Sodium Carbonate-Activated Slag
NH	Sodium Hydroxide
OPC	Ordinary Portland Cement

PP	Polypropylene Fiber
PV	Plastic Viscosity
RSM	Response Surface Methodology
SEM	Scanning Electron Microscope
ST	Steel Fiber
TGA	Thermogravimetric Analysis
XRD	X-ray Diffraction
XRF	X-ray Fluorescence
YS	Yield Stress
2FI	Two Factorial Interactions
3D	Three Dimensional

LIST OF FIGURES

LIST OF TABLES

ABSTRACT

Influence of Potential Modifiers on Sodium Carbonate Activated Slag: Early Age Characterization, Microstructural Evolution and Performance

Büşra AKTÜRK

Department of Civil Engineering
Doctor of Philosophy Thesis

Advisor: Assist. Prof. Dr. Ahmet B. KIZILKANAT

In view of today's environmental issues, the production process of construction materials must be designed and applied on the basis of minimum energy consumption. Considering the large amount of energy consumption and CO_2 emissions (5-8%) caused by cement production, the necessity and importance of more sustainable material production have been increased over time.

Alkali activated materials (AAMs) can be regarded as more environmental-friendly systems than ordinary Portland cement-based systems, since industrial wastes or byproducts such as slag, fly ash and/or natural pozzolanas that contain reactive silica and alumina have been used as raw materials in AAM production. Fineness and chemical composition of the precursor, type and concentration of the alkali activator, mixing procedure, and curing conditions are the main parameters affecting the characteristics of AAMs. The most common activators used in alkali activation are sodium/potassium hydroxides and sodium silicate as they have the dual effect of raising the pH and facilitating the dissolution of raw material. However, use of these activators may cause rapid setting, high drying shrinkage, and micro-cracking issues in practice. Moreover, high production costs and caustic nature make them less preferable. Therefore, in this study, it is aimed to use the naturally available sodium carbonate (NC) as main activator. NC is gaining attention as it is cost-effective, eco-friendly, and less harmful alternative to synthetic alkali hydroxides and silicates. Moreover, Turkey has the second largest NC reserves which increase the potential to use within this concept. However, prolonged setting time and delayed strength development are the

main drawbacks of NC-activated systems.

The aim of the current study is to produce a sustainable, applicable, and durable cementless construction material by utilizing slag and NC by overcoming the main drawbacks of NC. The first phase of the work focuses on accelerating the reaction mechanism of NC-activated slag (NCAS) by incorporating potential modifiers such as sodium hydroxide (NH) and calcium hydroxide (CH). The nature of the potential synergistic benefit of the modifiers is explored. The fresh-state characteristics such as setting time, yield stress, and plastic viscosity were determined. Strength development and the progress of hydration of the mixes are explained with the phase transformation and development of microstructural features through quantitative techniques such as thermogravimetric analysis and phase-identification techniques such as FTIR, and X-ray diffraction. The second phase of the work investigates the fracture response of plain and fiber-reinforced NCAS mortars through the double-K fracture toughness, fracture energy, and brittleness index. Moreover, drying shrinkage, water and chloride ion permeability of NCAS mixes are also investigated. Finally, all test results are statistically analysed and the optimum mixing proportions are obtained considering the desired multi-objective aims.

The results of this work indicate several key ideas:

- CH and NH can be potential modifiers for achieving the desired setting time,
- Mechanical properties are improved with the incorporation of the modifiers,
- Low water and chloride ion permeability can be obtained for NCAS with the presence of the modifiers, especially CH,
- A substantial improvement is observed in terms of strength, pore structure, drying shrinkage and permeability in case of the incorporation of CH along with NH.

It is anticipated that the results obtained from this study will provide as yet unknown details on these novel binding systems.

Keywords: Sodium carbonate activated slag; rheology; microstructure; fracture; durability.

ÖZET

Potansiyel İyileştirici Malzemelerin Sodyum Karbonat ile Aktive Edilmiş Cürufun Özelliklerine Etkisi: Erken Yaş Karakterizasyonu, İçyapı Gelişimi ve Performansı

Büşra AKTÜRK

İnşaat Mühendisliği Anabilim Dalı
Doktora Tezi

Danışman: Dr. Öğr. Üyesi Ahmet B. KIZILKANAT

Günümüz çevresel sorunları dikkate alındığında, yapı malzemeleri üretimi minimum enerji tüketimi esas alınarak tasarlanmalı ve uygulanmalıdır. Çimento üretiminin neden olduğu yüksek miktardaki enerji tüketimi ve CO_2 emisyonu (%5-8) düşünüldüğünde, daha sürdürülebilir bir yapı malzemesi üretimi ihtiyacı ve önemi giderek artmaktadır. Alkalilerle aktive edilmiş malzemelerin (AAM) üretiminde reaktif silis ve alümin içeren cüruf, uçucu kül gibi endüstriyel atık veya yan ürünlerin ve/veya doğal puzolanların bağlayıcı olarak kullanılması nedeniyle, AAM'ler Portland çimentolu sistemlere göre daha çevre dostu olarak nitelendirilebilirler. Kullanılan bağlayıcı malzemenin inceliği, kimyasal kompozisyonu, aktivatör tipi ve konsantrasyonu ile karıştırma yöntemi ve kür koşulları AAM'lerin özelliklerini belirleyen ana parametrelerdir. pH değerini arttırması ve bağlayıcı malzemenin çözünmesini kolaylaştırması nedeniyle, alkali aktivasyonunda genellikle sodyum/potasyum hidroksit ve sodyum silikatler aktivatör olarak kullanılmaktadır. Ancak bu malzemeler, hızlı priz, yüksek kuruma rötresi ve mikro çatlak oluşumu gibi problemlere neden olabilmektedir. Ayrıca, yüksek üretim maliyeti ve yakıcı yapıları bu malzemeleri daha az tercih edilir kılmaktadır. Bu nedenle, bu çalışmada ana aktivatör olarak doğal yolla da elde edilebilen sodyum karbonatın (NC) kullanılması amaçlanmıştır. NC'nin, çevre dostu, ekonomik ve diğer sentetik alkali hidroksit ve silikatlere göre daha az zararlı olması dikkat çekmektedir. Bununla birlikte, Türkiye'nin dünyada ikinci en büyük NC rezervine sahip olması NC'nin bu amaçla kullanılabilme potansiyelini arttırmaktadır. Ancak, uzun priz süresi ve geciken dayanım gelişimi NC ile aktive edilen sistemlerin ana sorunlarıdır.

Bu çalışmada, olumsuz yönleri ortadan kaldırılarak cürufun NC ile aktive edilmesi ile oluşturulan, sürdürülebilir, uygulamada kullanılabilir ve durabilitesi yüksek çimentosuz bir yapı malzemesi üretimi amaçlanmıştır. Çalışmanın birinci aşamasında, NC ile aktive edilen cürufun reaksiyon mekanizmasını sodyum hidroksit (NH), kalsiyum hidroksit (CH) gibi potansiyel iyileştiriciler kullanarak hızlandırmaya odaklanılmıştır. Birlikte çalışma potansiyeli olan bu iyileştirici malzemelerin NC ile aktive edilmiş cüruf karışımlarına katkısı araştırılmıştır. Priz süresi, akma dayanımı, plastik viskozite gibi taze hal özellikleri belirlenmiştir. Karışımların dayanım gelişimi ve hidratasyon süreci, faz dönüşümü ve FTIR, X-ışını kırınımı gibi faz belirleme teknikleri ve termogravimetrik analiz gibi kantitatif yöntemler kullanılarak belirlenen içyapı özelliklerindeki gelişim ile açıklanmıştır. Çalışmanın ikinci aşamasında normal ve lif takviyeli NC ile aktive edilmiş cüruf harç karışımlarının kırılma davranışı, iki parametreli kırılma tokluğu, kırılma enerjisi ve gevreklik indeksi ile incelenmiştir. Ayrıca, karışımların kuruma rötresi, su ve klorür iyonu geçirimliliği de araştırılmıştır. Son olarak, tüm deney sonuçları istatistiksel olarak analiz edilmiş ve çok amaçlı hedefler için optimum karışım oranları belirlenmiştir. Çalışmadan elde edilen sonuçlar birkaç ana fikri işaret etmektedir:

- İstenilen priz süresini sağlamada potansiyel iyileştirici olarak CH ve NH'ın kullanılabileceği,
- İyileştirici malzemelerin mekanik özellikleri geliştirdiği,
- İyileştici malzemelerin kullanılması ile, özellikle CH kullanımı, NC ile aktive edilmiş cüruf karışımlarında düşük su ve klorür iyonu geçirimliliğinin elde edilebileceği,
- CH ve NH'ın birlikte kullanılması ile dayanım, boşluk yapısı, kuruma rötresi ve permeabilitenin yüksek miktarda geliştiği görülmüştür.

Bu çalışmadan elde edilen sonuçların, bu yeni bağlayıcı sistemler ile ilgili henüz çalışılmayan konular hakkında bilgi vereceği düşünülmektedir.

Anahtar Kelimeler: Sodyum karbonatla aktive edilmiş cüruf; reoloji; içyapı; kırılma; durabilite.

1
INTRODUCTION

1.1 General

Concrete is one of the most used construction material in the world. Ordinary Portland cement (OPC) is the main component used in concrete production. Demand for the Portland cement production gradually increases through the increase in worldwide civilization and industrialization in the last decades. During the manufacturing process of Portland cement, a high amount of energy is consumed. Calcination of the limestone and other raw materials up to a very high temperature (≈1400°C), and grinding clinker into the required fineness cause extensive energy consumption [1, 2]. It is indicated that approximately 4 GJ is needed during the production process of per ton of clinker [3]. Moreover, Portland cement production is responsible for approximately 7% of the total CO_2 emissions released into the atmosphere. Furthermore, this value increases to 10% in developing countries [1, 4].

The substitution of OPC with industrial byproducts such as ground granulated blast furnace slag and fly ash are known as an alternative method to reduce CO_2 emissions. For the last several decades, the concrete industry has consistently attempted to use sustainable methods by incorporating significant amounts of byproducts in concrete production. The use of these materials as sole binding material in concrete production instead of partial replacement with OPC is a new subject in recent studies to reduce the greenhouse gas emissions. These activated materials, composed entirely of silicium and aluminum rich waste materials such as slag or fly ash, are named as alkali-activated materials (AAMs).

AAM production decreases the environmental issues of OPC production with the utilization of byproducts as a precursor. It also decreases the need for virgin material, and also demand for landfill. Thus, it can be deduced that these materials improve sustainability by reducing the need for OPC and presents a better option in terms of utilizing, handling these waste materials. AAMs or geopolymers are new generation, sustainable, eco-friendly construction materials that are taking attention with their

superior mechanical and durability properties compared to OPC-based materials. Producing these new alternative construction materials is also motivation of the current study.

The history of the AAMs dates back to the beginning of the 1930s, the first main contribution was made by Purdon in the 1940s on alkali-activated slag binders [5]. Purdon activated the slag by sodium hydroxide (NH) and reported that activation develops in two steps. Firstly, silica, alumina, and lime liberate, calcium hydroxide takes place and then hydrated aluminates, calcium silicates forms, with the regeneration of caustic solution as well.

Researchers have described AAMs with different names. Glukhovsky attempted to develop a new type of binder and described it as "soil-cement" due to its ground rock soil-like appearance and its binding capacity. The "soil-cement" was composed of by mixing rich alkalis industrial wastes and ground aluminosilicate [6]. In 1979, Davidovits developed a new type of binder, named as "geopolymer", through the alkali-activation of metakaolin [7]. The activators used in the AAM production can be classified into six groups:

- Alkali hydroxides such as MOH,
- Weak acid salts such as M_2CO_3, M_2SO_3, M_3PO_4, MF,
- Alkali silicates such as $M_2O.\mathrm{n}SiO_3$,
- Alkali aluminates such as $M_2O.\mathrm{n}Al_2O_3$,
- Aluminosilicates such as $M_2O.Al_2O_3.(2-6)SiO_2$,
- Strong acid salts such as M_2SO_4

where M represents an alkali ion such as sodium and potassium [8]. Slag, fly ash, and metakaolin are commonly preferred raw materials in AAM production, whereas alkali hydroxides, silicates, and carbonates are the most effective activators. In many studies, sodium/potassium hydroxides and sodium silicates have been used in alkali activation as they have the dual effect of raising the pH of the medium as well as facilitating the dissolution of raw material [9]. However, they have several disadvantages such as they are expensive and are caustic in nature [10–12]. Moreover, the production process of these activators requires a high amount of energy. In addition, sodium silicate causes fast hardening and a high amount of shrinkage [13].

Sodium chloride obtained from seawater is used for most of the activator production. Sodium chloride can be transformed into sodium carbonate (NC) by the Solvay process,

or into sodium hydroxide (NH) by the chloralkali process. Sodium silicate, namely waterglass, can be produced by treating a mixture of silver sand (SiO_2), caustic soda (NaOH), and water [14]. On the other hand, NC can be acquired naturally, with 23 billion tonnes of trona ore in the USA, and hundreds of millions in Turkey, Mexico, etc. Every year, 50 million tonnes of NC products globally [9]. Turkey has the second-largest NC reserves with 840 million tons out of the more than 25 billion tons worldwide [15]. Therefore, naturally available NC is gaining attention as a cost-effective and eco-friendly alternative to synthetic alkali hydroxides and silicates [10, 16]. Utilization of this great potential in AAM production would contribute to sustainability. However, prolonged setting time and delayed strength development are the main issues to be overcome in NC-activated systems [10]. These issues make NC-activated systems less preferable and these systems have been less extensively studied compared to other activators. However, it has been reported that there are a few methods that can accelerate the reaction process and harden in a comparable time with the OPC. At further ages, it can demonstrate higher strength values compared to NH-activated systems.

1.2 Objectives and Outline of the Thesis

The overall aim of this research is to produce a sustainable, applicable, and durable cementless construction material by using slag as a precursor and NC as main activator. Within this concept, plenty of tests were conducted (Fig. 1.1) to achieve the aim of the study and the following objectives are established:

- To use NC as an activator which is less harmful compared to other activators, eco-friendly, promising and naturally available in Turkey,
- To obtain NC-activated slag (NCAS) mixes with high early and ultimate strength cured at room temperature,
- To achieve comparable setting time with OPC-based systems,
- To overcome the delayed setting and delayed strength development,
- To explain the slow reaction mechanism with the microstructural analysis,
- To determine and enhance the fracture properties of NCAS with fiber incorporation,
- To achieve better durability properties compared to OPC-based systems,
- To statistically analyse and optimize the early age characteristics, strength and durability properties of NCAS regarding mixing proportion,

- To bring recommendations for a better NCAS design

To accomplish the objectives written above, two different modifiers, NH and CH, were substituted at different ratios. NC replaced with 20% and 40% of NH by weight, while slag replaced with 3% of CH by weight. In addition, to observe the effect of activator concentration, two different concentrations were applied. With the aid of the modifiers, the established objectives are achieved. Detailed explanations concerning the reaction mechanism, microstructure evolution, fracture and durability properties of all mixes are presented in the following chapters.

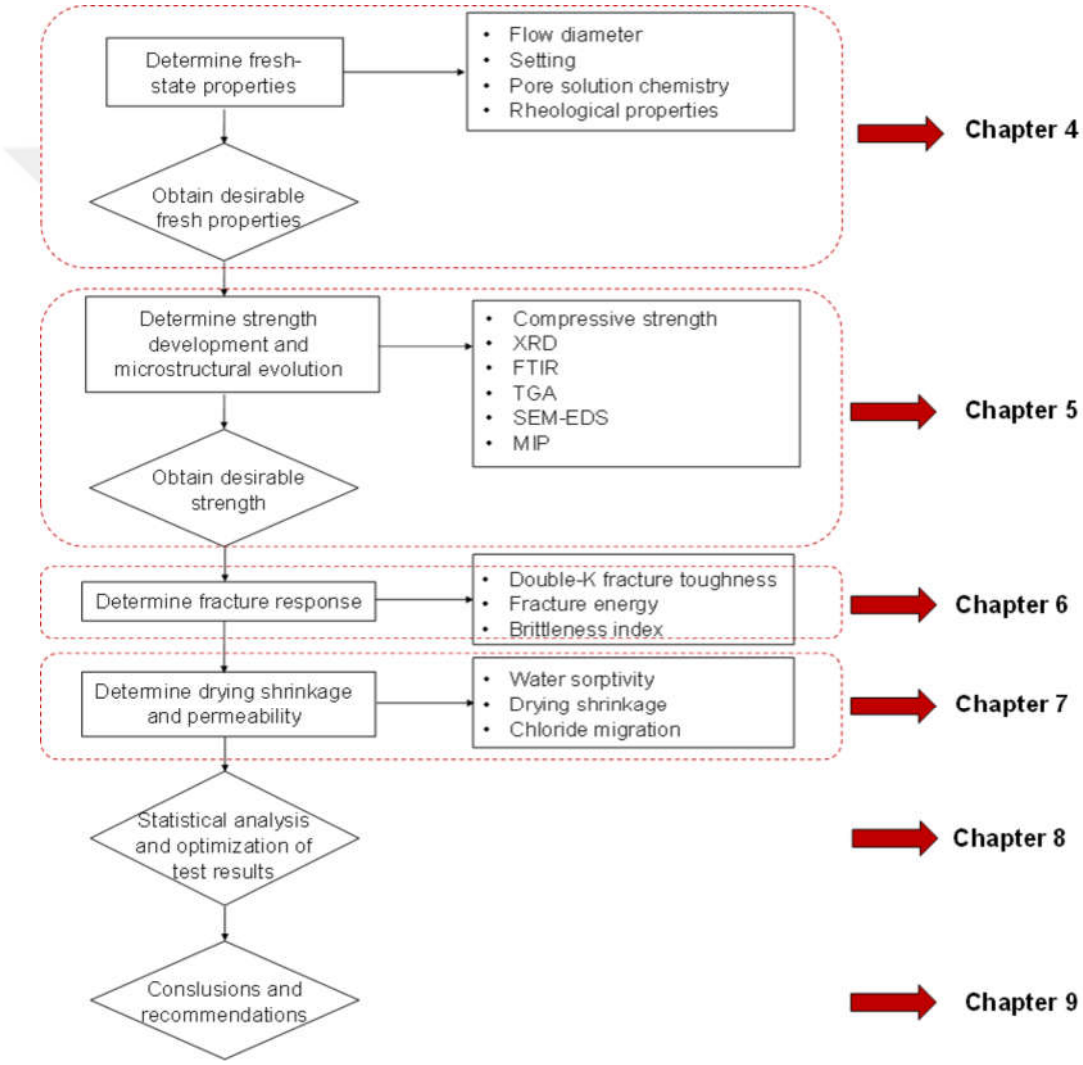

Figure 1.1 Outline of the thesis

This dissertation consists of 9 chapters (Fig.1.1). Chapter 1 provides a general view of the aim, motivation, and objectives of the thesis. The general literature view concerning the alkali activation mechanism is given in the second chapter. Chapter 3 provides material properties and applied test methods. Chapter 4 presents the fresh-state properties such as setting time, pH evolution, rheological properties of the

mixes. The importance of the fresh-state properties for NCAS mixes is emphasized in this chapter. In Chapter 5, microstructural evolution, the reaction mechanism of the different mixes are detailed. The relationship between microstructure and strength development is clarified. Chapter 6 investigates the fracture response of the plain and fiber-reinforced NCAS mixes. Chapter 7 observes the durability properties of NCAS mixes and compares the results with the OPC-based mixes. In Chapter 8, the fresh-state properties, compressive strength, and durability properties statistically analysed and optimization of NCAS mixes are reported. Chapter 9 summarizes all the results obtained and classifies the mixes according to their performance regarding early age properties, strength, and durability properties. In addition, key conclusions and suggested future works are provided.

1.3 Hypothesis

In literature, geopolymers and AAMs have been extensively studied, and important advances have been reported. The previous studies mostly focused on the mechanical and durability properties of these materials. Generally, alkali hydroxides and silicates are preferred as activators, slag and fly ash were used as precursors. NC-activated systems have attracted less attention due to its delayed setting time and compressive strength development. Thus, a broad section of early age and ultimate properties of NC-activated systems need to be analyzed. In NCAS systems, the reaction mechanism is delayed because of the high amount of the CO_3^{2-} ion concentration and low initial pH of the medium at the early age. In this study, it was aimed to accelerate the reaction mechanism of NCAS with the aid of modifiers, NH, CH, and the combination of NH+CH.

The use of NH and CH as modifiers accelerates the reaction kinetics of NCAS mixes by reducing the carbonate concentration and increasing the pH degree of the pore solution; thus, providing significant enhancement on hardened properties such as early and ultimate strength development, permeability and microstructure.

It was thought that the results of this study may contribute to further researches.

2
LITERATURE REVIEW

2.1 General

In this chapter, reaction mechanisms of low-calcium based and high-calcium based materials, advantages and disadvantages of NC-activated systems are given.

2.1.1 Alkali Activation of Low-Calcium Based Systems

In literature, geopolymers and AAMs are defined as different types of materials which mainly differ in chemistry, hydration process and hydration products. Geopolymers are synthesized with precursors containing a high amount of SiO_2 and Al_2O_3 and a low amount of calcium such as fly ash and metakaolin. They are inorganic polymers, can be activated by a highly alkaline solution. The reason for the name of "geopolymer" comes from the polymerization process of these materials. To define the chemical description of the geopolymers, Davidovits [17] proposed the name "polysialates", which is a nomenclature for aluminosilicate oxide.

A geopolymer structure is composed of AlO_4 and SiO_4 tetrahedral units, which linked randomly by sharing the oxygen atoms, yielding a nanometric macromolecules with a 3D structure (Fig. 2.1). The distribution of silicate and aluminate tetrahedra led to the formation of the Si-O-Si and Si-O-Al bonds, while Al-O-Al bonds are not formed. Thus, the Si/Al ratio of a geopolymer becomes at least 1 [18].

To have a stable aluminosilicate network, sufficient aluminum needs to exist. If each silicate tetrahedra was supposed to have at least one aluminate tetrahedral neighbour, the Si/Al ratio would increase to a maximum value of 4 [18].

Alkali metal cations such as sodium, potassium, lithium, calcium increase the pH level of the solution as well as the OH^- concentration. Thus, these ions improve the dissolubility of the alumina and silica from the aluminosilicate source. Moreover, alkali ions play a key role in the network of geopolymers, since they enhance stabilization of negative charge of the AlO_4 tetrahedron, where the trivalent ion Al^{3+} is four-coordinated. Hence,

the alkalis from the activation solution become part of the network.

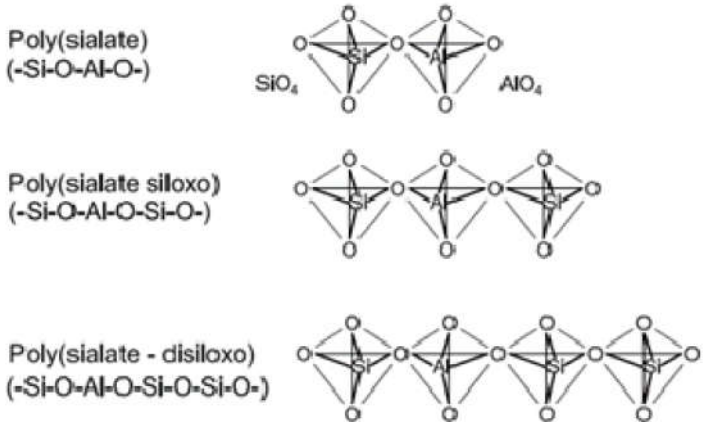

Figure 2.1 Chemical structures of polysialates [18]

Si-O-Al and Si-O-Si bonds can be defined as the two main bonds being formed in a geopolymer structure, which is called sialate and siloxo bonds, respectively. Thus, the configuration of the geopolymers are described by their Si/Al ratio, and the structure of polysialate can be described by the following formula:

$$M_n[\text{-}(SiO_2)_z\text{-}AlO_2]_n.wH_2O$$

where n is the polymerization degree, z is 1, 2, 3 and stands for the Si/Al ratio, and M is an alkali cation such as calcium, sodium, or potassium; the symbol "–" points the existence of a bond. In case of Si/Al=1 poly(sialate), Si/Al=2 poly(sialate-siloxo), and Si/Al=3 poly(sialate-disiloxo), Si/Al > 3 poly(sialate link) may form [19, 20]. The schematic formation of a geopolymer formed by polycondensation can be demonstrated in Fig. 2.2. Molecular graphics of a polymeric polysialate is related to the type of activator used (Fig. 2.3).

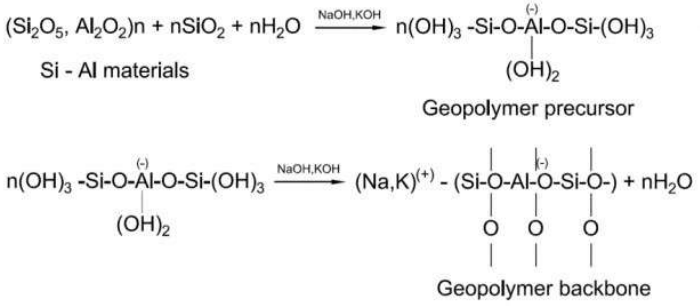

Figure 2.2 Schematic formation of geopolymer material [21]

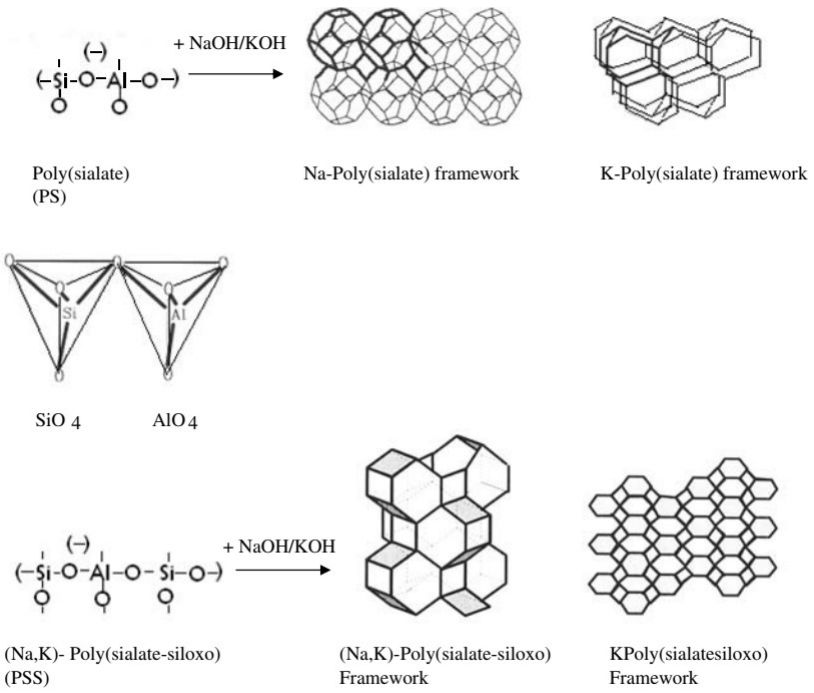

Figure 2.3 Molecular graphics of polysialate structures [22]

The coordination number of the silica and alumina is a key factor as some of the water and NH are expelled out during hardening. It was assumed that alkali metal hydroxide acts as a catalyst and leaches out from the hardened state alkali-activated binder. It can be deduced that alkali cation ions affect the final structure stability and thus leaching characteristics. Glukhovsky et al. [6, 23] explained the reaction mechanism of alkali activation of a precursor containing silica and reactive alumina with a model in the 1950s (Fig. 2.4). This model characterizes the main mechanism of the conversion of a solid aluminosilicate source into a synthetic aluminosilicate gel. According to Glukhovsky [6], the polymerization process consists of three main stages, which are defined as (i) destruction-coagulation, (ii) coagulation-condensation, (iii) condensation-crystallization processes. Later on, Glukhovsky's theories have been developed with further studies [24–26].

The first dissolution stage involves the disintegration of the covalent bonds of Si-O-Si and Al-O-Si from the vitreous glass phase of source, results in the Si-OH and Al-OH groups formation, which is called alkaline hydrolysis. The dissolution of solid aluminosilicate produces aluminate and silicate species. This process appears when the pH value of the alkaline solution increases and reaches to the satisfaction level. Once the species in the solution are integrated into the aqueous phase, a complex mixture of silicate, aluminate and aluminosilicate species is created.

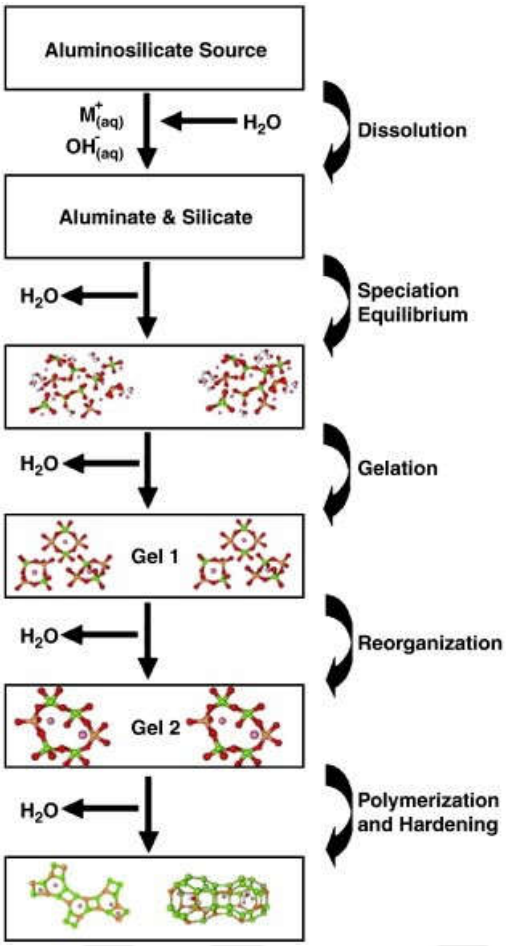

Figure 2.4 The conceptual model for alkali activation processes [27]

Due to the rapid dissolution of the glass phase at high pH levels developed by the activators, the solution quickly over-saturates. This phenomenon leads to the formation of an aluminum rich gel (Gel 1 in Fig. 2.4). Since Al-O bonds are weaker than the Si-O in the aluminosilicate binder, during the first hours of the reaction, a high concentration of aluminum can be expected to exist in the solution. As the reaction proceeds, higher Si-O participates in the solution, increases the silicon concentration in the solution as well as with the gel phase (Gel 2). At the last step, the system reorganizes and rearranges which is resulted in the 3D aluminosilicate network. Microstructure and pore distribution characteristics of the hardened geopolymer is mostly depended on this final process.

SiO_2, Al_2O_3, Fe_2O_3 can be placed as network formers, while CaO can be placed as a network modifier in a geopolymer structure [28].

In geopolymer production, generally low calcium-based binders such as Class F fly ash, metakaolin, red mud, etc. require high temperature curing at the early age of the reaction for the dissolution of monomers. On the other hand, high calcium-based materials such as slag can be activated at ambient temperature [29].

While the main reaction product formed in AAMs is C-A-S-H [30, 31], in geopolymers generally it is N-A-S-H [7, 32, 33]. The N-A-S-H gel is identified as a three-dimensional structure, which exhibits Na/Al and Al/Si ratio ranging between 0 to 1.85 and 0.05 to 0.43, respectively. At low pH, it behaves like zeolite and displays ion-exchange behavior. On the other hand, higher pH values promote higher polymerized structures [34].

When the fly ash is activated with sodium silicates, the existence of soluble silicates allows the bridging of the Q^4 structures with the Q^2 species. In addition, stable formation of the gel increases with the high-temperature curing. However, in the vacancy of the soluble silicates, this may turn amorphous structure. Therefore, if the sample exposed to very high temperatures, e.g. higher than 150°C or a long period of time more than 96 hours, compressive strength of the binder may decrease [35].

Fresh and hardened state properties of geopolymers significantly depend on the chemical composition, fineness, glass content and composition of the precursor, alkaline activator type, liquid-to-solid ratio, mixing procedure, and curing conditions [36–41].

2.1.2 Alkali Activation of High-Calcium Based Systems

High calcium-based alkali systems, differs from the geopolymers with its different reaction mechanism and hydration products. These materials do not require high-temperature curing, which makes them more feasible. Thus, it can be assumed that AAMs can be more preferable in terms of their lower cost, reduced energy consumption and minimal CO_2 emission.

Ground granulated blast furnace slag is the most used high-calcium based precursor in alkali activation due to its high binding capability. Slag is a byproduct obtained from the manufacturing process of iron. It was estimated that the annual production of slag reaches 270-320 Mt all over the world [42]. The production of slag requires approximately 1300 MJ of energy and produces only 70 kg of CO_2, while the same quantity of OPC requires 5000 MJ of energy and releases 970 kg of CO_2 (Table 2.1) [43, 44].

Table 2.1 Comparison of CO_2 emissions (CO_2 emission/t) for OPC and slag production [43, 44]

Parameters	OPC	Slag
$CaCO_3$ calcination	540	0
Fuel	340	20
Electricity generation	90	50
Total	970	70

For the last decades, various studies have been reported concerning the superior properties such as strength and durability of alkali-activated slag. However, it should be noted that these properties can vary depending on the nature of the precursor, activator type and curing methods.

The mineralogical component of slag mainly consists of two phases which are described with a mixture of gehlenite ($2CaO{\cdot}Al_2O_3{\cdot}SiO_2$) and akermanite ($2CaO.MgO{\cdot}2SiO_2$) phases [45]. The reaction mechanism of high-calcium based alkali activated systems differs from the low-calcium based alkali activated systems. Alkali activation process of the slag composed of mainly two steps; destruction and polycondensation. In high calcium-based systems, the main hydration product is calcium silicate hydrates. Silica tetrahedra are found in one-dimensional chains in AAMs rather than in 3D structures as observed in geopolymers (Fig. 2.5) [19].

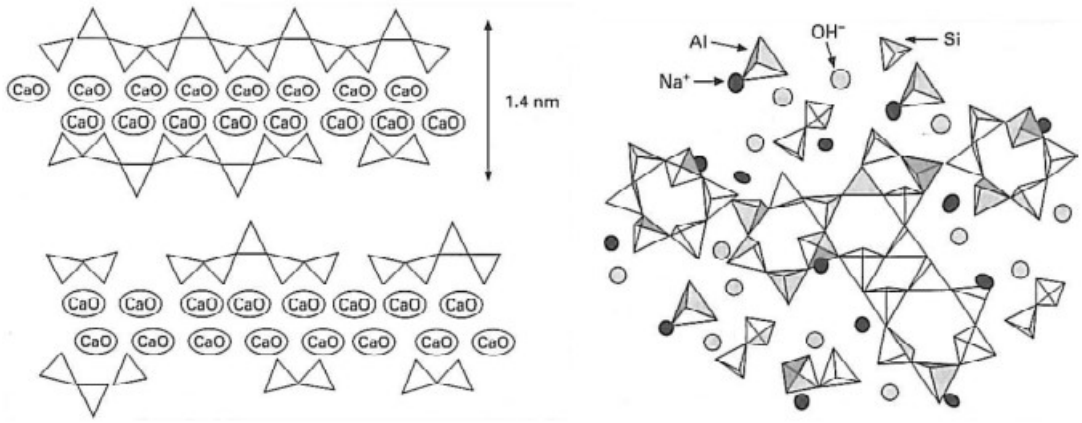

Figure 2.5 The chemical structure of one-dimensional C-S-H, and the 3D-structure of geopolymers [19]

Wang and Scrivener [46] proposed that at the early ages of the reaction, initial reaction products form by a dissolution and precipitation mechanism. However, at further ages, a solid mechanism is followed where the reaction occurs on the surface of the slag, dominated by the moderate diffusion of the ionic species into the unreacted core.

The initial pH value affects the initial dissolubility of the binder. The hydration products quite differ from the geopolymers. Typically C-(A)-S-H gel is found as the main reaction product, only with a lower Ca/Si such as ranging from 0.5 to 1.0, while it ranges from 1.5 to 2.0 for hydrated cement C-S-H. C-(A)-S-H gel chains in alkali-activated slag found as up to 13 tetrahedra, while in OPC systems it might be up to 3-5 tetrahedra, which means C-(A)-S-H gel chains are longer. Moreover, by replacing the silicium, it consists of aluminum in the gel structure [47].

Fig. 2.6 [48] presents a model of the dissolution mechanism of a glassy phase containing a high amount of Ca and a low amount of Al, both monovalent and divalent network-modifying cations. In Fig. 2.6, (A) represents the exchange of H^+ for Ca^{2+} and Na^+, (B) represents hydrolysis of Al-O-Si bonds, (C) represents the breakdown of the depolymerized glass network and (D) represents the release of Si and Al.

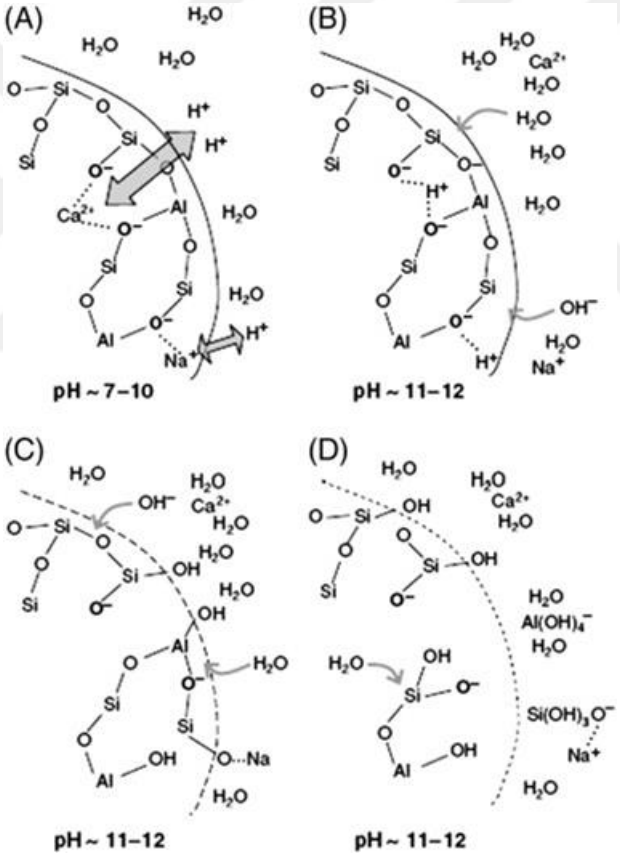

Figure 2.6 Dissolution mechanism of aluminosilicate binders [48]

It was reported that the reaction process starts with the breaking of the slag bonds, Ca-O, Mg-O, Si-O-Si, Al-O-Al, and Al-O-Si, and then proceeds with the formation of a Si-Al layer all over the slag grain surface and it is completed with the formation of the hydration products [45]. In another study [46], it was reported that the early age of the reaction consists of dissolution and precipitation mechanism, later on, the reaction may proceed by a solid-state mechanism. Bernal et al. [49] reported that the

reaction mechanism initiates with the dissolution of the precursor and proceeds with the polycondensation and the exchange among the dissolved species. As a result of the reaction, C-(N)-A-S-H type gel forms, moreover, secondary phases depend on the activator type and MgO concentration of the slag. For example, sodium silicate-activated slag forms zeolites and/or AFm phase, while NC-activated slag forms carbonates and hydrotalcite (Fig. 2.7).

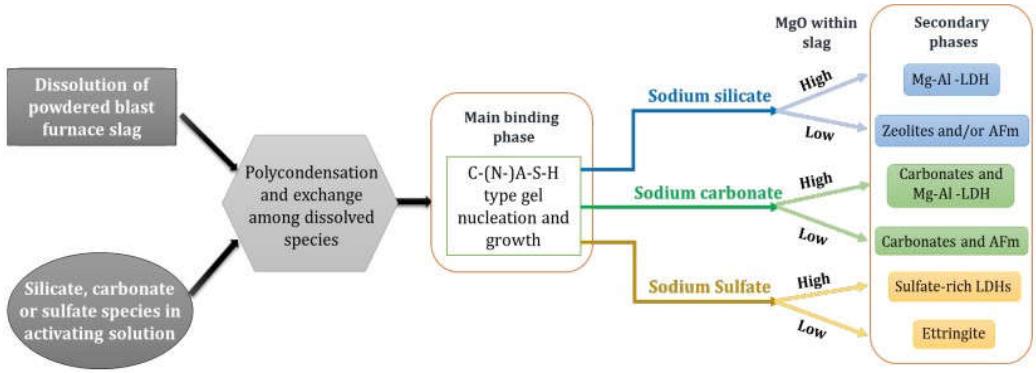

Figure 2.7 Simplified schematic diagram of the alkali-activation process of blast furnace slags [48]

In addition to the different reaction products, reaction mechanism and duration differs with the activator type. The detailed information about the reaction mechanism of NCAS is given in the next section.

2.1.3 Reaction Mechanism of Sodium Carbonate-Activated slag

Due to the slow reaction mechanism, NC-activated systems are not preferred to study extensively. Even though low early age strength has been reported for NC-activated systems, they may demonstrate higher strength values at later ages than that of NH-activated ones. The reason for the higher compressive strength of NC-activated mixes is related to the formation of carbonated compounds [50]. The reaction mechanism of NCAS has been explained in different studies. Fernandez-Jimenez and Puertas [50] reported that the reason for the prolonged stiffening of NCAS is the initial formation of carbonate salts. Bernal et al. [51] indicated that the CO_3^{2-} ion concentration in the pore solution and the initially precipitated calcium carbonate govern the activation process to a significant extent. It is known that dissolved Ca^{2+} ions from the slag first react with CO_3^{2-} from the NC solution and generate carbonate salts such as calcite ($CaCO_3$) and gaylussite ($Na_2CaCO_3.5H_2O$) and increase pH through the release of hydroxide ions. This reaction appears before the precipitation of C-(A)-S-H gel, which consumes Ca^{2+}, hinders the increase of pH and causes dissolution deceleration of silicate species. Therefore, both the hardening and stiffening processes are considerably low due to the lack of Ca^{2+} ions and the presence of CO_3^{2-} ions in the

system. Obviously, to accelerate the reaction, carbonate ions should be removed from the medium, and also additional Ca^{2+} sources might be helpful for quick precipitation of calcite, gaylussite and following with the C-(A)-S-H gel formation. Many studies were performed to accelerate the reaction mechanism by replacing the NC with a higher alkaline activator, by incorporating silica fume, OPC, CaO, MgO, slaked lime, etc. into the NC-activated systems. Temuujin et al. [52] observed an enhancement in the mechanical properties of fly ash-based geopolymers cured at room temperature with the addition of calcium compounds. In that study, calcium hydroxide was found to be more effective than calcium oxide, and it was reported that calcium compound addition negatively affected the mechanical properties of geopolymer cured at 70°C. On the other hand, according to Kim et al. [53] calcium oxide was found to be more effective than calcium hydroxide in activating slag. In another study [54], the effect of MgO and NC on the reaction kinetics of slag or fly ash activation was examined, and it was concluded that MgO incorporation significantly influenced the reaction rate. Increasing the alkali content resulted in an increase in the strength at all ages as well. Alternative accelerators like calcined layered double hydroxides, reactive magnesia, and reactive MgO have also been reported as effective additive by means of NC activation. Atis et al. [55] studied the influence of activ ator type on the strength development of alkali-activated slag mortar and found that NCAS mortar exhibited comparable setting time and strength with respect to OPC mortar. Li and Sun [56] activated slag by using only NC and combination of NC+NH. In addition, they replaced slag with fly ash and reported that although the compressive strength value reaches 60 MPa at 28 days, 10% NC does not give any strength at 3 days.

3
MATERIALS, MIX PROPORTIONS & METHODS

3.1 Material Composition and Particle Size Distribution

Ground granulated blast furnace slag conforming to ASTM C989 [57], with a basicity coefficient ($(CaO+MgO)/SiO_2$) of 1.02 and a hydration modulus ($(CaO+MgO+Al_2O_3)/SiO_2$) of 1.33, was used as a primary raw material supplied by Eregli Iron and Steel Plant, Turkey. Slaked lime (CH) was one of the modifiers that contributed to the formation of the strength-giving phases in NC-activated systems. CEM I 42.5 R type OPC based mixes were also produced for comparison. The chemical composition of the slag, CH and OPC were determined by X-ray fluorescence and the physico-chemical properties are represented in Table 3.1.

Table 3.1 Physico-chemical properties of materials

Materials		**Slag**	**CH**	**OPC**
Chemical composition (% of mass)	SiO_2	40.6	0.8	18.9
	Al_2O_3	12.6	0.4	4.8
	CaO	35.7	69.0	63.7
	Fe_2O_3	1.2	1.2	3.3
	MgO	5.8	1.3	1.5
	Na_2O	0.8	-	0.4
	K_2O	0.7	0.1	0.7
	SO_3	0.1	-	3.3
	TiO_2	0.7	<0.1	-
	Mn_2O_3	0.8	-	-
	S	0.7	0.22	-
	Cl (ppm)	187	226	600
LOI		0.13	26.0	2.9
Specific surface area (cm^2/g)		5136	-	3854
Specific gravity		2.93	2.20	3.10

The particle size distributions of slag, CH, and CEN Standard sand were determined by a laser diffraction analyzer. Particle sizes range from 0.1 to 8 μm, with a d_{50} of 2.2 μm and from 0.1 to 40 μm with a d_{50} of 8 μm for CH and slag, respectively (Fig. 3.1).

Phase identification of slag was determined by X-ray diffraction (XRD) and is given in Fig. 3.2.

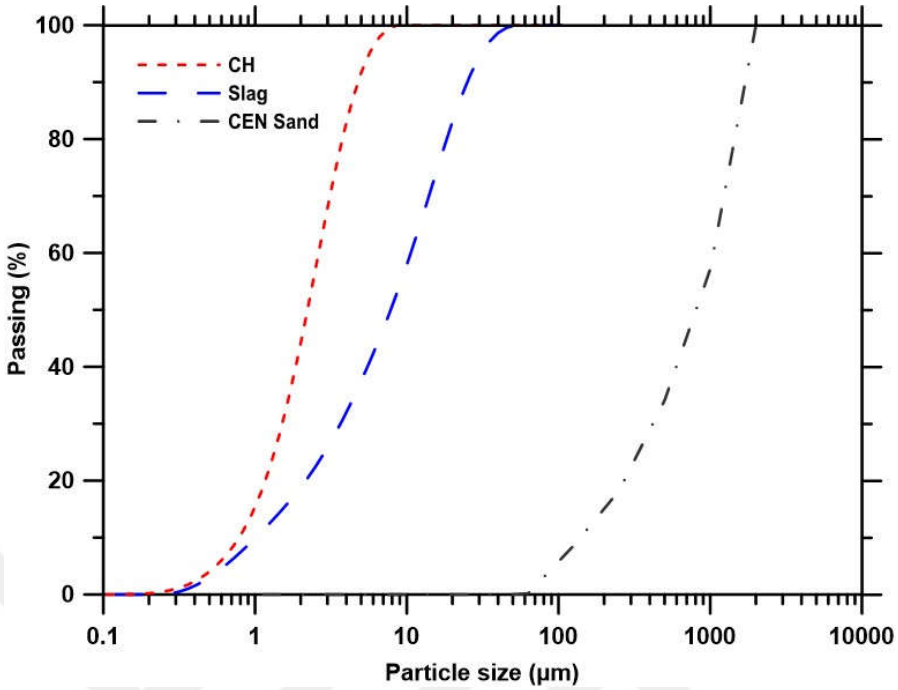

Figure 3.1 Particle size distribution of CH, slag and CEN standard sand

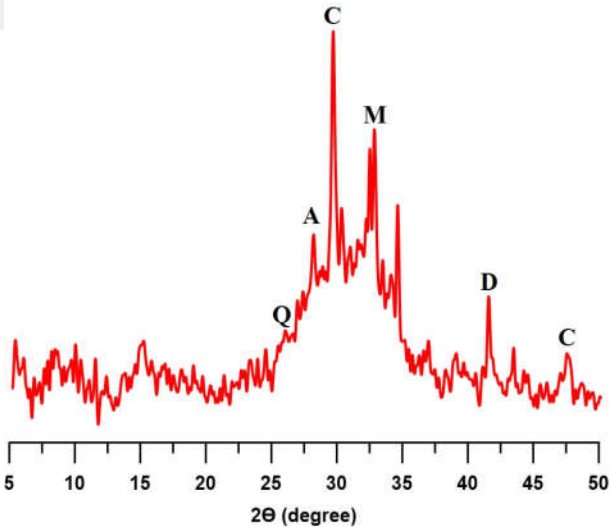

Figure 3.2 XRD pattern of slag. Q: Quartz, A: Akermanite, C: Calcite, M: Merwinite, D: Dolomite

Analytical grades of NC and NH were used as alkaline activators at 6% and 10% by weight of the binder and were prepared by pre-dissolving in tap water (Fig. 3.3). NC was selected as the primary activator, while NH was used as a secondary activator, replaced with NC at 20% and 40% by weight of the total activator amount. CH was used to accelerate the hydration process of the NCAS. The replacement ratio of CH

was chosen as 3% by weight of slag, which demonstrated the optimum amount to accelerate the stiffening sufficiently among a series of trial mixtures.

Figure 3.3 Activators

The water to binder ratio was set as 0.35 and 0.45 for paste and mortar mixes, respectively. In mortar production, CEN standard sand was used as aggregate proportioned with a volume of 50%. Table 3.2 provides the proportions of the mixes. A total of 12 NCAS mixtures were prepared and each mixture was coded as shown in Table 3.2, where NC refers to Na_2CO_3, the first number refers to NC percentage in the total activator concentration, the second number refers to total activator amount of mix by weight of the binder and "L" refers to lime (CH). Moreover, OPC based mixes that have the same proportions (water:binder:sand) of alkali-activated NCAS mixes were produced to compare the results.

Table 3.2 Mix proportions

Mixes	**Activator (%)**	**Binder types and proportions (%)**		**Activator types and percentages by weight**	
		Slag	**CH**	**NC**	**NH**
NC100-6	6	100	-	100	-
NC80-6				80	20
NC60-6				60	40
LNC100-6		97	3	100	-
LNC80-6				80	20
LNC60-6				60	40
NC100-10	10	100	-	100	-
NC80-10				80	20
NC60-10				60	40
LNC100-10		97	3	100	-
LNC80-10				80	20
LNC60-10				60	40

After the productions, all samples were stored in the laboratory conditions with a temperature of 20 ± 2°C and RH of 55 ± 5% until the testing day. To explore the effect of different type of fibers, selected NC-activated mixes were reinforced with polypropylene (PP) and steel (ST) fibers with a constant ratio of 2%. The properties and geometry of the fibers are shown in Table 3.3.

Table 3.3 Fiber properties

Fiber type	**Length (mm)**	**Diameter (μm)**	**Aspect ratio**	**Tensile strength (MPa)**	**Density (g/cm^3)**
Steel	13	150	87	3000	7.85
Polypropylene	12	30-40	300-400	570-660	0.91

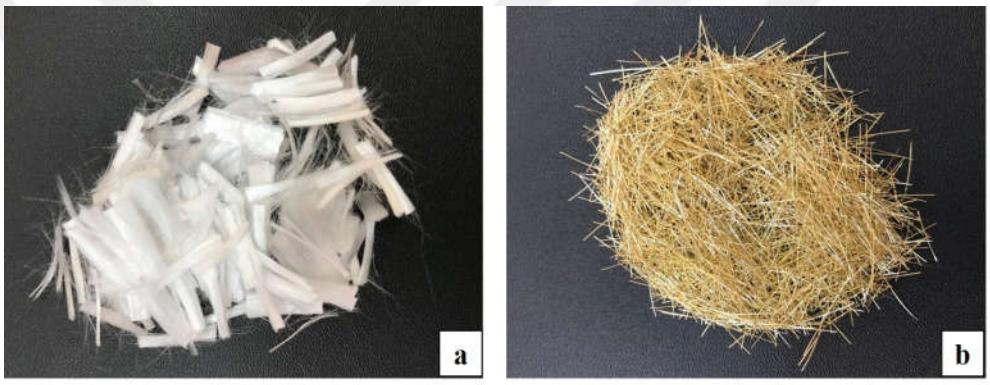

Figure 3.4 (a) Polypropylene and (b) steel fibers

3.2 Sample Preparation

Activator solutions were prepared 1 hour prior to mixing and allowed to cool to the ambient temperature (22 ± 2 °C). For the preparation of the paste samples, powder materials (slag and CH) were blended in a table-top mixer for 30 sec at a low speed (140 ± 5 rpm). Then, the activator solution was added and mixed at the low speed for 30 sec and at a high speed (285 ± 5 rpm) for 90 sec. The mixer was stopped at the end of two and a half min to scrape any adhering paste from the sides of the mixing bowl and paddle. After that, the pastes were mixed 3 more minutes at high speed. In mortar productions, CEN standard sand was first mixed with the raw material for 1 minute at low speed, and then the rest of the mixing procedure was repeated.

3.3 Fresh-State Properties

3.3.1 Flow Diameter Measurement

The flow of pastes was determined by the mini-slump test following the ASTM C1437 [58] (Fig. 3.5). The pastes were prepared in a bench-top mixer as the procedure explained above and then placed in flow mold; a Hägermann cone with standard dimensions of 70 mm top and 100 mm base diameters and a height of 50 mm. The fresh paste was initially filled into the flow mold and after about 15 s the mold was lifted vertically and the spread diameters of the paste were measured along with two perpendicular directions. The average diameter was considered as the flowability of the pastes. The initial flow of pastes was measured immediately after completing the mixing operation and repeated every 30 min up to 90 min.

Figure 3.5 Flow test set up

Total flow loss (Δ_{flow} (%)) of the mixes are determined as the ratio of the difference between initial (d_{ini}) and final flow diameter (d_{final}) to initial flow diameter (Eq. 3.1).

$$\Delta_{flow} = (1 - \frac{d_{final}}{d_{ini}}) \times 100 \tag{3.1}$$

3.3.2 Setting Time

The setting time of the mixes was determined following the ASTM C191 [59] with the automatic Vicat apparatus (Fig. 3.6). The paste samples are filled into the conical ring and the penetration depth of the Vicat needle was measured every 15 minutes. The initial setting time was determined by recording the elapsed time between the time of the initial contact of the binder with alkali solution and the total duration of the penetration of 25 mm. The final setting time was obtained by when the needle could not be able to penetrate into the paste first.

Figure 3.6 Automatic Vicat apparatus

3.3.3 pH Evolution

The liquid phases of the paste samples were extracted by centrifugation to carry out pH measurements. After the mixing procedure described in Section 3.2 was completed, 40 ml of the paste was injected into the tubes and then the mixtures were centrifuged at an acceleration of 9418 g for 20 minutes. Afterward, the solutions were filtered (0.45 μm) to obtain clean pore solutions (Fig. 3.7). The pH measurements were taken immediately using a glass electrode and Hanna pH meter with an accuracy of 0.01 (Fig. 3.8). Since the pH values of the final solution were too high (i.e., pH $>$ 14), they were diluted with a factor of 40 [60].

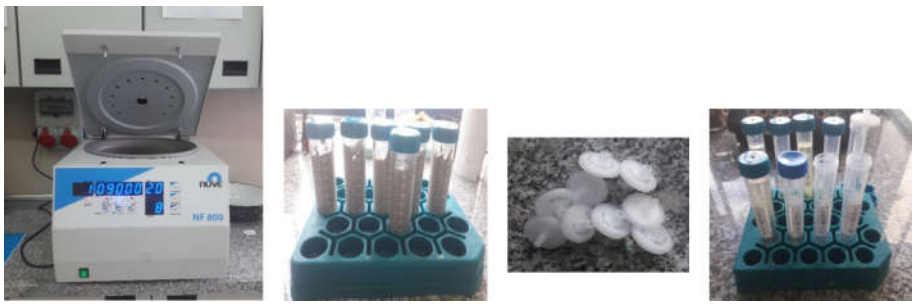

Figure 3.7 Pore solution extraction steps

It is known that initial pH is an important parameter which is effective in initiating the dissolution of slag [61]. In this thesis, to evaluate the reaction mechanism of NCAS, pH measurements were taken at 30, 90 and 180 min. 30 min was considered as the initial pH, while 90 and 180 min were the latest measurement times when the pore solution could be extracted from pastes for mixes containing 6% and 10% activator, respectively.

Figure 3.8 pH measurement

3.3.4 Carbonate Ion Concentration

Carbonate ion concentrations were determined in the extracted pore solutions by alkalinity [62] (Fig. 3.9). Measurements were taken at 30 and 90 min for NC-6 and LNC-6 mixes and at 30 and 180 min for NC-10 and LNC-10 mixes. To avoid precipitation, the solutions were analyzed immediately after the centrifugation process. CO_3^{2-} concentration was calculated according to the equations presented in Table 3.4.

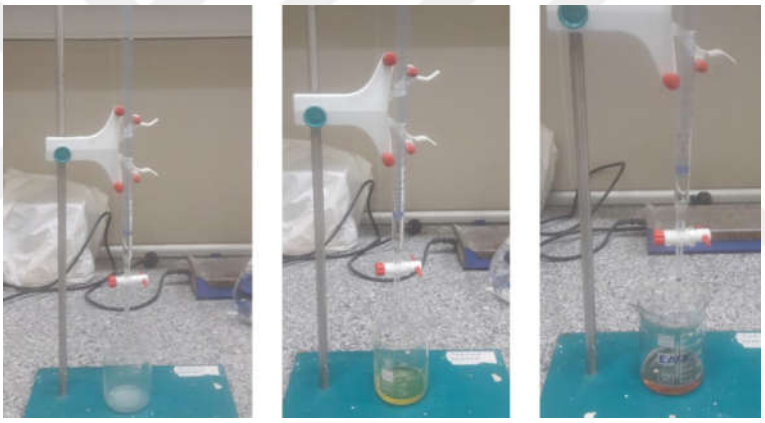

Figure 3.9 Alkalinity test

Table 3.4 Alkalinity relationships

Result of titration	Hydroxide alkalinity	Carbonate alkalinity	Bicarbonate alkalinity
P* = 0	0	0	T*
P < 1/2T	0	2P	T-2P
P = 1/2T	0	2P	0
P > 1/2T	2P-T	2(T-P)	0
P < 1/2T	T	0	0

P: Phenolphthalein alkalinity, T*: Total alkalinity*

3.3.5 Rheological Properties

To evaluate the fresh state properties of pastes, rheological tests were conducted using a commercial *Anton Paar Rheolab QC* rheometer (Fig. 3.10) with a four-blade vane (length of 40 mm and diameter of 11 mm) (Fig. 3.11). Approximately 35 ml of the paste sample was injected into the rheometer cup. The time elapsed between mixing and measurement was approximately 5 min. The temperature of the cup was kept at 20 ± 0.5°C during the test.

Figure 3.10 Rheometer

Figure 3.11 Four blade vane and cup

A strain-controlled mechanism was used to evaluate the yield stress and plastic viscosity of the samples. Shear stress (τ) and shear rate ($\dot{\gamma}$) are the fundamental characteristics studied in rheology as the former is the force per unit area that a fluid requires to start flowing and the latter one is the velocity gradient. In this study, the maximum shear rate was chosen as 100 s^{-1} because this rate also represents the practical conditions as stated by other researchers [63–66]. A wide range of shear rates is beneficial in obtaining a proper portion of the stress plateau in the shear stress–shear rate relationship [67]. Thus, a wide shear rate of 0.05-100 s^{-1} was applied, as generally considered in OPC pastes as well [63–68]. The rheological procedure consists of a constant pre-shear phase at 100 s^{-1} lasting for 30 s to obtain a homogeneous paste, followed by a stepped ramp up from 0.05 to 100 s^{-1}, and a stepped ramp down from 100 to 0.05 s^{-1} as

shown in Fig. 3.12. Each shear rate was applied for 20 sec to achieve the steady-state shear stress and the measurement completed approximately in 7 min. The data was recorded every second at each step, and the last 10 data points at a given shear rate were averaged to represent the average resultant shear stress.

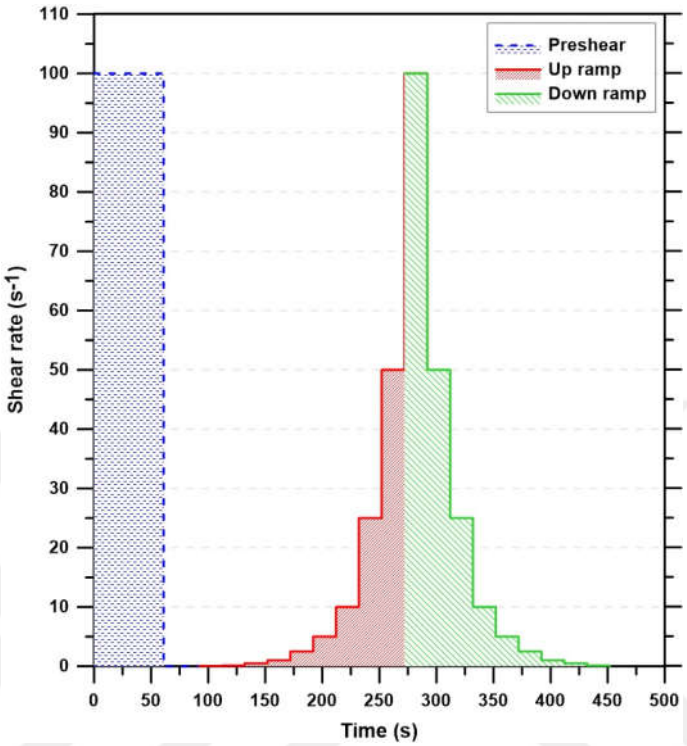

Figure 3.12 Applied shear rates versus time

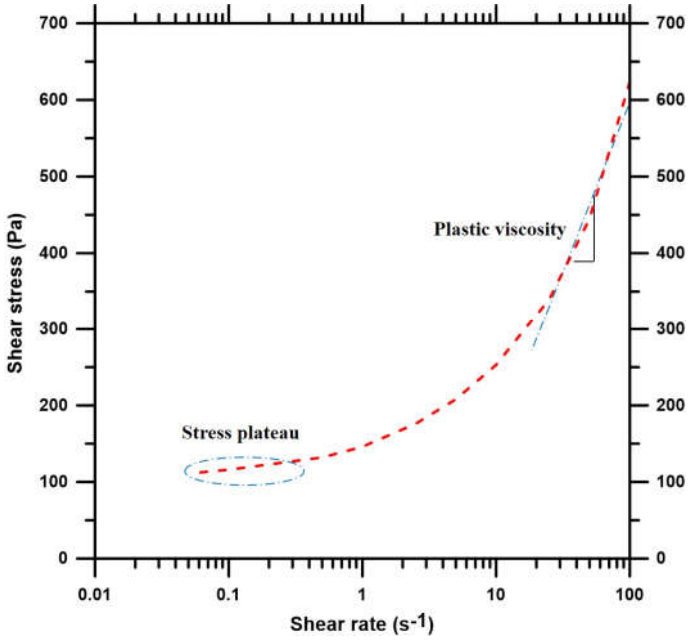

Figure 3.13 The procedure to determine the rheological parameters

The yield stress is defined as the limiting shear stress at which the material begins to flow while the plastic viscosity denotes the resistance of the fluid to continuous flow

[69]. The steady-state values of shear stress and the related shear rate in the down ramp were used to determine the rheological properties. The logarithmical mode was applied for the identification of yield stress in order to have a higher resolution at low shear rates. The plateau region obtained at low strain rates of the ramp downside was considered to be the yield stress. The slope of the line formed by ramp down values between the shear rate range of 25 s^{-1} and 100 s^{-1} was recorded as plastic viscosity (Fig. 3.13).

3.4 Compressive Strength Development & Microstructural Evolution

3.4.1 Compressive Strength Development

The compressive strength of mortar samples was determined according to the ASTM C109 [70]. The mortar samples were cast into 50 mm cubic molds. Afterward, the molds were covered with a plastic sheet to prevent any moisture loss. All specimens were kept in laboratory conditions (20 ± 2°C and RH 55 ± 5%) until the test day. The compressive strength test was carried out at 3, 7, 28 and 90 days (Fig. 3.14) and the average of three repetitions were considered as the compressive strength for each age.

Figure 3.14 Compressive strength test

3.4.2 X-ray Diffractometry

The X-ray diffractometry (XRD) analysis was performed by using a Cu tube (45 kV, 40 mA) *XPERT-PRO* diffractometer at 3, 7 and 28 days on the powder of the paste samples (Fig. 3.15). The patterns were collected in the range of 5° to 55° (2θ) with a step size of 0.02° (2θ) and a measuring time of 1 s/step.

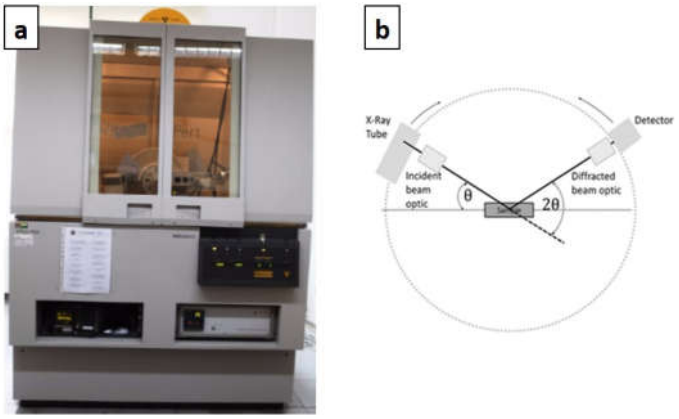

Figure 3.15 (a) X-ray diffractometer and (b) schematic diagram of X-ray diffractometer

3.4.3 Fourier Transform Infrared Spectroscopy Analysis

The Fourier transform infrared spectroscopy (FTIR) analysis was performed using a *Bruker Tensor 27* FTIR Spectrometer (Fig. 3.16). All spectra were obtained with 32 scans from 4000 to 400 cm^{-1} per spectrum. The band between 600 and 1800 cm^{-1} was considered for analyzing the results since the reaction products are determined at this range. This analysis was performed at 3, 7 and 28 days of curing.

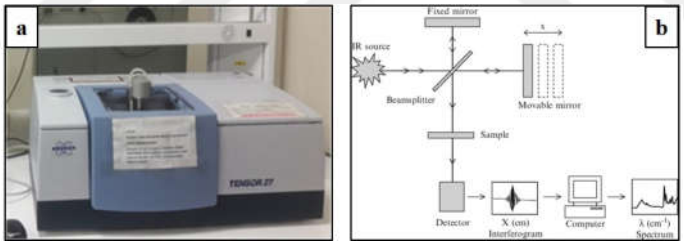

Figure 3.16 (a) FTIR spectrometer (b) schematic sketch of the FTIR spectrometer

3.4.4 Thermogravimetry Analysis

Thermogravimetric and derived thermogravimetric analyses (TGA-DTG) were performed using *EXSTAR 600* thermal analyzer (Fig. 3.17). About 20-25 mg powder of the paste samples were used and TGA-DTG analysis were conducted at the curing age of 28 days. The heating rate was 15°C/min from 20°C to 900°C using a platinum holder and nitrogen as the carrier gas. The mass loss at different temperatures was used to quantify the amounts of reaction products.

Figure 3.17 Thermogravimetric analyzer

3.4.5 Scanning Electron Microscopy

Scanning electron microscopy (SEM) analysis was performed on small, broken paste samples for the microstructural observation of selected samples. The samples were first impregnated with an epoxy resin. After 24 hours, the samples were ground with silicon carbide-based sandpapers, successively coarser to finer grit size of 180, 320, 500 grade (Fig. 3.18). Subsequently, all samples were polished using cloths embedded with a polycrystalline diamond suspension of sizes 6 and 0.20 μm. Each grinding and polishing stage was no longer than 3 minutes. Subsequently, the polished specimens were coated with Au and then analyzed at an accelerating voltage of 15 kV with a *ZEISS EVO LS10* (Fig. 3.19).

Figure 3.18 Sample preparation and grinding for SEM analyses

On the 28 and 56 days of the reaction, secondary and backscattered electron images were taken to determine the hydration products and to display the area fraction of the hydrated phase and unhydrated slag particles, representing the influence of different modifiers (CH and NH) on the hydration degree. Secondary electron imaging used to determine the morphology and hydration products in plain and modified NCAS mixes. Atomic ratios were determined using energy dispersive spectroscopy (EDS) measurement on the matrix phase with 80 spots per sample. The backscattered images (BSE) were used to determine the unhydrated slag particles of mixes. The BSE images were collected at 500× magnification.

Figure 3.19 Scanning electron microscope

To analyze the unhydrated slag particles, an image processing software (ImageJ) based on the maximization of the grey level histogram (GLH) curve was used to extract the area fraction of unhydrated slag (A_s). Images were prepared in two steps: first, by the entropy maximization of the GLH curves threshold, and thus a binarized image of the anhydrous slag particles was obtained; second, a phase of unhydrated slag was rebuilt and the A_s acquired.

3.4.6 Pore Size Distribution

The pore structure parameters such as pore volume and pore size distribution of the NCAS paste mixes were determined by using Mercury intrusion porosimetry (MIP) on the 56^{th} day of curing. The samples were kept at 60°C for 2 h to evaporate free water before the MIP test. The test was performed using *Quantachrome-Poremaster 60* porosimeter (Fig. 3.20), which enables to apply an injection pressure up to 55,000 psi and reaching a cylindrical pore diameter ranges from approximately 0.004 μm to 200 μm. The Washburn equation (Eq. (3.2)) was used to calculate the diameter of pores intruded by mercury at each pressure step [71].

$$\mathrm{D} = -\frac{4\gamma\cos\theta}{\mathrm{P}} \tag{3.2}$$

where D and P represent the pore diameter (μm) and the applied pressure (MPa), respectively. The contact angle (θ) and surface tension (γ) values used were 140°C and 0.480 N/m, respectively. Total porosity was calculated by multiplying the bulk

Figure 3.20 Mercury intrusion porosimeter

density of the material with the maximum intruded volume of mercury. The threshold pore diameter was extracted from the pore diameter corresponding to the highest rate of mercury intrusion per change in diameter (dV/dD) [72].

3.5 Fracture Characterization

3.5.1 Three-Point Bending Test

Flexural strength and fractural characterization are determined at 28 days of the reaction on four different 10% NCAS (NC100-10, NC60-10, LNC100-10, and LNC60-10) mixes. The mixes are selected considering the representing the effect of modifiers. To explore the effect of different types of fibers, PP and ST fiber was incorporated with a volume fraction of 2%. To compare the results, OPC-based mixes were also produced.

The rectangular, 330 mm (length) × 76 mm (depth) × 25 mm (width) sized beam specimens with a 25 mm notch at mid-length were produced (Fig. 3.21) and two replicate beams were tested for each mixture. The clear span length was 300 mm and the load was applied through displacement control at a rate of 0.03 mm/min using *MTS* closed-loop servo-controlled universal testing machine with the maximum capacity of 100 kN. Mid-span deflection was measured by using the two linear variable differential transducers (LVDT) installed on each face of the specimen. Additionally, the crack mouth opening displacement (CMOD) was measured by using a gauge clipped to the two 1.73 mm thick (H_0) steel knife edges fixed at the bottom of the beam (Fig. 3.22). The loading was terminated at a final CMOD limit of 0.2 mm and 2.25 mm for plain and fiber-reinforced mortar mixes, respectively.

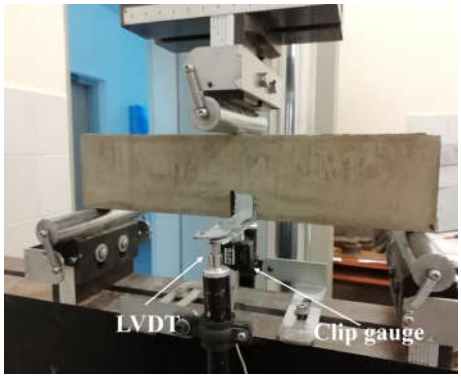

Figure 3.21 The test set up for the three-point bending test

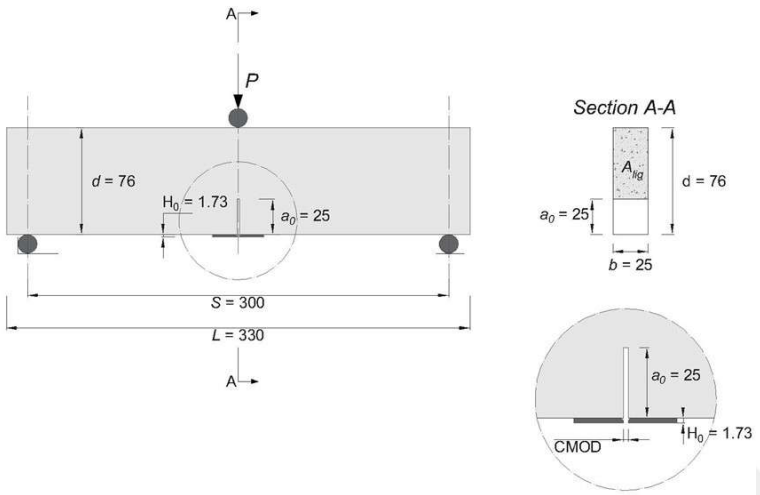

Figure 3.22 Test configuration and size of the notched beam specimen

The fracture properties were determined using the double-K fracture model. The fracture parameters, initiation toughness (K_{Ic}^{ini}), unstable fracture toughness (K_{Ic}^{un}), effective crack length (a_{eff}), critical crack tip opening displacement ($CTOD_c$) and fracture energy (G_f) were calculated by using the related equations given in Chapter 6. For a notched beam specimen with center-point loading, flexural strength is obtained using Eq. 3.3 as follows:

$$f = \frac{3PL}{2b(d-a_0)^2} \tag{3.3}$$

3.6 Durability Properties

3.6.1 Drying Shrinkage

Shrinkage measurement was performed following the ASTM C596 [73] on mortar prisms with a size of 25 × 25 × 285 mm. Two replicate prisms were used for each mix.

All samples were kept at laboratory conditions at 20 ± 2°C and relative humidity of 55 ± 5%. The length change measurements were taken by a digital length comparator up to 180 days (Fig. 3.23). The weight of each prism sample was also measured before each length measurement to determine the mass loss.

Figure 3.23 Length change measurement of prismatic mortar beams

3.6.2 Water Sorptivity

Water sorptivity test was performed at 56 days to determine the rate of water absorption through the surface of the mortar samples. The sorptivity of mortar samples was determined following the ASTM C1585 [74].

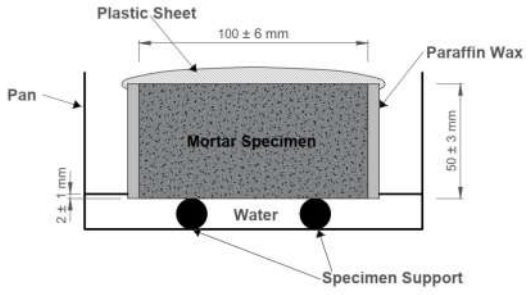

Figure 3.24 Sorptivity test set up

This test method consists of two main steps: first preconditioning of the mortar samples and then exposing only one surface of the sample to water for a definite time (Fig. 3.24). Samples were first kept at 50°C and 80% relative humidity for 3 days, and then placed in sealed containers and kept for 15 days at 23°C, which allows the redistribution of internal moisture throughout the sample. When the preconditioning was completed,

samples were taken from the chambers and the outer circumference surface of the samples was sealed with the paraffin wax. The top surface of the sample was covered with a plastic sheet to avoid evaporation (Fig. 3.24).

The change in mass was recorded at relatively frequent time intervals for the first 6 h once the sample was placed into the pan. Afterward, only one measurement was taken per day for the next 8 days. The initial and secondary absorption (I_{ini} and I_{sec}) were calculated using the following equation (Eq. 3.4).

$$\mathrm{I} = \frac{\mathrm{m}_t}{\mathrm{a} \times \rho} \tag{3.4}$$

where I and m_t represent the normalized absorbed fluid volume and the mass change of specimen at time t; a and ρ represents the area of the specimen exposed to the water and the density of water respectively. The sorptivity coefficient k was calculated with the following equation (Eq. 3.5).

$$\mathrm{k} = \frac{I}{\sqrt{t}} \tag{3.5}$$

The sorptivity coefficients were calculated using least-square methods since this method gives more accurate results than the slope of the best-fitted straight line. The primary sorptivity coefficient (k) was determined considering the values for the first 6 h, while the secondary sorptivity coefficient (k_{sec}) was determined considering the values between 1 and 8 days.

3.6.3 Chloride Migration Coefficient

The chloride migration test was carried out on mortar samples as per NT Build 492 [75]. The cylinder samples (ϕ100 × 200 mm) were sliced into two parts, each of 50 mm thickness after 56 days of curing at room temperature of 20 ± 2°C. The samples were preconditioned by vacuum saturation with a saturated $Ca(OH)_2$ solution. The catholyte and anolyte solutions used were 10% NaCl and 0.3 N NaOH, respectively. For most of the mixes, the test duration was maintained at 24 h and the appropriate range of voltages was applied according to the initial current (Fig. 3.25). At the end of the test, the specimens were split into two halves and sprayed with silver nitrate ($AgNO_3$) solution to determine the chloride penetration depth according to the precipitation of silver chloride (AgCl).

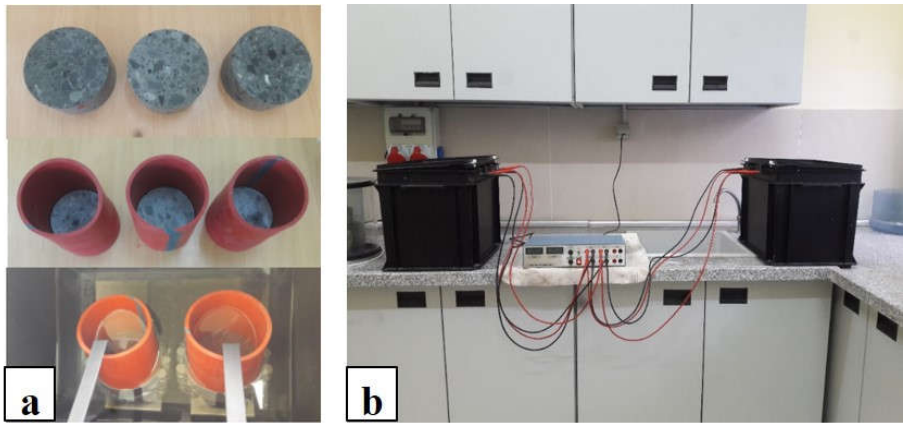

Figure 3.25 (a) Sample preparation and (b) chloride migration test set up

The non-steady state migration coefficient (D_{nssm}) was calculated by the following equations (3.6-3.8):

$$D_{nssm} = \frac{RT}{zFE} \frac{X_d - \alpha\sqrt{X_d}}{t} \tag{3.6}$$

$$E = \frac{(U-2)}{L} \tag{3.7}$$

$$\alpha = 2\sqrt{\frac{RT}{zFE}} \times erf^{-1}\left(1 - \frac{2c_d}{c_0}\right) \tag{3.8}$$

where U represents the absolute voltage (V), L represents the specimen thickness (m), z represents the valence of the chloride ion, F is the Faraday constant, R is the molar gas constant, T represents the average value of the initial and final temperatures in anolyte solution (K), X_d represents the average value of the penetration depth (m), t is the test duration (sec), c_d is the chloride concentration at which the color changes and c_0 is the chloride concentration of the catholyte solution.

4
FRESH-STATE PROPERTIES

4.1 Introduction

In previous studies, generally, the reaction kinetics of NH and sodium silicate activated slag system has been methodically studied and explained. Even though NC presents a great potential in AAMs, up till now, it has been used in a limited number of studies due to its delayed setting time and slow strength development [51, 54, 76, 77].

Since the pH of the NC solution is below 12, the dissolution process is slow [10]. Several arguments are reported by researchers in regard to how hydration proceeds in NCAS. Jimenez and Puertas [76] reported that the reason for the prolonged stiffening of NCAS is the initial formation of carbonate salts. Bernal et al. [51] indicated that the CO_3^{2-} ion concentration in the pore solution and the initially precipitated calcium carbonate govern the activation process to a significant extent. It is well known that Ca^{2+} ions from the slag react with CO_3^{2-} from activator and generate carbonate salts such as calcite ($CaCO_3$) and gaylussite ($Na_2CaCO_3 \cdot 5H_2O$), leading to increase in pH through the release of hydroxide ions. This reaction appears before the precipitation of C-(A)-S-H gel which consumes Ca^{2+}, hinders the increase of pH and causes dissolution deceleration of the silicate species. Since the excess amount of CO_3^{2-} ions existing in the system, the pH increases very slowly because of the opposing protonation process of the anhydrous slag. When the CO_3^{2-} ions are exhausted, the next stage of the reaction is similar to that of NH-activated slag, forming the typical phases such as C-(A)-S-H and hydrotalcite [10].

To accelerate the hydration process in NCAS, secondary additives and/or activators such as NH, sodium silicate, OPC, silica fume, CaO, and reactive MgO were used in the previous studies [13, 56, 78–81]. Ke et al. [10] investigated the reaction kinetics of NCAS by using calcined layered double hydroxides, which removed the CO_3^{2-} ions, yielding a significant rise in the pH and, consequently, resulted in a fast reaction. In another study [82], it was indicated that the combination of reactive MgO might be a suitable alternative for activation of slag. In a limited number of studies, it was found

that CH can accelerate the hydration process of NCAS efficiently and also increase the compressive strength [80, 82–84]. The primary reason for this acceleration is the removal of a higher amount of carbonate ions from fresh paste, which yields an increase in the pH [51]. Also, it involves in the formation of a strength-giving phase of C-(A)-S-H and provides extra surfaces for precipitation of reaction products [85].

It is obvious that the free carbonate concentration in pore solution, pH evolution, and formation of reaction products at the early stage, play an important role in the fresh state behavior of NCAS. As a result, a deeper understanding of the reaction process of NCAS, especially at an early age, is of great interest. Therefore, the main aim of this chapter is to explore the fresh state properties of NCAS including setting time, flowability and pore solution chemistry. To accelerate the setting process, two different modifiers were used. NH was used as a secondary activator and CH was added as a carbonate binding agent, and their effects on the hydration process are reported. Moreover, the relationship between setting time, carbonate ion concentration and pH evolution are discussed, rheological properties such as yield stress and plastic viscosity were also investigated.

4.2 Flow Diameter Measurement

The flow diameters of the pastes were determined by the mini-slump test and the results are shown in Table A.1 and Fig. 4.1. As can be seen from Fig. 4.1 that initial paste fluidity varied only slightly with the activator concentration (NC-6 and LNC-6 mixes ranged between 190 and 220 mm and NC-10 and LNC-10 mixes ranged between 198 and 225 mm), while NH-substitution increased from 0 to 40% flow diameter increased slightly for both NC and LNC mixes. On the other hand, OPC-based mixes presented the highest flow diameter for all measurement times.

It was observed that for all measurement times, the highest flow spread was achieved in 40% NH-substituted mixes (NC60-6 and NC60-10) among the NCAS mixes. Thus, it can be concluded that NH-substitution affected the flow spread rate positively, as a higher amount of NH led to a higher flowability. Moreover, NC60-6 and NC60-10 mixes presented the closest values to OPC. It was thought that the reason for this improvement might be associated with the delayed formation of reaction products.

Increase in activator amount, from 6% to 10%, increased the fluidity for both initial and further measurement times. Again, the reason for this can be related to the delayed formation of reaction products. In high alkali concentration, to initiate the formation of strength-giving phases more time is required.

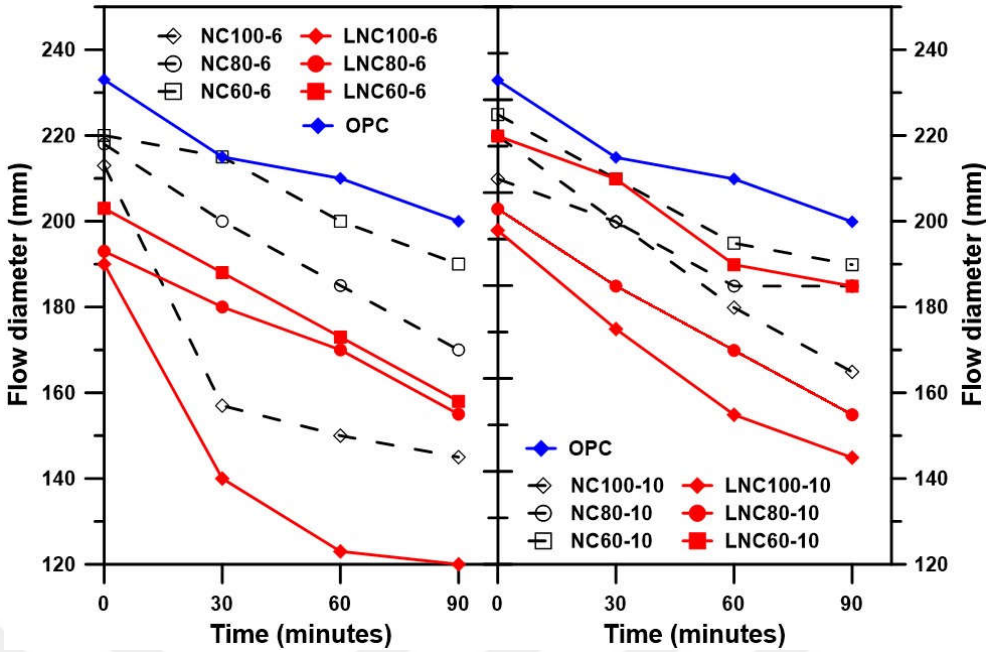

Figure 4.1 Flow diameter of NCAS and OPC-based mixes

CH-substituted (LNC) mixes presented lower flow spread values than the plain (NC) mixes. A few reasons may explain this issue: firstly, CH has finer particle size distribution than the slag (Fig. 3.1), so it has a higher specific surface area and thus absorbs a higher amount of water. Secondly, the reaction products which provide stiffening may form earlier than the plain NC mixes.

Flow loss values for each measurement time are given in Table A.2, and the total flow loss between the initial and final (90 min) measurements are given in Fig. 4.2.

It can be seen that the maximum loss for the 30 min measurement was observed in NC100-6 and LNC100-6 mixes with 26.3%, and most of the total loss was seen at this measurement time. OPC demonstrated the minimum total flow loss values (14.2%). Total flow loss reached the maximum values in the mixes activated by NC as a sole activator (NC100-6, LNC100-6, NC100-10 and LNC100-10) and generally, the flow loss decreased by NH-substitution.

One of the reasons for the flow loss of paste mixes can be due to the fast consumption of the CO_3^{2-} through the precipitation and formation of gaylussite and/or calcite with the presence of Ca^{2+} ions from slag and/or CH [85, 86]. The flowability might be affected negatively due to this early age reaction. To explain the effect of free CO_3^{2-} concentration on flowability, pore solutions were extracted by centrifugation process at 30-180 min after mixing. The results are presented and discussed in Section 4.5.

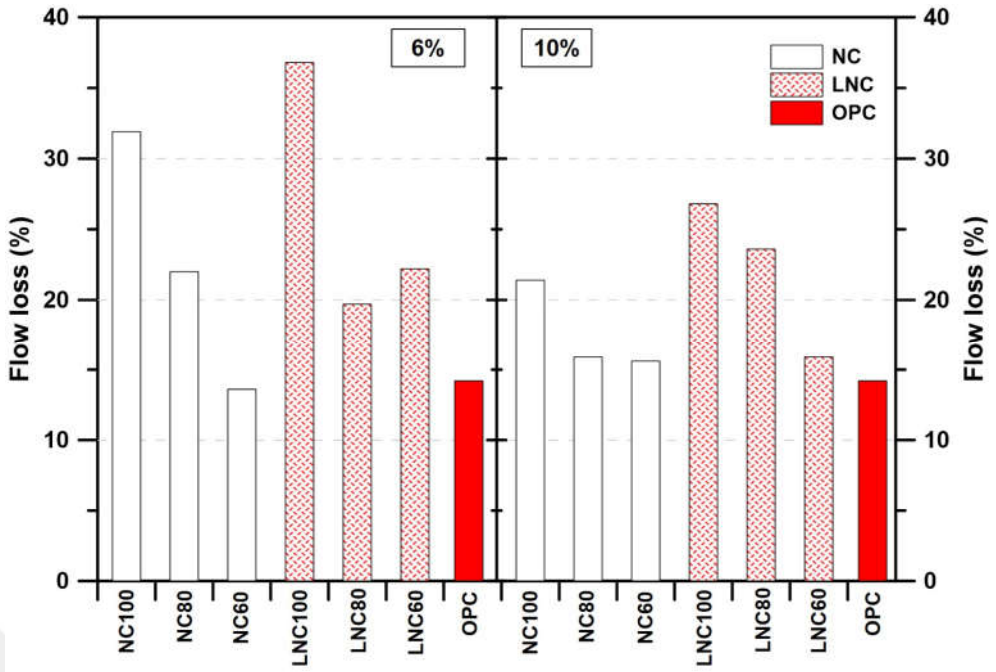

Figure 4.2 Flow loss of NCAS and OPC-based mixes

4.3 Setting Time

Setting time of NCAS system has investigated recently, however, the studies were performed only to compare the results of NC-activated systems with other activators [55, 76, 87–90]. In NC-activated systems, mostly prolonged reaction process is reported, i.e. 3-5 days [51, 76]. In a recent research [51], it was indicated that the prolonged reaction process of NCAS depends on the formation of $CaCO_3$ and removing CO_3^{2-} anions from the medium. It should also be noted that shorter setting times were also reported for NCAS samples in a few studies [54, 82, 91]. Jin et al. [82] activated slag with 4% and 8% NC by wt. and reported that the samples were able to demould the next day of production. Abdalqader et al. [54] reported that the NCAS samples could be demoulded after 2 days of curing. Table 4.1 summarizes the setting time and compressive strength values reported in previous studies. However, it is difficult to compare the results since many factors, e.g. chemical compositions, fineness of precursors, alkali concentration, curing method and temperature, are effective in setting time.

In this study, the setting time test was performed in order to ascertain the effects of two modifiers, NH and CH substitution, and the dual effect of these two modifiers. Table A.3 and Fig. 4.3 present both the initial (t_{ini}) and final setting times (t_{final}) of the NCAS pastes. It can be easily seen that plain NCAS mixes presented high setting values, more than 30 hours.

Table 4.1 Setting time and compressive strength values of NCAS in literature

References	Activator concentration (%) and fineness (m^2/kg)	Initial setting time	Final setting time	28-days compressive strength (MPa)
[78]	4% Na_2O/460	> 3 days	> 3 days	50.2
[55]	4% Na	190 min	306 min	24.7
	6% Na	180 min	294 min	27.6
	8% Na	170 min	288 min	35.7
[90]	7% Na	30 min	46 min	26.0
[91]	3% Na_2O/450	-	-	42.0
	3% Na_2O/900	-	-	50.0
	4% Na_2O/450	-	-	42.0
	4% Na_2O/900	-	-	56.0
[80]	3.5% Na_2O	455 min	-	55.0
[87]	3% NC	60 min	-	-
	5% NC	60 min	-	-
	7% NC	40 min	-	-
[92]	3% Na_2O	-	-	26.0
	5% Na_2O	-	-	50.0
[93]	4% Na_2O	60 min	135 min	29.2

The setting time of the NC-6 and NC-10 mixes ranged between 1140 and 1800 min and from 960 to 1860 min, respectively, which was quite higher than the OPC-based mixes (300 min). With the substitution of NH, e.g. 20%, the final setting time decreased to some extent. The decrement in the final setting times in NC80-6 and NC80-10 mixes as compared to NC100 mixes were 20% and 32%, respectively. Similar findings were reported in previous studies. Kovtun et al. [80] studied the activation of NCAS with different accelerators, e.g. silica fume, OPC, and slaked lime, and reported that these accelerating admixtures shortened the setting time and decreased the workability. Shi and Day [61] studied the early age reaction kinetics of slag activated by different types of activators, e.g. NaOH, $Na_2SiO_3.5H_2O$, Na_2CO_3, Na_3PO_4, Na_2HPO_4, and NaF, at different temperatures (25°C and 50°C). They concluded that pH plays an important role in the initial reaction rate. However, Ca compounds dominate the further reaction. Ke et al. [10] reported that the reaction of NCAS can be accelerated by using calcined layered double hydroxide (CLDH), since CLDH removes carbonate anion from the

medium, yielding a significant increase in the pH. Similarly, in this study, it was found that the reason for the acceleration of the reaction by NH-substitution is the higher pH values and lower carbonate ion concentrations.

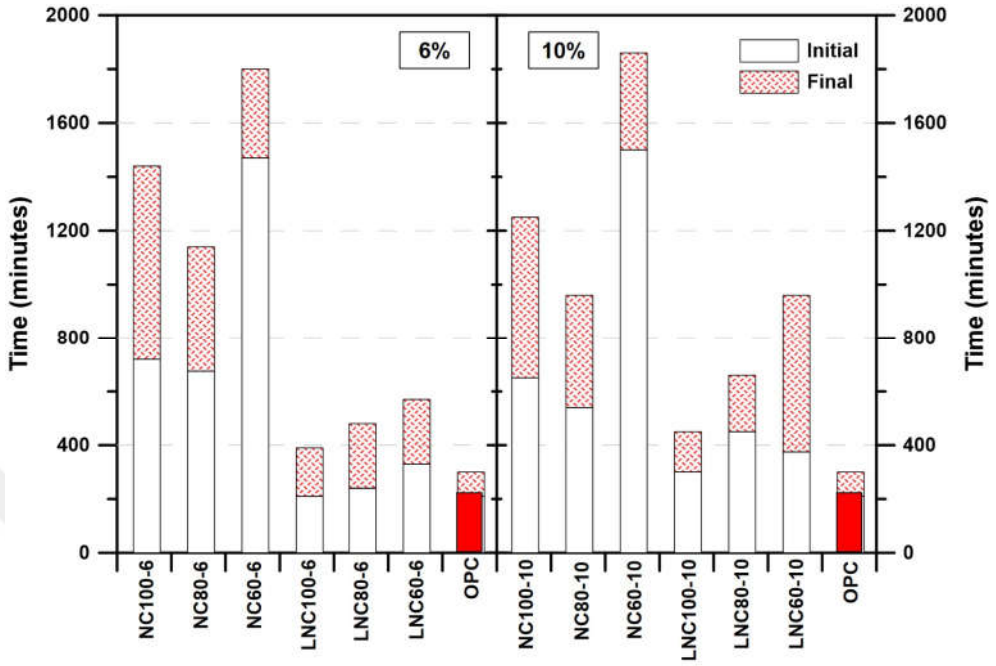

Figure 4.3 Setting values of NCAS and OPC-based mixes

The presence of NH induces a higher pH due to a higher amount of dissolved OH^- ions. Since high pH level of the medium provokes the dissolution of the raw material, higher pH levels affect the setting process of NCAS positively. Although the 20% NH replacement decreases the setting time, the further increase in NH replacement, i.e. 40%, led to longer setting time, even reached higher values than that of plain NCAS mixes (NC100-6 and NC100-10) (Fig. 4.3). The possible reason for this phenomenon explained as follows: with the increase of OH^- ions, dissolved ion concentration increases in the medium. This large amount of dissolved ions in the medium limits the ion mobility and lowers the rate of reactions. Limited ion mobility decelerates the reaction kinetics and formation of reaction products. Thus, limited ion mobility causes a delay in the formation of coagulated structures [94]. Alonso and Palomo [94] studied the metakaolin+calcium hydroxide activation with NH solution at different molarities ranges between 10 M and 18 M and indicated that there is a threshold concentration for NH amount for activating the metakaolin. Beyond a specific concentration, precipitation of the reaction products delayed because of the lower rate of metakaolin dissolution.

It should be emphasized that the setting time of the NCAS mixes mostly dependent on the dissolved CO_3^{2-} and Ca^{2+} concentration in the medium. A higher amount of Ca^{2+} enhances the fast consumption of carbonate ions from the medium by the formation of calcite and/or gaylussite, consequently results in the lower setting time [95].

As the amount of activator increased from 6% to 10%, the setting time decreased in plain and 20% NH-substituted mixes (NC100-10 and NC80-10), while almost no change was observed in 40% NH-substituted mixes (NC60-10). Actually, with the increase in activator concentration, a high amount of CO_3^{2-} releases and this phenomenon would be expected to cause a delay in the setting time. However, with the increase in activator dosage, pH increases and the change in pH level might be effective for dissolution of the slag and accordingly in the acceleration of the reaction. Yuan et al. [92] indicated that an increase in NC dosage, slightly accelerates the reaction.

On the other hand, in CH-substituted LNC-10 mixes, setting time increased. Insufficient dissolution of CH due to the common ion effect and/or low ion mobility might be the reasons for this delay. The common ion effect is defined as a suppression of the ionization of a weak acid or a weak base by the presence of a common ion from a strong electrolyte [96]. Since NH is a stronger base than CH, the solubility of CH might be suppressed by the presence of NH. Shi and Krivenko [13] indicated that the presence of alkalis decreases the solubility of Ca^{2+} due to the common ion effect. Granizo et al. [97] indicated that calcium ions dissolved from CH can take a part in the formation of C-(A)-S-H gel in low alkalinity systems. Conversely, high OH^- concentrations may hinder CH dissolution [69, 98]. With the CH-substitution, both initial and final setting times decreased substantially compared to the plain mixes. All LNC-6 and LNC-10 samples hardened within 9.5 h and 16 h, respectively (Fig. 4.3). The minimum initial and final setting time of 210 and 390 min was achieved in LNC100-6 mixes, which was comparable with the OPC-based mixes (210 and 300 min). The major reason for this significant decrease might be attributed to the removal of the higher amount of CO_3^{2-} ions from the pore solution, which yields an increase in the pH, as indicated in a previous study [51]. Reaction process steps in CH-substituted mixes might have occurred as follows: Inclusion of CH increased the pH, thus more slag particles could be dissolved at the early age of the reaction. In addition, CH releases a high amount of Ca^{2+} to the medium. Consequently, more Ca^{2+} ions were available from slag and CH, and quickly precipitated with CO_3^{2-} ions to generate reaction products such as calcite and gaylussite. When dissolved Ca^{2+} ions reached the critical value, the C-(A)-S-H gel precipitated. In addition, CH might have provided extra surface areas for the precipitation of the reaction products [85]. As it is seen in Figs. 4.1 and 4.3 that LNC60-10 mixes have higher flow diameter and lower flow loss than LNC60-6 mixes which also proves the prolonged setting time and delayed reaction product formation while the activator concentration increases from 6% to 10%. To determine whether this assumption actually holds or not, free carbonate concentrations were determined at the very early age of the reaction and the results are discussed in Section 4.4.

4.4 pH Evolution

Since the pH measurements on the extracted pore solutions give more reliable results than the pH strips or the direct insertion of a glass pH electrode into the mix [99], the centrifugal extraction method was chosen for pH evolution in this study. During the first hours of hydration, the liquid phase of the paste samples can be separated by vacuum filtration or centrifugation [100]. In many studies, centrifugation was used to determine ion concentrations in pore solutions [45, 96, 97]. Therefore, in this study, this method was chosen to measure pH values.

The measurements were taken at 30 min, 90 min, and 180 min right after the production. However, due to the early stiffening of NC100-6 and LNC100-6 mixes pH measurement could not be taken at 180 min. The exception was LNC100-6; the measurement could only be taken at 30 min since no pore solution could be extracted at further reaction times. On the other hand, for some mixes (e.g. NC80-6 and all NC-10 and LNC-10 mixes), 90 min measurement was not taken, since no significant change was seen between 30 min and 180 min values. The pH values of the pore solutions are shown in Table A.4 and Fig. 4.4.

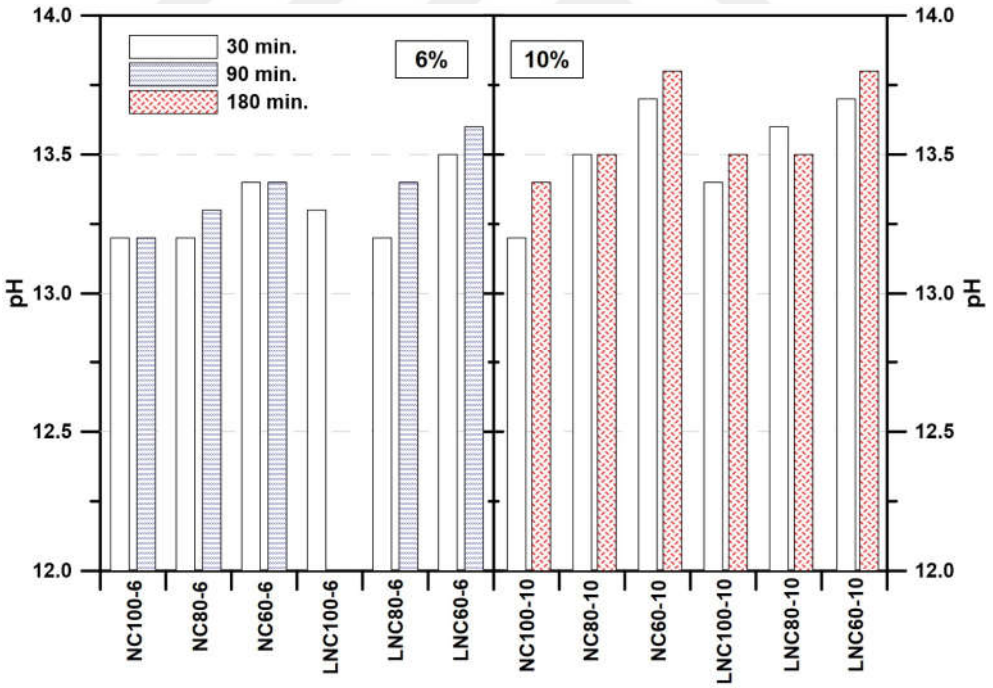

Figure 4.4 pH evolution of NCAS mixes

For most alkali-activated binder systems, an elevated pH is essential to initiate the dissolution and reaction of the solid aluminosilicate precursors [101]. The minimum pH for an effective alkali-activation reaction was defined as 11.5 or 12 in various studies [99, 100, 102]. If the pH is not at the desired level, a sufficient amount of OH^- ions does not exist in the pore solution to break the Ca-O, Mg-O, Si-O-Si, Al-O-Al, and

Al-O-Si bonds from slag for the formation of the hydration products. In this study, all pH values were higher than the critical value of 12, for all paste samples (Fig. 4.4). The pH values range between 13.2 and 13.8 and do not change considerably over time. As expected, higher activator dosage and NH replacement ratio caused a slight increase in the pH values. Moreover, all CH-substituted mixes (LNC) exhibited the same or slightly higher pH values than the NC ones.

It is obvious that the pH of the pore solution is already sufficient to dissolve slag particles at the early stage by releasing ions for the gelation of C-(A)-S-H and formation of the other strength-giving phases. In this case, the only barrier to the gelation process is the Ca^{2+} concentration that is controlled by the CO_3^{2-} concentration. Previous studies confirm that the accumulation of gaylussite and formation of hydrotalcite play a significant role in decreasing the CO_3^{2-} ions. This leads to the formation of the strength-giving phases, i.e. C-(A)-S-H gel and hydrotalcite [51].

Considering the setting times of the paste samples, it can be said that pH is not the sole parameter affecting the hydration process. For example; NC-6 and LNC-6 mixes presented very close initial pH values (Fig. 4.4), however, they exhibited quite different setting times (Fig. 4.3). Although the initial pH value plays an important role in initiating the reaction, it does not directly control the reaction rate [101]. The further reaction is mostly dependent on the calcium and carbonate concentration in the medium. Shi and Day [61] reported that the effect of anions in the activator is more important than pH in characterizing the hydration behavior of sodium-alkali activated slags.

4.5 Carbonate Concentration

Free carbonate (CO_3^{2-}) concentrations of the NCAS paste samples were determined after the centrifugation process at the very early stage of the reaction and the results are presented in Table A.5 and Fig. 4.5. As mentioned in the previous section, measurements could be taken at the first 30 and 90 minutes for the NC-6 and LNC-6 mixes and at 30 and 180 minutes for NC-10 and LNC-10 mixes.

The initial CO_3^{2-} concentration of NC mixes was higher than that of the LNC mixes for both activator dosages, expectedly. According to the test results at 30 min, the CO_3^{2-} concentrations varied between 29,000 and 40,000 mg/l for NC-6 mixes, and between 16,000 mg/l and 20,000 mg/l for the LNC-6 mixes. With the NH-substitution, 6.7% and 27.5% decrease obtained for 30 min measurement in the dissolved CO_3^{2-} concentration for NC80-6 and NC60-6 mixes, respectively (Fig. 4.5). At further measurement time (90 min) all NC-6 mixes presented similar values, approximately 29,000 mg/l. On the

other hand, NH-substitution decreased CO_3^{2-} concentration in LNC-6 mixes for both measurement times.

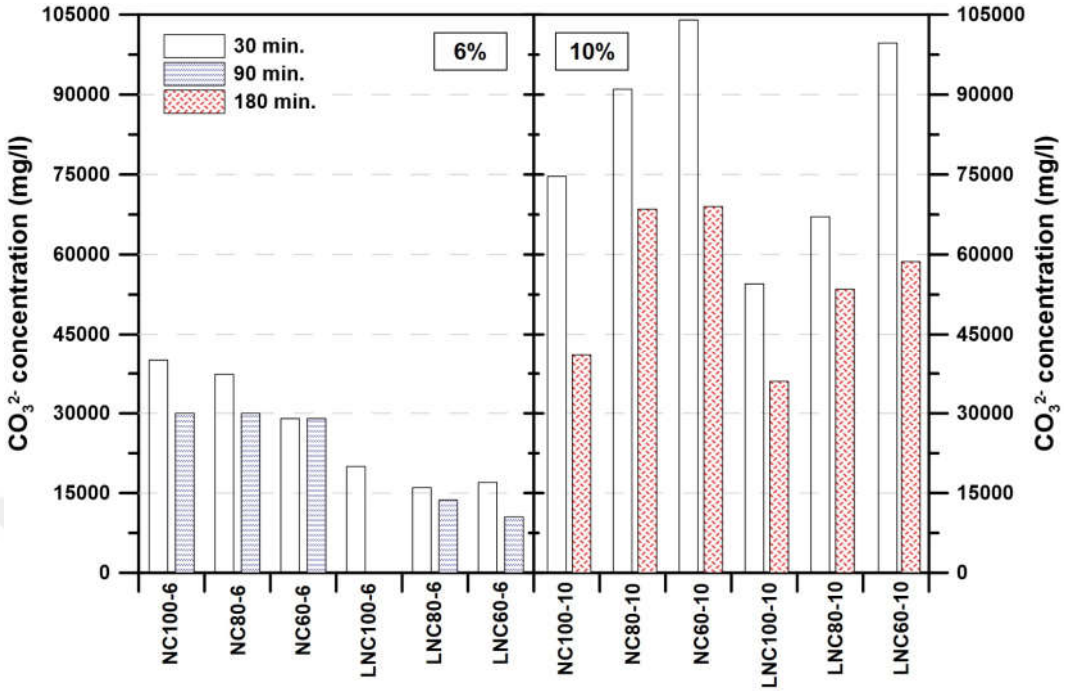

Figure 4.5 Carbonate concentration of mixes

Conversely to NC-6 and LNC-6 mixes, NH-substitution did not reduce CO_3^{2-} concentration in NC-10 and LNC-10 mixes. The reason for high carbonate ion concentration can be caused by a lower amount of calcium ions released into the medium for a certain time. In LNC80-10 and LNC60-10 mixes where NH and CH are incorporated into the system, common ion effect affects negatively the dissolution rate of CH, accordingly the calcium concentration released from the CH. Another reason might be the limited ion mobility. This statement can be explained by the dissolution rate of the slag at higher degree of pH which means that there exists higher amount of dissolved ion in the medium that delays the precipitation of calcite and gaylussite-like preliminary reaction products.

Expectedly, with an increase in the activator amount, from 6% to 10%, a substantial increase was seen in CO_3^{2-} concentrations. The maximum increase (259%) was observed between the NC60-6 and NC60-10 mixes at 30 minutes. This increased CO_3^{2-} concentration findings are generally consistent with the delayed setting time results obtained from the mixes containing 10% of activator (Figs. 4.3 and 4.5).

CH-substitution led to a reduction in CO_3^{2-} concentration for all CH-substituted mixes. In LNC-6 mixes the maximum reduction of 57% was observed, while in LNC-10 mixes the maximum reduction rate reached to 27% for the initial measurement. In addition,

CO_3^{2-} concentrations decreased by 27% and 35% in LNC100-10 and LNC80-10 mixes compared to NC100-10 and NC80-10, respectively. The reduction can be attributed to the existence of a higher amount of dissolved Ca^{2+} ions with the CH-substitution. However, LNC60-10 mixes presented similar values with the NC60-10 (approximately 104,000 mg/l). The reason for this might be the common ion effect and/or limited ion mobility. Moreover, carbonate consumption rate has reached to 63.8% and 21.9% over time in LNC-6 and LNC-10 mixes, respectively. Considering the different final measurement time (90 min and 180 min) values for LNC-6 and LNC-10 mixes, it can be deduced that the carbonate consumption rate is higher in LNC-6 mixes. Since the carbonate consumption rate can be attributed to the formation of reaction products such as calcite and gaylussite [92], it can be said that carbonate concentration results are generally consistent with the setting and fresh state properties. For example; at 30th minute of the reaction, NC100-6 had 40,000 mg/l, while LNC100-6 had 20,000 mg/l CO_3^{2-} concentrations. At the same time, NC100-6 presented 157 mm flow diameter, LNC100-6 presented 140 mm. In this case, it can be concluded that the consumption of CO_3^{2-} ions by the precipitation of preliminary reaction products such as calcite and gaylussite may be responsible for the decrease in the flow diameter.

4.6 Rheological Properties

All NCAS and OPC-based paste mixes presented shear thinning behavior under applied shear rate values. The behavior of all NCAS pastes fits to the Herschel-Bulkley model, as reported in [63]. Two examples of flow curves is given in Fig. 4.6 and the results of all of the mixes are shared in Appendix B. Tables A.6 and A.7 and Fig. 4.7 and 4.8 show the variation in yield stress (YS) and plastic viscosities (PV) of NCAS and OPC-based pastes.

The variations in YS and PV are associated with the dissolved ion concentrations and hardening process in NCAS mixes [63]. YS findings confirm this assumption since YS values were consistently lower in the NC and OPC-based mixes than in the LNC mixes at both activator dosages, at all measurement times (Fig. 4.7).

In the NC-6 mixes, YS values start from 57.5 Pa and rise up to 181 Pa. As the NH-substitution increase, the higher YS values are observed, especially for the NC60-6 mixes this increase is considerable. The increase in the activator amount did not cause a considerable change in YS values for NC mixes. The NC100-10 mixes exhibited similar values with the NC100-6. On the other hand, the OPC-based paste showed slight higher YS values than the NC100-6 and NC80-6 mixes at all measurement times.

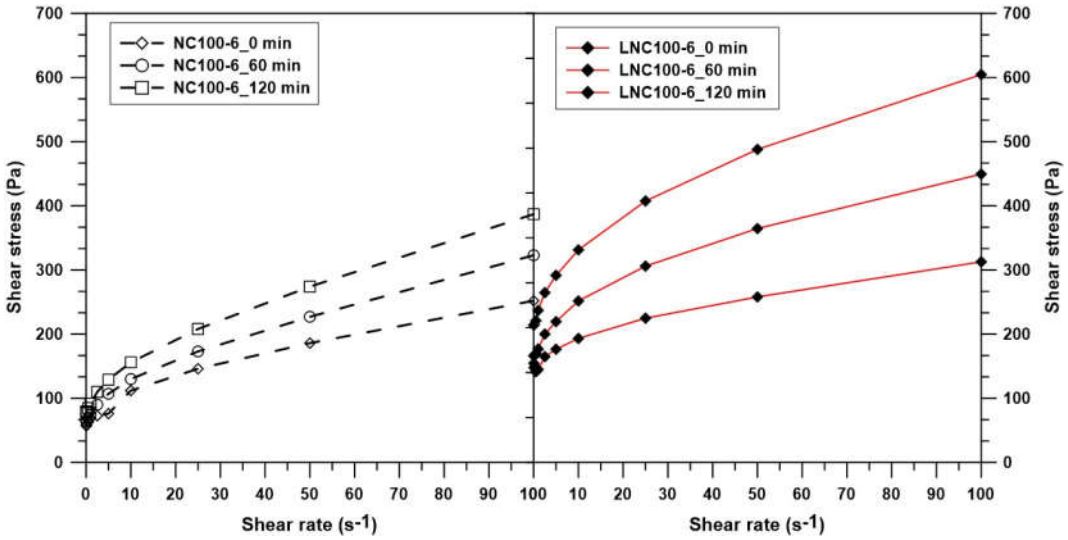

Figure 4.6 Flow curves of NC100-6 and LNC100-6 mixes

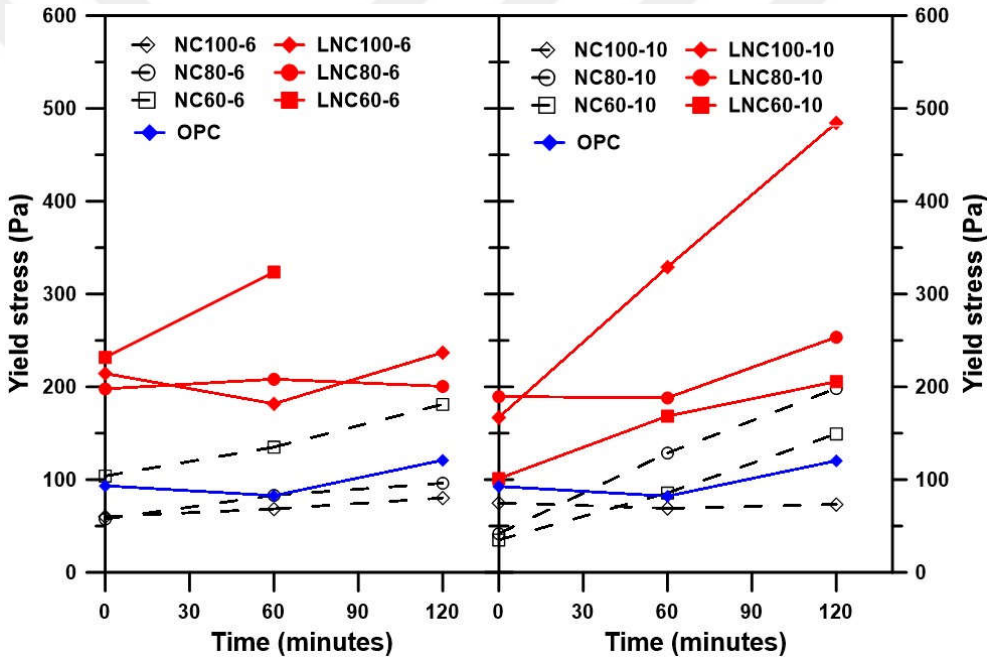

Figure 4.7 YS values of NCAS and OPC-based paste mixes

The YS values of the OPC paste increased slightly over time and reached a maximum value of 111.3 Pa at 120 min (Fig. 4.7).

In the CH-substituted mixes, a significant increase was seen compared to the NC mixes (Fig. 4.7). YS reached a maximum value of 485 Pa in the LNC100-10 mixes, while the NC100-10 mixes reached only 73.7 Pa at the 120 minutes. No measurement could be taken for LNC60-6 mixes at 120 minutes, due to the early stiffening of the paste. It is obvious that CH inclusion implies a substantial raise in YS. This increase is because of the decrease in the concentration of carbonate ions in the medium (see Fig. 4.5) along with the formation of carbonate compounds. Removing carbonate

ions favors slag dissolution and generates larger quantities of stable reaction products [103]. Considering the CO_3^{2-} concentration results, it may be deduced that CO_3^{2-} concentration and YS values are consistent for CH-substituted LNC mixes, as lower CO_3^{2-} concentration yields higher YS values.

The effect of the NH-substitution on the YS is variable. For example, in the LNC-6 mixes, a significant increase was observed with an increase of the NH ratio from 0% to 40%. This increase can be explained by the rise in OH^- ion concentration [78, 104] that yields higher pH and rapid formation of reaction products. However, the notable decrease was seen for the LNC-10 mixes as the NH ratio increased (Fig. 4.7). Deceleration is associated with the formation of a lower amount of reaction products at the measurement time of 60 min. Although a higher amount of dissolved ion species exists in the medium of the LNC-10 mixes, these ions cannot form reaction products due to low ion mobility [94]. It can be seen that setting test results are consistent with the YS values for all mixes (Fig. 4.3 and 4.7).

Plastic viscosity (PV) values of NCAS and OPC-based paste mixes showed similar trends with the YS (Fig. 4.8). The NC-6 and NC-10 mixes exhibited similar PV values, ranging between 1.1 and 3.9 Pa.s over time. On the other hand, the PV value of OPC-based paste slightly increase over time and reached 1.7 Pa.s at 120 min.

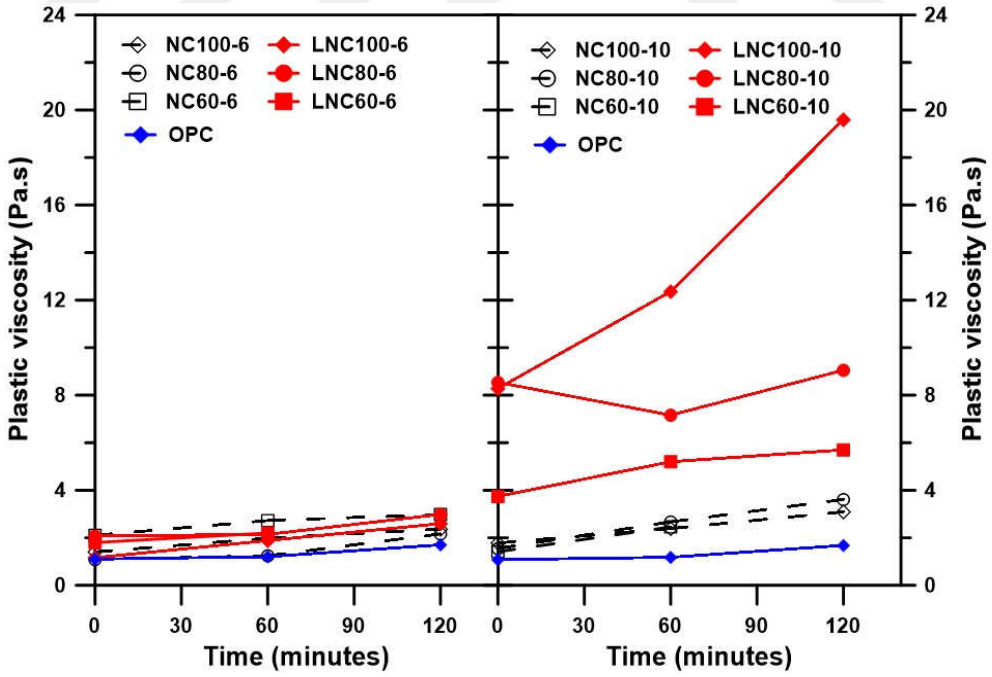

Figure 4.8 PV values of NCAS and OPC-based paste mixes

An increase in NH, from 20% to 40%, slightly increased the PV of NC-6 mixes, while almost no change was observed for NC-10 mixes. With the increase in the activator concentration, the PV values generally increased, especially in the CH-substituted mixes.

The substantial increase in YS with the inclusion of CH was not seen for PV, for all mixes. For mixes containing 6% activator dosage, CH-substitution did not considerably affect the PV values. On the other hand, mixes containing 10% activator dosage followed a different pattern; LNC-10 mixes exhibited up to 7 times higher values than the NC-10 mixes did. At 120 minutes, the inclusion of CH had a more remarkable effect on the variation of PV (Fig. 4.8). The LNC100-10 mixes reached the maximum PV value of 19.6 Pa.s, as the same trend occurred for YS.

4.7 Correlations between the Rheological Parameters

The results obtained in this chapter were used to establish a correlation between the flow diameter and rheological properties of NCAS mortars. For NC-10 and LNC-10 mixes, high correlation coefficients are found in terms of rheological parameters. The relationship between the flow diameter-yield stress and flow diameter-plastic viscosity are presented in Figs. 4.9 and 4.10, where it can be seen that they are correlated with each other, i.e. the lower flow diameter yields higher YS and higher PV.

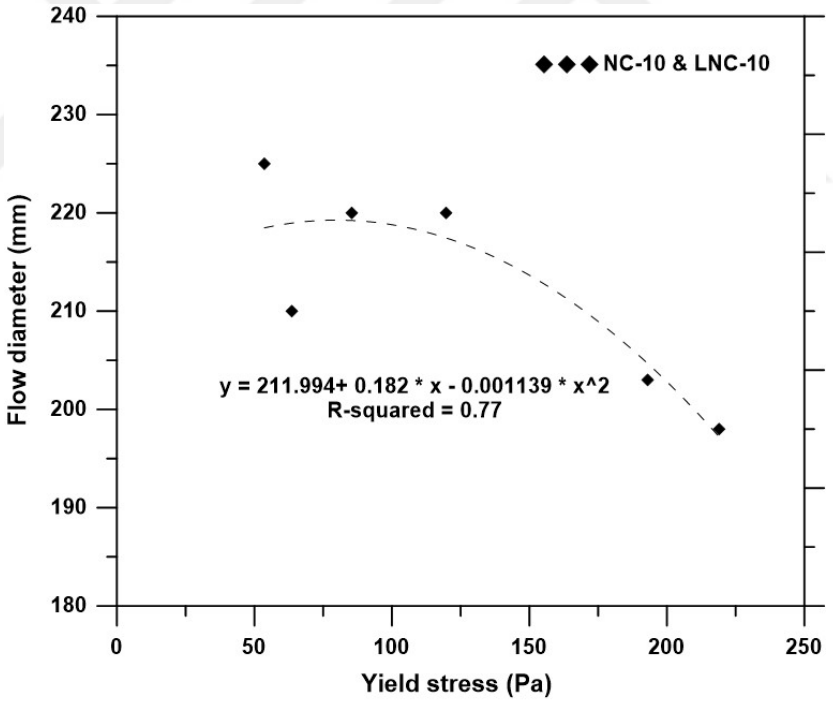

Figure 4.9 Flow spread diameter-yield stress correlation for NC-10 and LNC-10 mixess

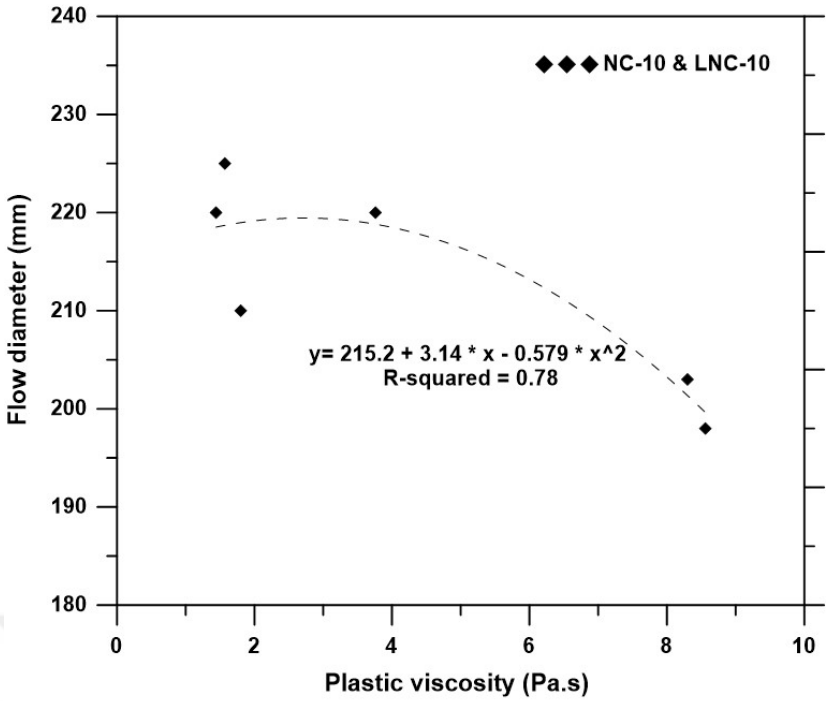

Figure 4.10 Flow spread diameter-plastic viscosity correlation for NC-10 and LNC-10 mixes

4.8 Discussion and Conclusions

In this chapter, the early age properties of NCAS are investigated. Test results showed that the fresh behavior of NCAS is greatly affected by the inclusion of the modifiers CH and NH. Controlling the reaction kinetics of NCAS paste to set within a comparable time with the OPC, is desirable for its adoption and implementation by the construction industry. Acceleration of the reaction kinetics is achieved by expediting the consumption of the carbonate ions from the medium. The lower setting time was achieved by the CH-substitution, even when used at low amounts (3% by wt.). The CH reacts directly with the activator in the aqueous solution, and yields calcite, gaylussite-like and hydrotalcite-like phase formation which means the fast consumption of carbonate ions in the system. Additionally, CH increases the pH of the medium by releasing OH^- ions, and facilitates the dissolving of the slag, depending upon the activator concentration in the alkali solution. However, the setting time extended unexpectedly when NH was used at 40%. The reason for this behavior is associated with the common ion effect. Thus, the solubility of CH and activator dosages in the mixes are the key parameters for the reaction kinetics of NCAS.

To prove the assumption regarding the consumption of carbonate ions by Ca^{2+} from the CH, carbonate ion concentration was determined in all mixes at the very early age of reaction. Results show that the time-dependent CO_3^{2-} concentration and initial

setting time values are consistent for most of the mixes (Fig. 4.3 and 4.5). The LNC-6 mixes exhibited the lowest amount of CO_3^{2-} at the initial measurement and the highest consumption rate of CO_3^{2-} among all mixes and resulted in the shortest setting times. Moreover, in the NC-10 mixes, there is a consistency between the CO_3^{2-} concentration and initial setting time. Also, the increase of setting time in CH-substituted mixes with the increase in the activator dosage can be explained by the CO_3^{2-} concentration. However, it may not be appropriate to directly relate carbonate concentration with setting time. For example, the NC60-6 and NC60-10 mixes showed almost the same initial setting time (Fig. 4.3), however, the carbonate concentration of NC60-6 was 29,000 mg/l while the latter had a carbonate concentration of 94,500 mg/l. So, it is not possible to identify a threshold value for the CO_3^{2-} concentration to estimate the setting time. Moreover, LNC-10 mixes had higher carbonate concentrations than the NC-6 ones, while the former had lower setting time (Fig. 4.3 and 4.5). It was thought that the carbonate concentration consumption rate of LNC-10 mixes might have increased at the further stages of the reaction (beyond 180 min). Briefly, carbonate concentration and its consumption rate, along with the other dissolved ions and concentrations play a significant role in the setting of NCAS [105].

The rheological parameters, YS and PV increased with the CH-substitution due to precipitation of the reaction products. The correlations between the rheological parameters and the flow are observed for some of the mixes.

The main conclusions of this part can be summarized as follows:

- Fresh state behavior of NCAS mostly depends on the dissolved carbonate ion concentration. Although the carbonate ion concentration is one of the most prominent parameters, reaction kinetics are also affected by the other dissolved ions and their concentrations.
- pH plays an important role in initiating the reaction process, but it does not directly control the early age reactions.
- The CH-substitution is the most effective method in terms of accelerating the reaction kinetics of NCAS, enabling the pastes to set within 6.5 h, reaching to comparable levels obtained in the OPC paste.
- Replacing NC with the NH improves the flowability and rheological properties, but also extends the setting time when used at a high replacement ratio, e.g. 40%.
- The rheological behavior of the NC and LNC pastes fits the Herschel-Bulkley model. The YS and PV values were higher for the LNC mixes most likely due

to the removal of carbonate ions, along with the formation of sodium/calcium carbonate-type compounds.

Improved fresh state properties can be achieved for NCAS mortars by the addition of small fractions of CH, as a consequence of a higher degree of reaction. One of the key factors controlling the reaction kinetics of NCAS pastes is found to be the carbonate concentration [105].

5
STRENGTH DEVELOPMENT & MICROSTRUCTURAL EVOLUTION

5.1 Introduction

The reaction mechanism of NCAS was explained in previous studies and different arguments were reported. Xu and Provis [106] reported that the mechanism starts with the dissolution of slag and dissolved Ca^{2+} ions forms $CaCO_3$ which decreases the pH. Then C-S-H gel takes Ca^{2+} from $CaCO_3$, releasing CO_3^{2-} to participate in another cycle of the reaction. However, the mechanism proposed in that study is about the ongoing process of NCAS rather than the initial reaction. Bernal et al. [51] described the early age reaction mechanism of NCAS and researched the chemistry of the pore solution. They reported that the reaction rate mostly depends on the chemistry of the pore solution. Within this concept, Na^{+}, OH^{-}, Si, Ca^{2+}, and CO_3^{2-} concentrations in the pore solution were determined. The reaction process is identified in three stages namely A, B, and C. The first day is named as Stage A, while Stage B is the period from 1 day to 5 days and finally Stage C is the period after 5 days (Fig. 5.1).

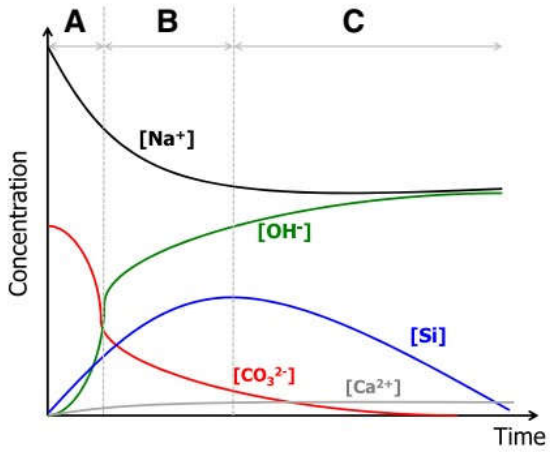

Figure 5.1 Conceptual description of pore solution chemistry of NCAS [51]

In addition, with the aid of microstructural analysis, they revealed a description regarding how the reaction mechanism proceeds in NCAS. According to their findings, the following results are obtained:

At the first stage (Stage A), dissolution of slag starts, NC reacts with Ca^{2+} from slag and forms gaylussite ($Na_2CaCO_3 \cdot 5H_2O$). On the other hand, Al and Si ions dissolved from slag react with Na from NC to form zeolite NaA ($Na_{12}Al_{12}Si_{12}O_{48} \cdot 18H_2O$) for the first 24 hours. Also, dissolved OH^- and Si concentrations increase in the pore solution. Later on, at the second stage (Stage B), dissolution of slag continues, gaylussite initiates to convert to $CaCO_3$ and releases Na followed by the formation of hydrotalcite ($Mg_6Al_2CO_3(OH)_{16} \cdot 4H_2O$). OH^- and Si concentrations still increase. Finally, at Stage C, the precipitation of C-(A)-S-H gel starts. CO_3^{2-} decreases while Ca^{2+} increase slightly since its solubility is no longer limited with the saturation of $CaCO_3$ polymorphs. This decrement promotes the precipitation of C-(A)-S-H gel. It can be seen that the reaction mechanism in NCAS initiates with the formation of relatively weaker and transient phases, then, proceeds with the formation of strength-giving phases such as hydrotalcite and C-(A)-S-H gel.

Gaylussite is defined as the transient phase, often formed in the first days of the reaction prior to the C-(A)-S-H and converts to more stable reaction products over time [51, 76]. The reason for the formation of gaylussite before the C-(A)-S-H gel formation is related to the fact that in lower alkalinity the priority of breakage of O-Ca and O-Mg bonds to release these species from slag rather than breakage of O-Al and O-Si bonds [61]. Thus, due to the high concentration of Na, the aqueous phase reaches saturation with regard to the gaylussite (Eq. 5.1).

$$5H_2O + 2Na^+ + Ca^{2+} + 2CO_3^{2-} \longrightarrow Na_2Ca(CO_3)_2 \cdot 5H_2O \tag{5.1}$$

When hydrotalcite and C-(A)-S-H initiate to precipitation, gaylussite starts to convert with the carbonate reprecipitating rapidly as $CaCO_3$ polymorphs (see Eq. 5.2) [107].

$$Na_2Ca(CO_3)_2 \cdot 5H_2O \longrightarrow CaCO_3 + 2Na^+ + CO_3^{2-} + 5H_2O \tag{5.2}$$

As can be seen from these statements that the consumption of carbonate ions and Ca^{2+} concentration plays an important role in the reaction. It is obvious that removing the carbonate ions from the solution at an early age seems to be required to accelerate the reaction mechanism.

There are very limited studies that investigate and compare the effect of the alkali

concentration and reactive admixtures on the strength development and microstructure analysis of NCAS in detail. The previous studies predominantly focused on the methods to accelerate the reaction kinetics of NCAS by either increasing the alkali content or incorporating reactive admixtures. Kovtun et al. [80] indicated that replacing NC with NH increases the pH and facilitates faster dissolution of the slag which will result in a noticeable acceleration of strength development. Temuujin et al. [52] observed the improvement in mechanical properties of fly ash-based geopolymers cured at room temperature with the addition of calcium compounds. In that study, calcium hydroxide is found to be more effective than calcium oxide and it was reported that calcium compound addition negatively affected the mechanical properties of geopolymer cured at 70°C. On the other hand, according to Kim et al. [53] calcium oxide was found to be more effective than calcium hydroxide in activating slag. In another research [54], the effect of combining MgO and NC on the reaction kinetics of slag/fly ash activation was examined and it was concluded that MgO incorporation significantly influenced the reaction rate. Increasing the alkali content resulted in an increase in the strength at all ages as well. Alternative accelerators like CLDH [10], reactive magnesia [54], and reactive MgO [82] are also reported as effective parameters in NC activation. Atis et al. [55] studied the influence of activator type on the strength development of alkali-activated slag mortar and found that NCAS mortar exhibited comparable strength with respect to OPC-based mortar. Jeong et al. [108] studied the activation of slag by using mainly CH and substituting or adding four different accelerators such as NH, NC, Na_2SO_4, and $CaSO_4 \cdot 2H_2O$. They investigated the compressive strength development on paste mixes and concluded that the addition of NC into the CH-activated mixes gives higher values compared to replacing CH with NC.

In this study, two different modifiers are chosen to accelerate the reaction and to increase the strength and durability characteristics as well. One of the modifiers was NH which substituted with NC at different percentages. It was thought that NH can increase the pH by releasing high amount of OH^- into the medium and thus increase the solubility of slag. Slaked lime (CH) was chosen as the second modifier. It was deduced that the presence of CH in NCAS activation might be effective since it could be potentially involved in the reaction of C-(A)-S-H gel formation. Moreover, Ca^{2+} ions can play an important role in removing carbonate ions from the medium by forming calcite at the early age of the reaction. In addition to this, the incorporation of CH contributes to strength improvement and lowers the cost.

In the previous chapter, it was mentioned that initial pH values, and especially carbonate concentration in the medium are the key parameters affecting the reaction rate. In this chapter, the time-dependent reaction product formations are determined. This chapter investigates the effect of CH incorporation and combination of different

activators (NC and NH) on the strength development and microstructure of NCAS paste mixes cured at ambient temperature. Within this concept, strength development and the progress of hydration of the mixes are studied with the phase transformation and development of microstructural features through quantitative techniques such as thermogravimetric analysis and phase-identification techniques such as Fourier transform infrared spectroscopy and X-ray diffraction.

5.2 Compressive Strength Development

The reaction kinetics and mechanical properties of NCAS are less extensively studied compared to other activators. Fernandez-Jimenez [91] activated slag with different types of activators and deduced that the compressive strength of alkali slag mortars are ranged greatest to lowest as follows:

$$Na_2SiO \cdot n\mathrm{H}_2O + \mathrm{NaOH} > Na_2CO_3 > \mathrm{NaOH}\ [91]$$

Increasing the alkali concentration [55], substituting NC with NH [109, 110] or incorporating waterglass [88], blending with MgO [54], and lime [80] are the previously reported solutions to accelerate the reaction kinetics of NCAS systems. Collins and Sanjayan [77] investigated the usability of NH and NC as a combination in room temperature cured slag activation and compared the results with the OPC. The authors found that with the addition of NC, 1-day compressive strength results are higher than the OPC when the activator dosage increased up to 4% and the increase in compressive strength was observed with higher amount of NC. In addition, Li and Sun [56] reported that a combination of NC+NH leads to higher strength values than using each individually. Fernandez and Puertas [78] reported that sodium silicate substitution increased the compressive strength of NCAS. The combination of NC+CH in slag activation enhances the strength over that using alone [83]. Bakhavrev et al. [109] and Collins et al. [77] replaced the NC with and NH and reported that a 1-day compressive strength of about 8 MPa was obtained, while at 7 days no further strength development was observed. MgO was found to be an efficient alternative activator for slag and it was reported that MgO substitution presented higher strengths than CH-activated slag at 28 days [111].

In previous studies, a wide range of compressive strength values is reported for NCAS (Table 4.1). Jin et al. [82] found that 90 days compressive strength of 4% NC+5% MgO-activated mixes presented the highest strength values with approximately 65 MPa, which was 45% higher than the plain NC mixes. Abdalqader et al. [54] reported that 3 days of compressive strength values ranged between 25-38 MPa, it should be noted

that these samples could be demoulded at 2 days of the reaction. Fernandez-Jimenez [91] indicated that compressive strength of NCAS mixes range between 24-42 MPa according to the amount of NC, type of slag and curing conditions.

The compressive strength development of the NCAS and OPC-based mortar mixes up to 90 days are determined and the compression test results are given in Table A.8 and Figs. 5.2 and 5.3. The 3, 7, 28 and 90 days compressive strength of mixes range from 0.5 to 20.4 MPa, 1.2 to 32.5 MPa, 3.1 to 44.4 MPa and 3.4 to 44.5 MPa, respectively, which shows that some of these mixes may be used in applications with different strength requirements. Plain NC mixes (NC100-6 and NC100-10) show the lowest strength at both the early age and the long term period of curing, in comparison to other mixes (Figs. 5.2 and 5.3), which confirms the results reported in [80]. The NC100-6 mixes exhibited hardly any strength throughout the entire curing. The compressive strength reached only 3.1 MPa at 28 days for this mix.

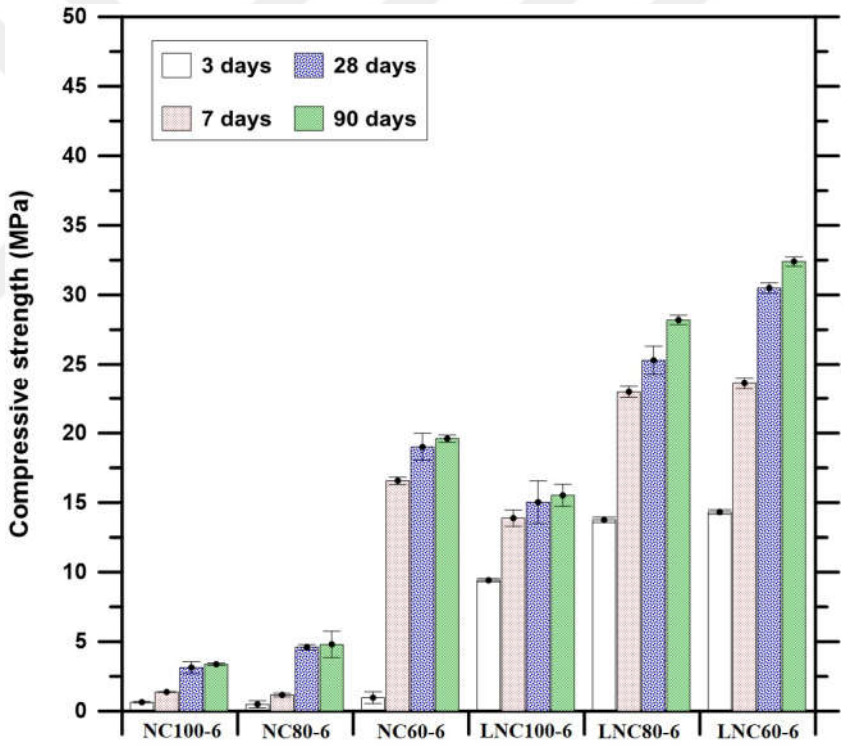

Figure 5.2 Compressive strength of NC-6 and LNC-6 mixes

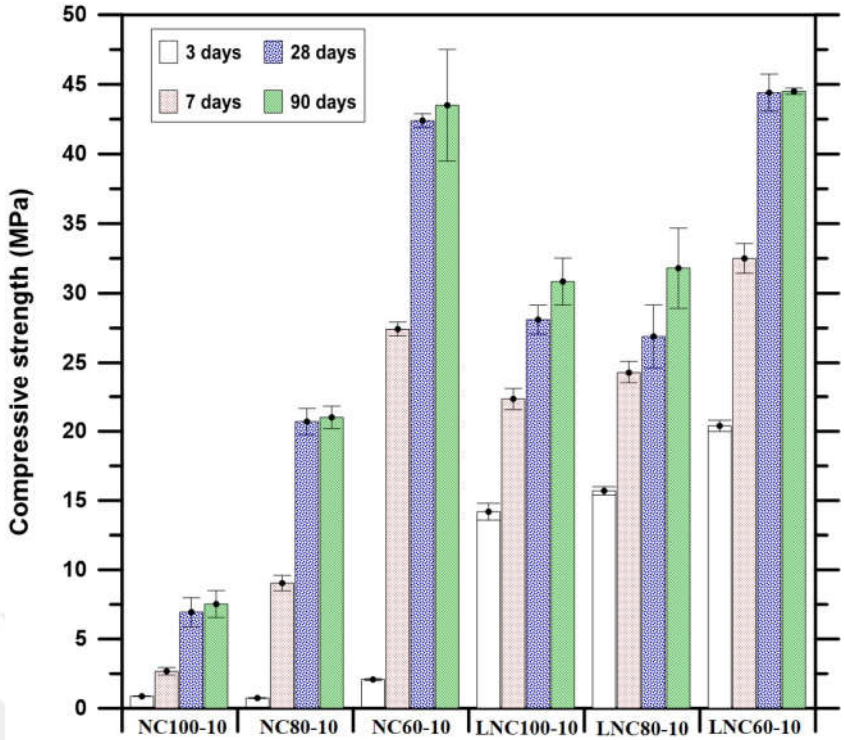

Figure 5.3 Compressive strength of NC-10 and LNC-10 mixes

An increase in activator dosage, from 6% to 10%, did not cause any change for 3 days, while an increase was seen for further curing ages. Most of the mixes, almost reach their ultimate strength at 28 days. Only a slight improvement was observed at 90 days. It can be said that there is an increase in the strength-giving phase formation such as hydrotalcite and C-(A)-S-H, from 3 to 7 days, especially for NC-60 mixes. Thereafter, the compressive strength increased gradually up to 44 MPa with an extended curing period.

NH-substitution did not cause any considerable change in compressive strength at an early age (3 days) for both activator dosages. At further ages, for NC-6 mixes, only a slight increase was seen with 20% NH-substitution, while 40% NH-substitution increased the compressive strength substantially for both activator dosages (NC60-6 and NC60-10 mixes). It can be deduced that NH-substitution was effective at the further ages of the reaction. Kovtun et al. [80] studied the acceleration of NCAS by replacing NC with NH at 20% and 50% by weight. They found that replacing NC with NH at a low dosage (20%) does not increase the compressive strength at 3 days. On the other hand, for both NH replacement dosages, compressive strength reaches higher values than plain NC mixes at 28 days.

In NH-modified mixes, the compressive strength increased notably when the activator dosage was raised to 10% (Fig. 5.3). NC60-10 reaches the maximum compressive strength value of 43.5 MPa at 28 days among the mixes without CH, although the

compressive strength of this mixture was only 2.1 MPa at 3 days. In a previous study [56], the compressive strength of 10% NC+NH-activated slag mortar was found as 0 MPa at 3 days and increased up to 60 MPa at 28 days.

It can be revealed that the contribution of NH on NCAS become more distinct at further ages. The very low early age compressive strength of NC mixes is due to the lower initial OH^- and higher CO_3^{2-} concentration. In the case of NC substitution with NH, initial OH^- concentration and the pH value increase. It is known that higher pH increases the dissolution of reactive species such as SiO_2 and Al_2O_3 and higher amount of Ca^{2+} exists in the medium. The higher dissolution rates and reduced CO_3^{2-} concentration provides more Ca^{2+} to participate in C-(A)-S-H gel formation which leads to the enhanced compressive strength [12, 51].

With the CH-substitution, especially at an early age, a significant increase was seen in compressive strength for all mixes irrespective of the NH-substitution and/or activator concentration (Figs. 5.2 and 5.3). This increase was more distinct for LNC80 mixes. For LNC80-6 and LNC80-10 mixes, 3 days compressive strength values were 27 and 22 times higher than those of NC80-6 and NC80-10 mixes, respectively. Only one exception is that NC60-10 mixes reached almost the same strength value with LNC60-10 mixes at 28 and 90 days. These mixes (NC60-10 and LNC60-10) presented the maximum compressive strength value with approximately 44 MPa at 28 days among all mixes. Obviously, CH plays a significant role in increasing the early and later age compressive strength. The increase in compressive strength with the CH-substitution can be attributed to a few main reasons:

(i) Dissolved CH in water releases Ca^{2+} and OH^- into the medium (Eq. 5.3).

$$Ca(OH)_2 \longrightarrow Ca^{2+} + 2OH^- \tag{5.3}$$

Dissolved Ca^{2+} ions consume the CO_3^{2-} releasing from NC and contribute to the formation of calcite and gaylussite. On the other hand, removing CO_3^{2-} ions from the pore solution as well as with the increased OH^- concentration increases pH. Thereby, the dissolution of slag facilitates. These dissolved ions (Ca^{2+}, Si^{4+}, and Al^{3+}) lead to an increased concentration of reaction products.

(ii) In addition, CH introduces a higher amount of Ca^{2+} into the medium required for C-(A)-S-H formation. The enhanced early alkalinity due to NaOH generation resulting from the reaction between CH and NC (Eq. 5.4) might be another reason for the

acceleration of slag dissolution [112].

$$Na_2CO_3 + Ca(OH)_2 \longrightarrow 2NaOH + CaCO_3 \tag{5.4}$$

(iii) Another reason for the high early-age strength might be the filling effect of the calcite ($CaCO_3$) leading to reduced porosity [113].

Basically, the reason for low early age strength depends on the hydration products. To understand the strength development mechanism in detail, it is necessary to investigate the time-dependent microstructure properties of the NCAS paste mixes, including the effect of NC and NH combinations, as well as the CH-substitution. The following sections are thus focused on the characterization of various aspects of NCAS and the effects of the modifiers (NH and CH).

5.3 X-ray Diffraction

Figs. 5.4-5.6 show the XRD patterns of the selected mixes at different curing ages such as 3, 7 and 28 days. The selected mixes are NC100-6, NC60-6, NC60-10, LNC100-6, and LNC60-10 which represent the effect of activator concentration, the substitution of CH, and a combination of NC and NH. It can be seen from Figs. 5.4-5.6, the main phases are C-(A)-S-H, hydrotalcite ($Mg_6Al_2CO_3(OH)_{16} \cdot 4H_2O$), calcite ($CaCO_3$) and gaylussite ($Na_2Ca(CO_3)_2 \cdot 5H_2O$), along with portlandite ($Ca(OH)_2$) and dolomite ($MgCa(CO_3)_2$).

The main binding phase C-(A)-S-H reflected at approximately 30° (2θ) [114, 115] was found in all specimens throughout all XRD measurements. This characteristic peak overlapped with a strong peak for calcite at the same position [80, 110]. In the previous studies, the reason for the overlapping was explained with the semi-amorphous nature of the C-S-H. It was reported that this peak appears with the background hump in the 2θ range of 25° – 35° [116–119]. Calcite was also identified at approximately 43° (2θ) and 47° (2θ) for all of the mixes at all curing days, which was due to the cation exchange reaction between NC and slag (CO_3^{2-} from NC and Ca^{2+} from slag), as well as atmospheric carbonation. In plain NC mixes (NC100-6 and NC100-10), due to the high concentration of CO_3^{2-}, the calcite precipitation occurs at a very early stage.

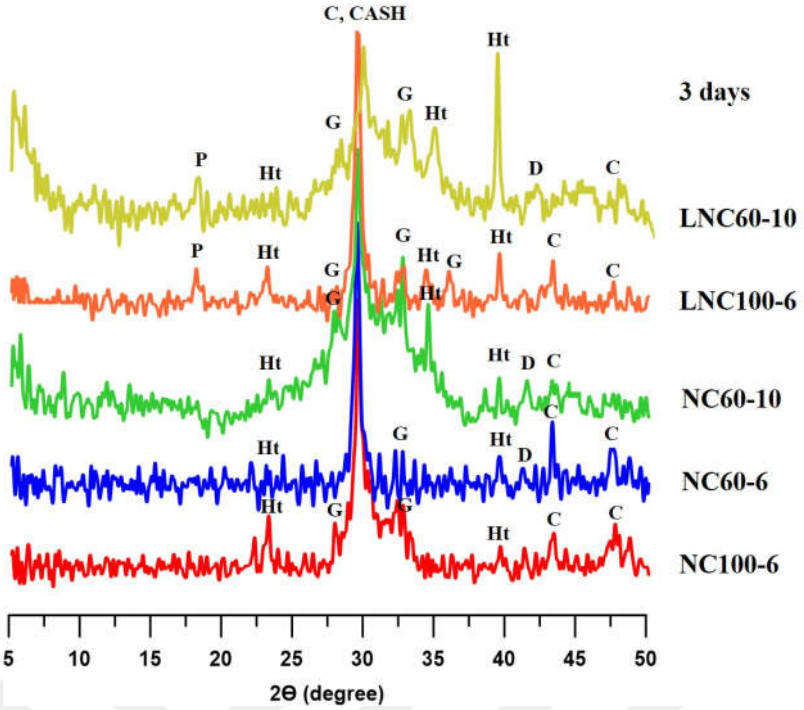

Figure 5.4 XRD patterns of selected mixes at 3 days *(C: calcite; CASH: calcium aluminosilicate hydrate; D: dolomite; G: gaylussite; Ht: hydrotalcite; P: portlandite)*

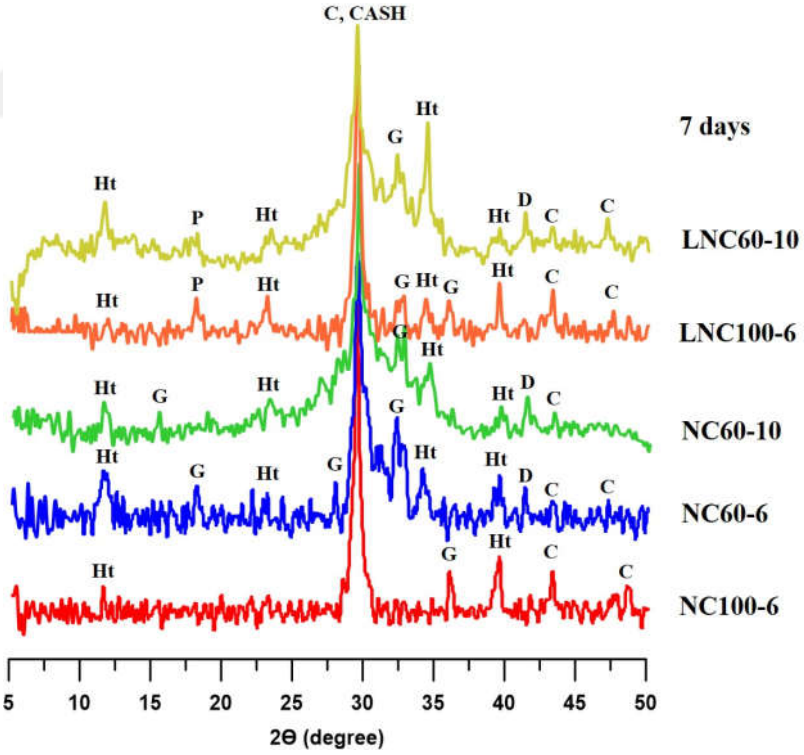

Figure 5.5 XRD patterns of selected mixes at 7 days *(C: calcite; CASH: calcium aluminosilicate hydrate; D: dolomite; G: gaylussite; Ht: hydrotalcite; P: portlandite)*

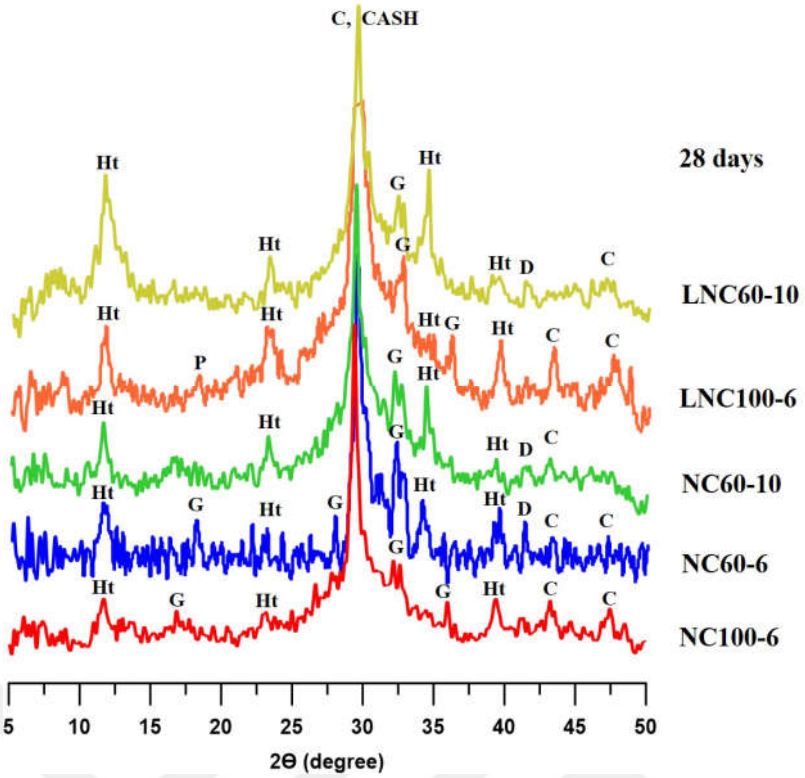

Figure 5.6 XRD patterns of selected mixes at 28 days *(C: calcite; CASH: calcium aluminosilicate hydrate; D: dolomite; G: gaylussite; Ht: hydrotalcite; P: portlandite)*

CH-substitution was expected to yield enhanced calcite peaks, however, this assumption was not proved by XRD results (Figs. 5.4-5.6). The contradiction can be explained by considering the formation of gaylussite instead of calcite. The more intensive reflections of gaylussite and hydrotalcite were presented by the incorporation of CH at the curing age of 3 days (Fig. 5.4).

Gaylussite was identified as a secondary reaction product at three different diffraction angles; approximately 28°, 32° and 36° (2θ). Only the peak at 32° (2θ) was seen for all mixes and all curing ages. The number of gaylussite peaks decreased in CH-modified mixes, especially after 7 days (Figs. 5.4-5.6) since gaylussite converts to more stable products such as calcite and hydrotalcite. Ke et al. [10] reported that gaylussite is a transient phase in NCAS, and its consumption is related to the formation of more stable carbonates. According to Kovtun et al. [80], the intensity of gaylussite decreased in the pastes produced using with accelerators such as NH and OPC. The characteristic peaks of hydrotalcite were identified at approximately 11.5°, 23°, 34° and 39° (2θ), the same diffraction peaks were reported in the previous studies [51, 110, 114, 116]. Moreover, in the CH-modified mixes, the intensities of hydrotalcite were higher than the plain NC mixes.

At an early age, hydrotalcite was observed only with poor reflections. However, as a

result of the ongoing reactions, its intensity increased substantially. A special example; the peak at around 11.5° (2θ) was not observed for any of the mixes at 3 days of the reaction but it appeared at 7 days and finally its intensity increased for all mixes at 28 days. The increased intensity of the hydrotalcite peak might be one of the reasons for the strength development from 3 to 7 days.

Portlandite was identified as a secondary reaction product as well and its diffraction peaks (≈18° 2θ) were only identified in CH-substituted mixes. In LNC60-10 mixes, the intensity of the peak was decreased from 3 to 7 days and disappeared at 28 days (Figs. 5.4-5.6). On the other hand, in the LNC100-6 mixes portlandite continued to appear at all reaction days, only its intensity decreased. Jeon et al. [84] reported that CH turns into the calcite and CSH at further ages of the reaction in alkali-activated systems.

The rapid consumption of CH in LNC60-10 mixes could be due to the formation of $CaCO_3$ from the initial reaction of CH and NC, which facilitated C-(A)-S-H formation through the reaction between the CH and the amorphous phase of the slag [120]. This assumption can be supported by the Figs. 5.2 and 5.3. It can be seen that LNC100-6 mixes did not gain a substantial compressive strength from 3 to 28 days, while LNC60-10 mixes presented a significant increase during the same period. A longer curing duration, 28 days (Fig. 5.6), promotes the development of a more crystalline structure compared with the 3 and 7-day samples (Figs. 5.4-5.6). Increasing the curing time did not generate new phases, but it increased the crystallinity of C-(A)-S-H type structure, especially in the series of NC60-10 and LNC60-10, visible by sharpening of the main peak at around 30° (2θ) [121].

The XRD test results may explain the compressive strength development of NCAS mortars. At the early age of the reaction (3 days), NH-substitution and activator dosage did not change compressive strength significantly. However, for 7 days and later on, a substantial increase was seen. This increment can be explained by the increase in the number and intensity of the peaks such as hydrotalcite and C-(A)-S-H. This trend was been observed for CH-modified mixes from 3 days. In CH-modified mixes, the peaks at higher degrees seen in XRD patterns were more intense than the NC mixes, which resulted in a decrease in interlayer distance reasoning for the higher compressive strength [122]. At 28 days of curing, the intensities of the peaks of main reaction products, calcite/C-(A)-S-H and especially hydrotalcite diffracted at 11.5° and 23° (2θ), increased for all mixes signifying a higher concentration of reaction products thus pointing to higher compressive strength. It is seen from Figs. 5.3, 5.4 and 5.6 that although NC60-10 exhibited lower compressive strength values than LNC60-10 at 3 days, both mixes were presented almost the same values at 28 days. Thus, different

XRD diffractograms for 3 days and similar XRD diffractograms for 28 days can be expected for these mixes. At 3 days, while a high amount of gaylussite and C-(A)-S-H and a moderate amount of hydrotalcite exist for NC60-10; substantially high amount of hydrotalcite and less amount of gaylussite exist for LNC60-10 mixes. Thus, it can be deduced that hydrotalcite, diffracts at approximately 39° (2θ), might have more contribution to compressive strength, compared to other phases. On the other hand, both mixes present the same peaks at the same diffraction angles with similar intensities at 28 days.

5.4 FTIR Analysis

The FTIR spectra of the anhydrous slag used in this experimental study and the selected paste samples at 3, 7 and 28 day-age are presented in Figs. 5.8-5.10. Although the analysis was conducted between 400 and 4000 cm^{-1}, only the wavelength between 600 and 1800 cm^{-1} was presented as there is no significant feature beyond this wavelength.

Table 5.1 shows the common FTIR spectra peaks identified in the literature for alkali-activated pastes and OPC [123].

Table 5.1 FTIR peaks of typical bonds [123]

Wavelength (cm^{-1})	**Chemical bond characteristic**
3400	O-H stretching (H_2O)
1430	C-O Asymmetric stretching
1100	S-O (Gypsum) Si-O-Si and Al-O-Si asymmetric stretching
960-800	Si-O, Al-O stretching
872	C-O bending
480	Si-O-Si and O-Si-O bending

For the anhydrous slag (Fig. 5.7), the distinct intensity band centered at around 901 cm^{-1} was related to the asymmetric stretching vibration mode of Si-O-T bonds, where T represents Si or Al, and the band position depended on the glass structures of the raw material and another small intense band at approximate 710 cm^{-1} represents the functional group of AlO_4 [12, 117]. Moreover, the band at 1423 cm^{-1} identified in the slag is attributed to the symmetric stretching mode of the O-C-O bonds of CO_3^{2-} groups regarded as weathering of the slag [12].

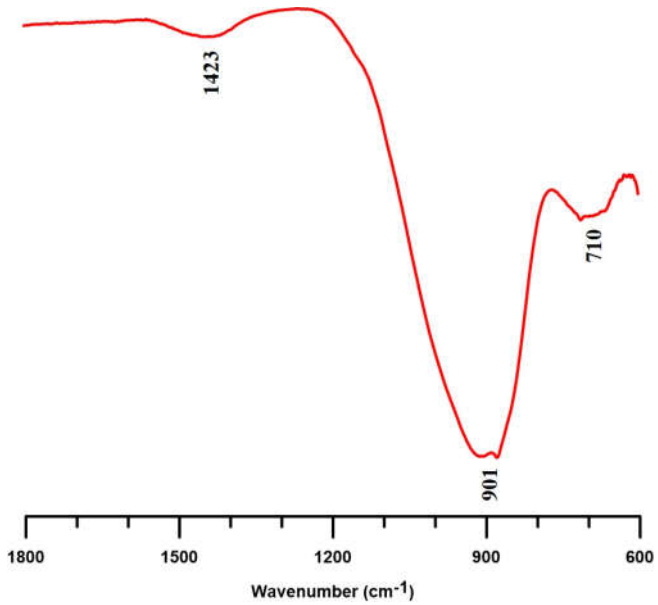

Figure 5.7 FTIR spectra of anhydrous slag

NC100-6, NC60-6, NC60-10, LNC100-6 and LNC60-10 mixes are chosen for further analysis in detail, which represents the activator concentration, NH and CH substitution effect on NCAS. All the paste mixes exhibited similar bands, indicating similar nature of the hydration products, irrespective of the activator dosage, NH or CH substitution. Major bands were identified at approximately 1430, 945, 870, 665 cm^{-1} for all mixes (Figs. 5.8-5.10). The band at about 665-712 cm^{-1} is associated with the stretching vibrations of Al-O bonds in the AlO_4 groups which could probably be related to the formation of hydrotalcite and C-(A)-S-H gel [110].

The bands at around 1420 and 870 cm^{-1} suggest the presence of CO_3^{2-}, which traces of the presence of gaylussite, calcite, hydrotalcite or dolomite [110], as identified by both XRD (Figs. 5.4-5.6) and TGA (Figs. 5.11 and 5.12). Generally, the vibration of CO_3^{2-} groups is related to the type of activator used. One of the reasons for the reflection at this range may also be due to the carbonation or weathering of the samples.

The main binder gel band, at approximately 945 cm^{-1}, corresponds to the Si-O-T asymmetric stretching bands in the SiO_4 tetrahedra [12]. This finding is in accordance with the formation of C-(A)-S-H of the slag activation, determined by XRD and also confirms in other studies [118, 119]. In all mixes, the Si-O-T band shifted slightly towards higher wavenumbers at further ages (Figs. 5.8-5.10). This shift is possibly due to the ongoing activation of slag, which increases the formation of more polymerized gel [124].

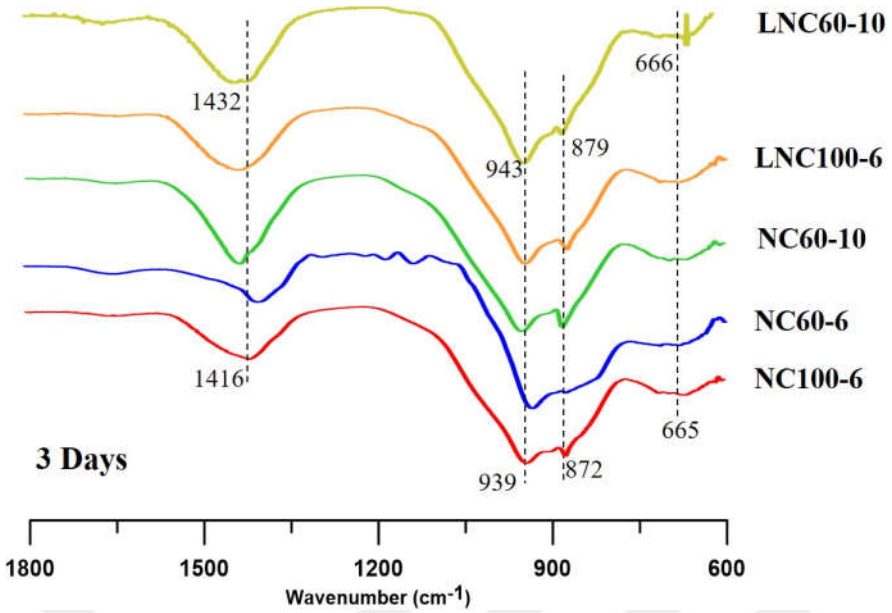

Figure 5.8 FTIR spectra of selected mixes at 3 days

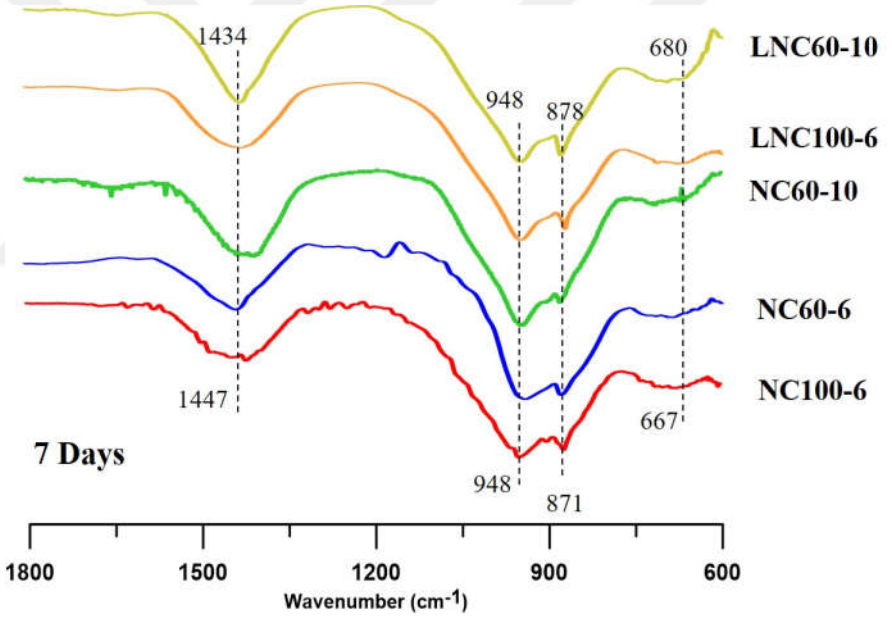

Figure 5.9 FTIR spectra of selected mixes at 7 days

Moreover, in the case of pastes modified with CH and with the combination of CH and NH, the Si-O-T band also shifts towards higher wavenumbers of 939 cm^{-1}. This behavior again attributed to the higher degree of polymerization. Since only slight shifting is seen on the Si-O-T band values of mixes, the gel structure of C-(A)-S-H represents only slight differences with the CH and/or NH substitution and also activator dosage.

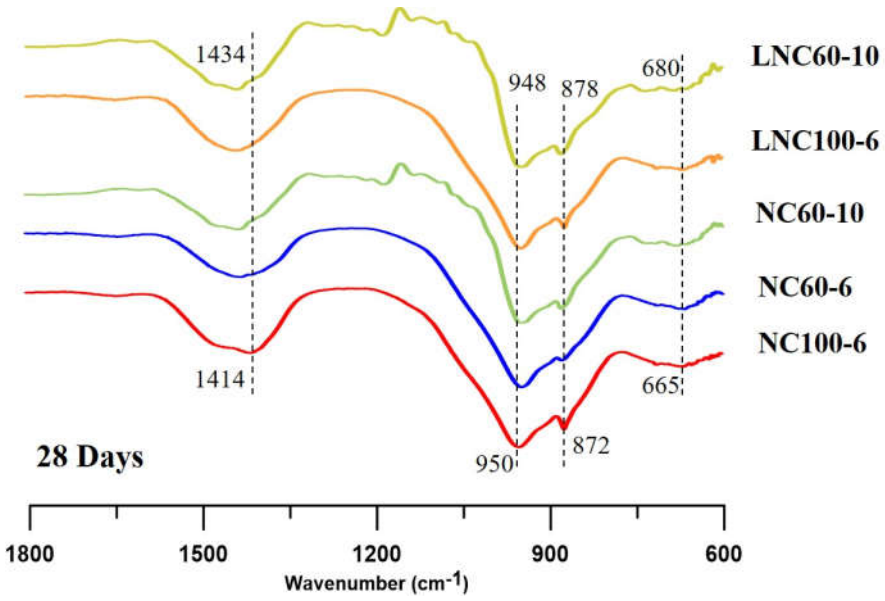

Figure 5.10 FTIR spectra of selected mixes at 28 days

The bands representing CO_3^{2-} ranged between approximately 1410 cm^{-1} and 1464 cm^{-1}. In the presence of NH and/or CH substitution, this band was observed at higher wavenumbers, which represents the stronger bonds (Figs. 5.8-5.10) and might indicate higher compressive strength.

5.5 Thermogravimetric Analysis

Figs. 5.11 and 5.12 depict the representative TGA and DTG results for selected mixes at the 28 days. All mixes possess similar patterns which show one main and three small peaks. Mass loss below 200°C was caused by the evaporation of free water and partly by the dehydration of C-(A)-S-H gel [125, 126] and gaylussite [127]. The peak between 250°C and 400°C attributed to the decomposition of hydrotalcite [116, 128], which agrees well with the XRD results. The decomposition of hydrotalcite is generally categorized into three stages [114, 129, 130]: firstly evaporation of interlayer water under 200°C; secondly, decomposition of structural hydroxyl groups around 350°C and finally decomposition of interlayer carbonate ions around 440°C. The second decomposition peak around 300°C (Fig. 5.12) can be attributed to the dehydroxylation of brucite-like layers of hydrotalcite and the small shoulder between 400 and 560°C could be the decarbonization of hydrotalcite. LNC-10 mixes exhibited an additional tiny peak for $Ca(OH)_2$ decomposition between 400°C and 450°C which agrees well with the results of Kim et al. [53]. This peak was more distinct in LNC60-10 among all LNC-10 mixes (Fig. 5.12).

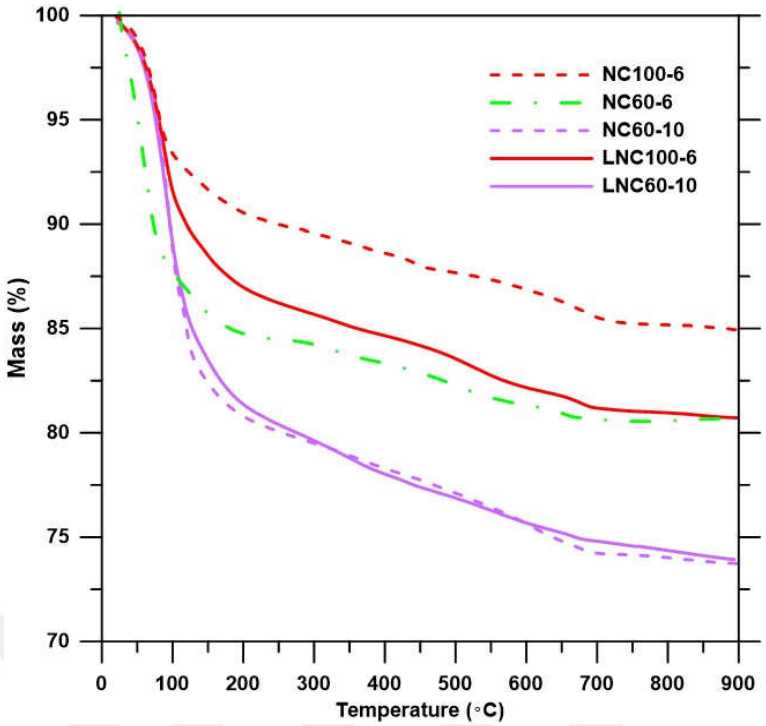

Figure 5.11 TGA curves of selected mixes

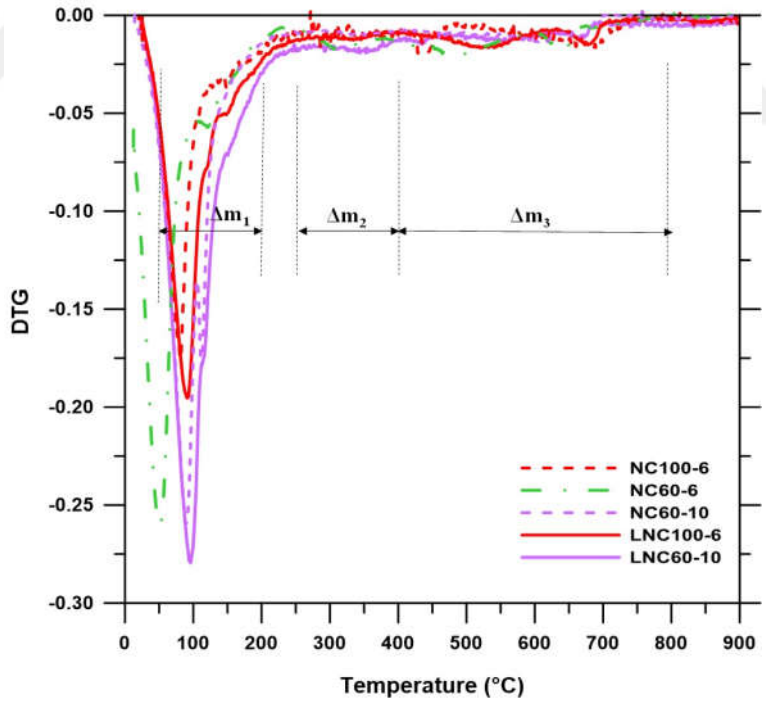

Figure 5.12 DTG curves of selected mixes

The mass loss occurred at the temperatures between 400°C and 600°C can be defined as the decomposition of poorly crystalline $CaCO_3$ [52, 131] or magnesium silicate hydrates (M-S-H) [12]. Since M-S-H was not observed from the XRD and the existence of $CaCO_3$ was proved by both XRD and SEM, it can be deduced that the mass loss at

the temperature range of 400-600°C caused by the decomposition of poorly crystalline $CaCO_3$. The decomposition of the carbonate-containing phases occurred between 600-800°C, including calcite [132], gaylussite [127] and hydrotalcite [133]. Gaylussite thermal behavior consists of three main features: (i) Dehydration up to 250°C; (ii) Crystal transformations between 250°C and 500°C; and (iii) melting and carbonate decomposition from 500°C to 1050°C [127].

The mass loss of mixtures at different temperature ranges are given in Table 5.2, representing different reaction products as discussed above. In this study, the mass loss is divided into three groups and denoted as Δm_1, Δm_2 and Δm_3 with the ranges of 50-200°C, 250-400°C and 400-800°C where C-(A)-S-H; hydrotalcite; CH and CO_3^{2-} containing phases decomposes, respectively. The maximum mass loss occurred between 50°C and 200°C (Δm_1) for all mixes and mass change between these temperatures ranged between 9.9% and 23.9%. Although the decomposition of other phases (dehydration of gaylussite and loss of interlayer water of hydrotalcite) overlaps with C-(A)-S-H within this range, their influence is supposed to be insignificant due to their relatively small amounts.

Table 5.2 Weight losses (%) of mixes

Mixes	Δm_1	Δm_2	Δm_3
NC100-6	9.9	1.6	5.2
NC80-6	12.0	1.9	4.6
NC60-6	13.7	1.9	2.6
LNC100-6	14.3	1.9	5.0
LNC80-6	14.9	1.9	4.0
LNC60-6	13.7	1.9	2.6
NC100-10	16.8	2.1	5.8
NC80-10	23.9	2.6	5.0
NC60-10	23.1	2.3	3.4
LNC1000-10	17.6	2.2	5.9
LNC80-10	23.1	2.6	5.4
LNC60-10	22.4	3.0	4.9

Table 5.2 shows that the weight loss of C-(A)-S-H ranged between 9.9% and 14.9% for NC-6 and LNC-6 mixes and it gradually increased to 16.8% and 23.9% for NC-10 and LNC-10 mixes. Δm_1 increased with the increase in activator dosage, NH replacement, and CH inclusion. Higher mass losses for this temperature range indicate a higher degree of reaction and this is consistent with the compressive strength results. This is expected that more slag particles are dissolved, consequently leads to a higher degree of the strength-giving phase formation. The mass loss between 250°C and 400°C (Δm_2) slightly increased with the NH and CH-substitution, and higher activator dosage (Table 5.2). It was also observed that the value of Δm_3 decreased with the NH-substitution and increased with the higher activator dosage and CH inclusion, which means that the CO_3 containing phases are more at these mixes.

5.6 Scanning Electron Microscopy

The selected secondary electron SEM images of the mixes cured for 28 days are shown in Figs. 5.13-5.16 and the EDS quantifications of the atomic ratios are given in Table 5.3.

A higher amount of the micro-cracks which negatively affect the strength are seen on the matrix phase of NC mixes compared to LNC mixes (Fig. 5.13). These micro-cracks might be the reason for the lower strength of the NC mixes.

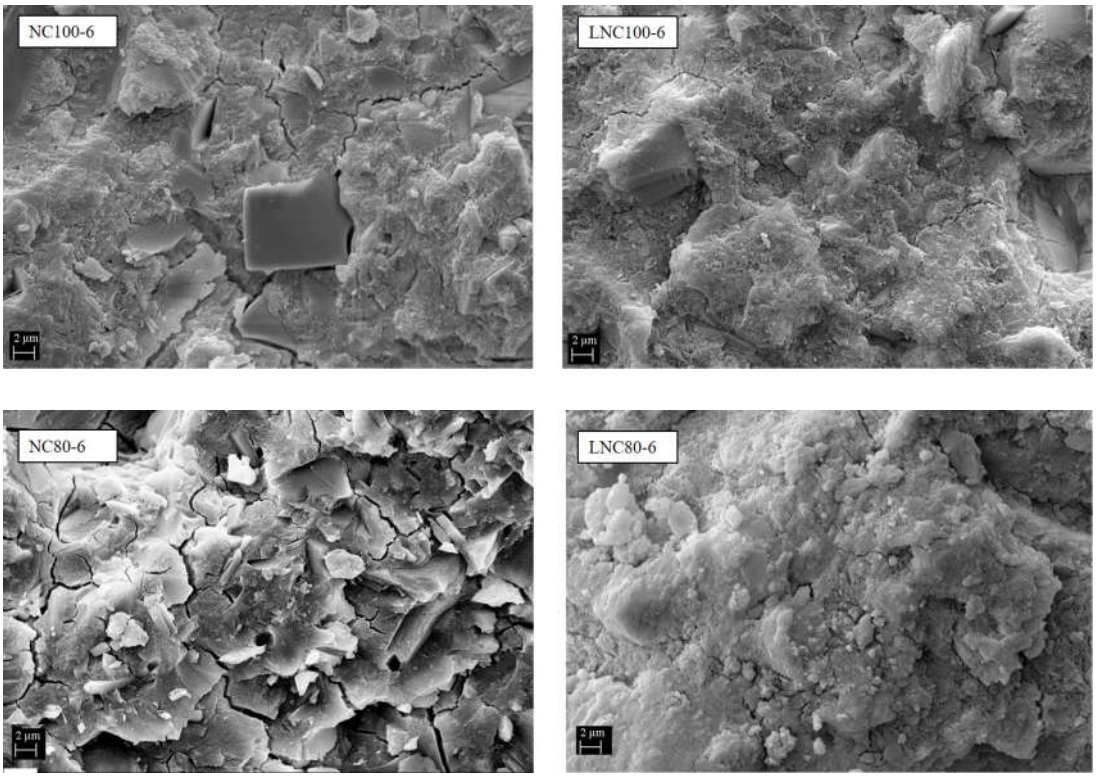

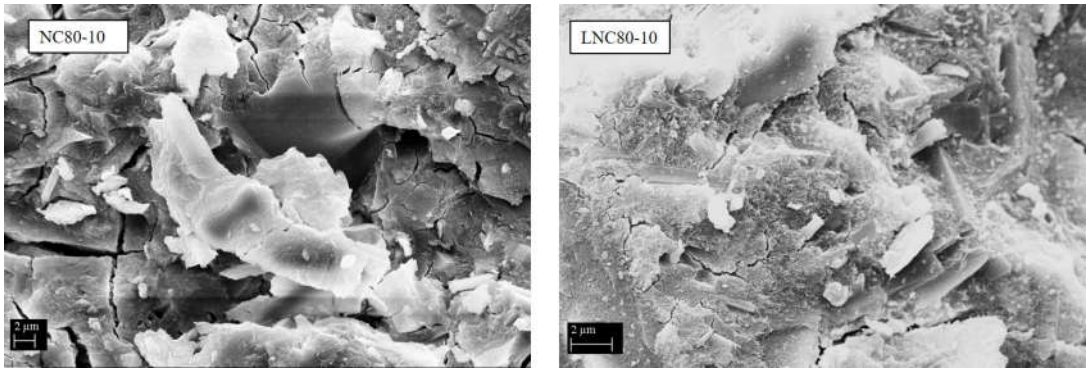

Figure 5.13 Comparison of NC and LNC paste mixes in terms of crack patterns

Micro pores and sharp edges particles were mostly seen in NC100-10 mixes compared to NH-substituted NC60-10 mixes (Fig. 5.14). Similar findings were reported, in which the matrices looked rather dense with increasing NH concentration [134]. This is attributed to the formation of higher amounts of C-(A)-S-H gels caused by the increase in pH of pore solution [82, 125].

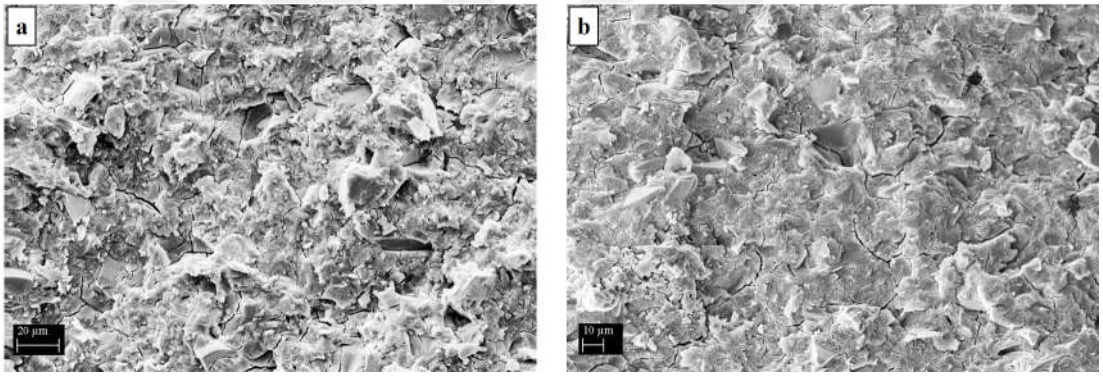

Figure 5.14 Comparison of (a) NC 100-10 and (b) NC60-10 mixes

The deposition of a high amount of calcium carbonates was observed in all mixes with various sizes (Fig. 5.15), especially for CH-substituted mixes. They are seen on the surface of the slag particles and C-(A)-S-H gel. The filling effect of the calcite may also contribute to the denser microstructure of the matrix, and thus a slight increase in compressive strength as well. The presence of calcite which is seen in XRD patterns is proved with these SEM images (Figs. 5.4-5.7, 5.15).

In all mixes, hydrotalcite was observed as well as with the flaky C-(A)-S-H gel (Figs. 5.16 (a) and (b)). In NH and CH-substituted mixes, the amount of these strength-giving reaction products (hydrotalcite and C-(A)-S-H gel) was much more pronounced (Figs. 5.16 (c) and (d)).

Hydration products such as calcite and C-(A)-S-H gel are defined with the aid of EDS spectrums (Figs. 5.17 (a) and (b)).

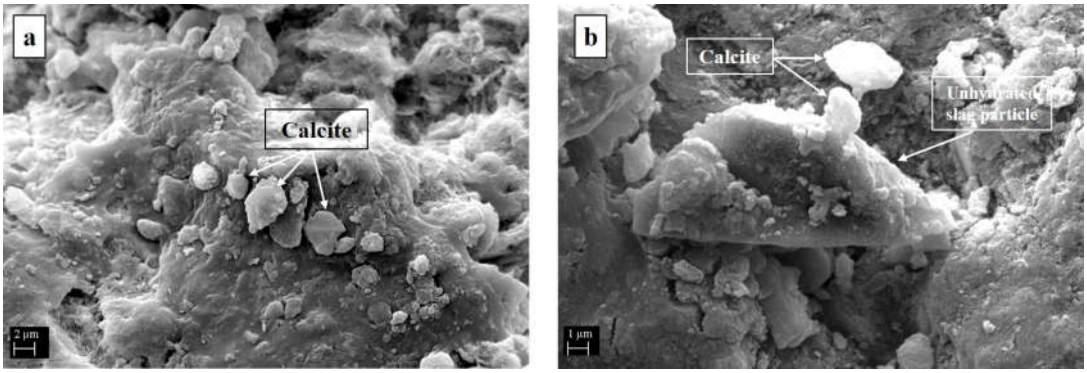

Figure 5.15 Depositions of calcium carbonates (a) LNC80-6 and (b) LNC60-6 mixes

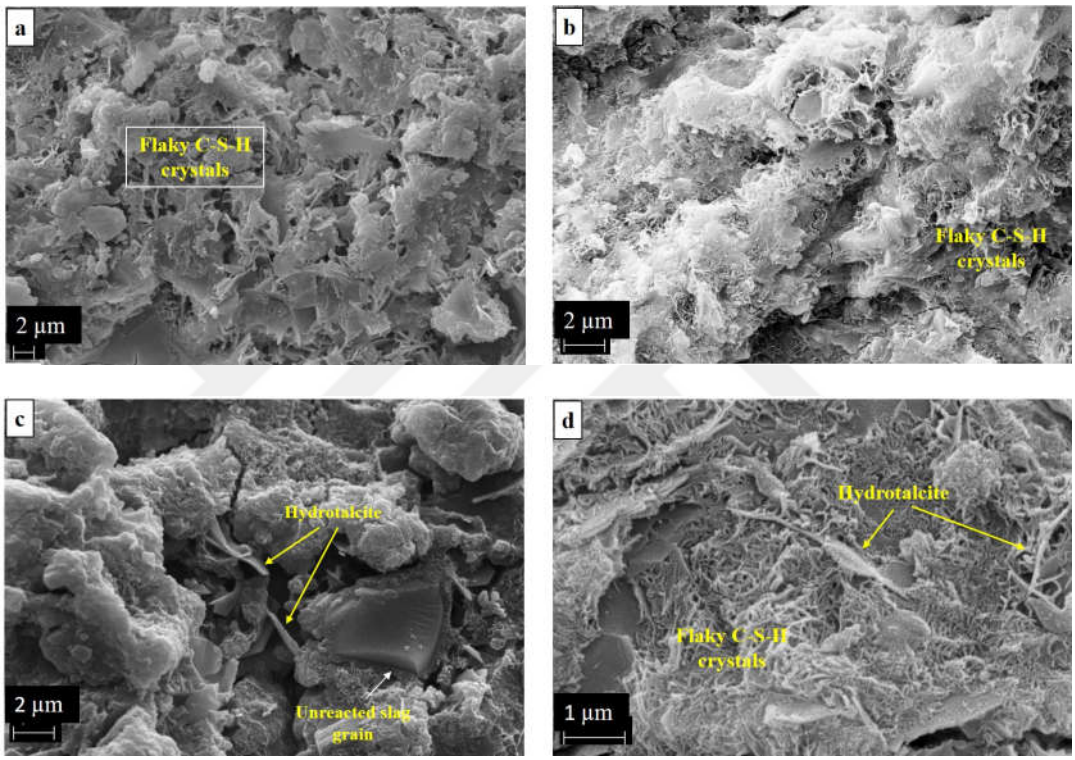

Figure 5.16 (a)(b) C-(A)-S-H and (c)(d) hydrotalcite formation

The differences in the elemental composition of the hydrated phases were observed with EDS analysis. The difference of various atomic ratios between NC and LNC mixes changes with the activator dosage and NH-substitutions and designate different hydration products.

The results showed that the major elements were Ca, Na and Si and the minor elements were Al and Mg (Table 5.3). The major elements were mainly attributed to the formation of C-(A)-S-H and also gaylussite and the minor elements were assigned to the hydrotalcite, which was proved by the XRD and FTIR results.

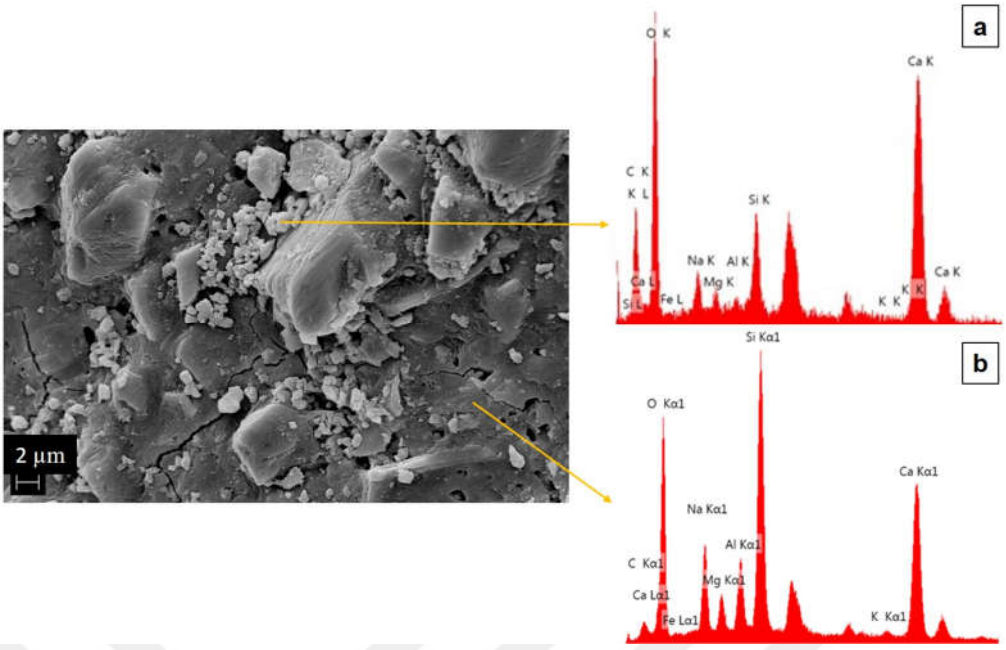

Figure 5.17 (a) Calcite and (b) C-(A)-S-H gel formation

Table 5.3 Average atomic ratios

Mixes	Ca/Si	Ca/Na	Al/Si
NC100-6	0.86	3.00	0.32
NC80-6	0.93	3.13	0.33
NC60-6	0.93	2.78	0.33
LNC100-6	1.08	4.00	0.31
LNC80-6	1.11	4.75	0.32
LNC60-6	1.18	4.13	0.36
NC100-10	0.80	2.00	0.32
NC80-10	0.80	2.00	0.32
NC60-10	0.96	2.54	0.31
LNC1000-10	0.96	2.30	0.29
LNC80-10	1.29	3.44	0.29
LNC60-10	1.38	2.78	0.29

The Ca/Si ratio of C-S-H gel depends on the type of activator, curing condition and chemical composition of slag and ranges from 0.6 to 2.3 [117, 128–130]. In this study, the Ca/Si ratios of all pastes were in the range of 0.80-1.38. LNC mixes have higher Ca/Si ratios compared to NC ones, which should be caused by the inclusion of CH. The increase of Ca/Si ratio is also seen with the replacement of NH, and that is attributed

to the increased Ca^{2+} ions dissolved from slag and hence higher amount of Ca^{2+} ion occupied in C-(A)-S-H gel. The maximum Ca/Si ratios were recorded as 0.96 and 1.38 in 6% and 10% mixes, respectively. The higher activator dosage resulted in the higher Ca/Si ratio, which could lead to increased Ca^{2+} ion dissolution from the slag in the higher alkaline environment. Higher Ca/Si is indicative of the formation of denser, calcium-rich products with an increased activator [82] and CH substitution, which was consistent with the compressive strength development.

The Al/Si ratio did not vary significantly with changes in activator concentration and NH and CH-substitution, for all mixes, the ratio ranged between 0.29 and 0.36. Lloyd et al. [130] announced that the more Al can be incorporated in the gel structure with increasing the activator concentration. Wang and Scrivener [129] reported that actual Al/Si ratios were in the range between 0.16 and 0.22, depending on activator type and age.

The Ca/Na ratios of all pastes were in the range of 2.00-4.75. The values were higher in CH-modified mixes compared to NC ones and were lower for 10% activator concentration. These results are expected to be considering CH-substituted mixes that contain CH and higher amount of Ca^{2+} and mixes contain 10% activator dosage which provides a higher amount of Na^{2+} into the mixes. Na is defined in [82, 125, 134] as charge-balancer for negatively charged Al-O-Si monomers in the formation of C/N-A-S-H. Magnesium and a part of aluminum can be referred to the hydrotalcite which was found in all mixes by XRD analysis (Figs. 5.4-5.7).

Backscattered electron (BSE) images taken from the well-prepared specimens can be used to identify the type of phases formed with the grey level distribution. Entropy maximization of the grey level histogram image processing can be conducted to determine the area fraction of the objective phase of the BSE images. BSE images should be taken with proper parameters that would make unhydrated slag distinguishable from all other phases in the paste. Zhao and Darwin [135] and Feng et al. [136] reported that accelerating voltage and magnification plays an important role in the assessment of the area fraction of unyhdrated slag particles (A_s). In this study, only one magnification and accelerating voltage were applied and the difference between the mixes was explored. Since the microstructure of cementitious materials is not equal at each point, the area fraction varies from field to field. Thus, to evaluate the area fraction results, three measurements were taken to make the results more representative. C-(A)-S-H gel formation and the unhydrated slag particles of mixes are identified with the energy dispersive spectroscopy (EDS) measurement (Fig. 5.18). Fig. 5.19 shows the BSE of selected NCAS mixes, designating the effect of modifiers. In these images light grey, dark grey and black colored regions were observed, representing

unhydrated slag grains, C-(A)-S-H gel, pores, and cracks, respectively.

In secondary electron images, denser microstructure determined in CH-substituted LNC mixes compared to the NC ones (Fig. 5.19). It can be easily seen that NC100-10 has the highest unhydrated slag particle area fraction, on the other hand, LNC60-10 has the lowest (Table 5.4). With the CH and NH substitution, an enhanced gel structure was obtained, providing a reduction in the permeability properties.

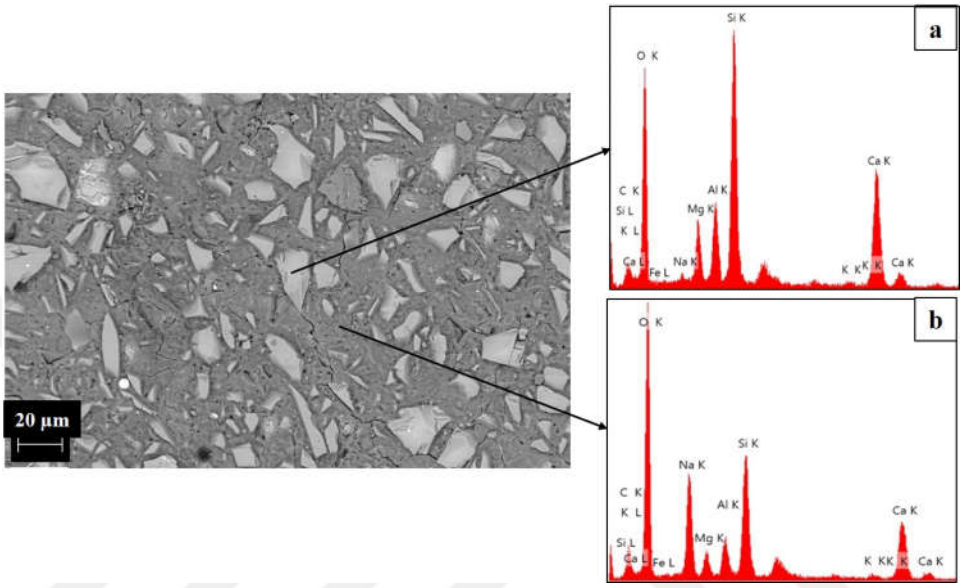

Figure 5.18 EDS spectrums of (a) unhydrated slag particle, (b) C-(A)-S-H gel

Table 5.4 Total area and area fraction of unhydrated slag particles of selected mixess

Mixes	**Total Area (mm^2)**	**Area fraction (%)**
NC100-10	0.075	44.00
NC60-10	0.048	29.3
LNC60-10	0.040	23.3

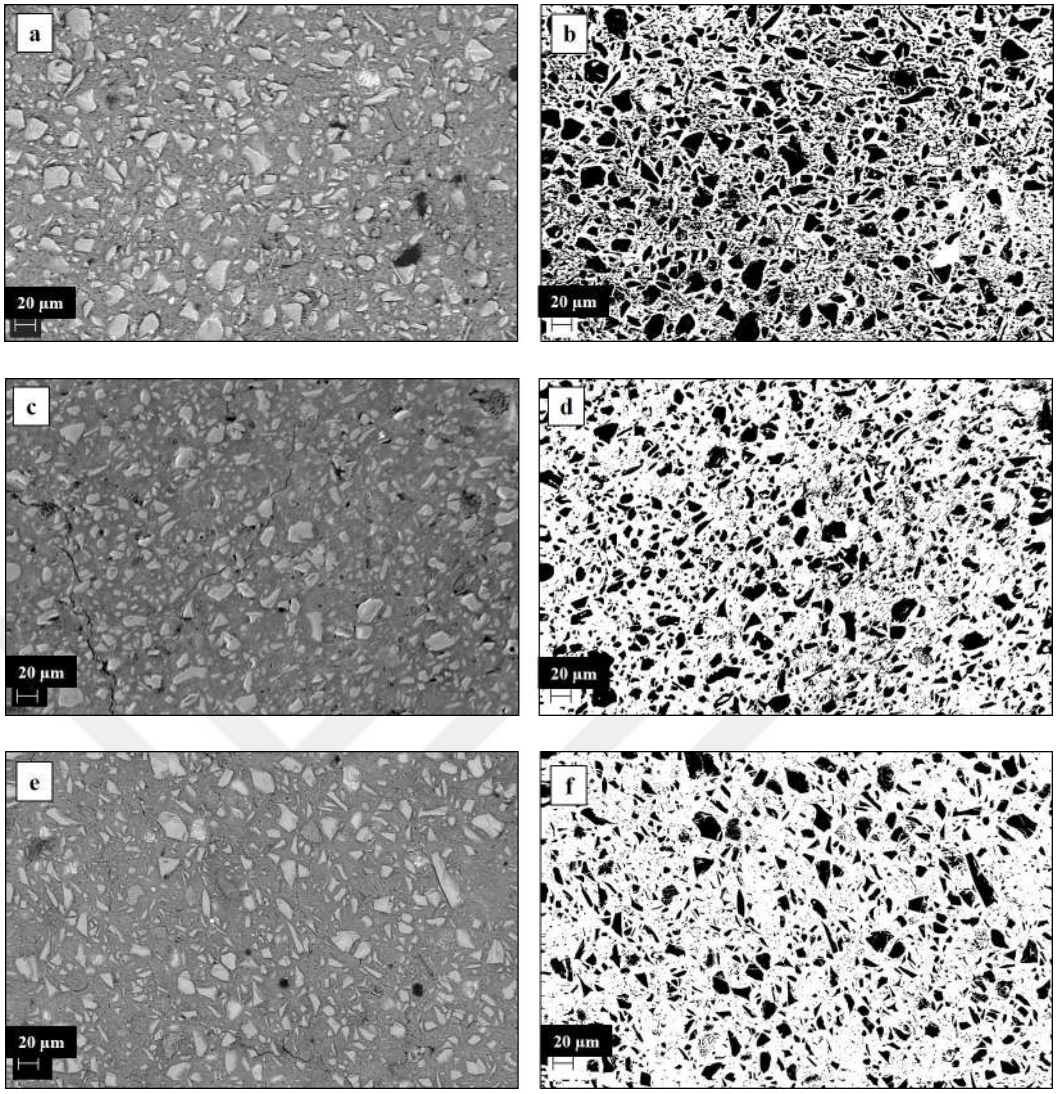

Figure 5.19 BSE images of (a) NC100-10, (c) NC60-10 and (e) LNC60-10 mixes; binary images of (b) NC100-10, (d) NC60-10 and (f) LNC60-10 mixes

5.7 Pore Size Distribution

MIP is known as a reliable test method to determine the pore volume fraction in cementitious systems but has restrictions due to the "ink bottle effect" [137, 138]. However, pore sizes determined using MIP can be employed as a useful comparative tool as mentioned in several publications [139–142]. It has been shown that the AAMs have a microporous framework that is governed by type or mixture of the alkali cations used in the activation process [143]. Figs. 5.20-5.25 show the pore size distribution and differential curves of NCAS mixes at 56 days of the reaction. Total pore volume was classified into the two size ranges considering the IUPAC recommendations [144], from 0.004 to 0.05 μm, and $>$ 0.05 μm. The IUPAC classification implies the smallest pore size group as having a size range of from 0.002 to 0.05 μm, but due to the detection limit of 0.004 μm of the MIP, it is defined as 0.004 to 0.05 μm in the current study.

This smaller sized pores (0.004 to 0.05 μm) can be named as mesopores, mostly affect the permeability and shrinkage behavior. The pores > 0.05 μm size range which can be classified as macropores are influential in strength behavior and impermeability properties [2].

The pore size characteristics were measured by the MIP test and both the cumulative and differential pore size distribution are determined and presented in Figs. 5.20-5.25. The NC100-6 mixes, which have the highest sorptivity, presented the highest cumulative pore volume with a diameter ranging from 0.006 to 0.060 μm. On the other hand, the cumulative intruded pore volume is least for the LNC60-10 mixes. Generally, the total pore volume of LNC mixes is lower than those in NC mixes, which is in line with the other permeability results. Similarly, an increase in the activator dosage, from 6% to 10%, decreases the total pore volume, especially in NC mixes. This trend, again, compatible with the permeability results.

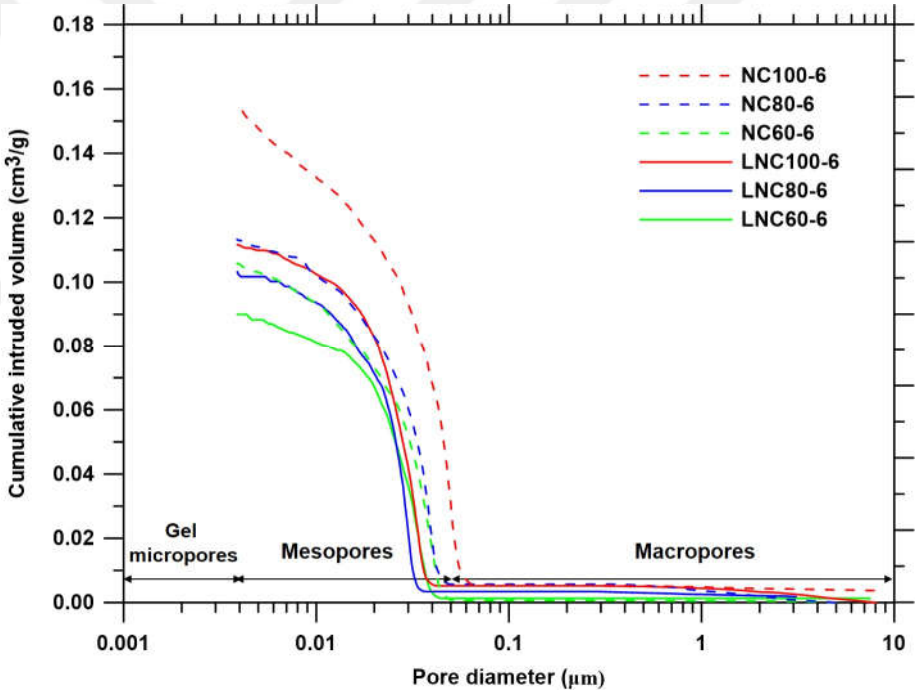

Figure 5.20 Pore size distributions of NC-6 and LNC-6 mixes

NH and CH substitution creates finer pore size distributions. Thus, denser microstructure and higher pore refinement, consequently higher resistance to sorptivity and chloride migration are achieved in NH and CH-modified mixes. The maximum reduction in the total pore volume was obtained with the CH-substitution in LNC100-6 with approximately 28% and the overall pore size distribution was shifted into finer-sized diameters (Figs. 5.22 and 5.23).

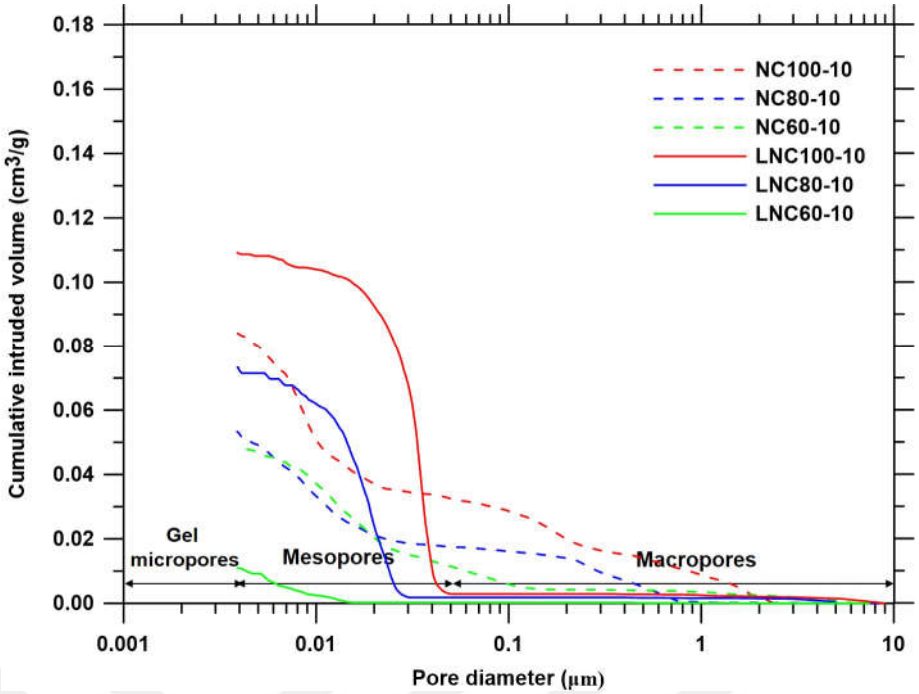

Figure 5.21 Pore size distributions of NC-10 and LNC-10 mixes

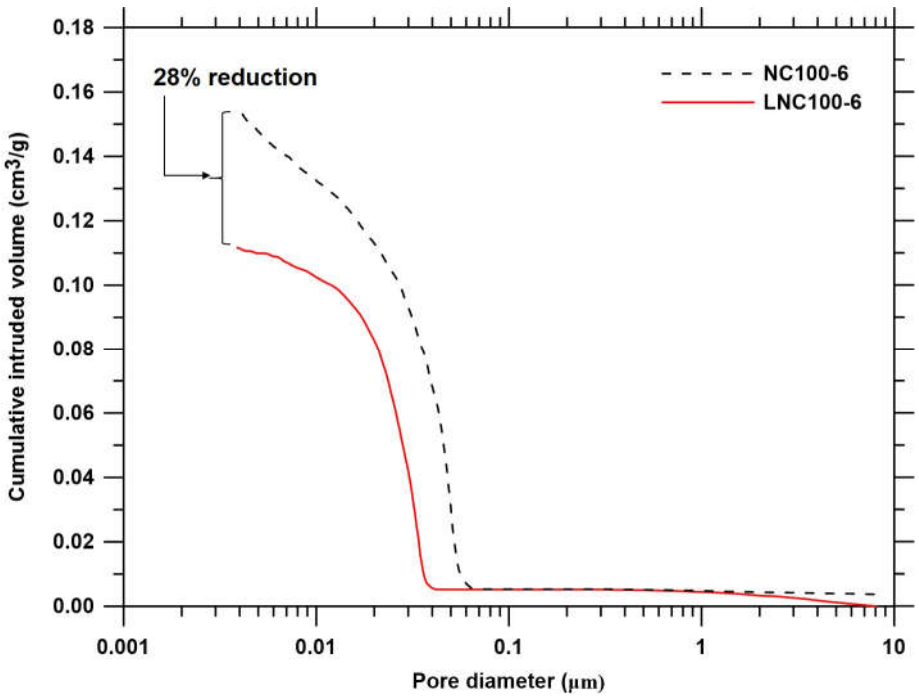

Figure 5.22 The cumulative pore volume of NC100-6 and LNC100-6 mixes

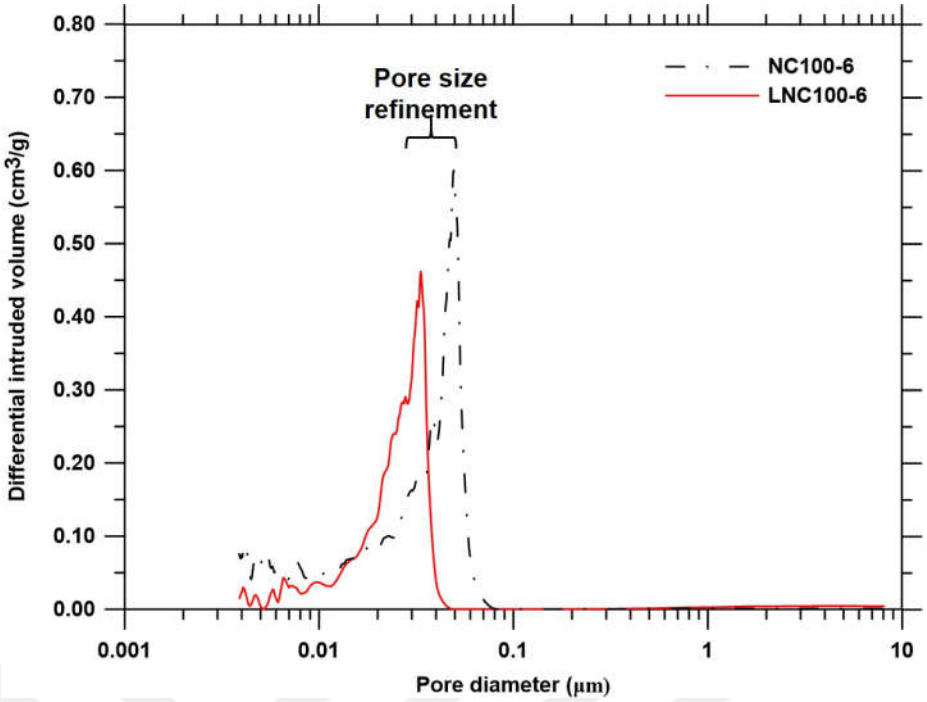

Figure 5.23 Differential pore size distribution of NC100-6 and LNC100-6 mixes

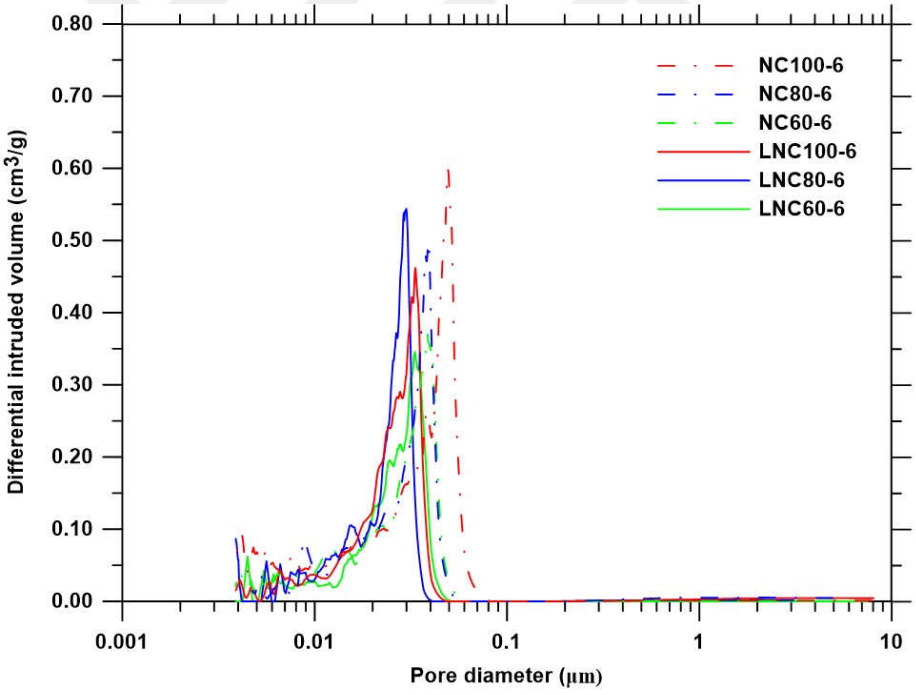

Figure 5.24 Differential pore size distribution of NC-6 and LNC-6 mixes

The threshold diameter is obtained by the cumulative pore volume curve of which the intruded pore volume distinctly increases (Fig. 5.26). The critical pore sizes range between 0.005 μm and 0.049 μm, which demonstrates a high amount of variation between the blends. This magnitude of difference in total pore volume and pore size range is responsible for the differences in permeability of the mixes. The CH-substitution reduced the threshold diameter in NC-6 and LNC-6 mixes, irrespective

of the NH-substitution, indicating refinement in the pore structure. However, NC-10 mixes demonstrated lower threshold diameter.

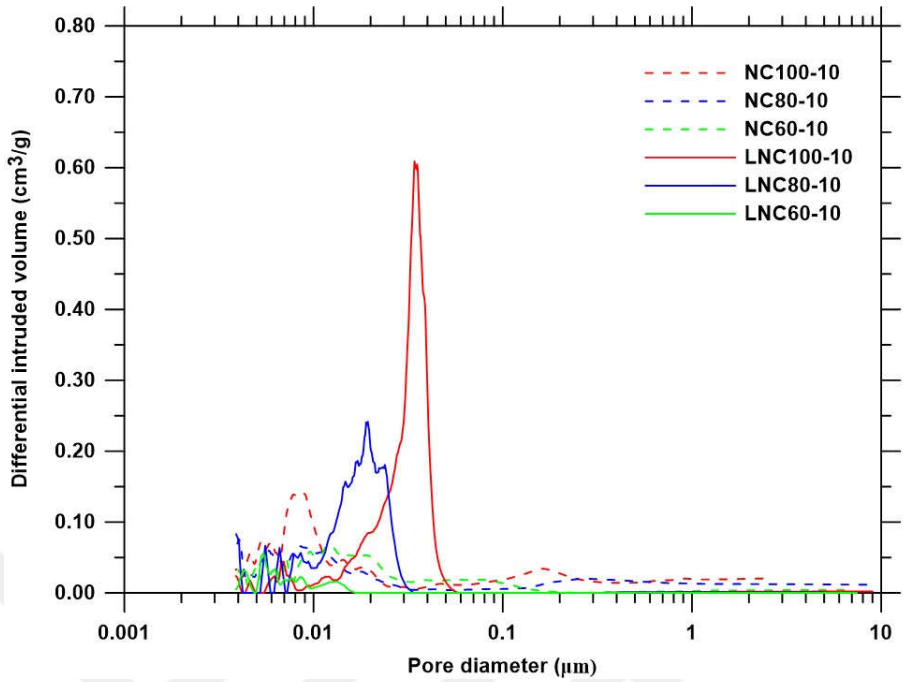

Figure 5.25 Differential pore size distribution of NC-10 and LNC-10 mixes

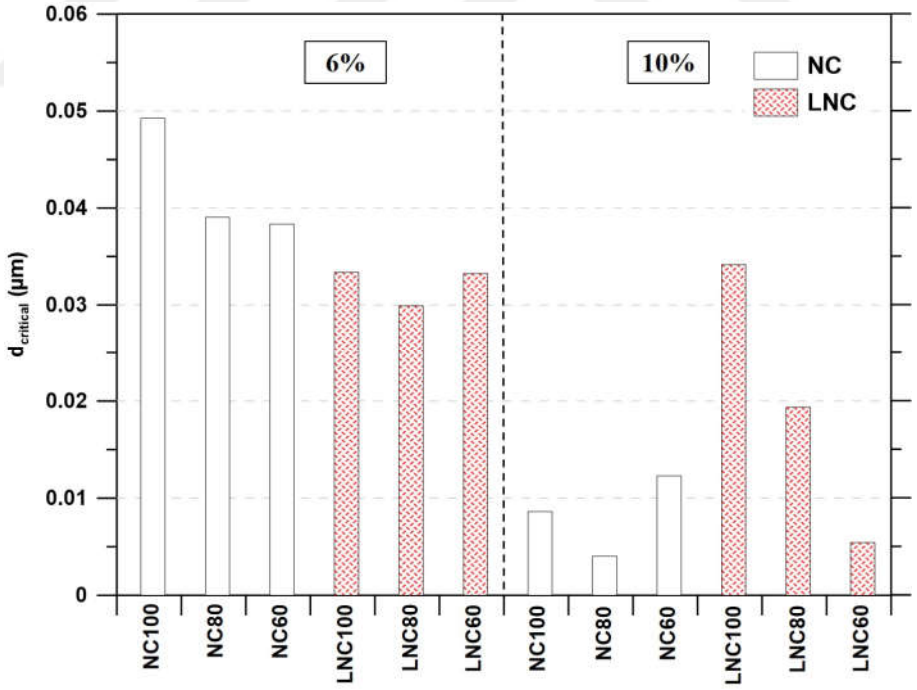

Figure 5.26 Critical pore size values of mixes

The classification of pores into different size ranges helps rationalize the permeability of mixes. Macropore and mesopore concentrations and with the percentages are given in Table A.9.

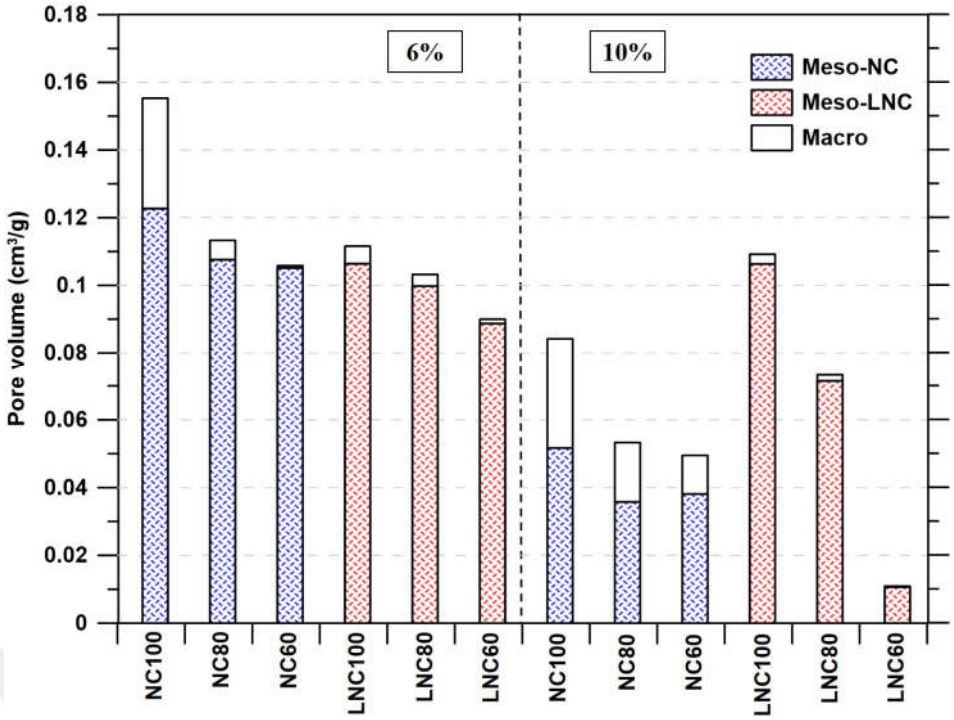

Figure 5.27 Total pore volume of mixes

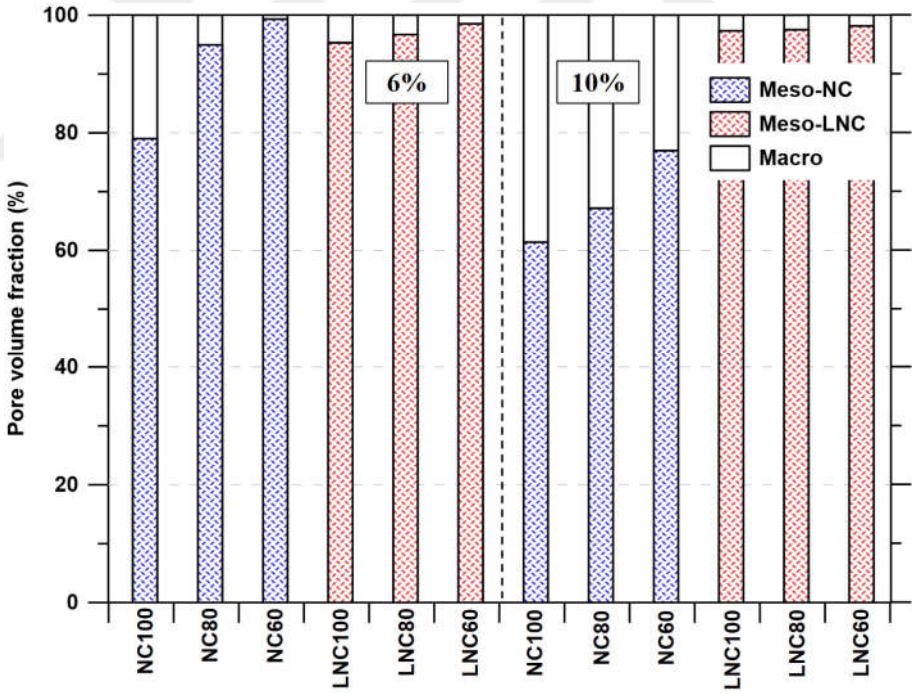

Figure 5.28 Pore volume fraction of mixes

It can be seen that for most of the mixes, pore sizes range between 0.004 μm and 0.050 μm, which means that the dominant pore sizes are the mesopores (Figs. 5.27 and 5.28). Only NC-10 mixes designate a different trend. The fraction of macropores is very limited in LNC mixes. With the substitution of NH and/or CH, the proportion of pores in the 0.004-0.050 μm size range increases significantly, indicating the formation

of additional reaction products, promoted by the secondary activator (NH). In terms of capillary pores (>50 nm), CH-modified mixes tend to have smaller capillary pore fraction, providing lower sorptivity.

The porosity of the mixes was calculated by multiplying the total pore volume and density of the mixes. The porosity of each mixes are given in Table A.9 and Fig. 5.29. It can be seen that NH and CH-substitution, along with the activator concentration reduced the porosity.

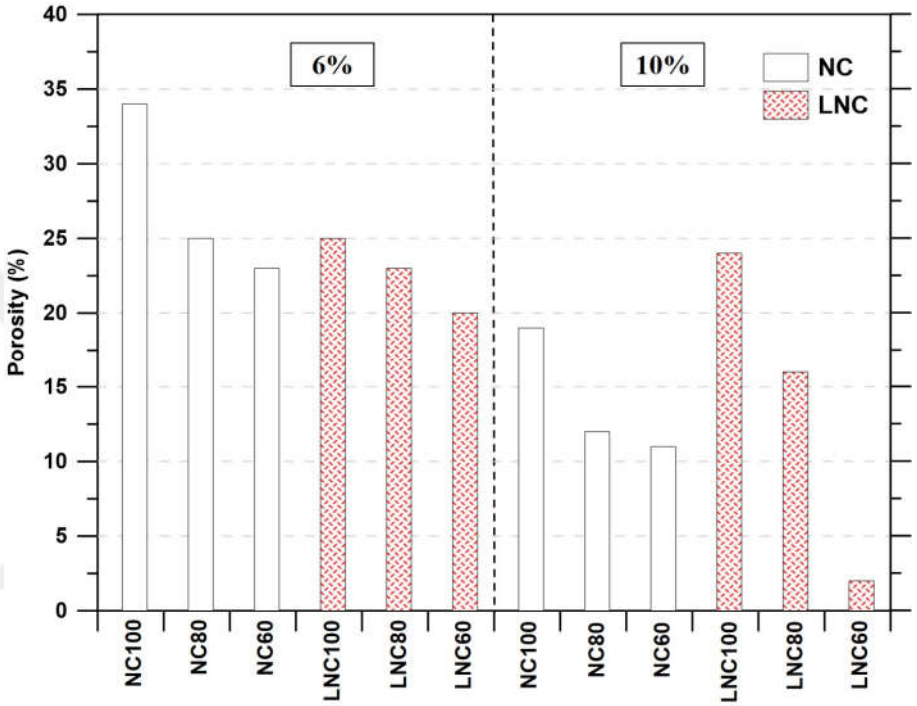

Figure 5.29 Porosity of mixes

Ma et al. [145] reported that increasing the concentration of the activator results in a lower porosity and a refined pore system, hence reduced the permeability of alkali activated fly ash paste. Collins and Sanjayan [146] showed that sodium metasilicate activated slag concrete presents finer pore size distribution and lower porosity than the OPC-based concrete.

5.8 Discussion and Conclusions

The strength development and microstructural evolution of NCAS mixes are evaluated in this chapter. The effect of different modifiers is investigated and the results are given in the text. Based on the presented test results, it was found that both NH and CH can be used as modifiers in NCAS systems. Moreover, the combination of the two modifiers gives better results in terms of strength development and ultimate strength.

The strength development was explained with the chemical changes in the paste mixes. The reaction mechanism was visualized with the schematic diagram with and without CH modifier (Fig. 5.30).

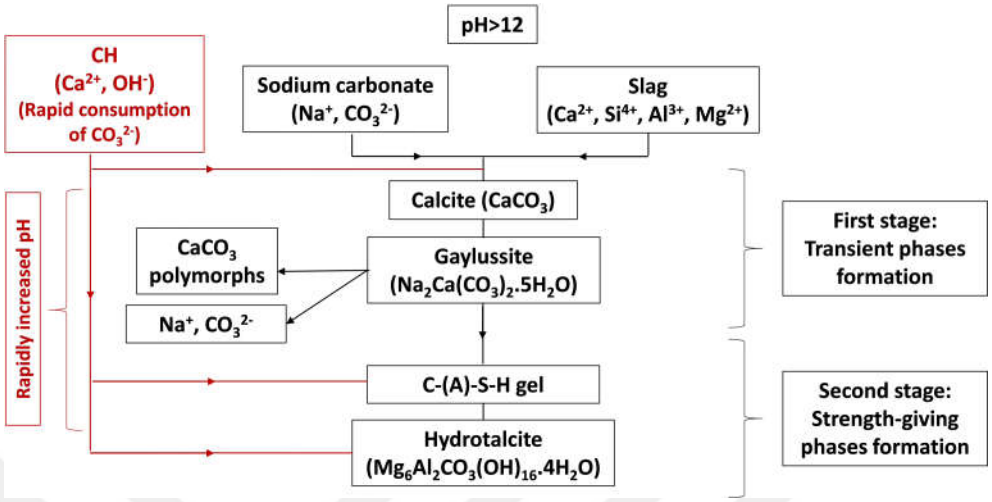

Figure 5.30 Schematic diagram of the reaction kinetics with and without CH

When the pH value exceeds the limit level (> 12), dissolution of slag initiates. In plain mixes, as a result of the preferential reaction between Ca^{2+} from slag and CO_3^{2-} from NC, calcite and gaylussite forms. On the other hand, dissolution of slag continues. Unfortunately, calcite and gaylussite do not give a high degree of cohesion required for the development of high early mechanical strength. The reaction proceeds gradually due to the slow dissolution mechanism of slag under the lower pH induced by NC. Once the CO_3^{2-} is exhausted, the reaction rate expedites.

With the presence of CH in the medium, pH increases as a consequence of the dissolution of CH. A high amount of calcium released into the medium and carbonate ions are removed from the medium by the formation of calcite and gaylussite. With the consumption of carbonates, a further increase can be seen in pH and with the further dissolved ions from slag, strength-giving phases, e.g. hydrotalcite and CASH forms. Moreover, calcium from CH involves in the C-(A)S-H gel and the hydrotalcite. It can be deduced that CH acts as a carbonate binding agent and modifies the chemistry of the system. In summary, the CH expedites the hardening mechanism and strength of NCAS via several mechanisms, including:

- Increases the pH of the medium (Fig. 4.4),
- Accelerates consumption of carbonate ions (Fig. 4.5)
- Involves in C-(A)S-H gel formation,

- Enables the formation of a higher amount of strength-giving phases, as observed in XRD patterns (Figs. 5.6-5.8) and SEM images (Figs. 5.13-5.16)

The compressive strength results are compatible with the microstructural analysis results.

Summarized conclusions of this chapter can be drawn as follows:

- Activation of slag with NC as sole activator exhibited hardly any strength (≈7 MPa) cured at room temperature up to 90 days.
- NH-substitution did not cause any considerable change in compressive strength at an early age for both activator dosages. However, a significant increase was seen at further ages, especially when used at high dosages (e.g. 40%).
- NC replacement with NH and the presence of CH in the binder as a replacement of the slag enhances the rate of dissolution of slag leading to faster strength development. CH-substitution significantly increased the compressive strength even at 3 days.
- The presence of CH in the binder as a replacement of the slag led to a substantial increase in compressive strength irrespective of the NH usage and/or activator concentration. Enhanced strength development mainly caused by removing the carbonate from the medium and providing additional Ca^{2+} resources.
- Activator dosage also plays an important role in strength development as well as with the modifiers.
- Formation of strength-giving phases such as hydrotalcite and C-(A)-S-H is confirmed with the microstructure analysis and explains the strength development.
- The intensities of the XRD peaks of main reaction products, C-(A)-S-H and hydrotalcite, increased for all mixes signifying a higher concentration of reaction products thus pointing to higher compressive strength.
- Increasing the curing time did not generate new phases, however, it increased the crystallinity of C-(A)-S-H type structure.
- In CH-modified LNC mixes, the peaks at higher degrees in XRD patterns were more intense than the NC mixes, which resulted in a decrease in interlayer distance reasoning for the higher compressive strength.

- In CH-modified and CH+NH-modified mixes, the Si-O-T band shifted to the higher wavenumbers which attributed to the higher degree of polymerization, and higher strength.
- The presence of reaction products approved by TGA as well, indicated higher mass losses higher degree of reaction which consistent with the compressive strength results.
- The main hydration products such as C-(A)-S-H gel, hydrotalcite and calcite were determined with the secondary electron SEM images and EDS measurements. BSE images are used to identify the fraction of unhydrated slag particles for different NCAS mixes. With the CH and NH substitution, an enhanced gel structure was obtained.
- The pore size distribution is refined into a smaller diameter region and the total pore volume is reduced by 28% with the CH-substitution due to the formation of a denser microstructure.
- The detailed characterization of the microstructural development with the progress of hydration in mixes serves to an enhanced understanding of the strength development as a consequence of chemical changes.

6
FRACTURE RESPONSE

6.1 Introduction

It is known that alkali-activated reinforced concrete exhibits similar load-bearing capacity when compared to the OPC concrete. Thus, it is believed that these environmentally friendly materials are proper for construction [147]. However, the fracture properties of AAMs should also be evaluated in detail, considering structural designs where concrete brittleness is needed to be determined.

The fracture properties of cementitious materials mostly related to the formation and propagation of cracks. The resistance of a material against crack propagation and failure can be estimated by evaluating the fracture energy (G_F), fracture toughness (K_{Ic}), and critical crack tip opening displacement ($CTOD_c$) [148].

Similar to the OPC binder matrix, quasi-brittle characteristics of AAMs can be turned into ductile characteristics with the introduction of fibers to the matrix. It is well known that fibers improve the flexural strength, fracture toughness and impact resistance of cementitious composites since the cracking and widening of the cracks can be controlled by fiber bridging. Therefore, the energy demand for crack propagation increases. In one of the recent studies, the incorporation of steel (ST) fiber into the geopolymer matrix provided significant improvement in both the energy absorption capacity and the flexural strength [149]. Polypropylene (PP) fibers exhibit poor performance compared to ST fibers in terms of flexural strength. Beyond the type of fiber used, the type and concentration of alkaline activator, curing regime and chemical composition of precursors have deterministic effects on the fracture performance of AAMs.

In a limited number of studies, the effect of incorporation of different types of fibers, e.g. glass and carbon [150], polyvinyl alcohol [150–153], PP [149], polyethylene [154], basalt fibers [155], organic fibers like cotton, flax [156, 157], and ST fibers [158–162] in AAMs were studied. Bhutta et al. [163] investigated the bond strength of ST and PP fibers in alkali-activated fly ash mortars and concluded that alkali concentration and

heat curing had beneficial effects on the strength and the energy absorption capacity of AAMs. In another study [164], the flexural strength of waterglass activated slag mortar was reported to be higher than that of fly ash and OPC-based mortars. The employment of both ST and PP macro fibers also resulted in enhancement of flexural toughness of alkali-activated composites, but the length-deformed (twisted) geometry of the PP macro fiber was found to be responsible for poor flexural strength, because of the poor adhesion between fiber and matrix, which is the prominent factor affecting the mechanical properties [165]. Beglarigale et al. [166] reported that the fiber-matrix bond mechanism of alkali-activated slag mixes was significantly affected by silicate modulus (M_s) of alkali solution, curing regime, and partial replacement of slag with metakaolin, silica fume or fly ash. The higher M_s and substitution of fly ash and silica fume enhance the fiber-matrix transition zone.

In previous sections, the contribution of CH has been distinguished by reasonable setting time as opposed to NH replacement. CH-substitution was found as the most effective method to accelerate the reaction kinetics of NCAS. On the other hand, the replacement of NC with NH resulted in higher compressive strength at later ages. Moreover, the presence of CH in the binder leads to a substantial increase in compressive strength caused by removing the carbonate from the medium and providing extra Ca^{2+} ions. In this chapter, the effect of the modifiers such as NH and CH, and fiber addition on fracture parameters of fiber-reinforced NCAS has been aimed to reveal. Fractural behavior of plain and fiber-reinforced NCAS mortars experimentally determined by flexural strength, fracture toughness, fracture energy, and brittleness index parameters.

6.2 Influence of Fiber Reinforcement on Compressive and Flexural Strength

Four different NCAS mortar mixes were prepared to understand the effects of the alkali combination and CH-substitution on the compressive and flexural strength of plain, PP and ST fiber-reinforced NCAS mortars. The compressive and flexural strengths of different mixtures and OPC-based mortar for comparison are reported in Figs. 6.1 and 6.3. The reaction mechanism and the variation of the compressive strength of plain mixes considering the type of alkali activator used and slag replacement were detailed in Chapters 4 and 5.

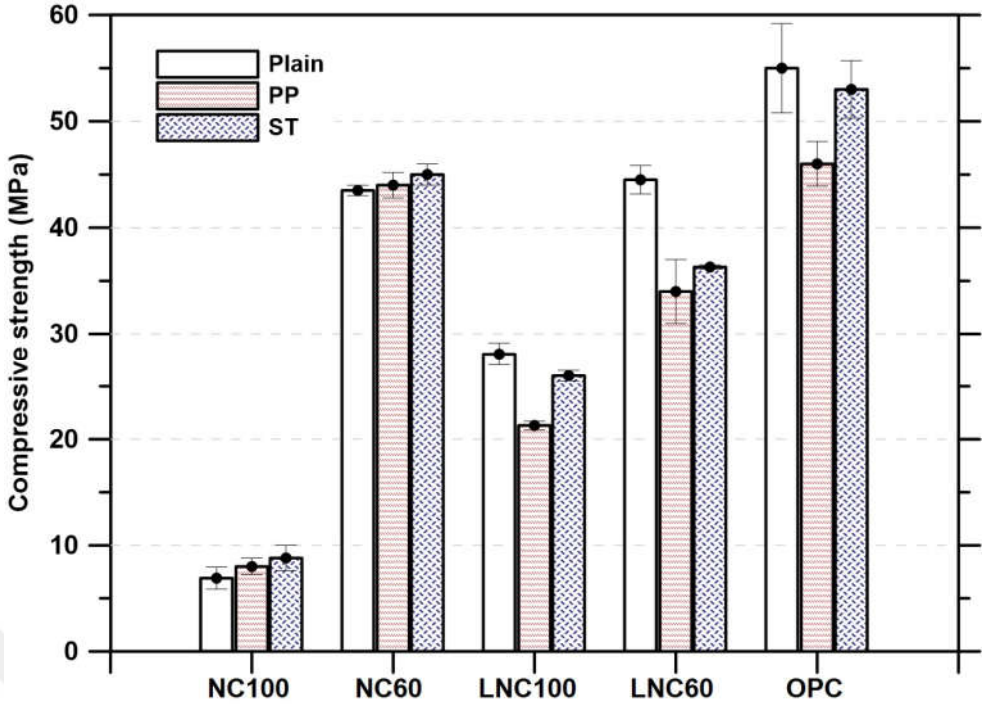

Figure 6.1 Compressive strength of plain and fiber-reinforced mixes

It is seen from Fig. 6.2 that PP and ST fiber reinforced samples exhibit ductile behavior with the evaluation of several curtailed cracks while the plain samples have a typical failure of brittle material when the failure modes under compression were observed.

Figure 6.2 Failure modes of (a) plain, (b) PP, and (c) ST fiber-reinforced NCAS mortars under compression

The inclusion of either PP or ST fibers caused a slight increase in the compressive strength of NC100 and NC60, which might be due to the delayed formation of initial cracks in the paste phase [167, 168]. However, fiber inclusion adversely affected the compressive strength of OPC and CH-modified LNC mixes. The effect of PP fiber in reduction of compressive strength was higher compared to that of the ST fiber. According to the flow test performed on NC and LNC paste samples, the fluidity of CH-substituted mixes was found to be lower than that of the plain NC mixes (Fig. 4.1). Besides, it was reported in a previous study [169] that the workability of concrete may decrease with fiber addition, depending on the type and content of fiber . Kuder et al.

[170] stated that incorporation of fiber reinforcement can make mixing more difficult, resulting in excessive voids. Belkadi et al. [171] reported that fiber incorporation creates additional voids in fiber-reinforced samples. Puertas et al. [164] reported that incorporating 1% of PP fiber caused approximately 12% compressive strength reduction in waterglass activated slag mixes. This behavior is mainly related to the presence of PP fiber which affects the workability of mixes. Considering the findings of the previous studies, such a decrease in compressive strength might be attributed to the fact that incorporating PP and ST fibers is responsible for low workability, which in turn would introduce relatively high void content in CH-substituted and OPC-based mixes.

The effect of mixture variation on the flexural strength of plain and fiber-reinforced mortars is depicted in Fig 6.3. The flexural strength of plain mixes slightly increased with the NH and/or CH-substitution. Among plain mixes, NC100 mixes presented the lowest value with 1.9 MPa, while NH-substited mixes (NC60) reached the maximum value of 2.8 MPa with a 47% increase.

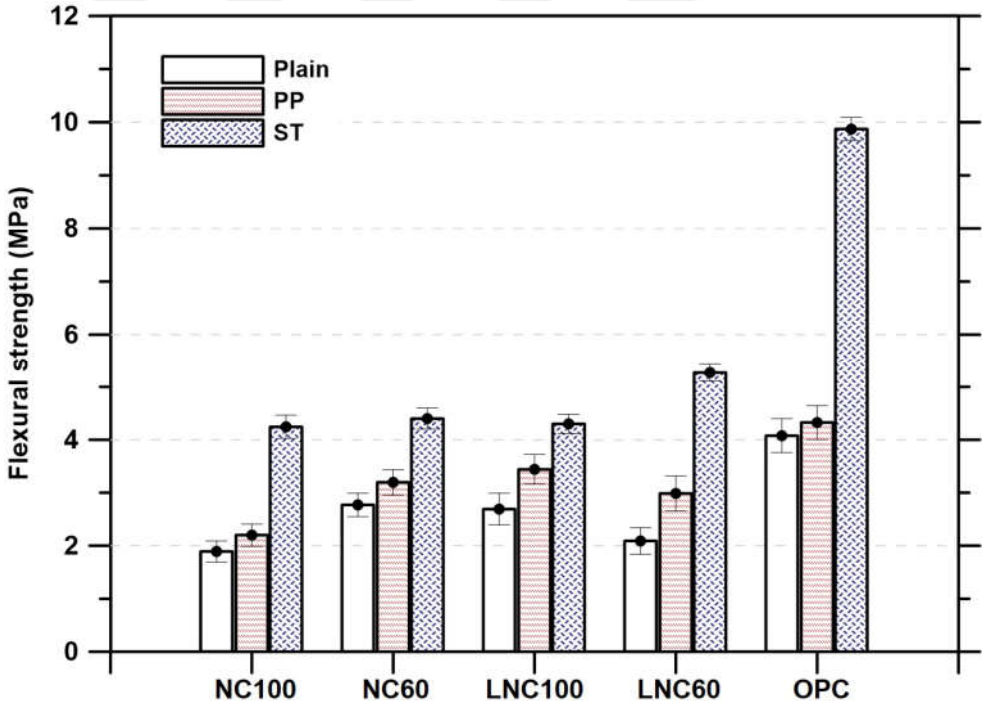

Figure 6.3 Flexural strength of mixes

Fiber incorporation had a beneficial effect on the flexural strength of all mixes, as expected. Fig. 6.3 shows that the flexural strength of the samples with ST fiber was higher than the PP reinforced samples. In the case of PP reinforcement, the improvement in flexural strength ranges between 16% and 43% considering plain groups, while the ST fiber-reinforced specimens showed better improvement in the

flexural strength ranging between 59%-152%. Similarly, significant enhancement was found in flexural strength of alkali-activated, 2% PP fiber-reinforced slag mortar compared to plain mortar [172]. Conversely, the studies performed by Puertas et al. [164] and Ranjbar et al. [149] have shown that PP fiber negatively affected the flexural strength of alkali-activated slag mortars. Generally, PP fiber reinforced mortars or concretes exhibit higher flexural strength than the materials without fiber reinforcement, however conflicting results are also reported in the literature [149, 164]. This inconsistency is potentially due to the difficulties in casting, compaction and vibration of the material in fresh state [173], which results in inadequate fiber dispersion and bond between fiber and matrix interface.

The maximum increase was obtained in LNC60 mixes for both types of fibers, and it may be attributed to the good adhesion between fiber and the matrix. The reason for better adhesion in LNC60 mixes is because of the CH and NH substitution which leads to denser microstructure in the matrix [174]. The improvement due to the PP fiber inclusion was more prominent in LNC100 and the flexural strength of LNC100 reached the highest value (3.4 MPa) among the PP fiber-reinforced NCAS mortars. On the other hand, ST fiber-reinforced LNC60 had the maximum flexural strength value among the ST fiber-reinforced NCAS mortars. It can be deduced that NH and CH substitution enhances the flexural strength of fiber-reinforced NCAS mixes.

The contribution of ST fiber on flexural strength was much more pronounced than that of PP fiber. The OPC based mortar with ST fiber exhibited the highest flexural strength (9.9 MPa), while the ST fiber-reinforced NCAS mortars had almost half of the flexural strength of OPC.

6.3 Influence of Fiber Reinforcement on Fracture Parameters

The influence of fiber reinforcement on compressive and flexural strength of NCAS mortars were explained in the previous section, this section explains the effect of PP and ST fiber reinforcement on fracture response of the NCAS mortars. The fracture parameters are characterized using a double-K fracture model proposed by Xu and Reinhardt [175].

6.3.1 Load-CMOD Responses and Fracture Energy

Figs. 6.4 (a-c) represent the load-crack mouth opening displacement (CMOD) curves of plain, PP and ST fiber reinforced mortars up to 2.25 mm, respectively. The average values of load-CMOD curves were obtained accurately using the procedure detailed in [176–178].

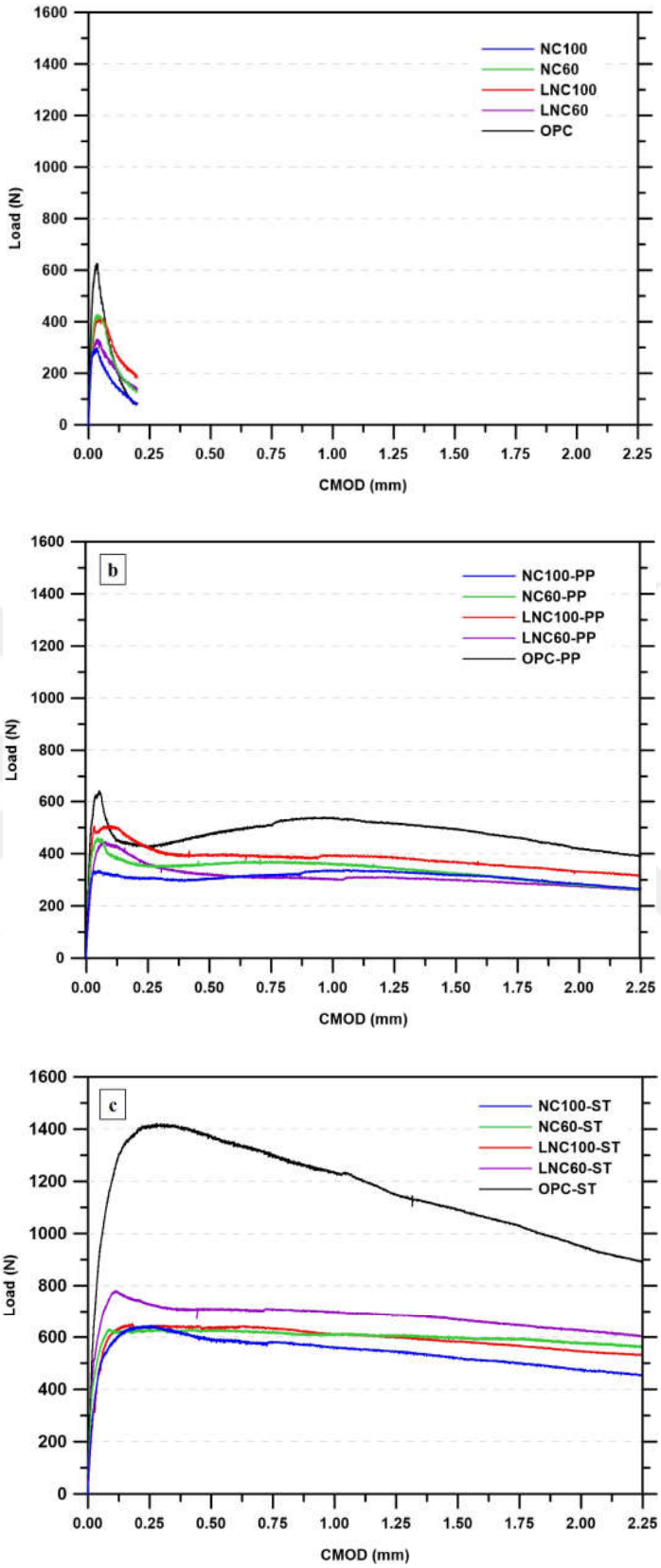

Figure 6.4 Load-CMOD curves of (a) plain mixes, (b) PP fiber-reinforced mixes (c) ST fiber-reinforced mixes

As clearly seen in Figs. 6.4 (a-c), incorporation of fibers increased the peak load and significantly improved the post-peak behavior of NCAS mortars, which implies an improved toughness. Similar results were reported in previous researches focused on cotton fiber [179], macro ST and PP fiber reinforced fly ash/slag based AAMs [165, 180].

Moreover, the pre-peak behavior of the samples is similar and the slope of the curves is found to be similar. After the limit of proportionality, both the ST and PP fiber-reinforced samples suddenly reached the peak load. Since the elastic part of the pre-peak behavior of the fiber-reinforced samples is similar, it can be said that the adherence characteristic of the fiber does not play an important role in this region. However, the wettability of the material is accounted for a major parameter in adherence between fiber and matrix [149]. Based on the tests performed by Ranjbar et al. [149], it was reported that PP fibers had weak contact with the binder because of its hydrophobic characteristics. The type of fiber significantly affected the post-peak behavior. In a previous study, it was mentioned that synthetic fibers, e.g. PP, polyvinyl alcohol, polyethylene, were effective in improvement of the post crack strain hardening behavior rather than improving the first crack control or the ultimate load [181].

The load-CMOD curves of the PP reinforced samples have three distinct turning points, namely, peak load (P1), the minimum post-peak load (P2) and the maximum post-peak load (P3) (Fig. 6.5). A sudden drop is seen following the peak load, then the residual load increases slightly with the increase of the CMOD up to 1 mm and decreases with further loading until failure. The change in load-bearing behavior between the points (P2) and (P3) means that the PP fibers start absorbing the energy by bridging at the point (P2) and the energy absorption capacity reaches the maximum at the point (P3) [172].

Similar trends were observed in previous studies [165, 182]. Sukontasukkul et al. [183] reported that PP fiber-reinforced geopolymers generally exhibited an extensive drop in load after the first crack. They also noted a lower maximum post-peak load, due to low stiffness and high flexibility of PP fiber. On the other hand, the ST fiber-reinforced samples represent different shapes in terms of load-CMOD levels. The difference between the points (P1) and (P2) is very small (Fig. 6.4 (c)) compared to PP fiber reinforced samples (Fig. 6.4 (b)) which means that ST fibers start bridging and energy absorption immediately after the initial cracking.

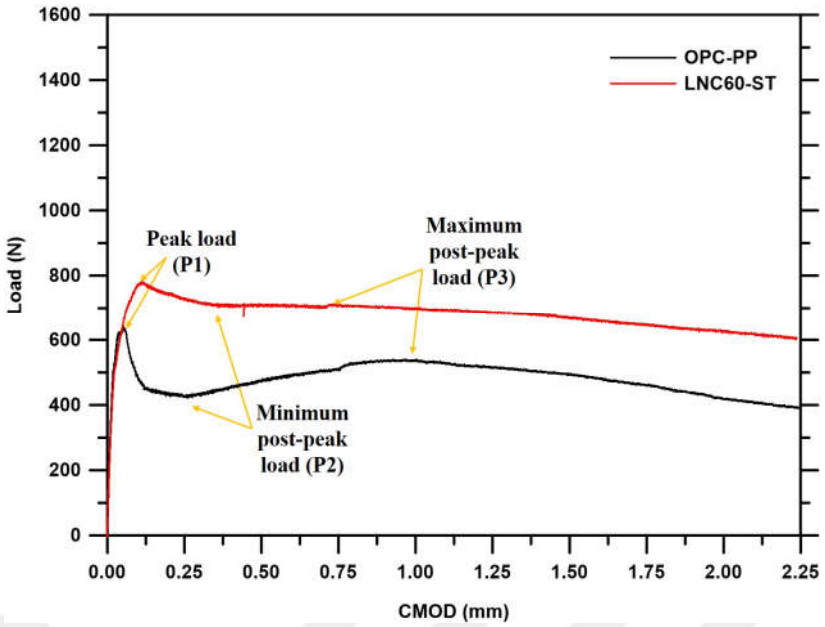

Figure 6.5 Typical load-CMOD curves of PP and ST reinforced mixes

Furthermore, the ST fiber reinforcement exhibited higher load-bearing capacity as compared to PP fiber reinforcement, which might be attributed to the higher mechanical properties, e.g. high strength and stiffness of ST fibers. Similarly, Sukontasukkul et al. [183] reported that the load drop ratio of ST fiber-reinforced geopolymer mixes was lower than that of the PP fiber reinforced mixes.

The CH-modified mixtures showed better performance in terms of the peak load, which indicates that CH-substitution offers better bonding properties between the fiber and matrix phase. It was mentioned in Chapter 5 that the CH-substitution increased the intensity of the strength-giving phases such as calcite and hydrotalcite in the NCAS system. However, the positive effect of CH-substitution on the flexural response of PP fiber reinforcement was higher than that of ST fiber. On the other hand, the enhancement in flexural response with ST fiber was found to be regardless of the matrix composition. Moreover, the area under the load-CMOD curve, which signifies the material toughness, increases with either PP or ST fiber reinforcement. The fracture energy (G_F) was calculated using the equation as shown in Eq. (6.1).

$$G_F = \frac{W_0 + mg\delta_{max}}{A_{lig}} \tag{6.1}$$

In this equation, W_0 is the area under the load-CMOD curve, mg is the weight of the specimen (N), A_{lig} is the ligament area (mm^2), δ_{max} is the displacement (m) corresponding to maximum load (P_{max}, N). The fracture energy values of plain, PP, and

ST fiber reinforced mortars are shown in Fig. 6.6.

As it can be seen from Fig. 6.6, the PP fiber performs inferior to the ST fiber. Two possible reasons might have caused this phenomenon; lower adherence between PP fiber and matrix and/or higher mechanical properties of the ST fiber. There is no discernible difference between the PP fiber-reinforced NCAS and OPC-based mortars.

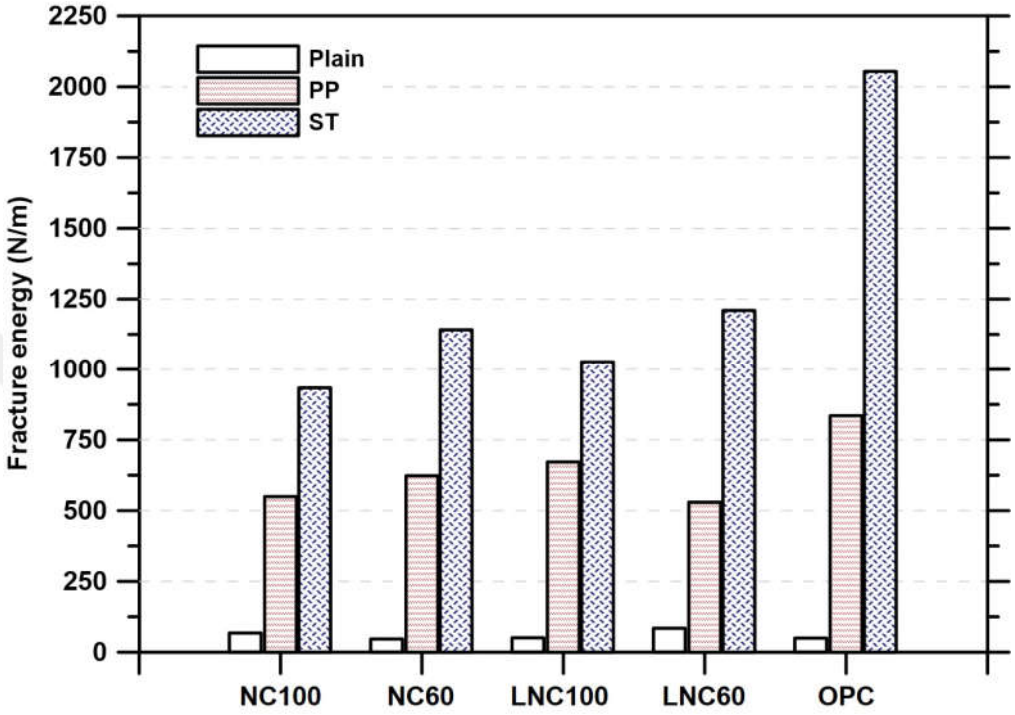

Figure 6.6 Fracture energy of NCAS and OPC-based mixes

The performance of PP fiber-reinforced OPC-based mortar is slightly above that of NCAS mortars. Interestingly, the fracture energy enhancement of OPC mortar due to ST fiber reinforcement was almost two times higher compared to NCAS mortars. For example, the fracture energy value of 1027 N/m was calculated for ST reinforced LNC-100 mortar while the value of 2053 N/m was calculated for ST reinforced OPC mortar. This observation indicates that the performance of ST fiber regarding the fracture energy depends on the mechanical properties of the matrix and the adhesion between matrix and fiber. The same statement can be deduced from the results of NCAS mixes. The fracture energy of ST fiber-reinforced plain NCAS (NC-100) is increased by 22% with NH-substitution (NC-60). Moreover, NH-substitution increased the fracture energy of LNC mixes by 18%, as well. The maximum increase was seen with the combination of NH+CH substitution (LNC60-ST) by 30%. However, the deviation in fracture energy among PP fiber-reinforced NCAS mortars is not as high as that of ST fiber-reinforced ones. The compatibility between the matrix and fiber is very important because it governs the post-peak behavior of the composite [184]. Moreover, it can be concluded that the mechanical properties of matrix and fiber determine the

performance of fiber-reinforced concrete. Ding and Bai [185] investigated the fracture properties of plain and ST fiber-reinforced sodium silicate+sodium hydroxide activated slag mortars. They reported that the fracture energy of plain geopolymer mixes was 97.4 N/m, whereas this value significantly increased and reached to 4188.0 N/m (approximately 43 times higher) with the incorporation of ST fiber.

6.3.2 Double-K Fracture Parameters

The stress intensity factor, in other words, the fracture toughness, is defined as the capacity of a material to resist against cracking. In general, the fracture process of quasi-brittle materials has three different states: crack initiation, stable crack propagation and unstable fracture [186]. In the present study, the double-K fracture model proposed by Xu and Reinhardt [186] was used for evaluating the different states in the fracture process. This model introduces the two size-independent fracture parameters in terms of stress intensity factor: K_{Ic}^{ini}, called as initiation toughness, and K_{Ic}^{un}, called as unstable fracture toughness. This model also gives information regarding crack initiation and propagation. If the toughness is smaller than the K_{Ic}^{ini}, there is no crack on the material, if the toughness is greater than the K_{Ic}^{ini} the crack has already occurred and grows stably, if the toughness is equal or greater than the K_{Ic}^{un}, it means that the crack develops unstably [186, 187].

The values of K_{Ic}^{ini} and K_{Ic}^{un} were calculated using the initial cracking load and the maximum load recorded during the three-point bending test on notched mortar beams. The K_{Ic}^{ini} and K_{Ic}^{un} values were computed using the equations given below (Eqs. 6.2-6.5):

$$K_{Ic}^{ini} = \frac{3P_{ini}S\sqrt{a_0}}{2bd^2} f(\frac{a_0}{d}) \tag{6.2}$$

$$f(\frac{a_0}{d}) = \frac{1.99-\frac{a_0}{d}(1-\frac{a_0}{d})(2.15-3.93\frac{a_0}{d}+2.7(\frac{a_0}{d})^2}{(1+2\frac{a_0}{d})(1-\frac{a_0}{d})^{1.5}} \tag{6.3}$$

where K_{Ic}^{ini} is the initial fracture toughness ($MPa.m^{1/2}$); P_{ini} is the initial cracking load (N); S is the span length (m); d and b are the height (m) and width (m) of the sample, respectively; and a_0 (m) is the depth of pre-cutting crack of the sample. P_{ini} was determined according to the ASTM C1018 [188].

$$K_{Ic}^{un} = \frac{3P_{max}S\sqrt{a_{eff}}}{2bd^2} f(\frac{a_{eff}}{d}) \tag{6.4}$$

$$f(\frac{a_{eff}}{d}) = \frac{1.99-\frac{a_{eff}}{d}(1-\frac{a_{eff}}{d})(2.15-3.93\frac{a_{eff}}{d}+2.7(\frac{a_{eff}}{d})^2}{(1+2\frac{a_{eff}}{d})(1-\frac{a_{eff}}{d})^{1.5}} \tag{6.5}$$

where K_{Ic}^{un} is the unstable fracture toughness ($MPa.m^{1/2}$); P_{max} is the maximum load (N); and a_{eff} (m) is the effective crack length of the sample. The effective crack length was calculated using the Eq. (6.6) given below:

$$a_{eff} = \frac{2}{\Pi}(d+H_0)\arctan\sqrt{\frac{BECMOD_c}{32.6P_{max}}-0.1135}-H_0 \tag{6.6}$$

where H_0 is the thickness of knife-edge used to fix the clip gauge and is 1.73 mm, $CMOD_c$ is the crack mouth opening displacement corresponding maximum load (P_{max}), B is the width of the specimen and E (MPa) (Eqs. 6.7 and 6.8) is the modulus of elasticity (MOE) which can be expressed as:

$$E = \frac{1}{Bc_i}(3.70+32.60\tan^2(\frac{\pi}{2}V_h)) \tag{6.7}$$

where

$$V_h = \frac{a_0+H_0}{d+H_0} \tag{6.8}$$

in which a_0 is the initial notched length and is about 25 mm, c_i is the initial compliance extracted from the linear part of the load-CMOD curve.

From Table A.12 and Fig. 6.7 it is seen that the MOE is in the range of 10469 MPa - 13340 MPa for PP fiber-reinforced, and in the range of 9519 MPa - 12599 MPa for ST fiber-reinforced NCAS mortars, while the modulus of elasticity of OPC based PP and ST fiber reinforced mortars are found to be 19511 MPa and 19848 MPa, respectively.

Obviously, most of the MOE values belonging to the NCAS mixes are just over half of the MOE of OPC-based mixes. It is known that MOE depends on the constituents of a composite material. Pan et al. [147] showed that the MOE of fly ash-based geopolymer paste which was activated with sodium silicate+sodium hydroxide presented approximately 27% lower values compared to its cement-based counterpart. Lately, another research [189] showed that the elastic modulus of PVA fiber incorporated geopolymer composites reached to only 7.6 GPa. These previous studies, support the results of the present study.

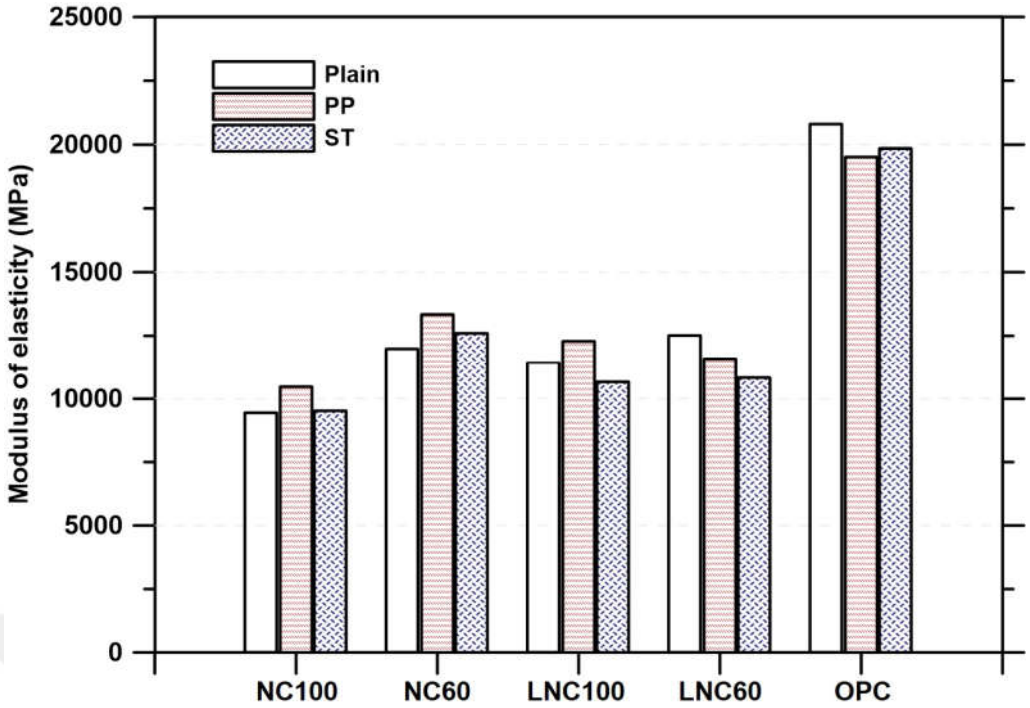

Figure 6.7 Modulus of elasticity of mixes

It was observed that fiber addition decreased the MOE of the OPC-based mortar by 5%. On the other hand, fiber addition slightly increased the MOE of NCAS mortars except for ST fiber-reinforced LNC100 and fiber-reinforced LNC60 groups. The MOE increases with NH and/or CH substitution. In the case of NC replacement by NH, the MOE increased by 27%, in addition to this, CH-substitution (LNC60) increased the MOE by 33% when compared to the plain NCAS mortar (NC100). Khan et al. [190] investigated the MOE of fiber-reinforced NH+sodium silicate-activated geopolymer mixes and reported that the MOE of geopolymer mixes ranged between 18.5 GPa and 26.2 GPa. They also included that an increase in ST fiber fraction improved the elastic behavior slightly.

Fig. 6.8 shows another parameter, effective crack length (a_{eff}) at which fracture becomes unstable, associated with the mix proportion and fiber incorporation. It can be seen that fiber incorporation increases the a_{eff} and the effect of ST fiber on a_{eff} is significant. It can be said that the type of fiber has a strong influence on effective crack length. For example, ST fiber gives 1.5 times higher effective crack length than PP fiber in NC60 mixes.

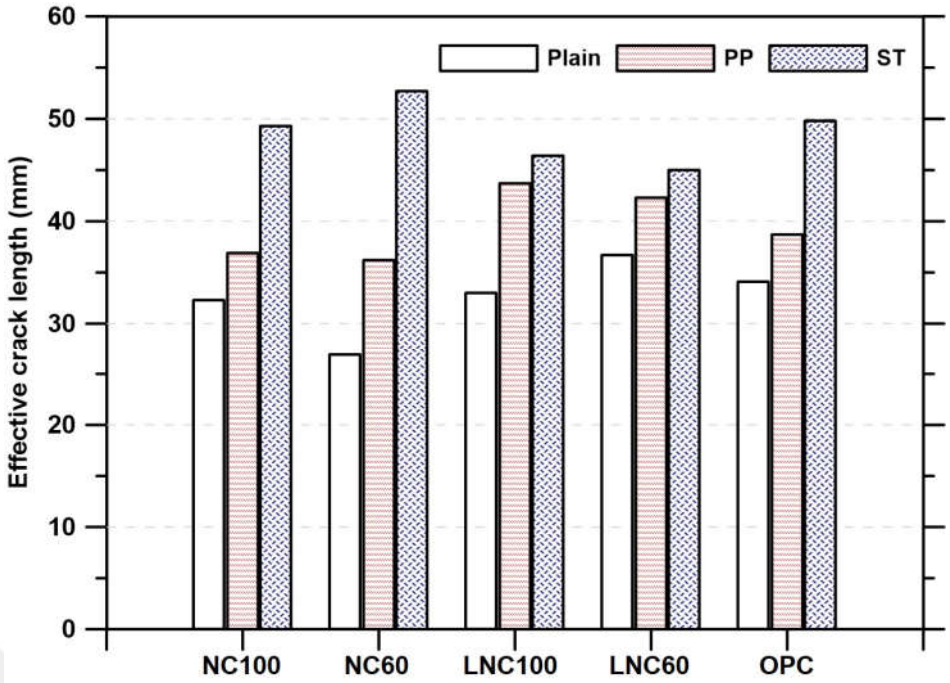

Figure 6.8 Effective crack length of mixes

Calculated values of double-K fracture parameters according to Eqs. (6.2-6.5) are presented in Fig. 6.9. K_{Ic}^{ini} of plain mixes ranges between 0.16 and 0.19 $MPa.m^{1/2}$, indicating that the matrix phase is not effective on the initiation toughness of NCAS mixes. PP fiber-reinforcement increased the K_{Ic}^{ini} slightly (from 13% to 25%), while ST fiber-reinforcement increased substantially (from 30% to 112%). It is seen from Fig. 6.9 that K_{Ic}^{ini} and K_{Ic}^{un} increase with PP and ST fiber incorporation. However, the effect of fiber incorporation on K_{Ic}^{ini} is negligible for low strength mortar, e.g. NC100 mixes. For normal compressive strength NCAS mortars (NC60 and LNC60), the difference in the K_{Ic}^{ini} is more distinct, especially in the case of ST fiber-reinforcement. It is also worth to note that OPC-based mortars showed better performance, the same trend was observed for K_{Ic}^{un} values. Although PP fiber improved the fracture toughness of mortar, this contribution was observed to a certain extent such the ratios from 27% up to 96%. However, the increase in the K_{Ic}^{un} values in ST fiber incorporated mortars were in the range of 192% to 434%. It can be deduced that for this study, the fiber type is the most important parameter affecting the fracture toughness.

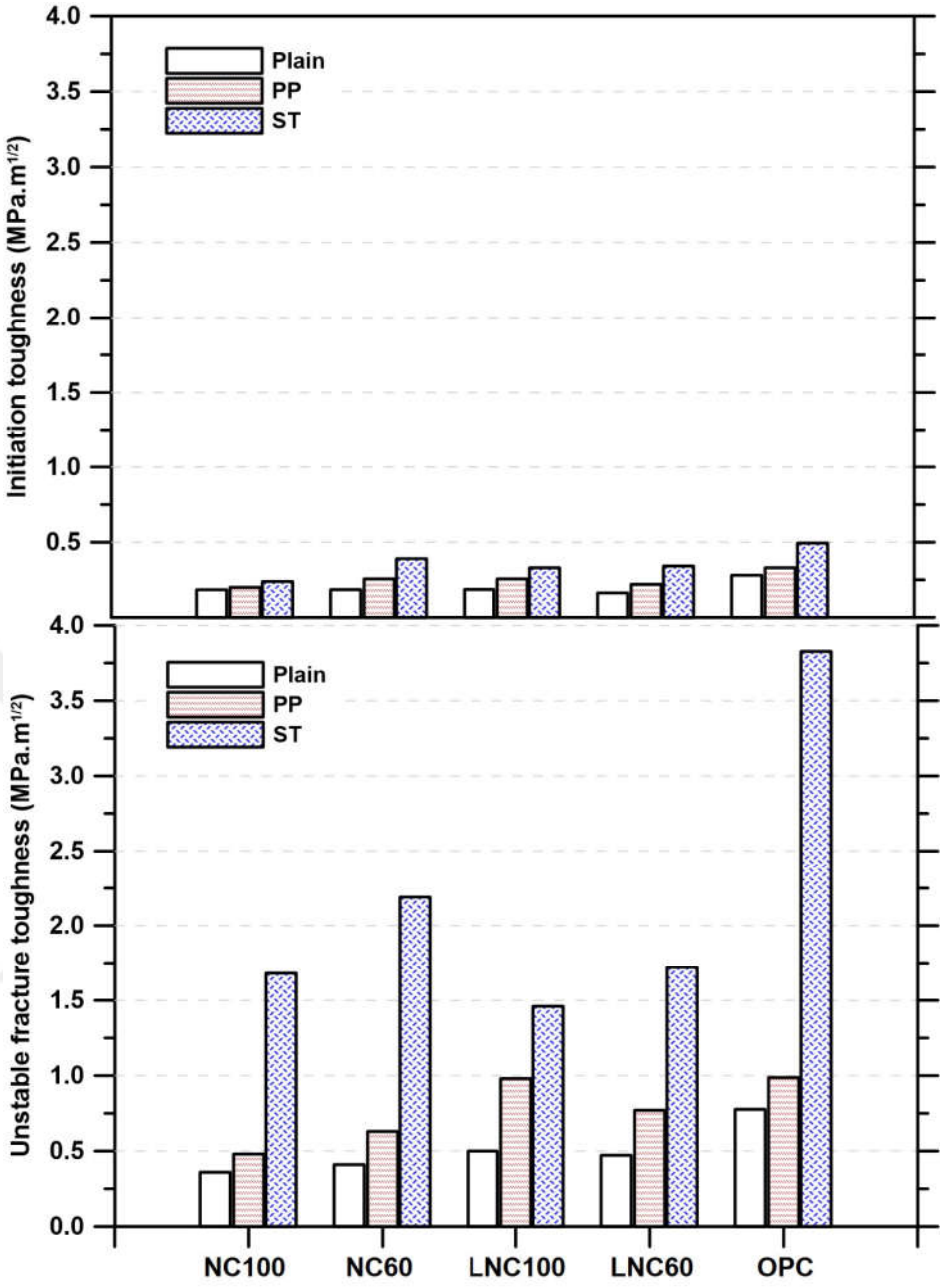

Figure 6.9 Initiation and unstable toughness of plain and fiber-reinforced mixes

Many studies concerning the mechanical properties of AAMs have been published so far. However, most of them focus only on determination of compressive and flexural strength, yet fracture properties of these materials have rarely been researched. Dias and Thaumaturgo [155] studied the fracture toughness of basalt fiber reinforced geopolymer and OPC based mixes. The results showed that basalt fiber incorporation increased the toughness significantly and basalt fibers were found to be more efficient in geopolymer mixes compared to OPC. The reason for this phenomenon was related to the nature of the bond between basalt fiber and the geopolymer matrix. Šimonová et al. [191] investigated the fracture characteristics of carbon fiber reinforced sodium silicate activated-slag. The authors recorded that carbon fiber reinforcement had no

significant effect on the fracture toughness, the values range between approximately 0.80 $MPa.m^{1/2}$ and 0.85 $MPa.m^{1/2}$. In another study [185], it was reported that plain slag mortar mixes reached fracture toughness of 1.01 $MPa.m^{1/2}$, while this value reached 4.29 $MPa.m^{1/2}$ with the incorporation of ST fiber.

6.3.3 Brittleness Index

The non-dimensional brittleness index (BI) proposed by Kumar and Barai [192] was applied to evaluate the brittleness of the mixes by using the ratio of K_{Ic}^{ini} and K_{Ic}^{un} (Eq. 6.9).

$$\beta = \frac{K_{Ic}^{ini}}{K_{Ic}^{un}} \tag{6.9}$$

As it is understood from Eq. (6.9), a lower BI indicates a higher ductility of a material. It can be seen that BI decreases from ≈0.50 to 0.33 with the NH and CH-substitution and LNC60 mixes reach a similar value with the OPC-based mixes. Considering the effect of the modifiers, the contribution of CH-substitution was found to be higher than the NH-substitution. On the other hand, the combination of two modifiers (LNC60) resulted in a 33% reduction and reached the lowest value of BI (0.35) among the plain mixes.

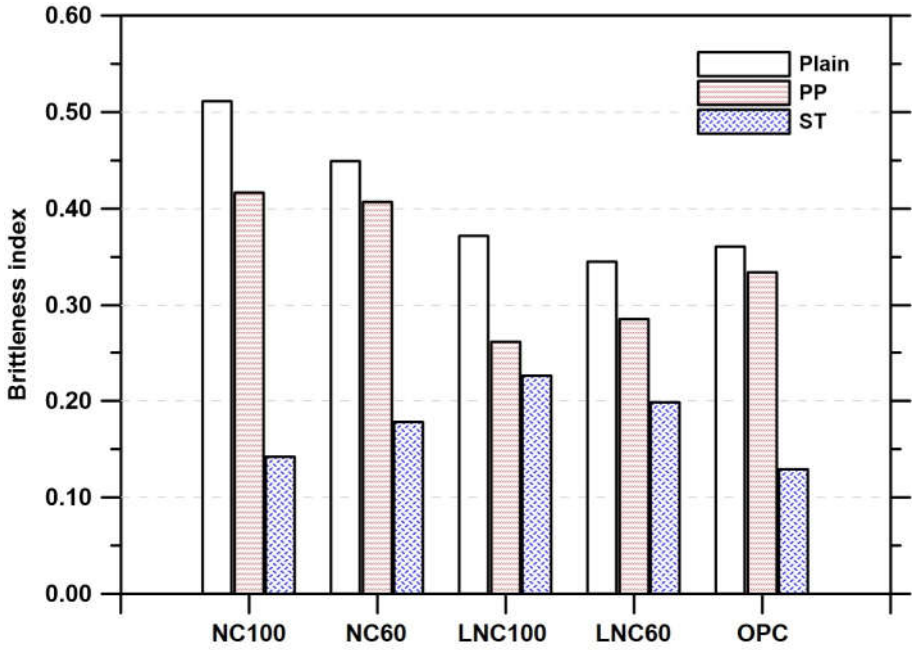

Figure 6.10 Brittleness index of plain and fiber-reinforced mixes

As expected, BI values decreased significantly with fiber incorporation. ST fiber contribution was much more than the PP fiber contribution. ST fiber absorbs more

energy than PP fiber at the ultimate displacement because of the higher load-bearing capacity of ST fiber reinforced mortars during the plastic deformation. For example, the BI decreases from 0.51 to 0.42 (≈18% reduction) when PP fiber added into the NC-100 mixes, while for the ST fiber added NC-100 mixes, the BI value decreases to 0.14 which means a significant reduction (73%). The significant contribution of ST fiber was observed in all mixes (Fig. 6.10). This improvement can be explained with the higher adhesion between fiber and matrix of NC and OPC-based mixes and higher strength of ST (Figs. 6.16 and 6.17). To validate this assumption holds or not SEM analysis was performed on selected mixes (Section 6.3.4).

The results obtained in this chapter were used to establish a correlation between the BI and other fracture parameters of fiber incorporated NCAS mortars. The relationship between the fracture properties are presented in Figs. 6.11-6.13, where it can be seen that they are correlated with each other, i.e. the lower effective crack length yields higher brittleness index, and higher fracture energy yields higher unstable fracture toughness. Strong correlations were established between brittleness index, fracture energy, and unstable fracture toughness of fiber reinforced NCAS mortar mixes.

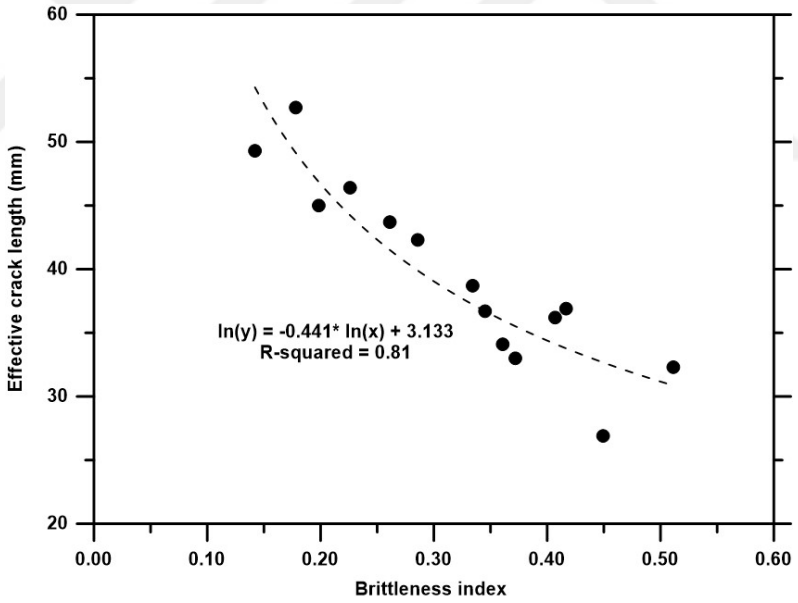

Figure 6.11 Effective crack length-brittleness index correlations

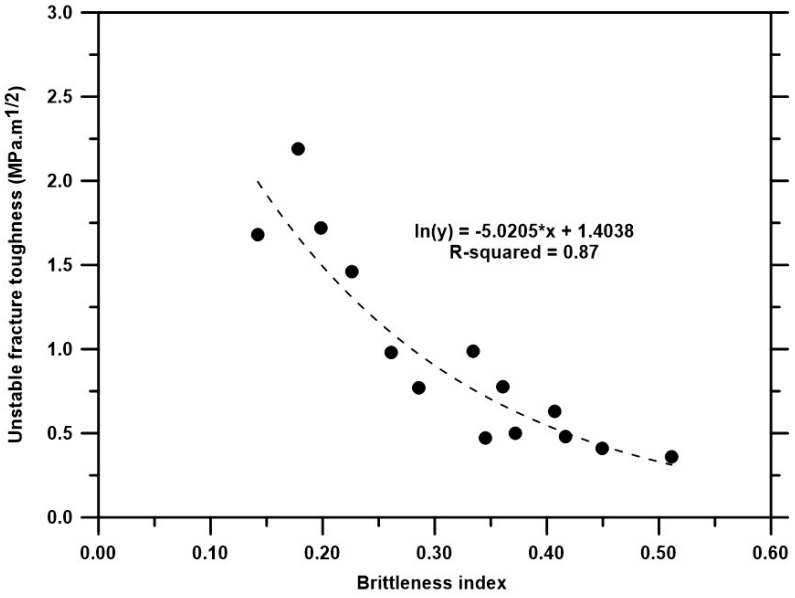

Figure 6.12 Unstable fracture toughness-brittleness index correlations

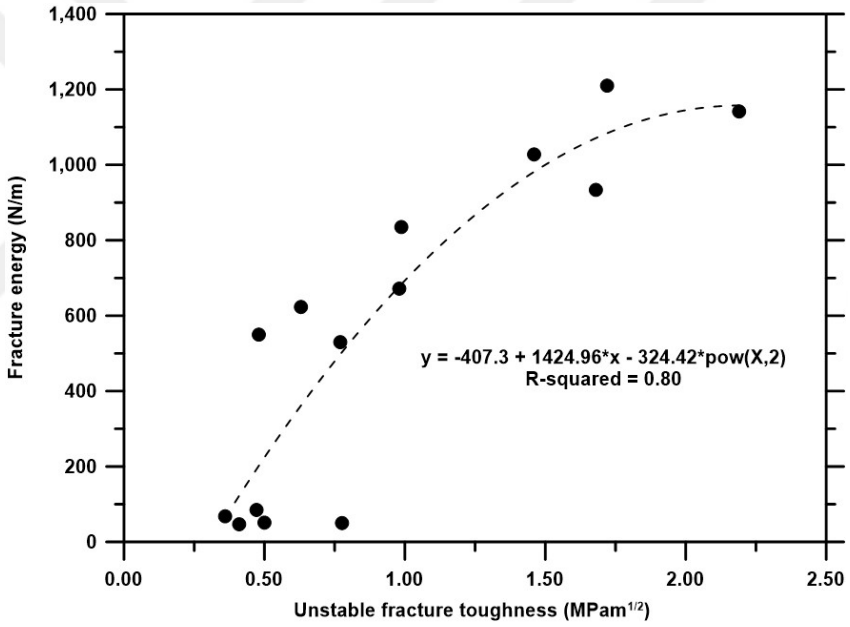

Figure 6.13 Fracture energy-unstable fracture toughness correlations

6.3.4 Fiber-Matrix Bond Performance

In all fiber-reinforced composites, the interaction between fiber-matrix interfaces plays an important role in the performance of any composite. The efficiency of fiber addition is mainly related to the bond-slip characteristics or frictional resistance in the fiber-matrix interface [193]. In addition, enhancement in the deformation capability of a composite also depends on the geometry and/or stiffness of fiber.

Additional energy is required to debond and pull-out or rupture the fibers at the crack interface in cementitious materials. This typical behavior may explain the varied

post-peak behavior between the plain and fiber-reinforced composites at the macroscale. In the present study, macro and microscale observations are conducted to reveal the effect of fiber addition, fiber type, and matrix proportion on fracture characteristics of NCAS mixes.

Fiber distribution is always an issue that needs to be overcome in fiber-reinforced composites. PP fibers tend to flocculate, resulting in the loss in workability and also a reduction in compressive strength. The images (Figs. 6.14 (a-c)) show the distribution of fibers in NCAS mixes and the fiber pull-out behavior under three-point bending tests. Typical brittle failure, a very sharp and flat fracture surface, is seen on the fracture surface of plain mixes, while the rougher surface is seen in all PP and ST-reinforced NCAS mortars. Moreover, it is seen that all fibers are randomly distributed in the matrix (Figs. 6.14 (b) and (c)).

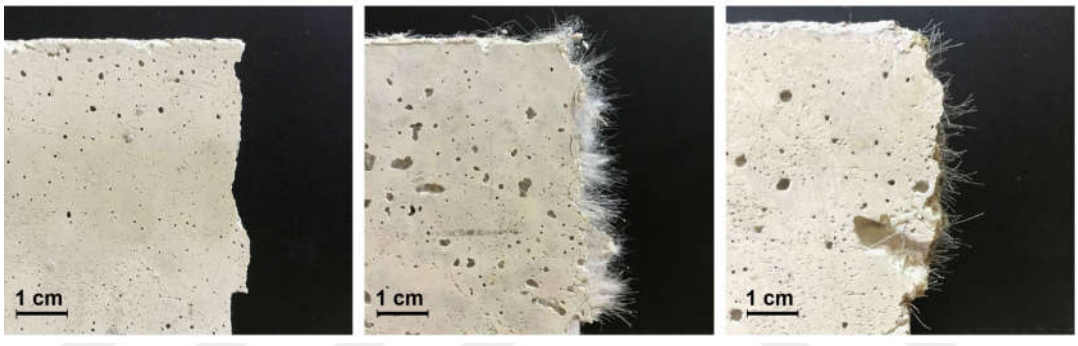

Figure 6.14 Fracture surface of (a) plain, (b) PP fiber-reinforced mixes, (c) ST fiber-reinforced mixes

Obviously, fiber bridging is seen as fiber elongation in PP fiber incorporated NCAS samples (Figs. 6.15 (a) and (c)). It can be said that most of the PP fibers are elongated under the flexural load. However, at some point, PP fibers are ruptured when the tensile stress exceeds the tensile strength of PP fibers. On the other hand, ST fibers are mostly presented pull-out behavior (Figs. 6.15 (b) and (d)).

In this study, both PP and ST fibers exhibited a high amount of fracture energy compared to plain mixes, which is likely due to their mechanical properties and frictional and mechanical bonding between the matrix and fibers [180]. It has been observed that, after the initiation of a single crack, a gradual fiber pull-out or debonding mechanism controls the failure process of ST fiber-reinforced composites. Due to a sudden debonding of ST fibers, generally, ST fibers cannot attain their full strength capacity. Even with this pull-out behavior of ST fibers, ST fiber-reinforced mixes presented better performance compared to PP fiber-reinforced mixes in terms of fracture response (Figs. 6.3-6.10). Similar findings are reported by Khan et al. [190].

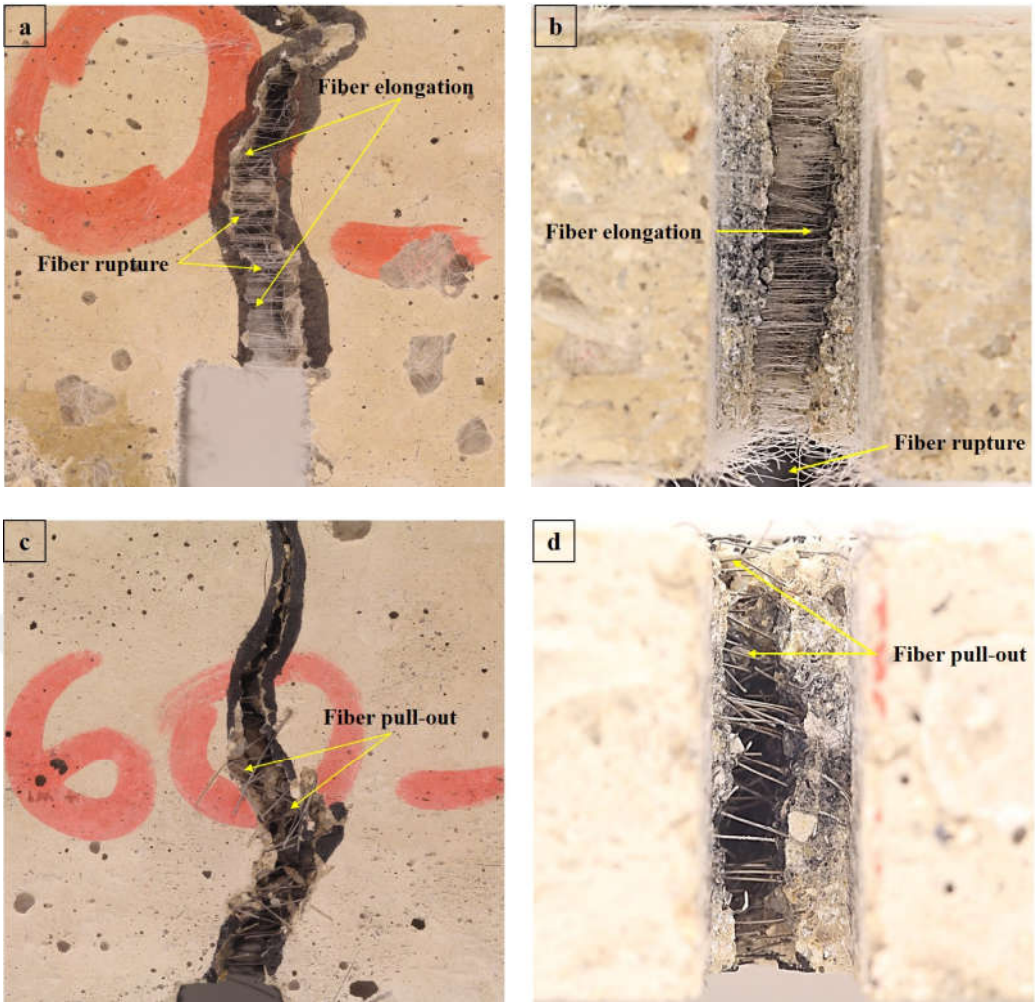

Figure 6.15 (a)(b) PP fiber-reinforced, (c)(d) ST fiber-reinforced mortar samples after bending test

SEM images were taken to characterize the fiber-matrix bond and failure mechanism of fiber in NCAS mortars. Figs. 6.16-6.20 show the SEM observations conducted on the PP and ST fiber-reinforced NCAS samples. Good adhesion between fiber and matrix was observed in CH-substituted LNC mixes, where a continuous interface was seen (Figs. 6.16 (b) and (d)), compared to the gap existing between the fibers and matrix of NC mixes (see Figs. 6.16 (a) and (c)). It can be concluded that the CH-substitution enhances the matrix-fiber interfacial properties of NCAS mixes. In addition, a high amount of matrix was seen covering the surface of ST fiber (Fig. 6.18), which implies a good mechanical bond and friction that resist pull-out failure. Thus, the sample's ductility was increased by improving the load-bearing capacity in the post cracking region. This corresponds to the obtained higher fracture properties in ST fiber-reinforced mixes than that of PP fiber-reinforced ones.

Moreover, it was observed that neither PP nor ST fibers presented a chemical deterioration in the alkali medium, only some of the PP fibers showed visible damage

due to the surface friction as fibers pulled out from mortar (Figs. 6.19 and 6.20). PP fiber rupture was also observed (Fig. 6.19) by virtue of enhanced interfacial fiber-matrix bonding.

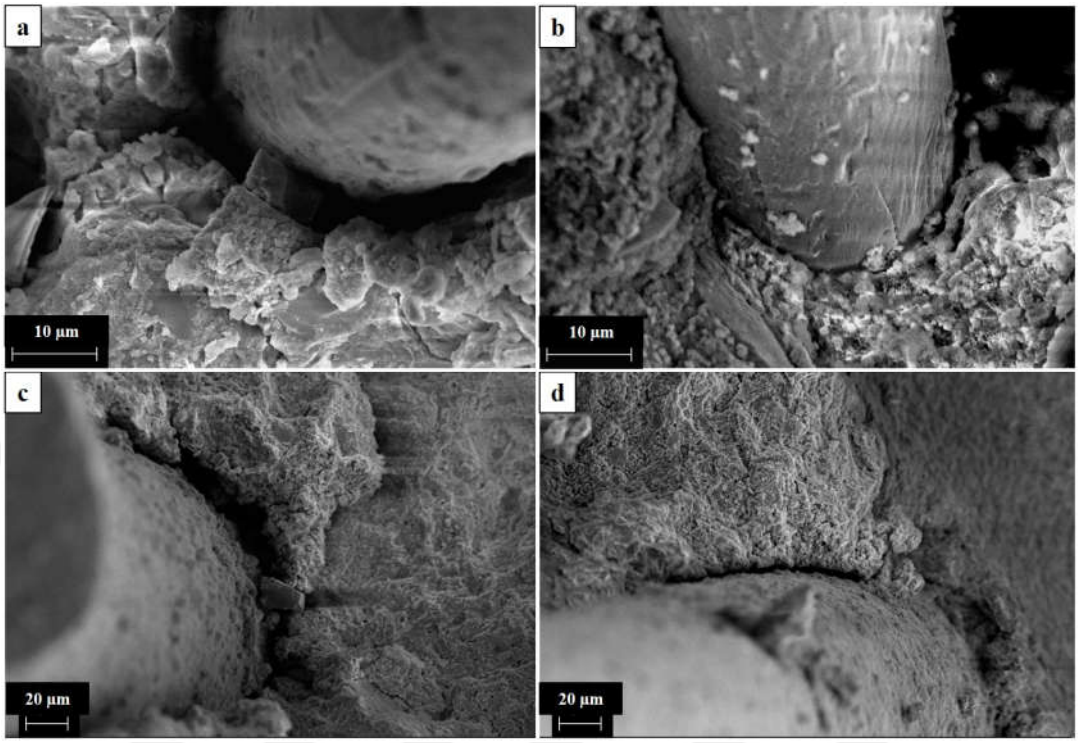

Figure 6.16 SEM images presenting fiber-matrix adhesion (a) PP fiber-reinforced NC mixes, (b) PP fiber-reinforced LNC mixes, (c) ST fiber-reinforced NC mixes, (d) ST fiber-reinforced LNC mixes

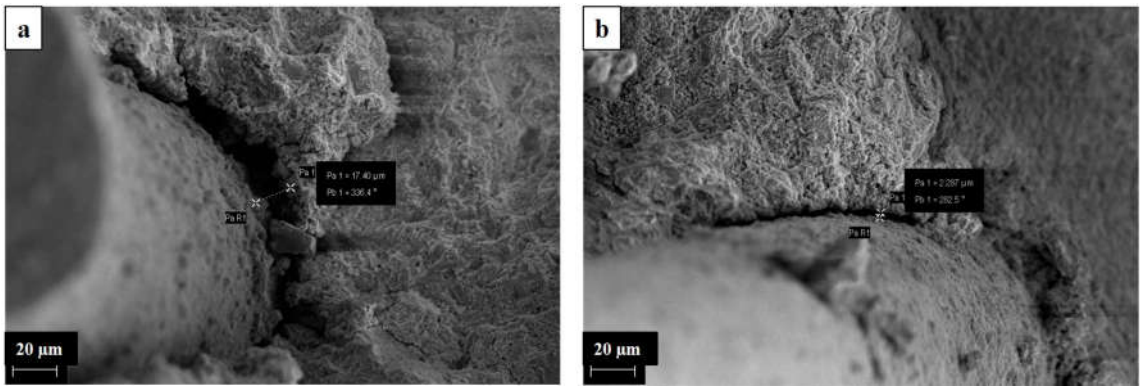

Figure 6.17 SEM image of the interface between ST fiber and (a) NCAS matrix and (b) CH-substituted NCAS matrix

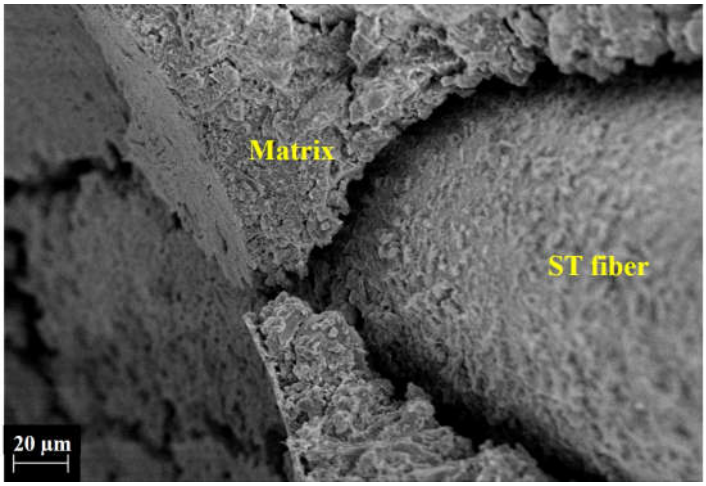

Figure 6.18 SEM image of the interface between ST fiber and NCAS matrix

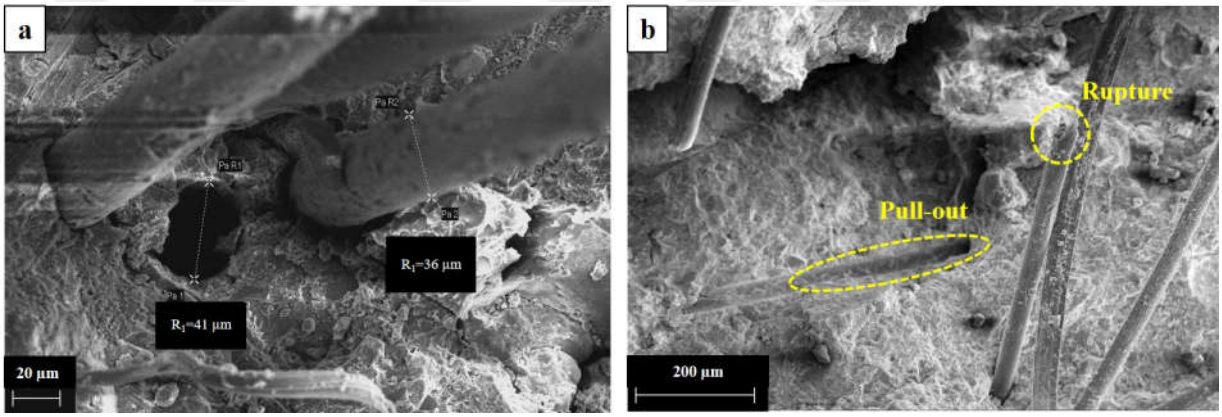

Figure 6.19 SEM image of the interface between ST fiber and NCAS matrix

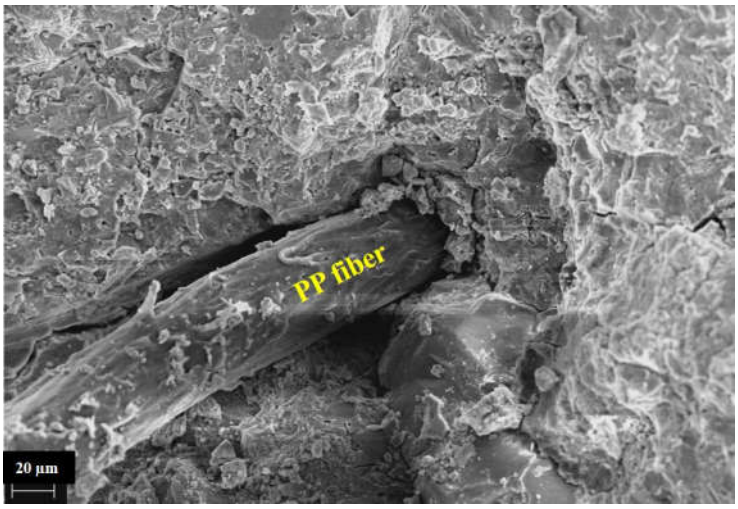

Figure 6.20 SEM image of deteriorated PP fiber

6.4 Conclusions

Fracture properties are one of the important parameters for all quasi-brittle materials. Even though many studies have been conducted on plain and fiber-reinforced OPC-based and sodium silicate+sodium hydroxide or NH-activated mixes, no literature was found regarding the fracture response of NCAS up to now.

In this chapter, it was aimed to improve the mechanical and fracture properties of NCAS and to reach comparable levels with the OPC and other AAMs.

The main and important outcomes were derived based on the experimental results in the study as follows:

- Fiber incorporation, especially PP fiber, exhibited a reduction in the compressive strength in CH-substituted LNC mixes. The main reasons for this phenomenon can be explained with the low stiffness of PP fibers and the voids caused by the fiber addition. As expected, fiber addition increased the flexural strength of the mixes.
- Type of fiber is more effective in the improvement of the fracture properties, such as fracture energy, and double-K fracture toughness, rather than the matrix features. It was found that fiber characteristics control the failure mechanism and fracture properties of the mixes.
- The fracture toughness of ST fiber-reinforced NCAS mixes was higher than that of the PP fiber-reinforced mixes and presented better performance with respect to crack resistance and ductility.
- As well as fiber characteristics, fiber-matrix interface and bonding mechanism play an important role in the fracture response of NCAS composites. The CH-substitution enhanced the matrix-fiber interfacial properties of NCAS mixes irrespective of the fiber type. The behavior of fibers such as elongation, pull-out or rupture mechanism under the flexural load assigns the fracture mechanism and accordingly fracture response.

It is clearly seen from the overall test results obtained that NCAS can be used as a structural material, the matrix can be improved with the modifiers and ductile behavior can be obtained with the fiber incorporation. The data presented here is thought to be valuable in the design and development of sustainable NCAS cement, and give foresight for better design in terms of improved fracture properties.

7
DRYING SHRINKAGE & PERMEABILITY

7.1 Introduction

In this chapter, water sorptivity, chloride ion permeability, and drying shrinkage performance of NCAS and OPC-based mixes are investigated and the tests results are discussed.

Shrinkage induced micro-cracks are responsible for the ingress of the hazardous ions substances that affect the service life and/or durability of cementitious materials. Previous studies reported that alkali nature [55], type of raw materials [194], curing [195], pore structure and reaction products are the main factors affecting the shrinkage performance. Atis et al. [55] indicated that NCAS present similar or lower shrinkage than OPC, while sodium silicate activated slag generally shows 3-6 times higher shrinkage than that of OPC mortar. Neto et al. [196] found that silicate contained in the activator is the key factor affecting the drying and autogenous shrinkage of sodium silicate-activated slag. Collins and Sanjayan [146] found that a high percentage of mesopores of sodium silicate-activated slag (up to 82%) could be responsible for the high drying shrinkage compared to that of OPC (36%). Jin et al. [82] studied the shrinkage of NCAS and reported that drying shrinkage of NCAS can be reduced with the incorporation of reactive MgO powder. Nevertheless, the influence of NH and/or CH substitution on drying shrinkage of NCAS has not been reported earlier.

AAMs present excellent performance against aggressive environments compared to the OPC-based systems. Mithun and Narasimhan [197] reported that sodium silicate-activated slag subjected to 10% sodium sulphate solution up to one year showed superior performance compared to OPC concrete concerning strength variation. In another study [198], alkali-activated slag was found more durable than OPC paste immersed in 5% $MgSO_4$ or 5% $MgCl_2$ solutions for 180 days. Moreover, the greater deterioration was observed on OPC samples compared to the alkali-activated slag/fly ash blended specimens under sulphate attack, which was attributed to the reactions between sulphate and calcium hydroxide and calcium monosulfoaluminates [199].

One of the critical durability parameters affecting the long term performance of reinforced concrete is the chloride penetration, depending mainly on the microstructure, connectivity, and tortuosity of the pore structure [200]. Bondar et al. [201] investigated the chloride diffusivity of NH and sodium silicate activated slag concrete with various alkali concentrations and silicate modulus. They found that despite the higher water to binder ratio, the chloride diffusion coefficient was still lower than the OPC concrete. This is related to the chloride binding ability of aluminosilicates, and the pore structure of the alkali-activated slag concrete. Increasing the calcium content is the most efficient method to reduce chloride diffusion by the formation of C-(A)-S-H gel [202].

Permeability and water absorption, the two most critical parameters, govern the durability of cementitious materials since the capillary pores in the system yield diffusion of the aggressive substances. These two parameters are mainly affected by the content and type of precursors [203]. Ismail et al. [204] reported that the volume of permeable pores increases when the proportion of fly ash is beyond 50% in alkali-activated slag mortar, which proves that the presence of more bound water in C-(A)-S-H type gel exhibits a higher pore filling capacity than the geopolymer type gels [205]. A similar statement is also reported in [206], the replacement of metakaolin with slag, promoting C-(A)-S-H formation induced by the presence of additional Ca^{2+} ions reduces the porosity and permeability.

The studies given above have mostly focused on the durability performance of either NH or NH+sodium silicate activated fly ash or slag systems. However, it is well known that these activators are highly caustic and a considerable amount of energy is needed during the manufacturing process [11, 13]. On the other hand, NC offers an option to produce more environmental friendly AAMs, with reduced alkalinity and a lower carbon footprint [207].

Although the durability performance of AAMs is well described in the literature, limited studies have been attempted to investigate the durability of NCAS. In a recent study [207], the effect of magnesia on water absorption, carbonation, sulphate, and acid resistance was investigated and it was concluded that the incorporation of magnesia into the NC-activated slag/fly ash mixes increased the sulphate and acid resistance while decreasing the water absorption and carbonation depth. In another research [55], the carbonation resistance of alkali-activated slag mortar samples were found to be lower than the OPC-based mortar. However, the highest carbonation values were observed in NC-activated mortar among alkali-activated samples. Moreover, Ke et al. [208] reported that the total porosity and chloride migration coefficient is higher in NCAS when compared with sodium silicate activated slag. However, the more refined pore structure and increased chloride binding capacity were achieved by the

incorporation of CLDH.

Considering the lack of studies on the durability of NCAS, the experimental investigation detailed in this thesis aims to give a contribution to the improvement of permeability and shrinkage parameters. The matrix phase of the mixes was improved with the aid of the two modifiers. In this chapter, the permeability and shrinkage performance of NCAS mixes were experimentally determined and the influence of modifiers was explored.

7.2 Drying Shrinkage

Time-dependent drying shrinkage values of NCAS and OPC-based mixes are shown in Table A.13 and Figs. 7.1 and 7.2.

Drying shrinkage of the NCAS mixes without CH was slightly higher than the OPC-based mixes at an early age, while this slight difference has increased over time and reached more than two times higher values at 28 days of curing. For most of the mixes, the rate of shrinkage was high during the early ages up to 35 days and stabilized after this age. As can be seen from Figs. 7.1 and 7.2, the plain mixes (NC100-6 and NC100-10) shrink rapidly and reach the ultimate drying shrinkage strain around 2300 microstrain at 180 days.

The ultimate (180-day) drying shrinkage of the NCAS mixes ranges between 1304 and 2358 microstrain, the lowest value belonging to LNC60-10 mixes is very close to the value of OPC mixes (1244 microstrain). This magnitude of ultimate drying shrinkage is approximately two times higher than the OPC based paste. However, the ultimate drying shrinkage strain value of NC mixes is still acceptable compared to other alkali-activated binder systems formed by using other activators e.g. NH and Na_2SiO_3. Atis et al. [55] reported that NCAS has a similar or lower shrinkage than OPC mortar, while sodium silicate activated slag generally shows 3 to 6 times higher than that of OPC mortar. Bakharev et al. [90] mentioned that sodium silicate activated slag presented significantly higher shrinkage (≈2400 microstrain) values compared to NCAS (≈1000 microstrain).

An increase in activator dosage did not increase the ultimate shrinkage in NC mixes, only a slight increase was seen in the CH-modified LNC mixes. Moreover, lower values were observed in NH-substituted mixes. Similar results were reported by Jin et al. [82] as well. They found that increasing the NC dosage from 4% to 6% reduced the drying shrinkage by up to 53%. Jiao et al. [209] studied the combination of NH and NC on drying shrinkage of slag paste and reported that an increase in activator dosage

decreased the shrinkage and higher NH molar ratio led to a decrease in shrinkage.

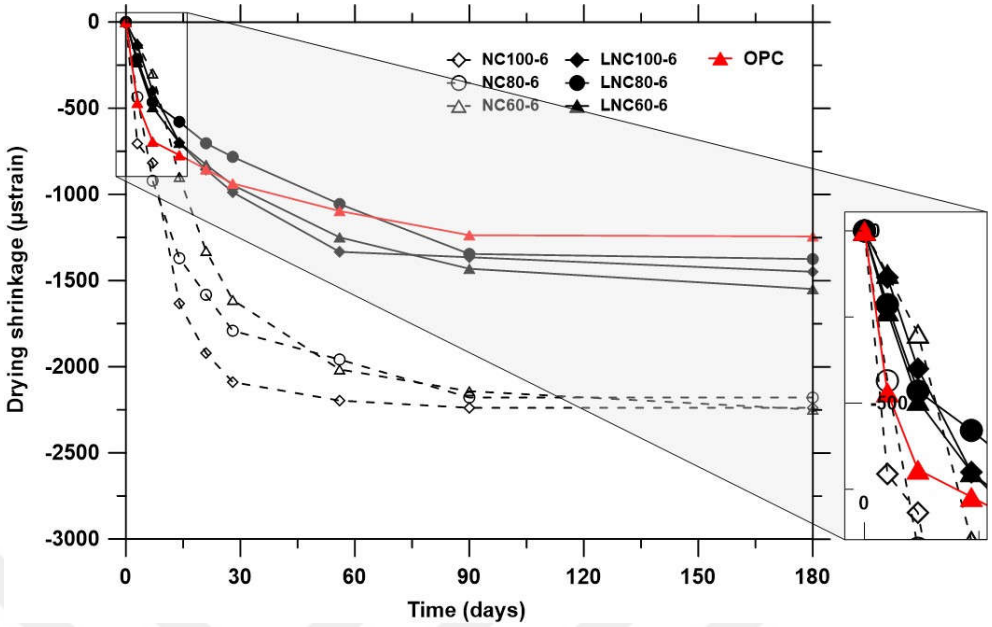

Figure 7.1 Drying shrinkage of NC-6, LNC-6, and OPC mixes

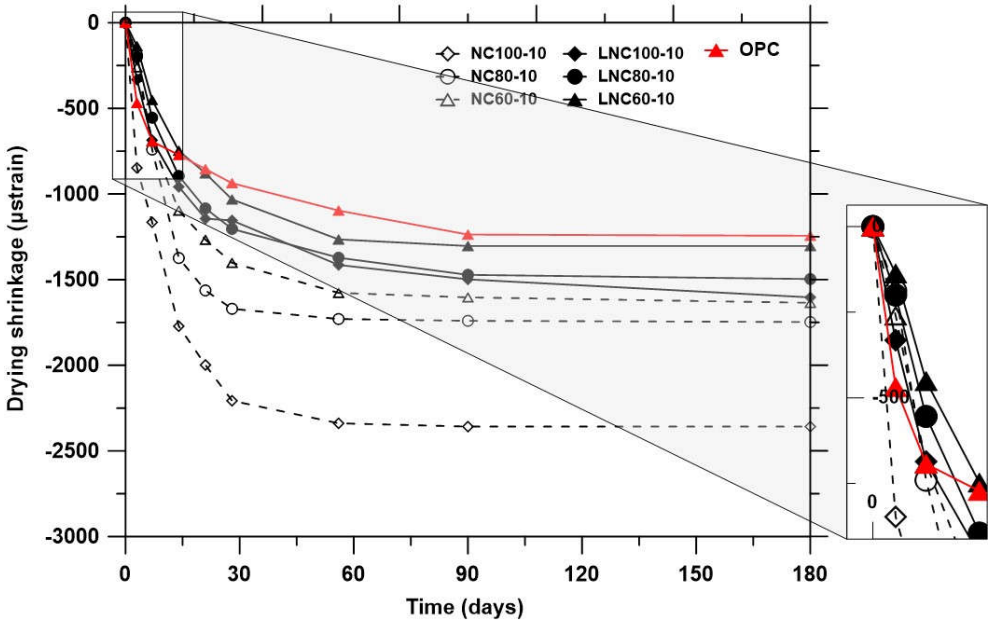

Figure 7.2 Drying shrinkage of NC-10, LNC-10, and OPC mixes

Incorporating modifiers into the system may lead to exhibit comparable shrinkage values with the OPC. Many studies have investigated the effects of different admixtures, additives and curing conditions on the drying shrinkage of AAMs. Metakaolin, limestone powder or MgO incorporation, along with the high-temperature curing was reported as an effective method in terms of mitigating the shrinkage. Matalkah et al. [210] reported that the addition of limestone powder reduced the total shrinkage by 17%. This reduction results from the acting of limestone powder as nucleation sites for

hydration products, accelerating the hydration process that reduces the uncombined water content causing the drying shrinkage, along with the filler effect of the limestone powder particles.

In this chapter, the effect of CH and NH on drying shrinkage of NCAS mortars was investigated and it can be seen that both NH and CH-substitution decreased the ultimate shrinkage values (Figs. 7.1 and 7.2). NH-substitution decreased the shrinkage values at the early age, however, at 90 days these mixes reached similar values. Furthermore, the shrinkage of NC60-10 mixes, produced with 40% NH substitution, presents a 30% lower shrinkage than the plain NC mixes (NC100-10). The lower drying shrinkage of the NH-substituted mixes can be attributed to the presence of less interconnected capillary network of the matrix. This assumption can be proved with the MIP results, as it can be seen that both NH and CH substitution enhance pore refinement (Figs. 5.22 and 5.23).

The CH-substitution did not increase the drying shrinkage, in fact, it had a positive effect and exhibited lower ultimate values compared to the mixes without CH and presented similar or lower values than the OPC based mixes at the early age. Incorporation of CH yields the highest decrease (≈37%) in the shrinkage of LNC80-6 mixes, though it is slightly higher than the OPC-based mixes. The lower shrinkage values obtained by CH-substitution were found to be irrespective of the NH substitution. The reason for the mitigation might be the change in the microstructure of the matrix phase and the increase in the strength-giving phase formation, along with a denser microstructure promoted by the CH [174]. Hence, it can be concluded that both NH and CH substitution can be a suitable method to mitigate the drying shrinkage and the effect of the CH seems to be more pronounced.

The reduction in mass loss may designate the reduced drying shrinkage. The weight change of the shrinkage prisms is expressed as the weight change percentage of the specimen in Figs. 7.3 and 7.4. The weight change of mixes varies between 3.8% and 6.7% which are the lowest and the highest change in mass belongs to LNC60-10 and NC100-6 mixes respectively. While NC-6 and LNC-6 mixes present similar behavior in terms of weight loss, LNC-10 mixes present higher values than the NC-10 ones, except LNC60-10. With the NH and CH substitution, only a slight decrease was observed.

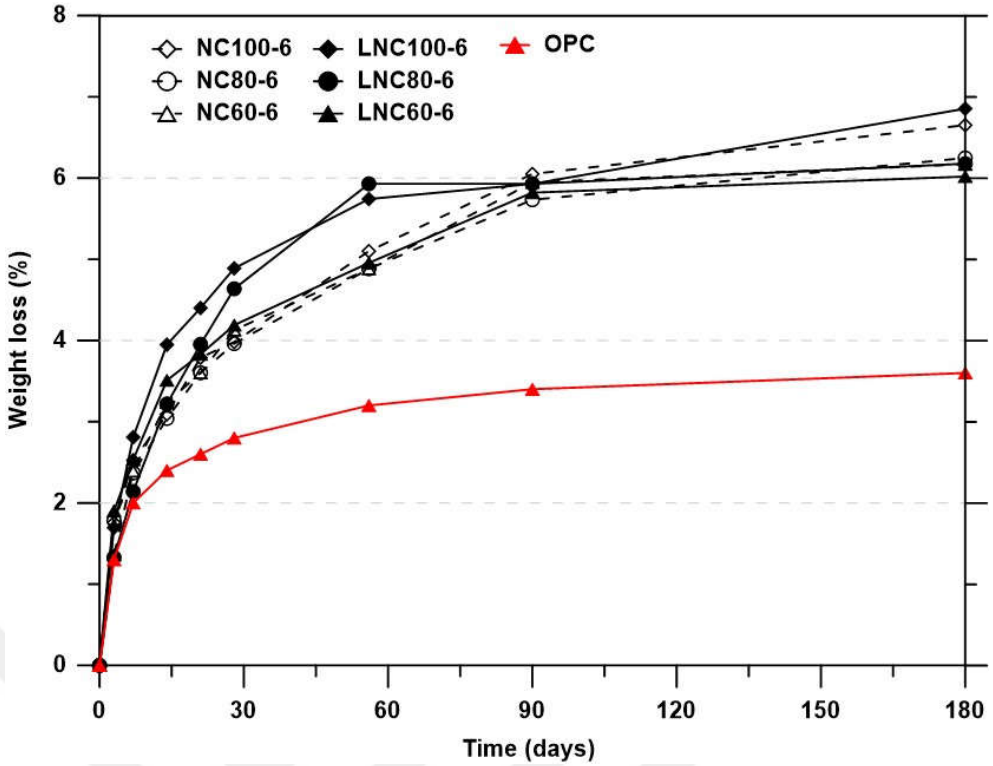

Figure 7.3 Weight loss of NC-6 and LNC-6 mixes

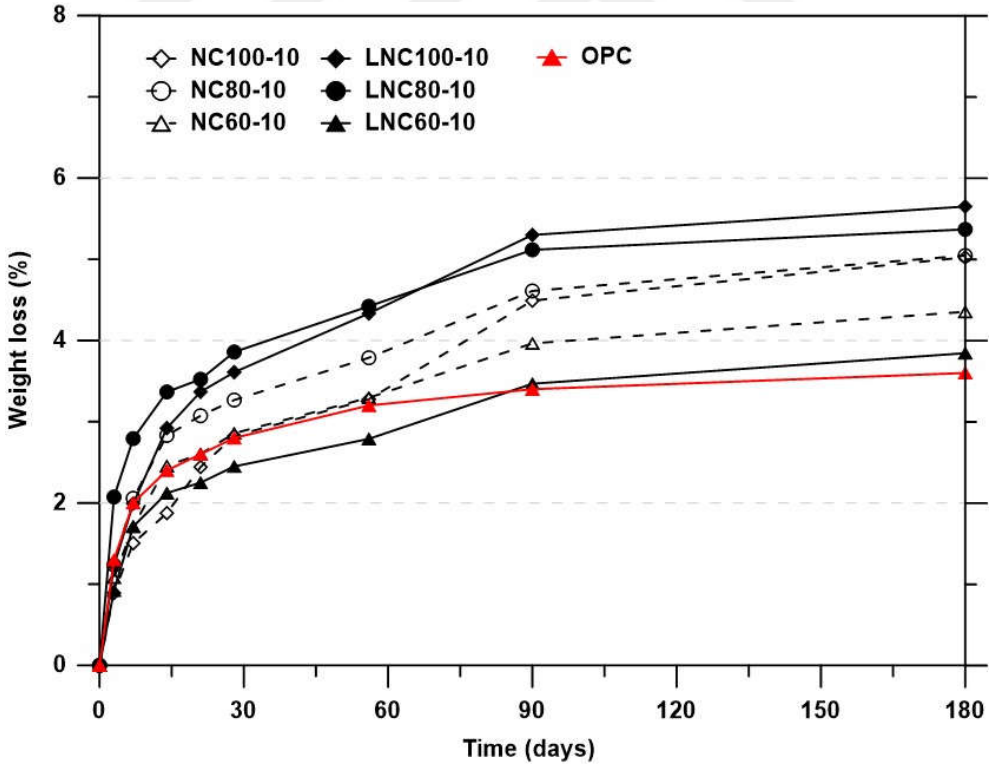

Figure 7.4 Weight loss of NC-10 and LNC-10 mixes

In practice, the shrinkage is mainly related to the loss of water from the mesopores [211]. Higher content of mesopore causes higher capillary stress and therefore induces greater shrinkage during drying [212]. It should be noted that crystallinity equivalent

of C-S-H is known as a key parameter for weight loss [95] which directly affects the degree of shrinkage. According to the MIP test results, although LNC-10 mixes presented a higher amount of mesopore volume than NC-10 mixes (Figs. 5.21 and 5.27), the crystallinity of C-(A)-S-H was improved by CH-substitution (Figs. 5.4-5.6) and resulted in lower shrinkage in LNC-10 mixes. It can be deduced that along with the total pore volume, the crystallinity of C-S-H governs the shrinkage mechanism of AAMs.

7.3 Water Sorptivity

Table 7.1 shows the initial and secondary absorptions, along with the primary and secondary sorptivity coefficients of all mixes. Sorptivity results indicate that for the first hours of the test, saturation develops on the surface of the paste phase. It can be seen that the secondary absorption values are higher than the initial. The first 6 h of the water sorptivity was considered in the discussion since most of the absorption rates were observed in this period.

Table 7.1 Water sorptivity (mm) and sorptivity coefficient ($mm/s^{1/2}$) of mixes

Mixes	$I_{ini}(mm)$	$I_{sec}(mm)$	k ($mm/s^{1/2}$)	k_{sec}(mm/$s^{1/2}$)
NC100-6	0.983	1.420	0.007	0.002
NC80-6	0.868	1.026	0.007	0.002
NC60-6	0.503	0.645	0.005	0.001
LNC100-6	0.392	0.512	0.005	0.001
LNC80-6	0.321	0.422	0.003	0.001
LNC60-6	0.253	0.323	0.003	0.001
NC100-6	0.983	1.420	0.007	0.002
NC100-10	0.544	0.936	0.005	0.002
NC80-10	0.652	0.766	0.004	0.001
NC60-10	0.292	0.361	0.002	0.001
LNC100-10	0.366	0.523	0.003	0.001
LNC80-10	0.348	0.537	0.003	0.001
LNC60-10	0.085	0.152	0.001	0.001
OPC	0.247	0.405	0.002	0.001

Initial absorption values range from 0.085 to 0.983 mm, while secondary absorption values range from 0.152 to 1.420 mm. It can be easily seen that NH and

CH-substitutions decrease the sorptivity (initial absorption, I_{ini}) of mixes and the sorptivity is reduced with increasing NH content as observed in Figs. 7.5 and 7.6. Moreover, the effect of CH-substitution was much more pronounced. It was thought that the formation of high amount of calcite and its filling ability is one of the reasons for lower sorptivity for the CH-modified mixes. According to the test results, with the CH-substitution maximum reduction of 71% in initial absorption was observed between NC60-10 and LNC60-10 mixes. Although the NH-substitution generally shows lower reduction rates compared to the CH-substitution, the dual effect of CH and NH on sorptivity has provided further improvement. For example, the initial sorptivity decreases by approximately 84% when NC100-10 is compared with LNC60-10 (Table 7.1).

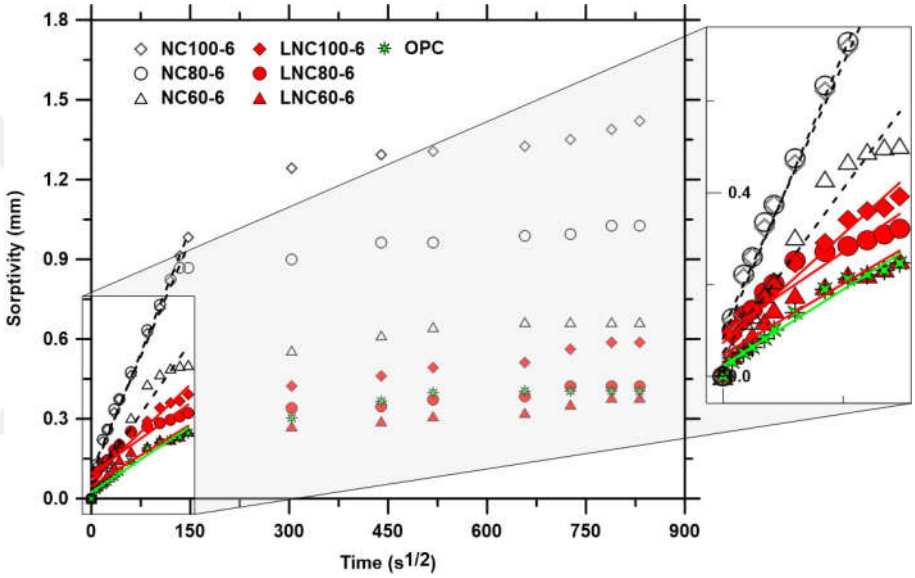

Figure 7.5 Sorptivity of NC-6, LNC-6 and OPC mixes

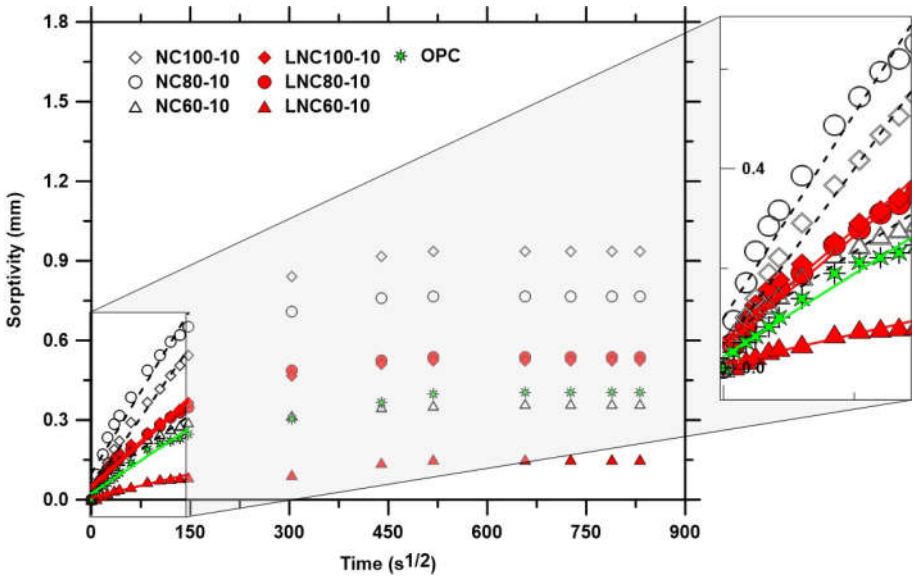

Figure 7.6 Sorptivity of NC-10, LNC-10, and OPC mixes

The primary sorptivity coefficient k followed a similar trend with the absorption values (Fig. 7.7). While the primary sorptivity coefficient of NC mixes is ranged between 0.002 – 0.007 $mm/s^{1/2}$, for LNC mixes, it is ranged between 0.001 and 0.005 $mm/s^{1/2}$. The minimum and maximum sorptivity coefficient values were obtained in LNC60-10 and NC100-6 mixes respectively, which is in line with the sorptivity values. OPC, NC60-10 and LNC60-10 mixes present the lowest sorptivity around 0.002 $mm/s^{1/2}$. While other LNC mixes are only slightly higher than that of these mixes, NC mixes have higher values. It can be concluded that CH-modified mixes exhibited better performance than NH-modification in terms of the sorptivity.

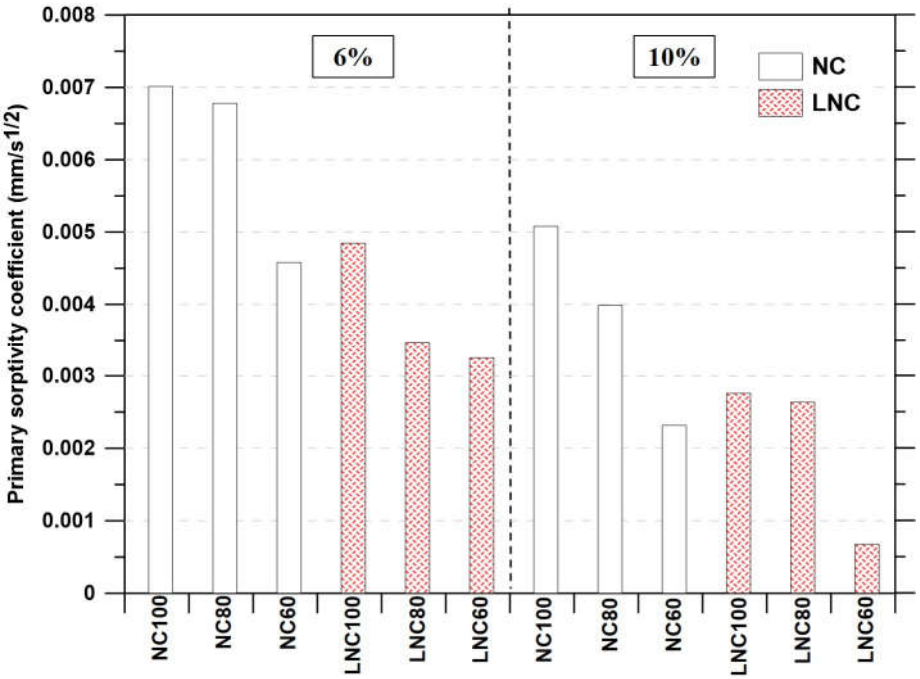

Figure 7.7 Primary sorptivity coefficient of mixes

Law et al. [213] have compared the sorptivity values of sodium silicate-activated slag concrete with different silicate modulus. The authors reported that alkali-activated slag concretes present higher sorptivity values compared to the OPC and OPC/Slag concretes. It was also indicated that an increase in silicate modulus led to a decrease in the sorptivity.

The sorptivity value can be indicative in terms of the durability of the material. Pore structure and the hydration degree of the mixes are influential factors in terms of the sorptivity. Neithalath [214] reported that the initial and secondary sorptivity can be used to evaluate the connectivity of the pore network, which is consistent with the results of the current study. Lower sorptivity of CH-modified mixes is related to the reduced porosity and refined pore structure. High correlation (0.80) between the sorptivity and pore volume was observed (Fig. 7.8). Moreover, sorptivity-compressive

strength and initial sorptivity-compressive strength values are found to be correlated as well (Figs. 7.9 and 7.10).

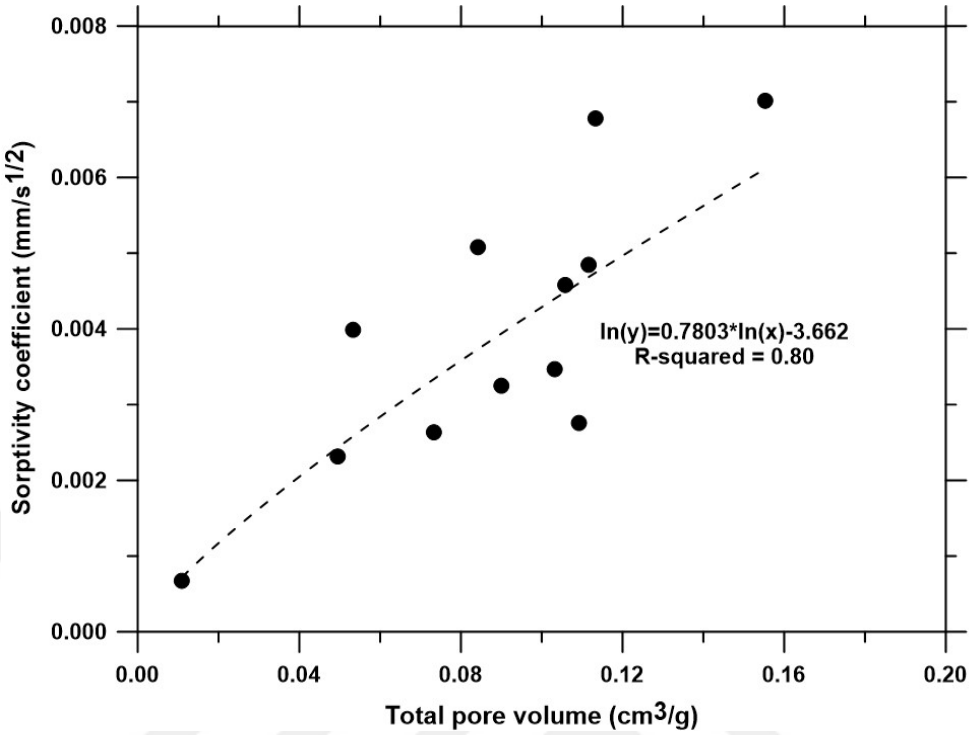

Figure 7.8 Sorptivity coefficient and total pore volume correlation

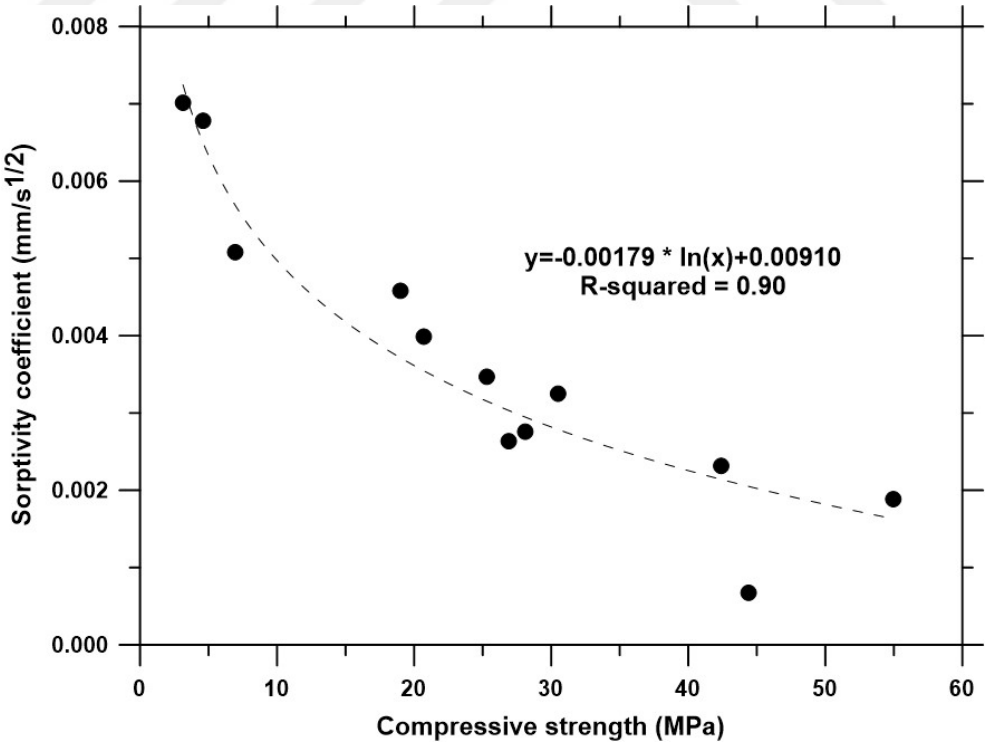

Figure 7.9 Sorptivity coefficient and compressive strength correlation

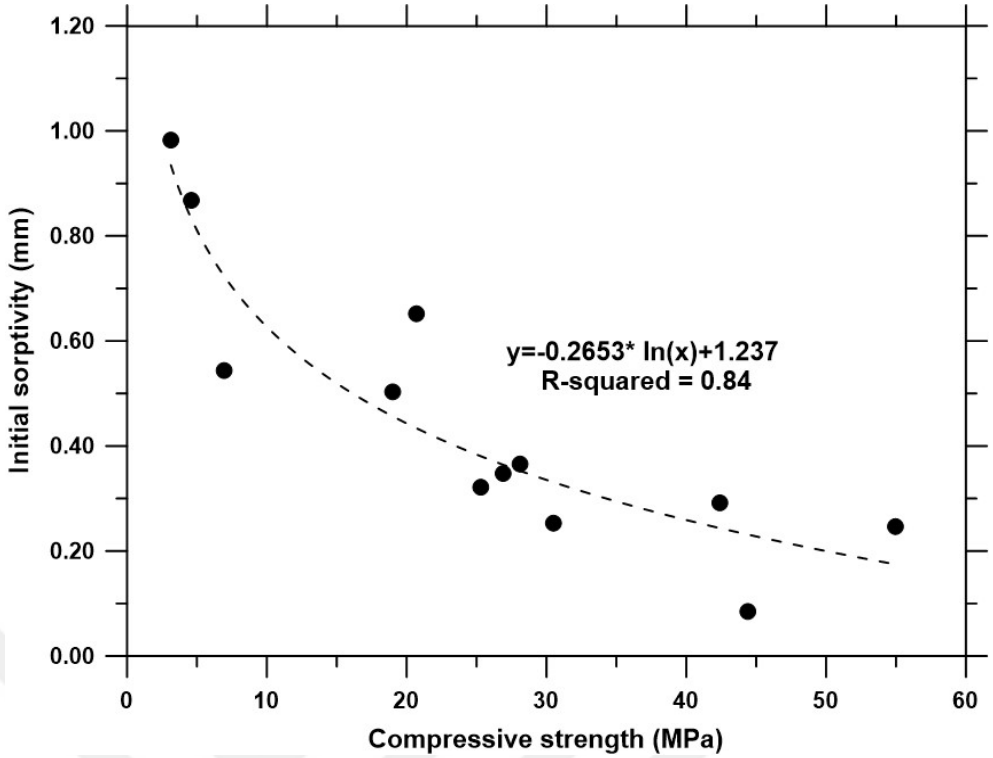

Figure 7.10 Initial sorptivity and compressive strength correlation

7.4 Non-steady State Chloride Migration

The chloride permeability can be defined as the penetration ability of chloride ions into the concrete medium. This is one of the most important durability characteristics of the concrete since the rebar may have damaged by chloride-induced corrosion in reinforced concrete. The number of studies has shown that AAMs designate better performance compared to the OPC-based systems [204, 215–218] in terms of resistance to chloride ingress. Nord Test Build 492 [75] is reported to be one of the appropriate measurement methods for determining the chloride ion migration properties in AAMs [219, 220].

The lowest and highest chloride migration coefficients have been calculated based on the minimum and maximum chloride penetration depth of the two repetitive samples. Chloride penetration depth was determined with the spraying silver nitrate ($AgNO_3$) on the freshly split samples. Because of the possible leakage of the test solutions through the sides of test samples, a 10 mm edge was omitted in chloride penetration results. As a result of the reaction with the silver nitrate and the chloride ions, precipitation of white silver chloride (AgCl) and dark brown silver oxide (Ag_2O) forms (Eqs. 7.1 and 7.2) [204].

$$Ag^+ + Cl^- \rightarrow AgCl \downarrow (silver - white) \tag{7.1}$$

$$Ag^{+} + OH^{-} \rightarrow Ag_2O \downarrow (brown) \tag{7.2}$$

The visible boundary of the precipitated AgCl is marked in all mixes and three examples are shown in Fig. 7.11. It can be seen that NH and CH-substituted NCAS mortar mixes presented lower values than the OPC mortar.

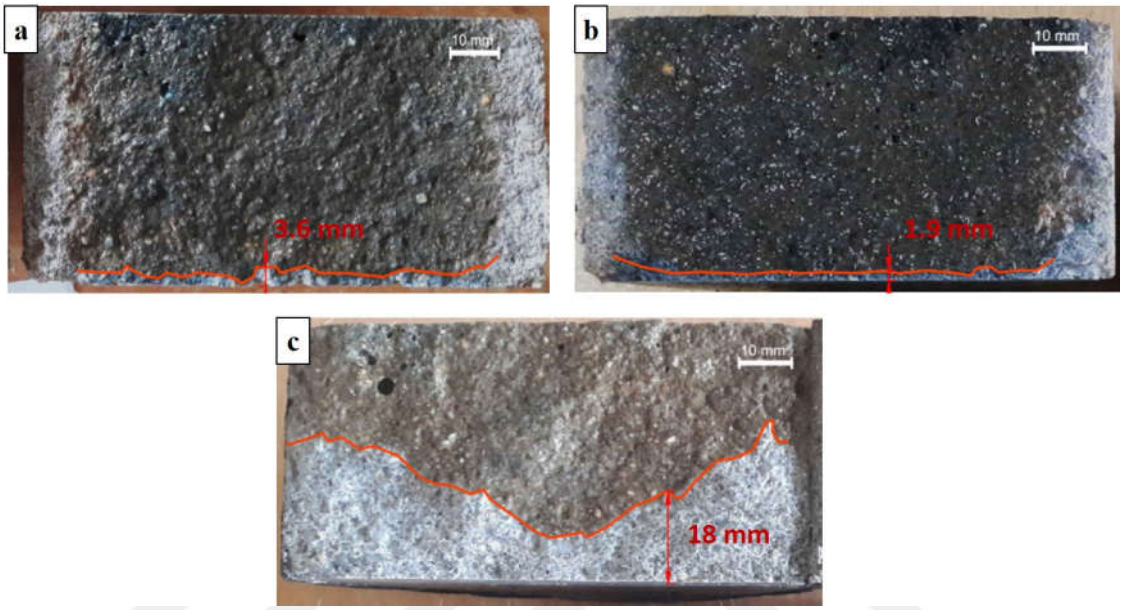

Figure 7.11 Chloride penetration depths of (a) LNC60-6 (b) LNC60-10 (c) OPC mixes

The average chloride migration coefficients are given in Table A.14 and the minimum and maximum chloride migration coefficients of four selected NCAS (NC60-6, NC60-10, LNC100-10, LNC60-10) and OPC-based mixes are given in Fig. 7.12. The selected mixes are chosen considering the representing effect of activator dosage, along with the NH and CH-substitution.

The minimum and maximum values of chloride migration coefficients give more details than roughly estimating the average depth of ingress over an entire sample. These parameters provide more information about the possibility of failure under the chloride attack on reinforced concrete [208]. The maximum range is observed in NC60-6 and the minimum is obtained in CH+NH-modified LNC60-10 mixes. The high range of NC60-6 mixes might be attributed to the inhomogeneity of the sample.

Both the highest and lowest chloride migration coefficients decrease significantly with the NH and CH-substitution. However, the results show a maximum reduction of 96% between NC60-6 and NC60-10 mixes, which means that increasing the alkali concentration enhances the resistance against chloride migration. This is one of the most important observations in Fig. 7.12 that shows the chloride migration coefficient

is significantly reduced when the activator concentration is increased from 6% to 10%.

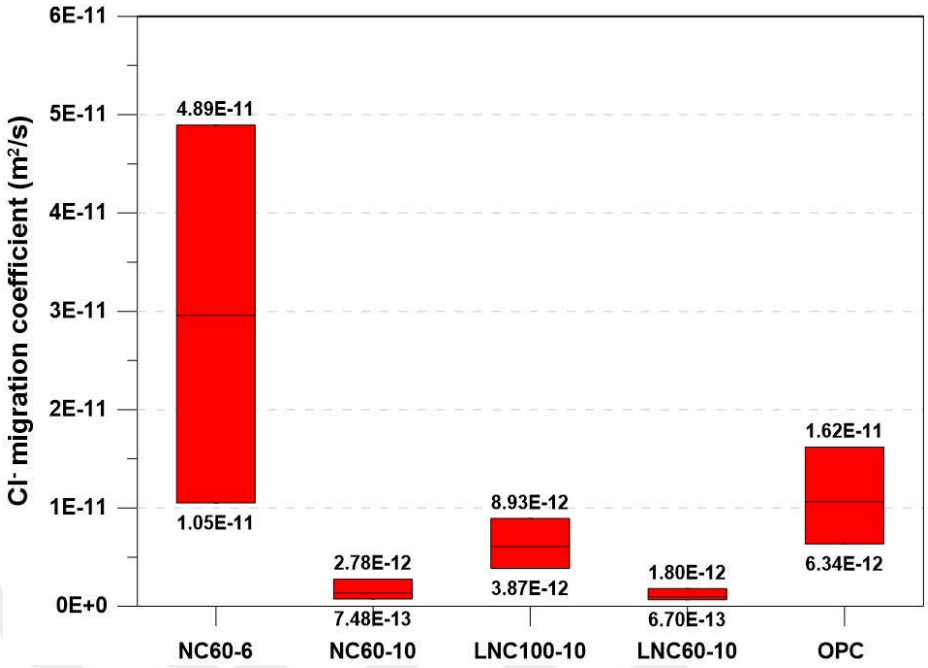

Figure 7.12 Chloride migration coefficients of the selected mixes

OPC-based mixes presented higher chloride migration values compared to NC-10 and LNC-10 mixes. In this study, CH-substitution resulted in the minimum chloride migration coefficients (Fig. 7.12) which can be attributed to the denser microstructure and lower porosity promoted by CH which facilitates extra Ca^{2+} ions and enables the formations of strength-giving phase such as hydrotalcite and C-(A)-S-H gel (Figs. 5.3-5.5). It can be concluded that CH-modified NCAS mixes exhibit higher chloride transport resistance than plain NCAS mixes. Moreover, lower chloride migration results of CH-substituted mixes are consistent with the reduced sorptivity (Figs. 7.7 and 7.12). NH-substitution is also effective in the reduction of the chloride migration as well (Table A.14). The improvement was attributed to the (i) formation of higher amounts of strength-giving phases and (ii) lower porosity (Fig. 5.29) which are the most effective parameters on chloride migration resistance. Lee and Lee [221] and Ismail et al. [204] studied the chloride migration in alkali-activated fly ash-slag systems and reported that the addition of slag into the alkali-activated fly ash-slag systems increase C-(A)-S-H gel formation following low depth chloride penetration in these systems. Ke et al. [208] stated that NCAS has higher porosity and higher chloride migration coefficient than the sodium silicate-activated slag. However, with the incorporation of 5 wt% CLDH, the chloride binding capacity was increased by up to 120% and binding capacities were found as higher than the sodium silicate-activated slag.

7.5 Conclusions

Shrinkage and permeability characteristics are the main durability issues for all types of AAMs. Even though NC presents better performance than the other generally used activators, such as sodium silicate and NH, high drying shrinkage is still a problem for alkali-activated slag systems.

In this chapter, it was aimed to mitigate the drying shrinkage and improve the permeability characteristics of NCAS to comparable levels with OPC-based materials. To achieve this, two different modifiers e.g. CH and NH were used. To observe the effectiveness of these modifiers on the drying shrinkage and permeability characteristics are determined.

The main and important outcomes were derived based on the obtained experimental results in the chapter as follows:

- The incorporation of CH and NH is found to be an effective method to reduce the drying shrinkage of NCAS. A significant reduction in shrinkage is related to the presence of less interconnected capillary network and denser microstructure of the matrix. NH+CH-modified mixes reached to the comparable shrinkage values with the OPC mixes.
- Generally, CH-modified and CH+NH-modified NCAS mixes presented superior performance than the OPC mixes in terms of chloride migration and sorptivity. The presence of CH is much more pronounced than the incorporation of NH in terms of the chloride migration resistance and sorptivity enhancement.
- Higher activator concentration is effective in improving the permeability such as chloride migration and water sorptivity.
- The SEM results given in Chapter 5 indicate that CH-modified mixes presented denser matrix and lower unhydrated slag particle fraction than the plain NC mixes, offering enhanced permeability characteristics.

It is clearly seen from the overall test results that the CH-substitution has a great influence on the durability performance of NCAS mixes. The improvement is achieved with the denser microstructure, higher degree of hydration and pore refinement. The data presented here is thought to be valuable in the design and development of sustainable and durable NCAS cement, and give foresight for better design in terms of improved performance on shrinkage and permeability characteristics.

8
OPTIMIZATION & COST ANALYSIS

8.1 General

Fresh properties, strength development, and durability characteristics of NCAS were determined, and the results are discussed in previous chapters. In this chapter, the effect of mix proportions on the fresh properties, strength development and durability properties of NCAS are statistically investigated. Moreover, to obtain a moderate setting time, strength development, and superior durability properties compared to OPC, optimization was performed to calculate optimum design variables. Since response surface methodology (RSM) involves a combination of mathematical and statistical techniques, RSM is employed to optimize the parameters.

8.2 Statistical Analysis

Fresh and hardened state properties are evaluated to clarify how independent variables influence the dependent variables. To define significant variables and their contribution level to the experimental results which should be at least 95% confidence level (p-level<0.05) ANOVA software was used to perform statistical analyses. "p-level" demonstrates the degree of interactions of each parameter. A parameter can be described as an effective parameter if only its p-value is lower than 0.05 [222]. After that, regression models, governed by the independent variables such as linear, two factorial interactions (2FI), quadratic or cubic, can be performed. Among those models, a statistically significant one with the highest correlation coefficient was chosen and accepted as the regression model of the dependent variable.

A commercially available statistical program *Design-Expert 12* was employed to perform the statistical analysis and optimization. The proposed statistical models were generated to model the initial (t_{ini}) and final setting (t_{final}) time, compressive strength (f_c), ultimate drying shrinkage (ϵ), chloride migration coefficient (D_{nssm}) etc. of NCAS by using the three independent variables; slag from 97% to 100%, activator concentration from 6% to 10%, and NC from 60% to 100%. Slag, activator, and NC

percentages (A, B, and C) are found to be significant model terms since the p-values are lower than 0.05.

Outputs of the variance analysis are given for each dependent variable in the separate sections. Each proposed models have high correlation coefficients (> 0.88), designating that they properly represent the experimental results. $2FI$ model was found to be fit to the experimental data best for each parameters, presented the smallest p-value and the highest R-square, for all test results among the proposed models.

8.3 Statistical Analysis of Fresh-State Properties

The correlation coefficients of the proposed regression models for initial and final setting time were found as 0.99, and 0.96, respectively.

The low difference between adjusted R-square and predicted R-square values (ranged between 0.99-0.99 and 0.96-0.95, for initial and final setting time, respectively) indicates an acceptable degree of compatibility with each other. Moreover, the standard deviation was found as 0.13 and 0.17 for initial and final setting time, respectively. Furthermore, the coefficient of variation (CV) is lower than 10% (5.11% and 6.04%) for both paramaters. As a consequence, it can be deduced that the relationship between independent and dependent variables is fairly strong and meaningful test results are obtained in this study.

3D response surface and contour graphs are used to visualize the models (Figs. 8.1-8.6).

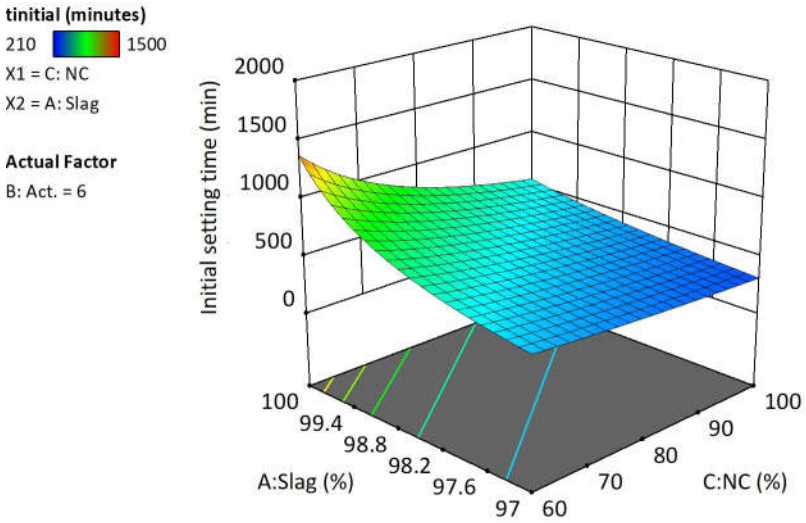

Figure 8.1 3D response surface diagram for initial setting time for low activator concentration (6%)

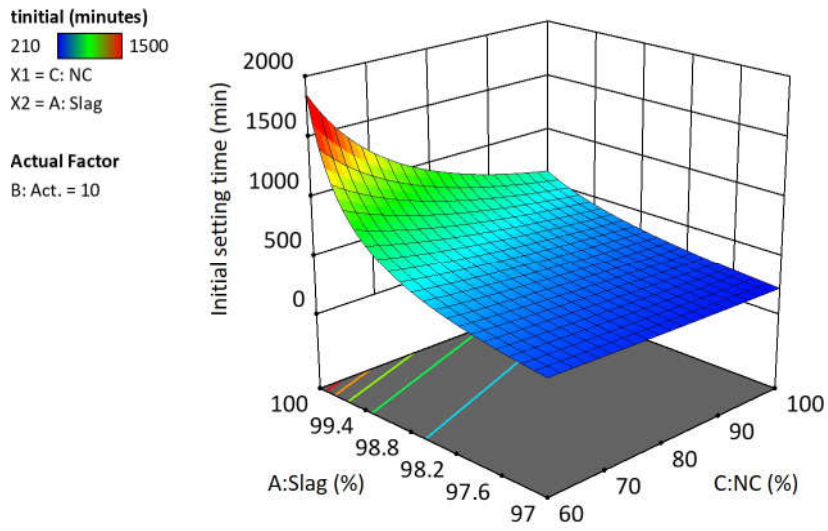

Figure 8.2 3D response surface diagram for initial setting time for high activator concentration (10%)

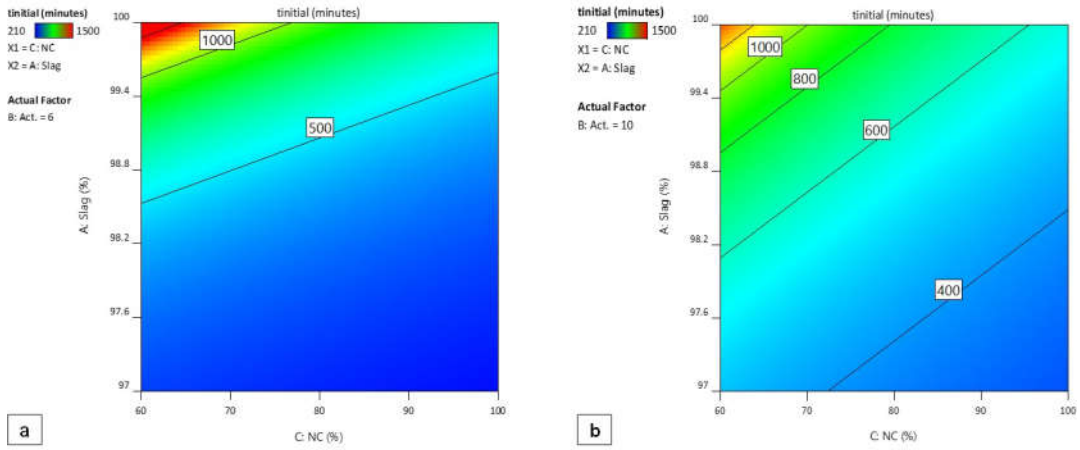

Figure 8.3 Interaction effects of independent parameters on initial setting time (a) for low activator concentration (6%), (b) for high activator concentration (10%)

It can be seen that activator dosage significantly affects the initial setting time. The initial setting time decreases when the activator dosage is used at high dosage (10%) in the mixes without CH-substitution (Figs. 8.1-8.3). On the other hand, NH-substitution increased slightly both initial and final setting times. It is obvious that the effect of slag percentage, in other words, CH incorporation is much more pronounced than the activator concentration or NC concentration in terms of setting time.

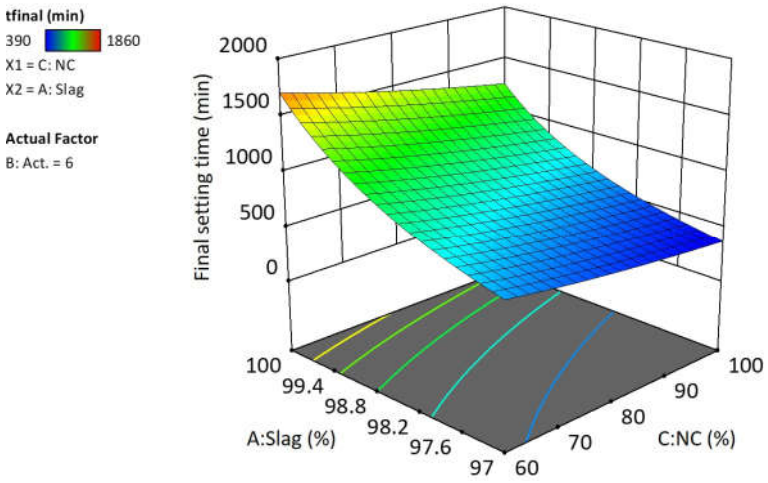

Figure 8.4 3D response surface diagram for final setting time for low activator concentration (6%)

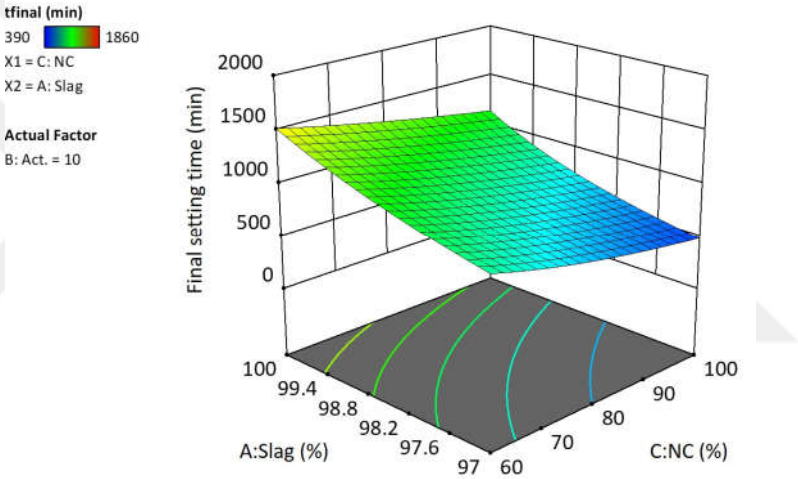

Figure 8.5 3D response surface diagram for final setting time for high activator concentration (10%)

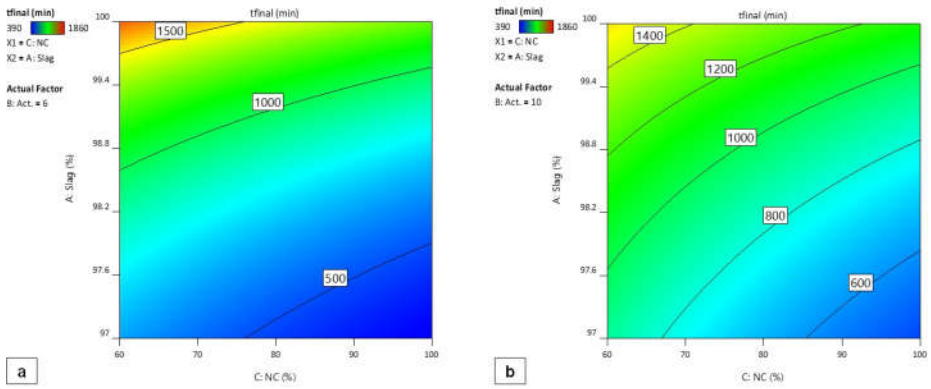

Figure 8.6 Interaction effects of independent parameters on final setting time (a) for low activator concentration (6%), (b) for high activator concentration (10%)

Proposed ANOVA equations for initial (t_{ini}) and final setting time (t_{final}) obtained by *Design-Expert* are given in Table 8.1, which represents the effect of mix proportion on initial and final setting time.

Table 8.1 ANOVA equations for initial and final setting time

$t_{ini} = (0.163 - 0.00164 \times Slag - 0.0117 \times Act. + 0.000025 \times NC + 0.00012 \times Slag \times Act.)^{-1}$
$t_{final} = (0.544 - 0.000527 \times Slag - 0.0664 \times Act. + 0.00666 \times NC + 0.000667 \times Slag \times Act. - 0.000066 \times Slag \times NC)^{-2}$

The correlation coefficients of the proposed regression models for flow diameter, yield stress, and plastic viscosity are obtained as 0.91, 0.88, and 0.92, respectively. The adjusted R-square and predicted R-square values were ranged between 0.89 and 0.86, 0.87 and 0.84, 0.90 and 0.88, for flow diameter, yield stress, and plastic viscosity, respectively. The low difference between these two values indicates an acceptable degree of compatibility with each other. Moreover, the standard deviation was found as 0.04, 1.20, and 0.20 for flow diameter, yield stress, and plastic viscosity, respectively. Furthermore, CV values were lower than 10% for flow diameter and yield stress (0.87, 9.71). Therefore, it can be deduced that the relationship between independent and dependent variables is fairly strong and meaningful test results are obtained in this study. 3D response surface and contour graphs are used to visualize the models (Figs. 8.7-8.15).

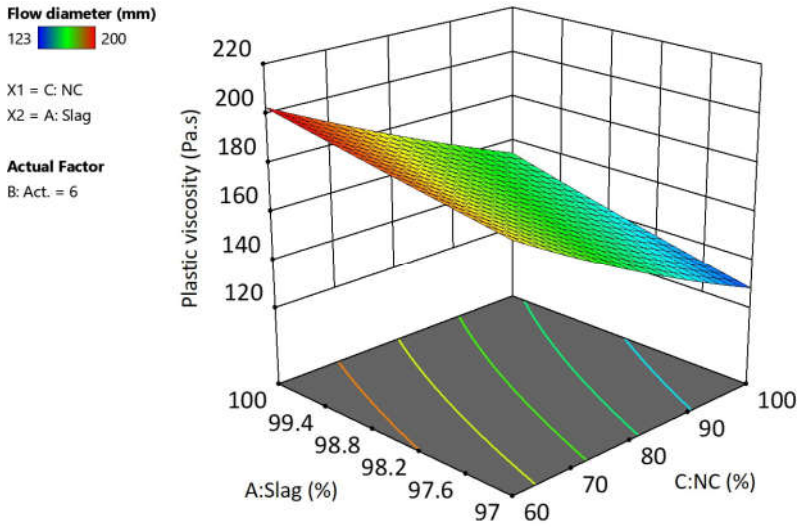

Figure 8.7 3D response surface diagram of flow diameter for low activator concentration (6%)

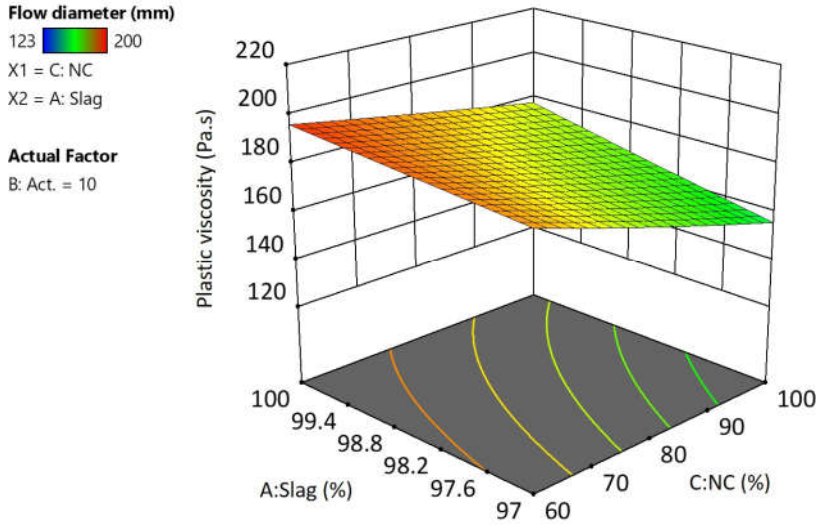

Figure 8.8 3D response surface diagram of flow diameter for high activator concentration (10%)

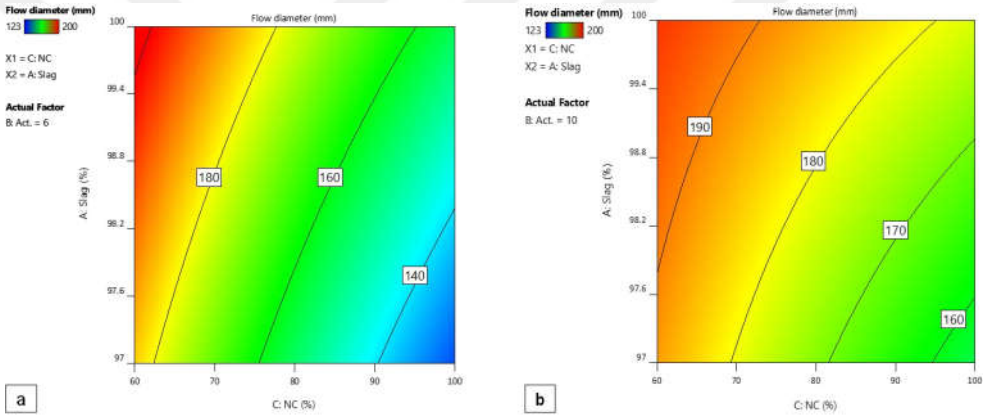

Figure 8.9 Interaction effects of independent parameters on flow diameter (a) for low activator concentration (6%), (b) for high activator concentration (10%)

For low concentration activated mixes, flow diameter values ranged extensively, while for high concentration activated mixes variation was lower. CH-substitution decreased the flowability for both activator dosages, whereas NH-substitution increased it (Figs. 8.7-8.9). It can be seen that when activator dosage is low (6%), both NH and CH-substitution increased the YS. On the other hand, NH-substitution decreased the YS significantly in 10% mixes, while CH-substitution increased (Figs. 8.10-8.12).

Plastic viscosity values did not vary significantly with either NC or slag concentration, all mixes presented similar values (Figs. 8.13-8.15). On the other hand, CH-substitution increased it slightly when the activator concentration increased. CH-substituted plain NC mixes (NC100-10) presented the highest values of PV. Generally, NH-substitution decreased the PV (Fig. 8.15).

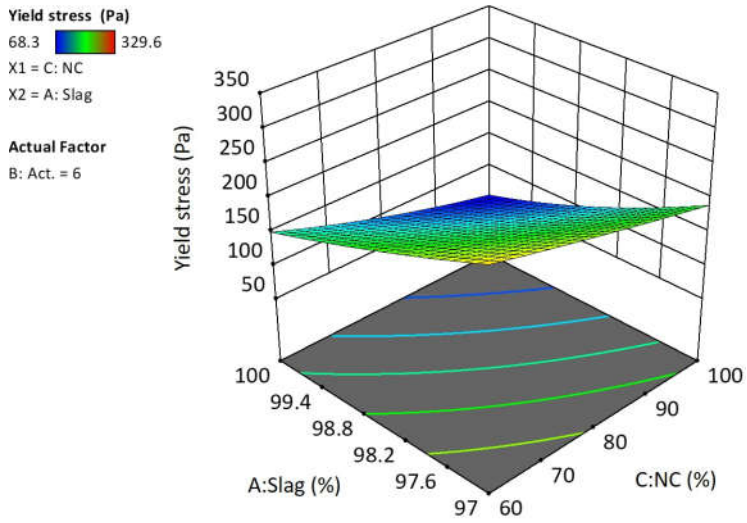

Figure 8.10 3D response surface diagram of yield stress for low activator concentration (6%)

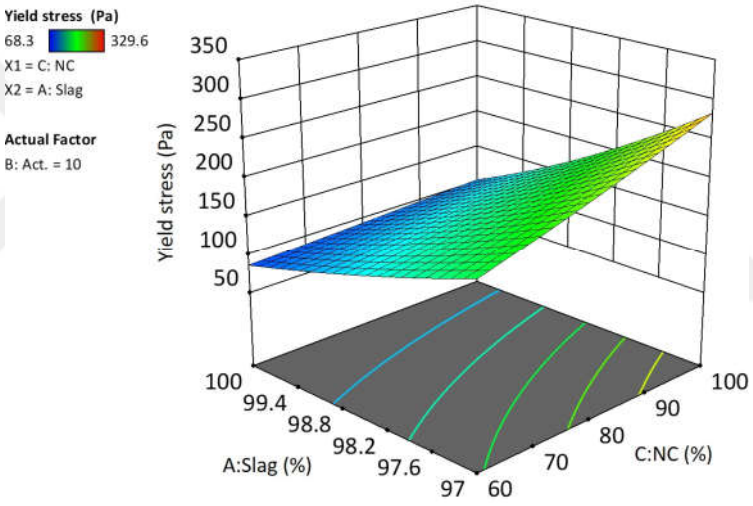

Figure 8.11 3D response surface diagram of yield stress for high activator concentration (10%)

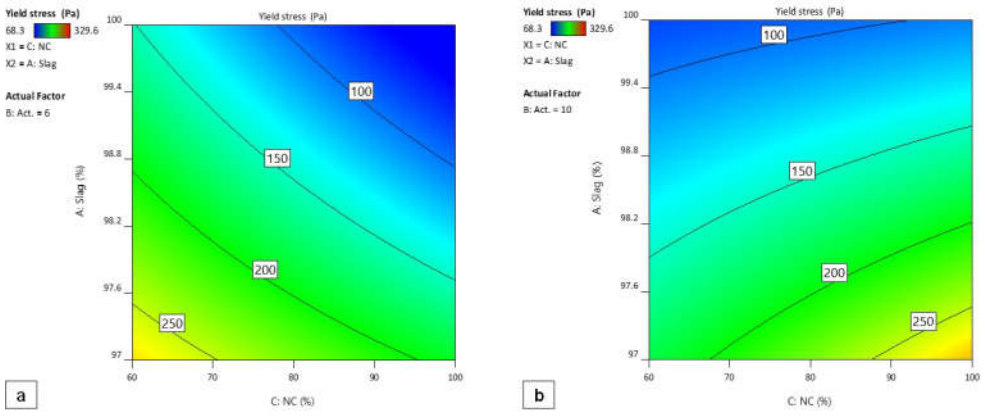

Figure 8.12 Interaction effects of independent parameters on yield stress (a) for low activator concentration (6%), (b) for high activator concentration (10%)

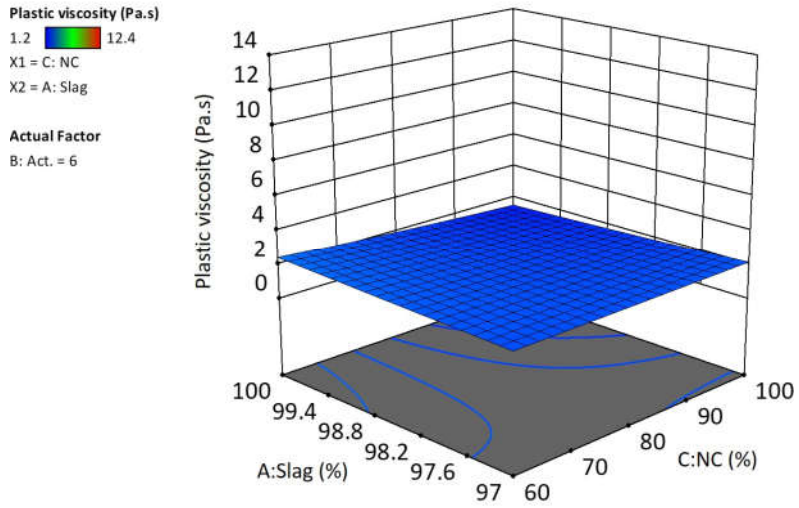

Figure 8.13 3D response surface diagram of plastic viscosity for low activator concentration (6%)

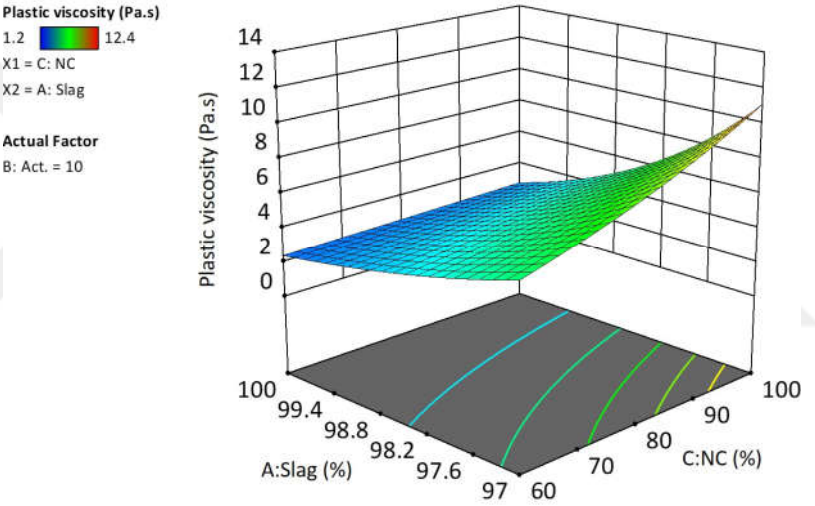

Figure 8.14 3D response surface diagram of plastic viscosity for high activator concentration (10%)

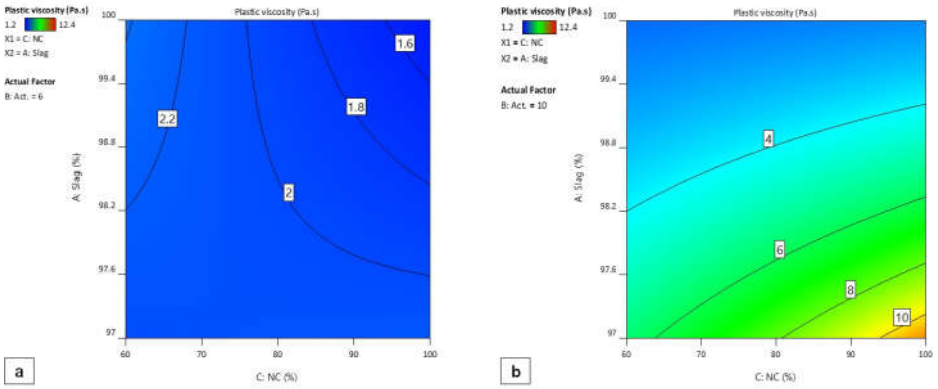

Figure 8.15 Interaction effects of independent parameters on plastic viscosity (a) for low activator concentration (6%), (b) for high activator concentration (10%)

Proposed ANOVA equations for flow diameter, (d_{flow}), YS, and PV are given in Table 8.2, which represents the effect of mix proportion on rheological properties.

Table 8.2 ANOVA equations for flow diameter, plastic viscosity, and yield stress

$d_{flow} = e^{(4.49+0.0165\times Slag+0.39\times Act.-0.087\times NC-0.0046\times Slag\times Act.+0.00074\times Slag\times NC+0.0011\times Act.\times NC)}$
$PV = e^{(-79.9+0.83\times Slag+8.23\times Act.+0.407\times NC-0.085\times Slag\times Act.+0.0044\times Slag\times NC+0.004\times Act.\times NC)}$
$YS = (31.54-0.18\times Slag + 1.99 \times NC - 0.021 \times Slag \times NC + 0.0011 \times Act. \times NC)^2$

8.4 Statistical Analysis of Compressive Strength

The correlation coefficients of the proposed regression models for 3-days, and 28-days, compressive strength are 0.99, and 0.95, respectively. The adjusted R-square and predicted R-square values were 0.99 and 0.96 for 3-days and 28-days compressive strength, respectively which designates acceptable degree of compatibility with each other.

In addition, standard deviation was found as 0.13, and 0.17 for 3-days and 28-days compressive strength, respectively. Moreover, CV values are found as 5.11, and 6.04 which are lower than 10%. As a consequence, it can be deduced that the relationship between independent and dependent variables is fairly strong and meaningful test results were obtained in this study.

3D response surfaces and contour graphs for 3-days, and 28-days, compressive strength results are used to visualize the models (Figs. 8.16-8.18). It is obvious that both CH and NH-substitution are very effective to obtain the higher compressive strength at 3 days. The combination of two modifiers gives the highest values when activator concentration is 6%. The same trend can be seen when activator concentration is 10%.

Both NH-substitution and NH+CH-substitution increase the compressive strength and contribution of NH was much more pronounced at 28 days compared to 3 days (Figs. 8.19-8.21). When the activator amount increased to 10%, the compressive strength increases for all mixes, the dual effect of NH+CH is much more pronounced (Fig. 8.21). When the ultimate compressive strength is considered, it can be deduced that the effect of NH and NH+CH substitution is similar.

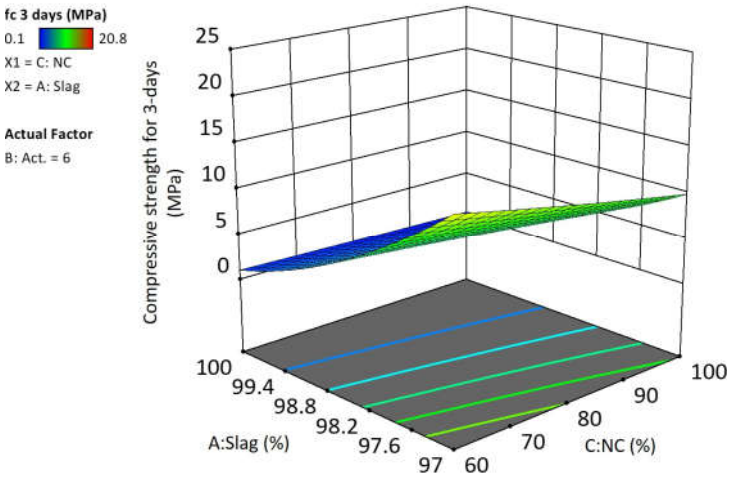

Figure 8.16 3D response surface diagram of 3-days compressive strength for low activator concentration (6%)

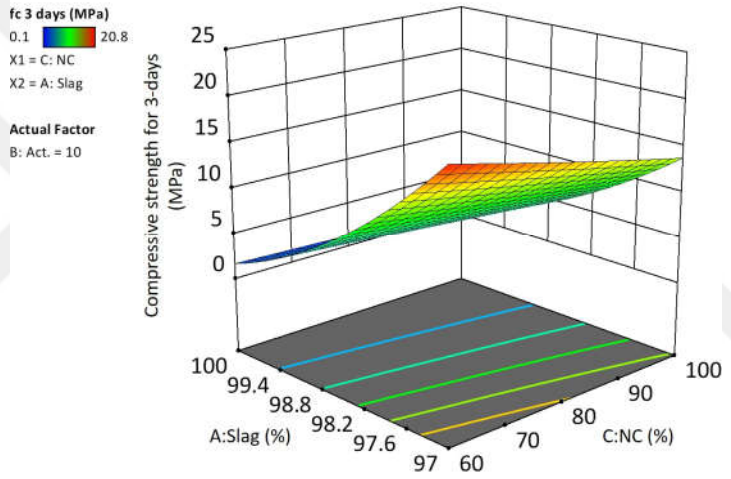

Figure 8.17 3D response surface diagram of 3-days compressive strength for high activator concentration (10%)

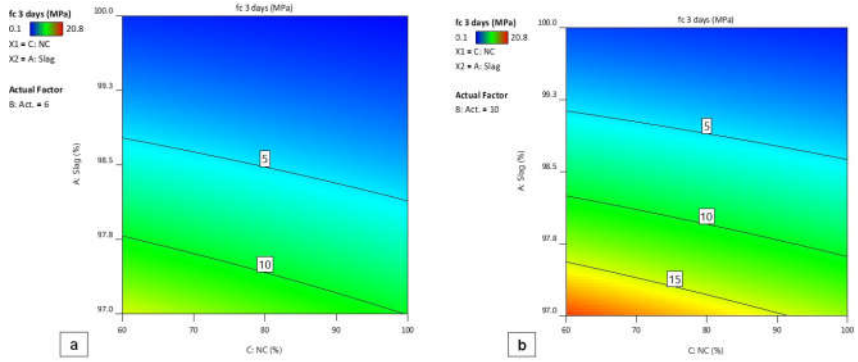

Figure 8.18 Interaction effects of independent parameters on 3-days compressive strength (a) for low activator concentration (6%), (b) for high activator concentration (10%)

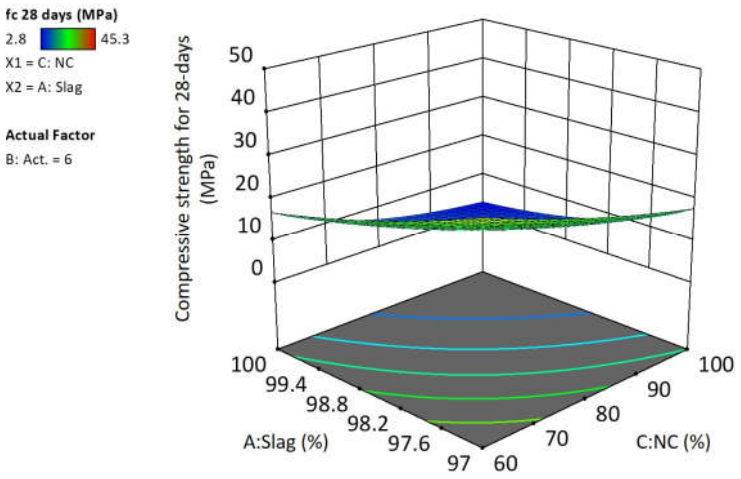

Figure 8.19 3D response surface diagram of 28-days compressive strength for low activator concentration (6%)

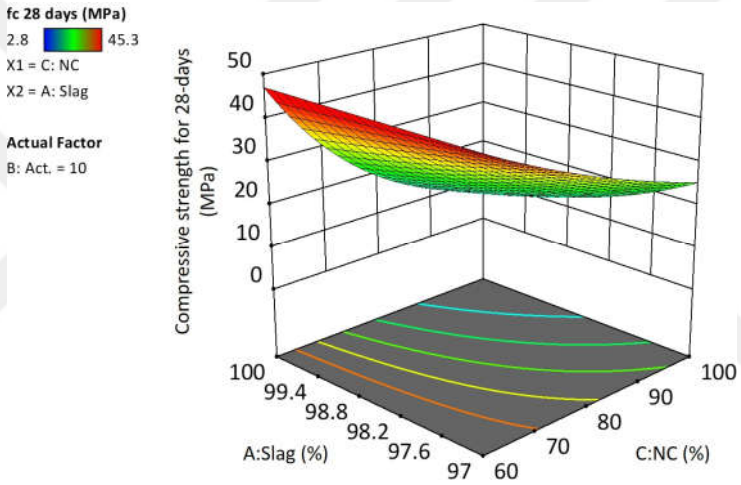

Figure 8.20 3D response surface diagram of 28-days compressive strength for high activator concentration (10%)

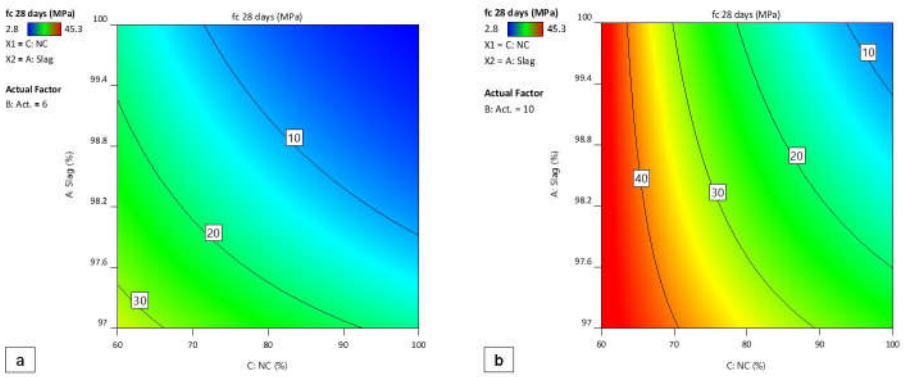

Figure 8.21 Interaction effects of independent parameters on 28-days compressive strength (a) for low activator concentration (6%), (b) for high activator concentration (10%)

Proposed regression equations for 3-day and 28-day compressive strengths ($f_{c,3}$ and $f_{c,28}$) obtained by *Design-Expert* are given in Table 8.4, which represent the effect of mix proportions.

Table 8.3 ANOVA equations for 3-days and 28-days compressive strength

$f_{c,3} = -0.50+95.62-0.942\times Slag-2.67\times Act.+0.327\times NC+0.026\times Slag\times Act.$ $+0.00318\times Slag\times NC)^2$
$f_{c,28} = e^{(-1.567+0.056\times Slag-5.304\times Act.+0.975\times NC+0.056\times Slag\times Act.-0.0102\times Slag)}$

8.5 Statistical Analysis of Durability Properties

The correlation coefficients of the proposed regression models for ultimate drying shrinkage and chloride migration coefficient are found as 0.94, and 0.96, respectively. The difference between adjusted R-square and predicted R-square values were very low which designates an acceptable degree of compatibility with each other (0.95-0.94 and 0.93-0.91 for ultimate drying shrinkage and chloride migration coefficient, respectively). In addition, standard deviation was found as 0.40, 84.8 for each parameter, respectively. Thus, it can be deduced that the relationship between independent and dependent variables is fairly strong and meaningful test results are obtained in terms of shrinkage and chloride migration.

Figs. 8.22-8.27 present the graphical illustration of the models for ultimate drying shrinkage and chloride migration coefficient. It can be seen that for low activator concentration, plain mixes (NC100-6) present the highest shrinkage values, and almost no changes were observed with the NH-substitution. However, with the CH-substitution shrinkage decreases significantly (Figs. 8.22-8.25). On the other hand, both NH and CH-substitution was found as effective in terms of reducing the ultimate drying shrinkage when activator concentration was high. The contribution of combination of two modifiers was higher than using the modifiers individually.

In the case of low activator concentration, NH-substitution was very effective for reducing chloride migration, especially when slag was used as sole binder. CH-substitution decreased the chloride migration as well, however, combination of the two modifiers was higher than using modifiers individually.

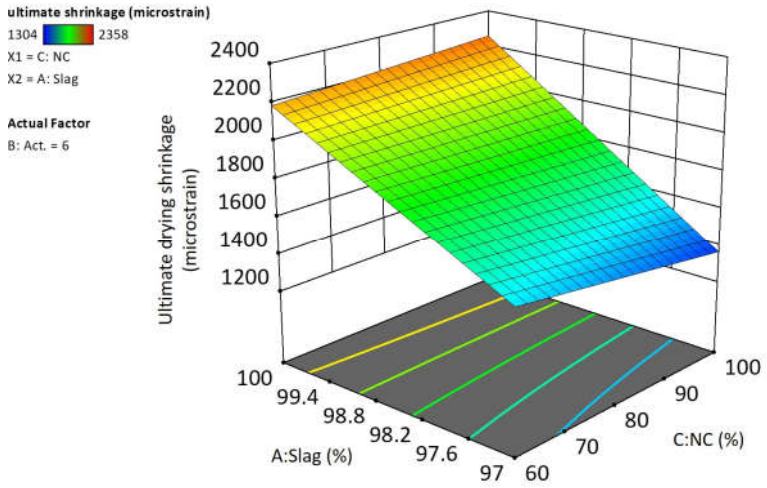

Figure 8.22 3D response surface diagram of ultimate drying shrinkage for low activator concentration (6%)

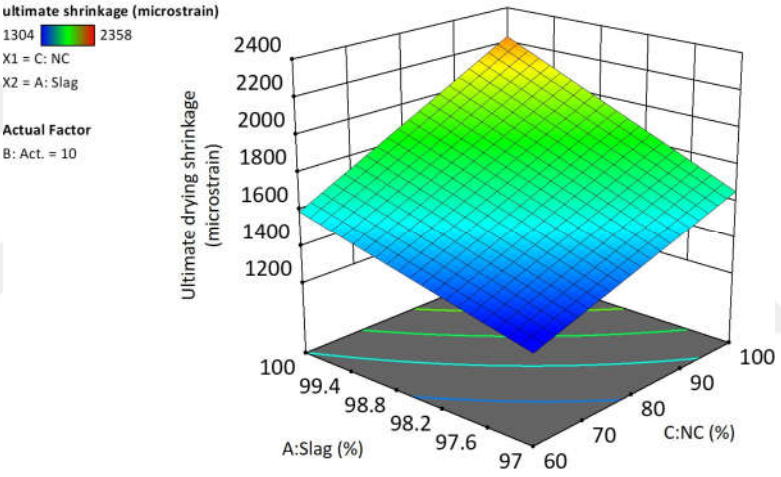

Figure 8.23 3D response surface diagram of ultimate drying shrinkage for high activator concentration (10%)

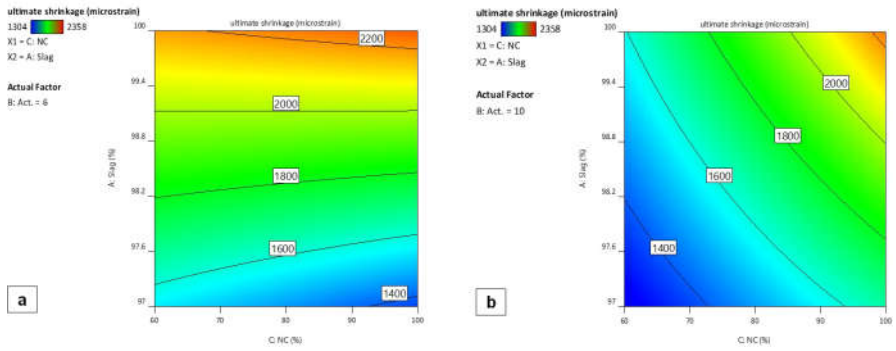

Figure 8.24 Interaction effects of independent parameters on ultimate drying shrinkage (a) for low activator concentration (6%), (b) for high activator concentration (10%)

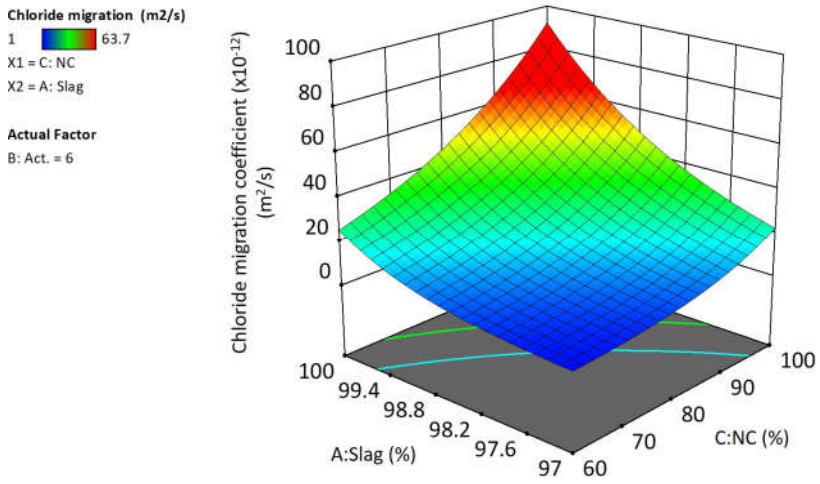

Figure 8.25 3D response surface diagram of chloride migration coefficient for low activator concentration (6%)

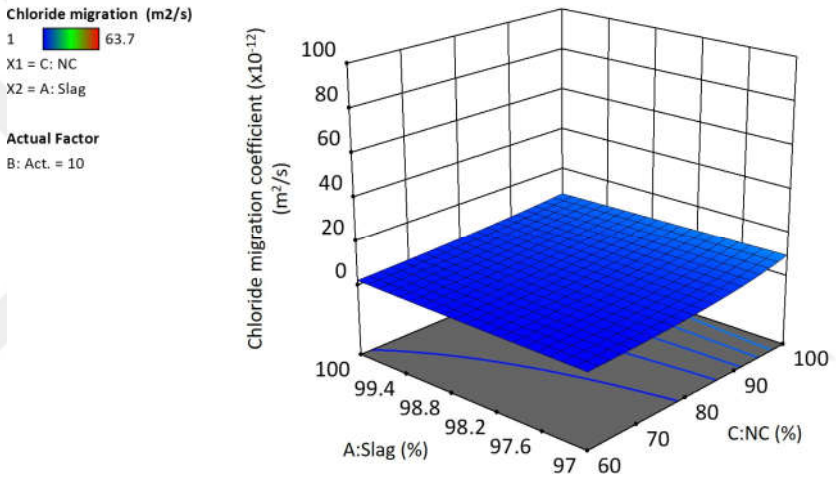

Figure 8.26 3D response surface diagram of chloride migration coefficient for high activator concentration (10%)

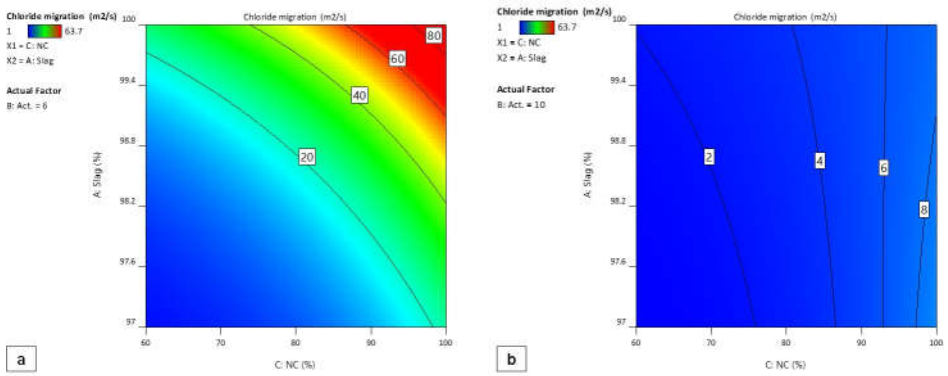

Figure 8.27 Interaction effects of independent parameters on chloride migration coefficient (a) for low activator concentration (6%), (b) for high activator concentration (10%)

When activator dosage increased, the efficiency of the modifiers decreased. Similar to low activator concentration mixes, both NH and CH substitution decreased the chloride migration, but the reduction percentage was lower. It can be inferred that modifiers were more effective when activator concentration was low (6%) (Figs. 8.24-8.27), the contribution of increase in activator and NH+CH-substitution was similar in terms of chloride migration coefficient.

Proposed regression equations for ultimate drying shrinkage (ϵ) and chloride migration coefficient (D_{nssm}) obtained by Design-Expert are given in Table 8.4, which represent the effect of mixing proportions on compressive strength at different days.

Table 8.4 ANOVA equations for ultimate drying shrinkage and chloride migration coefficient

$\epsilon = -20097.5 + 243.37 \times Slag + 2295.42 \times Act. - 232.88 \times NC - 26.56 \times Slag \times Act. + 2.14 \times Slag \times NC + 3.5 \times Act. \times NC$
$\mathrm{D}_{nssm} = e^{(-235.2+2.402 \times Slag+13.29 \times Act.+1.13 \times NC-0.14 \times Slag \times Act.-0.011 \times Slag \times NC)}$

8.6 Multi-objective Optimization of NCAS mixes

In the current study, a multi-objective optimization was performed when the variable analyzing completed. The response models were used to optimize the mix design for desired responses (Table 8.5). Two multi-objective optimizations were performed considering the parameters affecting the fresh and hardened state properties of NCAS. For each objective, optimizations were performed separately.

Table 8.5 Multi-objective optimizations

#1	Minimum initial setting time
	Flow diameter in the range from 140 to 200 mm
	Maximum early age strength at 3 days
	Maximum compressive strength at 28 days
#2	Maximum compressive strength at 28 days
	Minimum drying shrinkage
	Minimum chloride migration coefficient

The value of desirability function based on each response varies between 0 and 1, in which 0 indicates completely undesirable, and 1 refers to a perfectly desired response. In the literature, desirability is classified into three levels, the range between 0.80 and 1.00 is described as excellent, 0.80 and 0.63 is described as moderate, and 0.63 and

0.37 is defined as acceptable [223]. To optimize the desirable responses simultaneously, desirability functions were defined for each objective by using a numerical optimization technique.

The independent and dependent variables used in the multi-objective optimizations are given in Tables 8.6 and 8.8 for each objective defined in Table 8.5. For the first objective, 53 different solutions were obtained from the optimization study. The desirability ranges between 0.72 and 0.51. The first three solutions are shared in Table 8.7 and the graphical ramp view of the first solution for the first objective is shown in Fig. 8.28. According to the finest solution, in order to ensure the minimum initial setting time, maximum compressive strength at 3 and 28-days with minimum activator dosage, slag and NC percentages should be at 97% and 60%, respectively.

Table 8.6 Independent and dependent parameters of the first multi-objective problem

#	Independent and dependent parameters	Goal	Lower limit	Upper limit
1	Slag (%)	In the range	97	100
2	Activator concentration (%)	Minimize	6	10
3	NC (%)	In the range	60	100
4	3-days compressive strength (MPa)	Maximize	10	15
5	28-days compressive strength (MPa)	Maximize	25	45
6	Initial setting (min)	Minimize	210	600
7	Flow diameter	In the range	140	200

Table 8.7 Optimum first three solutions for the first objective

#	Slag (%)	Act. (%)	NC (%)	fc_3 (MPa)	fc_{28} (MPa)	t_{ini} (min)	d_{flow} (mm)	Desirability
1	97	6.012	60.000	15.29	32.55	287	183.7	0.72
2	97	6.010	60.002	15.29	32.55	287	183.7	0.72
3	97	6.000	60.000	15.27	32.52	287	183.7	0.72

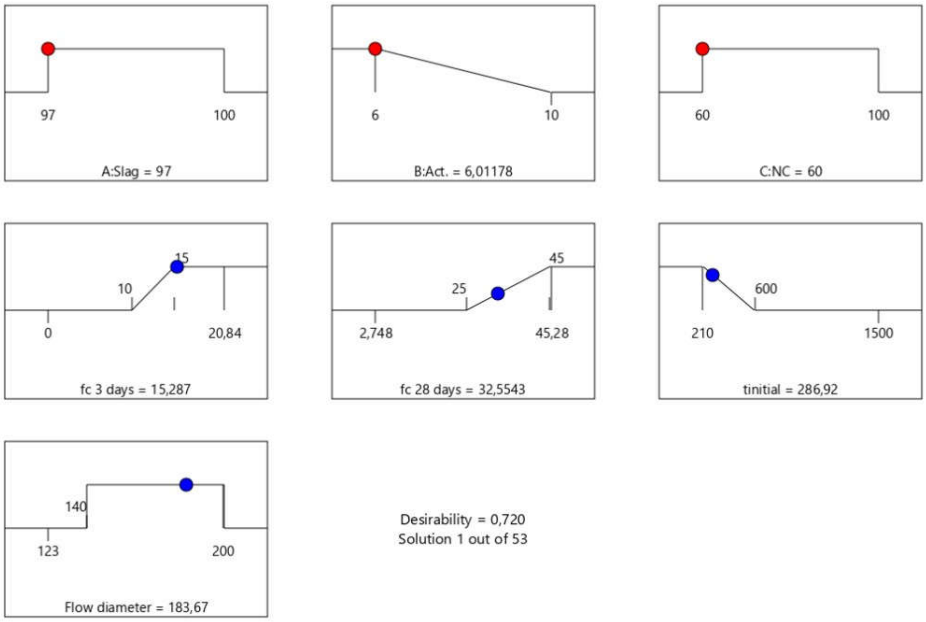

Figure 8.28 Graphical ramp views for the first objective

For the second objective, 66 different solutions were obtained from the optimization study. The desirability ranges between 0.92 and 0.44. The first three solutions are shared in Table 8.9 and the graphical ramp view of the second solution for the second objective is shown in Fig. 8.29. According to the finest solution, in order to ensure maximum compressive strength and minimum ultimate drying shrinkage and chloride migration, slag and NC percentages should be at low level (97% and 60%, respectively) and activator concentration should be at a high level (9.66%). The optimization results confirm that the defined responses can be achieved with high desirability.

Table 8.8 Independent and dependent parameters of the second multi-objective problem

#	Independent and dependent parameters	Goal	Lower limit	Upper limit
1	Slag (%)	In the range	97	100
2	Activator concentration (%)	Minimize	6	10
3	NC (%)	In the range	60	100
4	28-days compressive strength (MPa)	Maximize	35	45
5	Drying shrinkage (microstrain)	Minimize	1303	1800
6	Chloride migration $(\times 10^{12})(m^2/s)$	Minimize	1	10

Table 8.9 Optimum first three solutions for the second objective

#	Slag (%)	Act. (%)	NC (%)	fc_{28} (MPa)	ϵ (μstrain)	D_{nssm} (m^2/s)	Desirability
1	97	9.66	60.00	45.0	1411.5	0.708	0.92
2	97	9.68	60.02	45.1	1411.6	0.706	0.92
3	97	9.80	60.00	45.6	1411.7	0.688	0.92

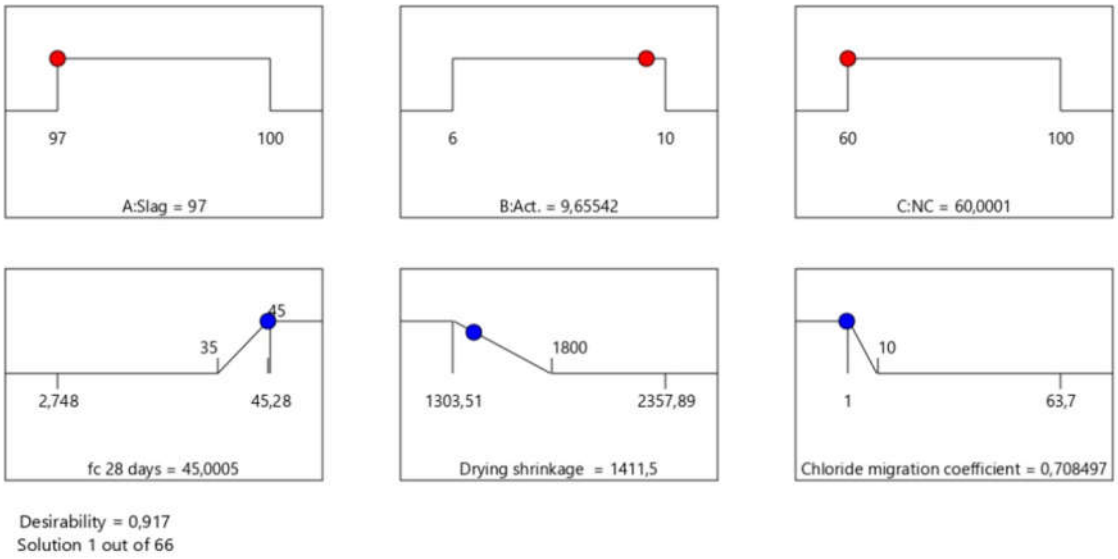

Figure 8.29 Graphical ramp views for the second objective

8.7 Cost Analysis of Sodium Carbonate Activated Slag and OPC-based Mortars

Fresh and hardened state properties of the NCAS mixes has proven to be comparable or superior to conventional OPC-based mixes. However, the cost assessment should be considered to attract interest from investors. The activators such as sodium hydroxides and sodium silicates have become the major contributor to the total costs, while raw materials account for the smallest expense of alkali activated binders since the raw materials are industrial by-products. In this study, NC and NC+NH mixes were used as activators while slag was used as the main precursor.

The broad approach in the evaluation of cost analysis of the alkali activated systems is very complex because of the varieties in the database, then the simplified analysis is preferred since it is thought that simple cost analysis is sufficient to meet the required level for basic comparison between OPC and alkali activated mortars. Two mix proportions obtained from the optimization (Table 8.7 and 8.9) and national pricing of the materials were used for cost analysis. Table 8.10 and 8.11 show the per unit prices

of the materials and mix proportions and costs of 1 m^3 mortar for different mixes, respectively.

Table 8.10 Costs of materials

Materials	Cost per unit ($/ton)
Slag	28.6
NC	170
NH	125
CH	73.9
Water	0
Aggregate	3.73
OPC	42

As can be seen, the total cost of Opt.1 mixes is approximately 10% lower than that of the OPC-based mixes. Moreover, Opt.2 mixes has the same price compared to OPC-based mixes. It should be noted that the calculated results only compares the wholesale prices of the materials. The comparison of the costs would be more reliable if the whole production process of materials was considered.

Table 8.11 Mix design and cost analysis for 1 m^3 of mortar

Quantity (kg)	Opt.1	Opt.2	OPC
Slag	591.3	580.4	649.4
NC	22.0	34.7	-
NH	14.7	23.1	-
CH	18.3	18.0	-
Water	274.3	269.3	292.2
Aggregate	1335.0	1335.0	1335.0
Price ($)			
Slag	16.9	16.6	27.3
NC	3.7	5.9	-
NH	1.8	2.9	-
CH	1.4	1.4	-
Water	0.0	0.0	0.0
Aggregate	5.0	5.0	5.0
Total	28.8	31.7	32.3

9
CONCLUSIONS & RECOMMENDATIONS

The conclusions obtained from the main results of this thesis are reported in the following sections.

9.1 Fresh-State Properties

- pH plays an important role in initiating the reaction process, but it does not directly control the early age reactions.
- The key factor controlling the reaction kinetics of NCAS pastes is the carbonate ion concentration. Setting time of NCAS mostly depends on the concentration of the carbonate ions in the pore solution.
- Although the carbonate ion concentration is one of the most prominent parameters, reaction kinetics are also affected by the other dissolved ions and their concentrations.
- The CH-substitution is the most effective method in terms of accelerating the reaction kinetics of NCAS, enabling the pastes to set within 6.5 h.
- Replacing NC with the NH improves the flowability and rheological properties, but also extends the setting time when used at a high replacement ratio, e.g. 40%.
- The rheological behavior of the NC and LNC pastes fits the Herschel-Bulkley model. The yield stress and plastic viscosity values were higher for the LNC mixes most likely due to the decrease of carbonate ions through the formation of sodium/calcium carbonate-type compounds at the beginning of the reaction.

9.2 Strength Development and Mictostructural Evolution

- NC replacement with NH and the presence of CH in the binder as a replacement of the slag enhances the rate of dissolution of slag leading to desired strength development. CH-substitution significantly increased the compressive strength even at 3 days. On the other hand, NH-substitution is effective at later ages of the reaction, especially when used at high dosages (e.g. 40%). Formation of strength-giving phases such as hydrotalcite and C-(A)-S-H is confirmed with the microstructure analysis and explains the strength development.

- The presence of CH in the binder led to a substantial increase in compressive strength irrespective of the NH usage and/or activator concentration. Enhanced strength development mainly caused by removing the carbonate ion from the medium and providing additional Ca^{2+} resources.

- Formation of the strength-giving phases such as hydrotalcite and C-(A)-S-H plays an important role in the strength development of NCAS.

- The intensities of the XRD peaks of main reaction products, calcite/C-(A)-S-H and hydrotalcite increased for all mixes signifying a higher concentration of reaction products thus pointing to higher compressive strength.

- Longer curing duration (28 days) promotes the development of a more crystalline structure compared with the 3 and 7-day samples. Increasing the curing time does not generate new phases, however, it increases the crystallinity of C-(A)-S-H type structure.

- In CH-modified LNC mixes, the peaks at higher degrees in XRD patterns were more intense than the NC mixes, which resultes in a decrease in interlayer distance reasoning for the higher compressive strength.

- In CH-modified and CH+NH-modified mixes, higher wavenumber of Si-O-T bands is related to the higher degree of polymerization which is resulted in higher strength.

- The SEM results indicate that CH-modified mixes presents a denser matrix and higher hydration degree of slag particles than the plain NC mixes, offering enhanced permeability characteristics.

- The pore size distribution is refined into a smaller diameter with the CH-substitution.

- The detailed characterization of the microstructural development with the progress of hydration in mixes serves to an enhanced understanding of the strength development as a consequence of chemical changes.

9.3 Compressive Strength and Fracture Response

- The compressive strength of the NCAS mortars has been improved and reached to a comparable level with the OPC mortar without heat treatment. However, fiber incorporation, especially PP fiber, exhibited a reduction in the compressive strength in CH-substituted LNC mixes. The main reasons for this phenomenon can be explained with the low stiffness of PP fibers and the voids caused by the fiber addition. As expected, fiber addition increased the flexural strength of the mortars.

- Fiber incorporation and type of fiber are more effective in the improvement of the fracture properties, such as fracture energy, and double-K fracture toughness, rather than the matrix features. It was found that fiber characteristics control the failure mechanism and fracture properties of the NCAS mortars.

- The fracture toughness of ST fiber-reinforced NCAS mortars is higher than that of the PP fiber-reinforced mortars and presents better performance with respect to crack resistance and ductility.

- In addition to the type of fiber used, the fiber-matrix interface and bonding mechanism play an important role in the fracture response of NCAS composites. The CH-substitution enhances the matrix-fiber interfacial properties of NCAS mortars irrespective of the fiber type. The behavior of fibers such as elongation, pull-out or rupture mechanism under the flexural load assigns the fracture mechanism and accordingly fracture response.

9.4 Drying Shrinkage and Permeability

- The incorporation of CH and NH is found to be an effective method to reduce the drying shrinkage of NCAS. A significant reduction in shrinkage is related to the presence of less interconnected capillary network and denser microstructure of the matrix. The NH+CH-modified mixes reached to comparable shrinkage values of the OPC mixes.

- Generally, the CH-modified NCAS mixes are presented for superior performance than the OPC mixes in terms of chloride migration and sorptivity. The presence

of CH is much more pronounced than the incorporation of NH in terms of the chloride migration resistance and sorptivity enhancement.

9.5 Optimization

- The impacts of parameters such as slag content, in other words, CH-substitution, activator dosage, and NC percentage on different responses were efficiently observed using a statistical tool RSM. The desired responses were predicted with high correlations by using ANOVA equations. The analysis reveals that the substitution of CH and activator dosages are the most important parameters to obtain desired level of fresh and hardened properties of NCAS systems, respectively.

9.6 Recommendations for Further Research

This study aims to present the great potential of NCAS as an alternative material to OPC and other AAMs. CH and NH substitution are able to overcome the issues of delayed setting time and low early age strength. It was designated that NCAS can be a suitable, applicable construction material with its superior durability properties. However, further researches are needed for understanding the performance of NCAS.

- The consumption rate of carbonate ions plays an important role in the reaction rate. The effect of carbonate concentration on setting time should be investigated in detail.
- Determining the calcium ion concentration in the medium, as well as with the silisium, aluminum and magnesium might be helpful in order to reveal the relation between the setting and concentration of dissolved ions in pore solution.
- A future perspective can be in the form of a study of the chemical reactions aided by molecular models that can effectively capture the hydration process of such AAMs.
- The chloride migration coefficient and water sorptivity of NCAS mixes were determined in this study. The performance of NCAS mixes under different aggressive environments such as acid and sulphate attack can be investigated.
- In this study, the paste and mortar mixes were produced. NCAS concrete mixes can be produced based on the proportions of the mortar mixes, and the performance can be investigated.

References

[1] E. Worrell, L. Price, N. Martin, C. Hendriks, L. O. Meida, "Carbon dioxide emissions from the global cement industry," *Annual Review of Energy and the Environment*, vol. 26, no. 1, pp. 303–329, 2001.

[2] P. K. Mehta P. J. Monteiro, *Concrete: Microstructure, properties and materials*, 2017.

[3] M. Taylor, C. Tam, D. Gielen, "Energy efficiency and CO_2 emissions from the global cement industry," *Korea*, vol. 50, no. 2.2, pp. 61–7, 2006.

[4] M. Ali, R. Saidur, M. Hossain, "A review on emission analysis in cement industries," *Renewable and Sustainable Energy Reviews*, vol. 15, no. 5, pp. 2252–2261, 2011.

[5] A. Purdon, "The action of alkalis on blast-furnace slag," *Journal of the Society of Chemical Industry*, vol. 59, no. 9, pp. 191–202, 1940.

[6] V. Glukhovsky, "Soil silicates," *Gosstroyizdat, Kiev*, p. 154, 1959.

[7] J. Davidovits, "Geopolymers: Inorganic polymeric new materials," *Journal of Thermal Analysis and Calorimetry*, vol. 37, no. 8, pp. 1633–1656, 1991.

[8] V. Glukhovsky, "Slag-alkali concretes produced from fine-grained aggregate," *Kiev: Vishcha Shkolay*, 1981.

[9] J. L. Provis J. S. Van Deventer, *Alkali activated materials: state-of-the-art report, RILEM TC 224-AAM*. Springer Science & Business Media, 2013, vol. 13.

[10] X. Ke, S. A. Bernal, J. L. Provis, "Controlling the reaction kinetics of sodium carbonate-activated slag cements using calcined layered double hydroxides," *Cement and Concrete Research*, vol. 81, pp. 24–37, 2016.

[11] L. K. Turner F. G. Collins, "Carbon dioxide equivalent (CO_2—e) emissions: A comparison between geopolymer and OPC cement concrete," *Construction and Building Materials*, vol. 43, pp. 125–130, 2013.

[12] A. F. Abdalqader, F. Jin, A. Al-Tabbaa, "Development of greener alkali-activated cement: Utilisation of sodium carbonate for activating slag and fly ash mixtures," *Journal of Cleaner Production*, vol. 113, pp. 66–75, 2016.

[13] C. Shi, D. Roy, P. Krivenko, *Alkali-activated cements and concretes*. Taylor and Francis, 2006.

[14] R. Vinai M. Soutsos, "Production of sodium silicate powder from waste glass cullet for alkali activation of alternative binders," *Cement and Concrete Research*, vol. 116, pp. 45–56, 2019.

[15] A. Marcu, W. Stoefs, D. Belis, K. Tuokko, "Sectoral case study–soda ash: Climate for sustainable growth," 2015.

[16] T. Luukkonen, Z. Abdollahnejad, J. Yliniemi, P. Kinnunen, M. Illikainen, "One-part alkali-activated materials: A review," *Cement and Concrete Research*, vol. 103, pp. 21–34, 2018.

[17] J. Davidovits, *Geopolymer chemistry and applications*. Geopolymer Institute, 2008.

[18] A. Buchwald, "What are geopolymers? Current state of research and technology, the opportunities they offer, and their significance for the precast industry," *Betonwerk+ Fertigteil-Technik*, vol. 72, no. 7, 2006.

[19] K. De Weerdt, "Geopolymers–state of the art: FA 1 Environmentally friendly concrete: SP 1.1 Low carbon-footprint binder systems," 2011.

[20] J. Davidovits, "Calcium based geopolymer," *Geopolymer Chemistry and Applications, 3rd ed., Geopolymer Institute, Saint Quentin, France*, pp. 201–244, 2011.

[21] J. Davidovits, "Chemistry of geopolymeric systems, terminology," in *Geopolymer*, Geopolymer International Conference, vol. 99, 1999, pp. 9–39.

[22] D. Khale R. Chaudhary, "Mechanism of geopolymerization and factors influencing its development: A review," *Journal of Materials Science*, vol. 42, no. 3, pp. 729–746, 2007.

[23] V. Glukhovsky, G. Rostovskaja, G. Rumyna, "High strength slag-alkaline cements," in *Proceedings of the Seventh International Congress on the Chemistry of Cement*, vol. 3, 1980, pp. 164–8.

[24] A. Fernández-Jiménez, A. Palomo, M. Criado, "Microstructure development of alkali-activated fly ash cement: A descriptive model," *Cement and Concrete Research*, vol. 35, no. 6, pp. 1204–1209, 2005.

[25] A. Fernández-Jiménez, A. Palomo, I. Sobrados, J. Sanz, "The role played by the reactive alumina content in the alkaline activation of fly ashes," *Microporous and Mesoporous Materials*, vol. 91, no. 1-3, pp. 111–119, 2006.

[26] J. L. Provis, G. C. Lukey, J. S. van Deventer, "Do geopolymers actually contain nanocrystalline zeolites? A reexamination of existing results," *Chemistry of Materials*, vol. 17, no. 12, pp. 3075–3085, 2005.

[27] P. Duxson, A. Fernández-Jiménez, J. L. Provis, G. C. Lukey, A. Palomo, J. S. van Deventer, "Geopolymer technology: The current state of the art," *Journal of Materials Science*, vol. 42, no. 9, pp. 2917–2933, 2007.

[28] L. Tchadjie S. Ekolu, "Enhancing the reactivity of aluminosilicate materials toward geopolymer synthesis," *Journal of Materials Science*, vol. 53, no. 7, pp. 4709–4733, 2018.

[29] P. Awoyera A. Adesina, "A critical review on application of alkali activated slag as a sustainable composite binder," *Case Studies in Construction Materials*, vol. 11, e00268, 2019.

[30] J. L. Provis S. A. Bernal, "Geopolymers and related alkali-activated materials," *Annual Review of Materials Research*, vol. 44, pp. 299–327, 2014.

[31] S. D. Wang, X. C. Pu, K. Scrivener, P. Pratt, "Alkali-activated slag cement and concrete: A review of properties and problems," *Advances in Cement Research*, vol. 7, no. 27, pp. 93–102, 1995.

[32] A. Palomo, S. Alonso, A. Fernandez-Jiménez, I. Sobrados, J. Sanz, "Alkaline activation of fly ashes: NMR study of the reaction products," *Journal of the American Ceramic Society*, vol. 87, no. 6, pp. 1141–1145, 2004.

[33] A. Palomo, M. Grutzeck, M. Blanco, "Alkali-activated fly ashes: A cement for the future," *Cement and Concrete Research*, vol. 29, no. 8, pp. 1323–1329, 1999.

[34] A. Dakhane, *Multiscale Engineering Response of Alkali Activated Aluminosilicate Binders*. Arizona State University, 2016.

[35] I. B. Topcu M. U. Toprak, "Properties of geopolymer from circulating fluidized bed combustion coal bottom ash," *Materials Science and Engineering: A*, vol. 528, no. 3, pp. 1472–1477, 2011.

[36] H. Xu J. Van Deventer, "The geopolymerisation of alumino-silicate minerals," *International Journal of Mineral Processing*, vol. 59, no. 3, pp. 247–266, 2000.

[37] S. Kumar R. Kumar, "Mechanical activation of fly ash: Effect on reaction, structure and properties of resulting geopolymer," *Ceramics International*, vol. 37, no. 2, pp. 533–541, 2011.

[38] C. Heah, H. Kamarudin, A. M. Al Bakri, M. Bnhussain, M. Luqman, I. K. Nizar, C. Ruzaidi, Y. Liew, "Study on solids-to-liquid and alkaline activator ratios on kaolin-based geopolymers," *Construction and Building Materials*, vol. 35, pp. 912–922, 2012.

[39] K. Komnitsas D. Zaharaki, "Geopolymerisation: A review and prospects for the minerals industry," *Minerals Engineering*, vol. 20, no. 14, pp. 1261–1277, 2007.

[40] U. Rattanasak P. Chindaprasirt, "Influence of NaOH solution on the synthesis of fly ash geopolymer," *Minerals Engineering*, vol. 22, no. 12, pp. 1073–1078, 2009.

[41] A. Gharzouni, E. Joussein, B. Samet, S. Baklouti, S. Rossignol, "Effect of the reactivity of alkaline solution and metakaolin on geopolymer formation," *Journal of Non-Crystalline Solids*, vol. 410, pp. 127–134, 2015.

[42] U. G. Survey, *Mineral Commodity Summaries, 2009*. Government Printing Office, 2009.

[43] L. F. Cabeza, C. Barreneche, L. Miró, J. M. Morera, E. Bartolı, A. I. Fernández, "Low carbon and low embodied energy materials in buildings: A review," *Renewable and Sustainable Energy Reviews*, vol. 23, pp. 536–542, 2013.

[44] R. McCaffrey, "Climate change and the cement industry," *Global Cement and Lime Magazine (Environmental special issue)*, vol. 15, p. 19, 2002.

[45] C. Li, H. Sun, L. Li, "A review: The comparison between alkali-activated slag (Si + Ca) and metakaolin (Si + Al) cements," *Cement and Concrete Research*, vol. 40, no. 9, pp. 1341–1349, 2010.

[46] S. D. Wang K. L. Scrivener, "Hydration products of alkali activated slag cement," *Cement and Concrete Research*, vol. 25, no. 3, pp. 561–571, 1995.

[47] F. Puertas, M. Palacios, H. Manzano, J. Dolado, A. Rico, J. Rodrıguez, "A model for the C-A-S-H gel formed in alkali-activated slag cements," *Journal of the European Ceramic Society*, vol. 31, no. 12, pp. 2043–2056, 2011.

[48] P. Duxson J. L. Provis, "Designing precursors for geopolymer cements," *Journal of the American Ceramic Society*, vol. 91, no. 12, pp. 3864–3869, 2008.

[49] S. A. Bernal, "Advances in near-neutral salts activation of blast furnace slags," *RILEM Technical Letters*, vol. 1, pp. 39–44, 2016.

[50] A. Fernández-Jiménez, I. Garcıa-Lodeiro, A. Palomo, "Durability of alkali-activated fly ash cementitious materials," *Journal of Materials Science*, vol. 42, no. 9, pp. 3055–3065, 2007.

[51] S. A. Bernal, J. L. Provis, R. J. Myers, R. San Nicolas, J. S. van Deventer, "Role of carbonates in the chemical evolution of sodium carbonate-activated slag binders," *Materials and Structures*, vol. 48, no. 3, pp. 517–529, 2015.

[52] J. Temuujin, A. Van Riessen, R. Williams, "Influence of calcium compounds on the mechanical properties of fly ash geopolymer pastes," *Journal of Hazardous Materials*, vol. 167, no. 1-3, pp. 82–88, 2009.

[53] M. S. Kim, Y. Jun, C. Lee, J. E. Oh, "Use of CaO as an activator for producing a price-competitive non-cement structural binder using ground granulated blast furnace slag," *Cement and Concrete Research*, vol. 54, pp. 208–214, 2013.

[54] A. F. Abdalqader, F. Jin, A. Al-Tabbaa, "Characterisation of reactive magnesia and sodium carbonate-activated fly ash/slag paste blends," *Construction and Building Materials*, vol. 93, pp. 506–513, 2015.

[55] C. D. Atiş, C. Bilim, Ö. Çelik, O. Karahan, "Influence of activator on the strength and drying shrinkage of alkali-activated slag mortar," *Construction and Building Materials*, vol. 23, no. 1, pp. 548–555, 2009.

[56] Y. Li Y. Sun, "Preliminary study on combined-alkali–slag paste materials," *Cement and Concrete Research*, vol. 30, no. 6, pp. 963–966, 2000.

[57] F. Hogan J. Rose, "ASTM specification for ground iron blast furnace slag: Its development, use, and future," *ASTM International, West Conshohocken, Pennsylvania*, vol. 91, pp. 1551–1576, 1986.

[58] ASTM, "ASTM C1437-Standard test method for flow of hydraulic cement mortar," *ASTM International, West Conshohocken, Pennsylvania*, 2015.

[59] ASTM, "ASTM C191-Standard test method for time of setting of hydraulic cement by vicat needle," *ASTM International, West Conshohocken, Pennsylvania*, 1993.

[60] J. A. Grubb, H. S. Limaye, A. M. Kakade, "Testing ph of concrete," *Concrete international*, vol. 29, no. 4, pp. 78–83, 2007.

[61] C. Shi R. L. Day, "A calorimetric study of early hydration of alkali-slag cements," *Cement and Concrete Research*, vol. 25, no. 6, pp. 1333–1346, 1995.

[62] W. E. Federation, A. P. H. Association, *et al.*, "Standard methods for the examination of water and wastewater," *American Public Health Association (APHA): Washington, DC, USA*, 2005.

[63] M. Torres-Carrasco, C. Rodrıguez-Puertas, M. del Mar Alonso, F. Puertas, "Alkali activated slag cements using waste glass as alternative activators. rheological behaviour," *Boletın de la Sociedad Española de Ceramica y Vıdrio*, vol. 54, no. 2, pp. 45–57, 2015.

[64] S. J. Choi, J. I. Choi, J. K. Song, B. Y. Lee, "Rheological and mechanical properties of fiber-reinforced alkali-activated composite," *Construction and Building Materials*, vol. 96, pp. 112–118, 2015.

[65] H. Mehdizadeh E. N. Kani, "Rheology and apparent activation energy of alkali activated phosphorous slag," *Construction and Building Materials*, vol. 171, pp. 197–204, 2018.

[66] D. P. Bentz, C. F. Ferraris, S. Z. Jones, D. Lootens, F. Zunino, "Limestone and silica powder replacements for cement: Early-age performance," *Cement and Concrete Composites*, vol. 78, pp. 43–56, 2017.

[67] K. Vance, G. Sant, N. Neithalath, "The rheology of cementitious suspensions: A closer look at experimental parameters and property determination using common rheological models," *Cement and Concrete Composites*, vol. 59, pp. 38–48, 2015.

[68] S. G. Erzengin, K. Kaya, S. P. Özkorucuklu, V. Özdemir, G. Yıldırım, "The properties of cement systems superplasticized with methacrylic ester-based polycarboxylates," *Construction and Building Materials*, vol. 166, pp. 96–109, 2018.

[69] P. F. G. Banfill *et al.*, "The rheology of fresh cement and concrete-a review," in *Proceedings of the 11th International Cement Chemistry Congress*, vol. 1, 2003, pp. 50–62.

[70] ASTM, "ASTM C109-Standard test method for compressive strength of hydraulic cement mortars," *ASTM International, Philadelphia, PA*, 2008.

[71] E. W. Washburn, "The dynamics of capillary flow," *Physical Review*, vol. 17, no. 3, p. 273, 1921.

[72] A. Katz A. Thompson, "Quantitative prediction of permeability in porous rock," *Physical Review B*, vol. 34, no. 11, p. 8179, 1986.

[73] ASTM, "ASTM C596-Standard test method for drying shrinkage of mortar containing hydraulic cement," *ASTM International, West Conshohocken, Pennsylvania*, 2018.

[74] ASTM, "ASTM C1585-standard test method for measurement of rate of absorption of water by hydraulic-cement concretes," *ASTM International, West Conshohocken, Pennsylvania*, 2011.

[75] Nordtest, *NT BUILD 492-Concrete, mortar and cement-based repair materials: Chloride migration coefficient from non-steady-state migration experiments*, 1999.

[76] A. Fernández-Jiménez F. Puertas, "Setting of alkali-activated slag cement. influence of activator nature," *Advances in Cement Research*, vol. 13, no. 3, pp. 115–121, 2001.

[77] F. Collins J. G. Sanjayan, "Early age strength and workability of slag pastes activated by NaOH and Na_2CO_3," *Cement and Concrete Research*, vol. 28, no. 5, pp. 655–664, 1998.

[78] A. Fernández-Jiménez, F. Puertas, *et al.*, "Effect of activator mix on the hydration and strength behaviour of alkali-activated slag cements," *Advances in Cement Research*, vol. 15, no. 3, pp. 129–136, 2003.

[79] S. A. Bernal, R. San Nicolas, J. S. Van Deventer, J. L. Provis, “Alkali-activated slag cements produced with a blended sodium carbonate/sodium silicate activator,” *Advances in Cement Research*, vol. 28, no. 4, pp. 262–273, 2016.

[80] M. Kovtun, E. P. Kearsley, J. Shekhovtsova, “Chemical acceleration of a neutral granulated blast-furnace slag activated by sodium carbonate,” *Cement and concrete Research*, vol. 72, pp. 1–9, 2015.

[81] U. Avila-López, J. Almanza-Robles, J. Escalante-Garcıa, “Investigation of novel waste glass and limestone binders using statistical methods,” *Construction and Building Materials*, vol. 82, pp. 296–303, 2015.

[82] F. Jin A. Al-Tabbaa, “Strength and drying shrinkage of slag paste activated by sodium carbonate and reactive MgO,” *Construction and Building Materials*, vol. 81, pp. 58–65, 2015.

[83] K. H. Yang, A. R. Cho, J. K. Song, S. H. Nam, “Hydration products and strength development of calcium hydroxide-based alkali-activated slag mortars,” *Construction and Building Materials*, vol. 29, pp. 410–419, 2012.

[84] D. Jeon, Y. Jun, Y. Jeong, J. E. Oh, “Microstructural and strength improvements through the use of Na_2CO_3 in a cementless $Ca(OH)_2$-activated class f fly ash system,” *Cement and Concrete Research*, vol. 67, pp. 215–225, 2015.

[85] B. Yuan, Q. Yu, H. Brouwers, “Assessing the chemical involvement of limestone powder in sodium carbonate activated slag,” *Materials and Structures*, vol. 50, no. 2, p. 136, 2017.

[86] F. N. Santos, S. R. G. de Sousa, A. J. F. Bombard, S. L. Vieira, “Rheological study of cement paste with metakaolin and/or limestone filler using mixture design of experiments,” *Construction and Building Materials*, vol. 143, pp. 92–103, 2017.

[87] V. Živica, “Effects of type and dosage of alkaline activator and temperature on the properties of alkali-activated slag mixtures,” *Construction and Building Materials*, vol. 21, no. 7, pp. 1463–1469, 2007.

[88] B. Yuan, Q. Yu, H. Brouwers, “Reaction kinetics, reaction products and compressive strength of ternary activators activated slag designed by Taguchi method,” *Materials & Design*, vol. 86, pp. 878–886, 2015.

[89] A. R. Sakulich, E. Anderson, C. Schauer, M. W. Barsoum, “Mechanical and microstructural characterization of an alkali-activated slag/limestone fine aggregate concrete,” *Construction and Building Materials*, vol. 23, no. 8, pp. 2951–2957, 2009.

[90] T. Bakharev, J. G. Sanjayan, Y. B. Cheng, “Alkali activation of Australian slag cements,” *Cement and Concrete Research*, vol. 29, no. 1, pp. 113–120, 1999.

[91] A. Fernández-Jiménez, J. Palomo, F. Puertas, “Alkali-activated slag mortars: Mechanical strength behaviour,” *Cement and Concrete Research*, vol. 29, no. 8, pp. 1313–1321, 1999.

[92] B. Yuan, Q. Yu, H. Brouwers, “Time-dependent characterization of Na_2CO_3 activated slag,” *Cement and Concrete Composites*, vol. 84, pp. 188–197, 2017.

[93] D. Rajesh, A. Narender Reddy, U. Venkata Tilak, M. Raghavendra, "Performance of alkali activated slag with various alkali activators," *International Journal of Innovative Research in Science, Engineering and Technology*, vol. 2, no. 2, pp. 378–86, 2013.

[94] S. Alonso A. Palomo, "Alkaline activation of metakaolin and calcium hydroxide mixtures: Influence of temperature, activator concentration and solids ratio," *Materials Letters*, vol. 47, no. 1-2, pp. 55–62, 2001.

[95] S. Song H. M. Jennings, "Pore solution chemistry of alkali-activated ground granulated blast-furnace slag," *Cement and Concrete Research*, vol. 29, no. 2, pp. 159–170, 1999.

[96] R. Chang *et al.*, *General chemistry: the essential concepts*. Boston: McGraw-Hill, 2008.

[97] M. L. Granizo, S. Alonso, M. T. Blanco-Varela, A. Palomo, "Alkaline activation of metakaolin: Effect of calcium hydroxide in the products of reaction," *Journal of the American Ceramic Society*, vol. 85, no. 1, pp. 225–231, 2002.

[98] B. Yuan, Q. Yu, H. Brouwers, "Evaluation of slag characteristics on the reaction kinetics and mechanical properties of Na_2CO_3 activated slag," *Construction and Building Materials*, vol. 131, pp. 334–346, 2017.

[99] A. Behnood, K. Van Tittelboom, N. De Belie, "Methods for measuring ph in concrete: A review," *Construction and Building Materials*, vol. 105, pp. 176–188, 2016.

[100] H. Konno, Y. Nanri, M. Kitamura, "Crystallization of aragonite in the causticizing reaction," *Powder Technology*, vol. 123, no. 1, pp. 33–39, 2002.

[101] A. Kashani, J. L. Provis, G. G. Qiao, J. S. van Deventer, "The interrelationship between surface chemistry and rheology in alkali activated slag paste," *Construction and Building Materials*, vol. 65, pp. 583–591, 2014.

[102] A. Vollpracht, B. Lothenbach, R. Snellings, J. Haufe, "The pore solution of blended cements: A review," *Materials and Structures*, vol. 49, no. 8, pp. 3341–3367, 2016.

[103] F. Puertas, C. Varga, M. Alonso, "Rheology of alkali-activated slag pastes. effect of the nature and concentration of the activating solution," *Cement and Concrete Composites*, vol. 53, pp. 279–288, 2014.

[104] S. H. Kang, S. G. Hong, J. Moon, "Absorption kinetics of superabsorbent polymers (SAP) in various cement-based solutions," *Cement and Concrete Research*, vol. 97, pp. 73–83, 2017.

[105] B. Akturk, A. B. Kizilkanat, N. Kabay, "Effect of calcium hydroxide on fresh state behavior of sodium carbonate activated blast furnace slag pastes," *Construction and Building Materials*, vol. 212, pp. 388–399, 2019.

[106] H. Xu, J. L. Provis, J. S. van Deventer, P. V. Krivenko, "Characterization of aged slag concretes," *ACI Materials Journal*, vol. 105, no. 2, p. 131, 2008.

[107] J. L. Bischoff, D. B. Herbst, R. J. Rosenbauer, "Gaylussite formation at Mono Lake, California," *Geochimica et Cosmochimica Acta*, vol. 55, no. 6, pp. 1743–1747, 1991.

[108] Y. Jeong, J. E. Oh, Y. Jun, J. Park, J.-h. Ha, S. G. Sohn, "Influence of four additional activators on hydrated-lime [$Ca(OH)_2$] activated ground granulated blast-furnace slag," *Cement and Concrete Composites*, vol. 65, pp. 1–10, 2016.

[109] T. Bakharev, J. G. Sanjayan, Y. B. Cheng, "Effect of admixtures on properties of alkali-activated slag concrete," *Cement and Concrete Research*, vol. 30, no. 9, pp. 1367–1374, 2000.

[110] F. Puertas M. Torres-Carrasco, "Use of glass waste as an activator in the preparation of alkali-activated slag. Mechanical strength and paste characterisation," *Cement and Concrete Research*, vol. 57, pp. 95–104, 2014.

[111] Y. Yi, M. Liska, A. Al-Tabbaa, "Properties and microstructure of ggbs–magnesia pastes," *Advances in Cement Research*, vol. 26, no. 2, pp. 114–122, 2014.

[112] B. Yuan, C. Straub, S. Segers, Q. Yu, H. Brouwers, "Sodium carbonate activated slag as cement replacement in autoclaved aerated concrete," *Ceramics International*, vol. 43, no. 8, pp. 6039–6047, 2017.

[113] J. Wang, X. Lyu, L. Wang, X. Cao, Q. Liu, H. Zang, "Influence of the combination of calcium oxide and sodium carbonate on the hydration reactivity of alkali-activated slag binders," *Journal of Cleaner Production*, vol. 171, pp. 622–629, 2018.

[114] A. M. Rashad, S. R. Zeedan, A. A. Hassan, "Influence of the activator concentration of sodium silicate on the thermal properties of alkali-activated slag pastes," *Construction and Building Materials*, vol. 102, pp. 811–820, 2016.

[115] R. Martinez-Lopez J. I. Escalante-Garcia, "Alkali activated composite binders of waste silica soda lime glass and blast furnace slag: Strength as a function of the composition," *Construction and Building Materials*, vol. 119, pp. 119–129, 2016.

[116] K. Gu, F. Jin, A. Al-Tabbaa, B. Shi, J. Liu, "Mechanical and hydration properties of ground granulated blastfurnace slag pastes activated with MgO–CaO mixtures," *Construction and Building Materials*, vol. 69, pp. 101–108, 2014.

[117] M. B. Haha, G. Le Saout, F. Winnefeld, B. Lothenbach, "Influence of activator type on hydration kinetics, hydrate assemblage and microstructural development of alkali activated blast-furnace slags," *Cement and Concrete Research*, vol. 41, no. 3, pp. 301–310, 2011.

[118] J. I. Escalante-Garcıa, A. F. Fuentes, A. Gorokhovsky, P. E. Fraire-Luna, G. Mendoza-Suarez, "Hydration products and reactivity of blast-furnace slag activated by various alkalis," *Journal of the American Ceramic Society*, vol. 86, no. 12, pp. 2148–2153, 2003.

[119] M. B. Haha, B. Lothenbach, G. Le Saout, F. Winnefeld, "Influence of slag chemistry on the hydration of alkali-activated blast-furnace slag—part II: Effect of Al_2O_3," *Cement and Concrete Research*, vol. 42, no. 1, pp. 74–83, 2012.

[120] C. Shi R. L. Day, "Pozzolanic reaction in the presence of chemical activators: Part II—reaction products and mechanism," *Cement and Concrete Research*, vol. 30, no. 4, pp. 607–613, 2000.

[121] S. A. Bernal, J. L. Provis, V. Rose, R. M. de Gutiérrez, "High-resolution x-ray diffraction and fluorescence microscopy characterization of alkali-activated slag-metakaolin binders," *Journal of the American Ceramic Society*, vol. 96, no. 6, pp. 1951–1957, 2013.

[122] U. Sikander, S. Sufian, M. Salam, "A review of hydrotalcite based catalysts for hydrogen production systems," *International Journal of Hydrogen Energy*, vol. 42, no. 31, pp. 19 851–19 868, 2017.

[123] P. Yu, R. J. Kirkpatrick, B. Poe, P. F. McMillan, X. Cong, "Structure of calcium silicate hydrate (C-S-H): Near-, mid-, and far-infrared spectroscopy," *Journal of the American Ceramic Society*, vol. 82, no. 3, pp. 742–748, 1999.

[124] F. Puertas A. Fernández-Jiménez, "Mineralogical and microstructural characterisation of alkali-activated fly ash/slag pastes," *Cement and Concrete composites*, vol. 25, no. 3, pp. 287–292, 2003.

[125] B. S. Gebregziabiher, R. Thomas, S. Peethamparan, "Very early-age reaction kinetics and microstructural development in alkali-activated slag," *Cement and Concrete Composites*, vol. 55, pp. 91–102, 2015.

[126] M. O. Yusuf, M. A. M. Johari, Z. A. Ahmad, M. Maslehuddin, "Effects of addition of $Al(OH)_3$ on the strength of alkaline activated ground blast furnace slag-ultrafine palm oil fuel ash (AAGU) based binder," *Construction and Building Materials*, vol. 50, pp. 361–367, 2014.

[127] D. R. Johnson W. A. Robb, "Gaylussite: Thermal properties by simultaneous thermal analysis," *American Mineralogist: Journal of Earth and Planetary Materials*, vol. 58, no. 7-8, pp. 778–784, 1973.

[128] J. M. Richardson, J. J. Biernacki, P. E. Stutzman, D. P. Bentz, "Stoichiometry of slag hydration with calcium hydroxide," *Journal of the American Ceramic Society*, vol. 85, no. 4, pp. 947–953, 2002.

[129] S. D. Wang K. L. Scrivener, "29Si and 27Al NMR study of alkali-activated slag," *Cement and Concrete Research*, vol. 33, no. 5, pp. 769–774, 2003.

[130] R. R. Lloyd, J. L. Provis, J. S. Van Deventer, "Pore solution composition and alkali diffusion in inorganic polymer cement," *Cement and Concrete Research*, vol. 40, no. 9, pp. 1386–1392, 2010.

[131] F. Puertas, S. Martınez-Ramırez, S. Alonso, T. Vazquez, "Alkali-activated fly ash/slag cements: Strength behaviour and hydration products," *Cement and Concrete Research*, vol. 30, no. 10, pp. 1625–1632, 2000.

[132] J. Dweck, P. Ferreira da Silva, P. Büchler, F. Cartledge, "Study by thermogravimetry of the evolution of ettringite phase during type II portland cement hydration," *Journal of Thermal Analysis and Calorimetry*, vol. 69, no. 1, pp. 179–186, 2002.

[133] P. Parashar, V. Sharma, D. D. Agarwal, N. Richhariya, "Rapid synthesis of hydrotalcite with high antacid activity," *Materials Letters*, vol. 74, pp. 93–95, 2012.

[134] A. M. Al Bakri, H. Kamarudin, M. Bnhussain, I. K. Nizar, A. Rafiza, Y. Zarina, "Microstructure of different NaOH molarity of fly ash-based green polymeric cement," *Journal of Engineering and Technology Research*, vol. 3, no. 2, pp. 44–49, 2011.

[135] H. Zhao D. Darwin, "Quantitative backscattered electron analysis of cement paste," *Cement and Concrete Research*, vol. 22, no. 4, pp. 695–706, 1992.

[136] S. Feng, P. Wang, X. Liu, "SEM-backscattered electron imaging and image processing for evaluation of unhydrated cement volume fraction in slag blended portland cement pastes," *Journal of Wuhan University of Technology-Mater. Sci. Ed.*, vol. 28, no. 5, pp. 968–972, 2013.

[137] M. Z. Bazant Z. P. Bažant, "Theory of sorption hysteresis in nanoporous solids: Part II molecular condensation," *Journal of the Mechanics and Physics of Solids*, vol. 60, no. 9, pp. 1660–1675, 2012.

[138] N. De Belie, J. Kratky, S. Van Vlierberghe, "Influence of pozzolans and slag on the microstructure of partially carbonated cement paste by means of water vapour and nitrogen sorption experiments and bet calculations," *Cement and Concrete Research*, vol. 40, no. 12, pp. 1723–1733, 2010.

[139] S. Das, D. Stone, D. Convey, N. Neithalath, "Pore-and micro-structural characterization of a novel structural binder based on iron carbonation," *Materials Characterization*, vol. 98, pp. 168–179, 2014.

[140] H. Y. Moon, H. S. Kim, D. S. Choi, "Relationship between average pore diameter and chloride diffusivity in various concretes," *Construction and Building Materials*, vol. 20, no. 9, pp. 725–732, 2006.

[141] V. Sánchez-Fajardo, M. Torres, A. Moreno, "Study of the pore structure of the lightweight concrete block with lapilli as an aggregate to predict the liquid permeability by dielectric spectroscopy," *Construction and Building Materials*, vol. 53, pp. 225–234, 2014.

[142] S. Carniglia, "Construction of the tortuosity factor from porosimetry," *Journal of Catalysis*, vol. 102, no. 2, pp. 401–418, 1986.

[143] W. M. Kriven J. L. Bell, "Effect of alkali choice on geopolymer properties," in *28th International Conference on Advanced Ceramics and Composites B: Ceramic Engineering and Science Proceedings*, vol. 25, 2008, pp. 99–104.

[144] J. Rouquerol, D. Avnir, C. Fairbridge, D. Everett, J. Haynes, N. Pernicone, J. Ramsay, K. Sing, K. Unger, "Recommendations for the characterization of porous solids (technical report)," *Pure and Applied Chemistry*, vol. 66, no. 8, pp. 1739–1758, 1994.

[145] Y. Ma, J. Hu, G. Ye, "The pore structure and permeability of alkali activated fly ash," *Fuel*, vol. 104, pp. 771–780, 2013.

[146] F. Collins J. G. Sanjayan, "Effect of pore size distribution on drying shrinking of alkali-activated slag concrete," *Cement and Concrete Research*, vol. 30, no. 9, pp. 1401–1406, 2000.

[147] Z. Pan, J. G. Sanjayan, B. V. Rangan, "Fracture properties of geopolymer paste and concrete," *Magazine of Concrete Research*, vol. 63, no. 10, pp. 763–771, 2011.

[148] B. Sabir, S. Wild, M. Asili, "On the tortuosity of the fracture surface in concrete," *Cement and Concrete Research*, vol. 27, no. 5, pp. 785–795, 1997.

[149] N. Ranjbar, S. Talebian, M. Mehrali, C. Kuenzel, H. S. C. Metselaar, M. Z. Jumaat, "Mechanisms of interfacial bond in steel and polypropylene fiber reinforced geopolymer composites," *Composites Science and Technology*, vol. 122, pp. 73–81, 2016.

[150] A. Natali, S. Manzi, M. Bignozzi, "Novel fiber-reinforced composite materials based on sustainable geopolymer matrix," *Procedia engineering*, vol. 21, pp. 1124–1131, 2011.

[151] Z. Yunsheng, S. Wei, L. Zongjin, Z. Xiangming, C. Chungkong, *et al.*, "Impact properties of geopolymer based extrudates incorporated with fly ash and pva short fiber," *Construction and Building Materials*, vol. 22, no. 3, pp. 370–383, 2008.

[152] B. Nematollahi, J. Sanjayan, F. U. A. Shaikh, "Comparative deflection hardening behavior of short fiber reinforced geopolymer composites," *Construction and Building Materials*, vol. 70, pp. 54–64, 2014.

[153] Z. Chen, Y. Yang, Y. Yao, "Quasi-static and dynamic compressive mechanical properties of engineered cementitious composite incorporating ground granulated blast furnace slag," *Materials & Design*, vol. 44, pp. 500–508, 2013.

[154] S. F. U. Ahmed Z. Ronnie, "Ductile behavior of polyethylene fibre reinforced geopolymer composite," in *MATEC Web of Conferences*, EDP Sciences, vol. 97, 2017, p. 01 047.

[155] D. P. Dias C. Thaumaturgo, "Fracture toughness of geopolymeric concretes reinforced with basalt fibers," *Cement and Concrete Composites*, vol. 27, no. 1, pp. 49–54, 2005.

[156] T. Alomayri, F. Shaikh, I. Low, "Characterisation of cotton fibre-reinforced geopolymer composites," *Composites Part B: Engineering*, vol. 50, pp. 1–6, 2013.

[157] H. Assaedi, F. Shaikh, I. M. Low, "Influence of mixing methods of nano silica on the microstructural and mechanical properties of flax fabric reinforced geopolymer composites," *Construction and Building Materials*, vol. 123, pp. 541–552, 2016.

[158] X. Gao, Q. Yu, R. Yu, H. Brouwers, "Evaluation of hybrid steel fiber reinforcement in high performance geopolymer composites," *Materials and Structures*, vol. 50, no. 2, p. 165, 2017.

[159] N. Ganesan, R. Abraham, S. D. Raj, "Durability characteristics of steel fibre reinforced geopolymer concrete," *Construction and Building Materials*, vol. 93, pp. 471–476, 2015.

[160] P. S. Ambily, K. Ravisankar, C. Umarani, J. K. Dattatreya, N. R. Iyer, "Development of ultra-high-performance geopolymer concrete," *Magazine of Concrete Research*, vol. 66, no. 2, pp. 82–89, 2014.

[161] T. S. Ng, A. Amin, S. J. Foster, "The behaviour of steel-fibre-reinforced geopolymer concrete beams in shear," *Magazine of Concrete Research*, vol. 65, no. 5, pp. 308–318, 2013.

[162] N. Ranjbar, M. Mehrali, M. Mehrali, U. J. Alengaram, M. Z. Jumaat, "High tensile strength fly ash based geopolymer composite using copper coated micro steel fiber," *Construction and Building Materials*, vol. 112, pp. 629–638, 2016.

[163] A. Bhutta, M. Farooq, C. Zanotti, N. Banthia, "Pull-out behavior of different fibers in geopolymer mortars: Effects of alkaline solution concentration and curing," *Materials and Structures*, vol. 50, no. 1, p. 80, 2017.

[164] F. Puertas, T. Amat, A. Fernández-Jiménez, T. Vázquez, "Mechanical and durable behaviour of alkaline cement mortars reinforced with polypropylene fibres," *Cement and Concrete Research*, vol. 33, no. 12, pp. 2031–2036, 2003.

[165] A. Bhutta, P. H. Borges, C. Zanotti, M. Farooq, N. Banthia, "Flexural behavior of geopolymer composites reinforced with steel and polypropylene macro fibers," *Cement and Concrete Composites*, vol. 80, pp. 31–40, 2017.

[166] A. Beglarigale, S. Aydın, C. Kızılırmak, "Fiber-matrix bond characteristics of alkali-activated slag cement–based composites," *Journal of Materials in Civil Engineering*, vol. 28, no. 11, p. 04 016 133, 2016.

[167] M. M. Hilles M. M. Ziara, "Mechanical behavior of high strength concrete reinforced with glass fiber," *Engineering Science and Technology, an International Journal*, 2019.

[168] E. T. Dawood M. Ramli, "High strength characteristics of cement mortar reinforced with hybrid fibres," *Construction and Building Materials*, vol. 25, no. 5, pp. 2240–2247, 2011.

[169] I. B. Topcu M. Canbaz, "Effect of different fibers on the mechanical properties of concrete containing fly ash," *Construction and Building Materials*, vol. 21, no. 7, pp. 1486–1491, 2007.

[170] K. G. Kuder, N. Ozyurt, E. B. Mu, S. P. Shah, "Rheology of fiber-reinforced cementitious materials," *Cement and Concrete Research*, vol. 37, no. 2, pp. 191–199, 2007.

[171] A. A. Belkadi, S. Aggoun, C. Amouri, A. Geuttala, H. Houari, "Effect of vegetable and synthetic fibers on mechanical performance and durability of metakaolin-based mortars," *Journal of Adhesion Science and Technology*, vol. 32, no. 15, pp. 1670–1686, 2018.

[172] H. Nguyen, V. Carvelli, E. Adesanya, P. Kinnunen, M. Illikainen, "High performance cementitious composite from alkali-activated ladle slag reinforced with polypropylene fibers," *Cement and Concrete Composites*, vol. 90, pp. 150–160, 2018.

[173] J.-Y. Wang, N. Banthia, M.-H. Zhang, "Effect of shrinkage reducing admixture on flexural behaviors of fiber reinforced cementitious composites," *Cement and Concrete Composites*, vol. 34, no. 4, pp. 443–450, 2012.

[174] B. Akturk, S. Nayak, S. Das, A. B. Kizilkanat, "Microstructure and strength development of sodium carbonate–activated blast furnace slags," *Journal of Materials in Civil Engineering*, vol. 31, no. 11, p. 04 019 283, 2019.

[175] S. Xu H. W. Reinhardt, "A simplified method for determining double-k fracture parameters for three-point bending tests," *International Journal of Fracture*, vol. 104, no. 2, pp. 181–209, 2000.

[176] A. B. Kizilkanat, N. Kabay, V. Akyüncü, S. Chowdhury, A. H. Akça, "Mechanical properties and fracture behavior of basalt and glass fiber reinforced concrete: An experimental study," *Construction and Building Materials*, vol. 100, pp. 218–224, 2015.

[177] Z. Zhao, S. H. Kwon, S. P. Shah, “Effect of specimen size on fracture energy and softening curve of concrete: Part i. experiments and fracture energy,” *Cement and Concrete Research*, vol. 38, no. 8-9, pp. 1049–1060, 2008.

[178] D. Y. Yoo, G. Zi, S. T. Kang, Y. S. Yoon, “Biaxial flexural behavior of ultra-high-performance fiber-reinforced concrete with different fiber lengths and placement methods,” *Cement and Concrete Composites*, vol. 63, pp. 51–66, 2015.

[179] T. Alomayri, F. Shaikh, I. M. Low, “Synthesis and mechanical properties of cotton fabric reinforced geopolymer composites,” *Composites Part B: Engineering*, vol. 60, pp. 36–42, 2014.

[180] A. Noushini, M. Hastings, A. Castel, F. Aslani, “Mechanical and flexural performance of synthetic fibre reinforced geopolymer concrete,” *Construction and Building Materials*, vol. 186, pp. 454–475, 2018.

[181] F. U. A. Shaikh, “Review of mechanical properties of short fibre reinforced geopolymer composites,” *Construction and Building Materials*, vol. 43, pp. 37–49, 2013.

[182] P. Sukontasukkul, W. Pomchiengpin, S. Songpiriyakij, “Post-crack (or post-peak) flexural response and toughness of fiber reinforced concrete after exposure to high temperature,” *Construction and Building Materials*, vol. 24, no. 10, pp. 1967–1974, 2010.

[183] P. Sukontasukkul, P. Pongsopha, P. Chindaprasirt, S. Songpiriyakij, “Flexural performance and toughness of hybrid steel and polypropylene fibre reinforced geopolymer,” *Construction and Building Materials*, vol. 161, pp. 37–44, 2018.

[184] Y. Şahin F. Köksal, “The influences of matrix and steel fibre tensile strengths on the fracture energy of high-strength concrete,” *Construction and Building Materials*, vol. 25, no. 4, pp. 1801–1806, 2011.

[185] Y. Ding Y.-L. Bai, “Fracture properties and softening curves of steel fiber-reinforced slag-based geopolymer mortar and concrete,” *Materials*, vol. 11, no. 8, p. 1445, 2018.

[186] S. Xu H. W. Reinhardt, “Determination of double-K criterion for crack propagation in quasi-brittle fracture, part I: Experimental investigation of crack propagation,” *International Journal of Fracture*, vol. 98, no. 2, pp. 111–149, 1999.

[187] S. Xu H. W. Reinhardt, “Determination of double-K criterion for crack propagation in quasi-brittle fracture, part II: Analytical evaluating and practical measuring methods for three-point bending notched beams,” *International Journal of Fracture*, vol. 98, no. 2, pp. 151–177, 1999.

[188] ASTM, “ASTM C1018-Standard test method for flexural toughness and first-crack strength of fiber-reinforced concrete (using beam with third-point loading,” *ASTM International, West Conshohocken, Pennsylvania*, 1997.

[189] B. Nematollahi, J. Sanjayan, F. U. A. Shaikh, “Matrix design of strain hardening fiber reinforced engineered geopolymer composite,” *Composites Part B: Engineering*, vol. 89, pp. 253–265, 2016.

[190] M. Z. N. Khan, Y. Hao, H. Hao, F. U. A. Shaikh, "Mechanical properties of ambient cured high strength hybrid steel and synthetic fibers reinforced geopolymer composites," *Cement and Concrete Composites*, vol. 85, pp. 133–152, 2018.

[191] H. Šimonová, L. Topolář, P. Schmid, Z. Keršner, P. Rovnanık, "Fracture response of alkali-activated slag mortars reinforced by carbon fibres," in *IOP Conference Series: Materials Science and Engineering*, IOP Publishing, vol. 379, 2018, p. 012 027.

[192] S. Kumar S. Barai, "Determining double-K fracture parameters of concrete for compact tension and wedge splitting tests using weight function," *Engineering Fracture Mechanics*, vol. 76, no. 7, pp. 935–948, 2009.

[193] B. Marchese G. Marchese, "Fibre pullout-microstructural relationships for cementitious mortars," *Journal of materials science letters*, vol. 12, no. 20, pp. 1592–1595, 1993.

[194] A. Özodabaş K. Yılmaz, "Improvement of the performance of alkali activated blast furnace slag mortars with very finely ground pumice," *Construction and Building Materials*, vol. 48, pp. 26–34, 2013.

[195] H. Ye A. Radlińska, "Shrinkage mechanisms of alkali-activated slag," *Cement and Concrete Research*, vol. 88, pp. 126–135, 2016.

[196] A. A. M. Neto, M. A. Cincotto, W. Repette, "Drying and autogenous shrinkage of pastes and mortars with activated slag cement," *Cement and Concrete Research*, vol. 38, no. 4, pp. 565–574, 2008.

[197] B. Mithun M. Narasimhan, "Performance of alkali activated slag concrete mixes incorporating copper slag as fine aggregate," *Journal of Cleaner Production*, vol. 112, pp. 837–844, 2016.

[198] M. Heikal, M. Nassar, G. El-Sayed, S. Ibrahim, "Physico-chemical, mechanical, microstructure and durability characteristics of alkali activated egyptian slag," *Construction and Building Materials*, vol. 69, pp. 60–72, 2014.

[199] W. G. Valencia Saavedra, D. E. Angulo, R. Mejia de Gutierrez, "Fly ash slag geopolymer concrete: Resistance to sodium and magnesium sulfate attack," *Journal of Materials in Civil Engineering*, vol. 28, no. 12, p. 04 016 148, 2016.

[200] R. Thomas, E. Ariyachandra, D. Lezama, S. Peethamparan, "Comparison of chloride permeability methods for alkali-activated concrete," *Construction and Building Materials*, vol. 165, pp. 104–111, 2018.

[201] D. Bondar, Q. Ma, M. Soutsos, M. Basheer, J. L. Provis, S. Nanukuttan, "Alkali activated slag concretes designed for a desired slump, strength and chloride diffusivity," *Construction and Building Materials*, vol. 190, pp. 191–199, 2018.

[202] M. Babaee A. Castel, "Chloride diffusivity, chloride threshold, and corrosion initiation in reinforced alkali-activated mortars: Role of calcium, alkali, and silicate content," *Cement and Concrete Research*, vol. 111, pp. 56–71, 2018.

[203] J. Zhang, C. Shi, Z. Zhang, Z. Ou, "Durability of alkali-activated materials in aggressive environments: A review on recent studies," *Construction and Building Materials*, vol. 152, pp. 598–613, 2017.

[204] I. Ismail, S. A. Bernal, J. L. Provis, R. San Nicolas, D. G. Brice, A. R. Kilcullen, S. Hamdan, J. S. van Deventer, "Influence of fly ash on the water and chloride permeability of alkali-activated slag mortars and concretes," *Construction and Building Materials*, vol. 48, pp. 1187–1201, 2013.

[205] J. L. Provis, R. J. Myers, C. E. White, V. Rose, J. S. Van Deventer, "X-ray microtomography shows pore structure and tortuosity in alkali-activated binders," *Cement and Concrete Research*, vol. 42, no. 6, pp. 855–864, 2012.

[206] H. A. Alcamand, P. H. Borges, F. A. Silva, A. C. C. Trindade, "The effect of matrix composition and calcium content on the sulfate durability of metakaolin and metakaolin/slag alkali-activated mortars," *Ceramics International*, vol. 44, no. 5, pp. 5037–5044, 2018.

[207] A. Abdalqader, F. Jin, A. Al-Tabbaa, "Performance of magnesia-modified sodium carbonate-activated slag/fly ash concrete," *Cement and Concrete Composites*, vol. 103, pp. 160–174, 2019.

[208] X. Ke, S. A. Bernal, O. H. Hussein, J. L. Provis, "Chloride binding and mobility in sodium carbonate-activated slag pastes and mortars," *Materials and Structures*, vol. 50, no. 6, p. 252, 2017.

[209] Z. Jiao, Y. Wang, W. Zheng, W. Huang, "Effect of dosage of sodium carbonate on the strength and drying shrinkage of sodium hydroxide based alkali-activated slag paste," *Construction and Building Materials*, vol. 179, pp. 11–24, 2018.

[210] F. Matalkah, T. Salem, M. Shaafaey, P. Soroushian, "Drying shrinkage of alkali activated binders cured at room temperature," *Construction and Building Materials*, vol. 201, pp. 563–570, 2019.

[211] Z. P. Bazant, *Mathematical modeling of creep and shrinkage of concrete*. Wiley, 1988.

[212] T. Häkkinen, "The influence of slag content on the microstructure, permeability and mechanical properties of concrete part 1-microstructural studies and basic mechanical properties," *Cement and Concrete Research*, vol. 23, no. 2, pp. 407–421, 1993.

[213] D. W. Law, A. A. Adam, T. K. Molyneaux, I. Patnaikuni, "Durability assessment of alkali activated slag (AAS) concrete," *Materials and Structures*, vol. 45, no. 9, pp. 1425–1437, 2012.

[214] N. Neithalath, "Analysis of moisture transport in mortars and concrete using sorption-diffusion approach," *ACI Materials Journal*, vol. 103, no. 3, p. 209, 2006.

[215] D. Ravikumar N. Neithalath, "An electrical impedance investigation into the chloride ion transport resistance of alkali silicate powder activated slag concretes," *Cement and Concrete Composites*, vol. 44, pp. 58–68, 2013.

[216] J. Miranda, A. Fernández-Jiménez, J. González, A. Palomo, "Corrosion resistance in activated fly ash mortars," *Cement and Concrete Research*, vol. 35, no. 6, pp. 1210–1217, 2005.

[217] K. Kannapiran, T. Sujatha, S. Nagan, "Resistance of reinforced geopolymer concrete beams to acid and chloride migration," *Asian Journal of Civil Engineering*, vol. 14, no. 2, pp. 225–238, 2013.

[218] K. Kupwade-Patil E. N. Allouche, “Examination of chloride-induced corrosion in reinforced geopolymer concretes,” *Journal of Materials in Civil Engineering*, vol. 25, no. 10, pp. 1465–1476, 2012.

[219] K. Arbi, M. Nedeljkovic, Y. Zuo, G. Ye, “A review on the durability of alkali-activated fly ash/slag systems: Advances, issues, and perspectives,” *Industrial & Engineering Chemistry Research*, vol. 55, no. 19, pp. 5439–5453, 2016.

[220] D. W. Law, A. A. Adam, T. K. Molyneaux, I. Patnaikuni, A. Wardhono, “Long term durability properties of class F fly ash geopolymer concrete,” *Materials and Structures*, vol. 48, no. 3, pp. 721–731, 2015.

[221] N. Lee H.-K. Lee, “Influence of the slag content on the chloride and sulfuric acid resistances of alkali-activated fly ash/slag paste,” *Cement and Concrete Composites*, vol. 72, pp. 168–179, 2016.

[222] M. Romagnoli, P. Sassatelli, M. L. Gualtieri, G. Tari, “Rheological characterization of fly ash-based suspensions,” *Construction and Building Materials*, vol. 65, pp. 526–534, 2014.

[223] Z. R. Lazic, *Design of experiments in chemical engineering: a practical guide*. John Wiley & Sons, 2006.

A Tables

Table A.1 Flow diameter (mm) of NCAS and OPC-based mixes

Mixes	0 min	30 min	60 min	90 min
NC100-6	213	157	150	145
NC80-6	218	200	185	170
NC60-6	220	215	200	190
LNC100-6	190	140	123	120
LNC80-6	193	180	170	155
LNC60-6	203	188	173	158
NC100-10	210	200	180	165
NC80-10	220	200	185	185
NC60-10	225	210	195	190
LNC100-10	198	175	155	145
LNC80-10	203	185	170	155
LNC60-10	220	210	190	185
OPC	233	2154	210	200

Table A.2 Flow loss (%) of NCAS and OPC-based mixes

Mixes	30 min	60 min	90 min
NC100-6	26.3	29.6	31.9
NC80-6	8.3	15.1	22.0
NC60-6	2.3	9.1	13.6
LNC100-6	26.3	35.3	36.8
LNC80-6	6.7	11.9	19.7
LNC60-6	7.4	14.8	22.2
NC100-10	4.8	14.3	21.4
NC80-10	9.1	15.9	15.9
NC60-10	6.7	13.3	15.6
LNC100-10	11.6	21.7	26.8
LNC80-10	8.9	16.3	23.6
LNC60-10	4.5	13.6	15.9
OPC	7.7	9.9	14.2

Table A.3 Setting values (min) of NCAS and OPC-based mixes

Mixes	t_{ini}	t_{final}	t_{set}
NC100-6	720	1440	720
NC80-6	675	1140	465
NC60-6	1470	1800	330
LNC100-6	210	390	180
LNC80-6	240	480	240
LNC60-6	330	570	240
NC100-10	650	1250	600
NC80-10	540	960	420
NC60-10	1500	1860	360
LNC100-10	300	450	150
LNC80-10	450	660	210
LNC60-10	375	960	585
OPC	210	300	90

Table A.4 pH values of NCAS and OPC-based mixes

Mixes	**30 min**	**90 min**	**180 min**
NC100-6	13.2	13.2	NA*
NC80-6	13.2	NM*	13.3
NC60-6	13.4	NM	13.4
LNC100-6	13.3	NA	NA
LNC80-6	13.2	13.2	NA
LNC60-6	13.5	13.6	NA
NC100-10	13.2	NM	13.4
NC80-10	13.5	NM	13.5
NC60-10	13.7	NM	13.8
LNC100-10	13.4	NM	13.5
LNC80-10	13.6	NM	13.5
LNC60-10	13.7	NM	13.8

NA:Not avaliable; NM*: Not measured*

Table A.5 Carbonate concentration (mg/l) of mixes

Mixes	30 min	90 min	180 min
NC100-6	40,000	30,000	NA*
NC80-6	37,333	30,000	30,000
NC60-6	29,000	29,000	NA
LNC100-6	20,000	NA	NA
LNC80-6	16,000	13,667	NA
LNC60-6	17,000	10,500	NA
NC100-10	74,667	NM*	41,000
NC80-10	91,000	NM	68,500
NC60-10	104,000	NM	69,000
LNC100-10	54,500	NM	36,000
LNC80-10	67,083	NM	53,500
LNC60-10	99,667	NM	58,667

NA: Not avaliable; NM*: Not measured*

Table A.6 YS (Pa) values of NCAS and OPC-based mixes

Mixes	0 min	60 min	120 min
NC100-6	60.0	68.3	80.1
NC80-6	57.5	83.0	96.1
NC60-6	103.8	134.9	181.0
LNC100-6	214.3	181.6	236.8
LNC80-6	197.7	208.1	200.4
LNC60-6	231.7	323.6	NA*
NC100-10	75.4	69.6	73.7
NC80-10	42.3	129.2	198.7
NC60-10	35.5	86.2	149.8
LNC100-10	167.4	329.6	485.0
LNC80-10	190	188.6	254.0
LNC60-10	101.6	168.9	206.1
OPC	93.2	82.6	120.8

NA: Not avaliable*

Table A.7 PV (Pa.s) values of NCAS and OPC-based mixes

Mixes	0 min	60 min	120 min
NC100-6	1.4	2.0	2.4
NC80-6	1.1	1.2	2.2
NC60-6	2.1	2.7	3.0
LNC100-6	1.2	1.9	2.6
LNC80-6	2.1	2.1	3.0
LNC60-6	1.8	2.2	NA*
NC100-10	1.8	2.4	3.1
NC80-10	1.6	2.7	NA
NC60-10	1.4	2.5	3.9
LNC100-10	8.3	12.4	19.6
LNC80-10	8.6	7.2	9.1
LNC60-10	3.8	5.2	5.7
OPC	1.1	1.2	1.7

NA: Not avaliable*

Table A.8 Compressive strength (MPa) of NCAS and OPC-based mixes

Mixes	3 days	7 days	28 days	90 days
NC100-6	0.6	1.4	3.1	3.4
NC80-6	0.5	1.2	4.6	4.8
NC60-6	1.0	16.6	19.0	19.6
LNC100-6	9.4	13.9	15.0	15.5
LNC80-6	13.8	23.0	25.3	28.2
LNC60-6	14.3	23.6	30.5	32.4
NC100-10	0.9	2.7	6.9	7.5
NC80-10	0.7	9.0	20.7	21.0
NC60-10	2.1	27.4	42.4	43.5
LNC100-10	14.2	22.3	28.1	30.8
LNC80-10	15.7	24.3	26.9	31.8
LNC60-10	20.4	32.5	44.4	44.5
OPC	51.6	54.3	55.0	57.7

Table A.9 Mesopore and macropore concentrations of NCAS mixes

Mixes	Mesopores (cm^3/g)	Macropores (cm^3/g)	Total pore volume (cm^3/g)
NC100-6	0.123	0.0326	0.155
NC80-6	0.108	0.0057	0.113
NC60-6	0.105	0.0007	0.106
LNC100-6	0.106	0.0052	0.112
LNC80-6	0.100	0.0034	0.103
LNC60-6	0.089	0.0013	0.090
NC100-10	0.052	0.0325	0.084
NC80-10	0.036	0.0175	0.053
NC60-10	0.038	0.0114	0.050
LNC100-10	0.106	0.0029	0.109
LNC80-10	0.072	0.0018	0.073
LNC60-10	0.011	0.0002	0.011

Table A.10 Mesopore and macropore ratios of NCAS mixes

Mixes	Mesopores (%)	Macropores (%)	Porosity (%)
NC100-6	79.0	21.0	34.0
NC80-6	95.0	5.0	25.0
NC60-6	99.3	0.7	23.0
LNC100-6	95.3	4.7	25.0
LNC80-6	96.7	3.3	23.0
LNC60-6	98.6	1.4	20.0
NC100-10	61.4	38.6	19.0
NC80-10	67.2	32.8	12.0
NC60-10	77.0	23.0	11.0
LNC100-10	97.3	2.7	24.0
LNC80-10	97.5	2.5	16.0
LNC60-10	98.2	1.8	2.0

Table A.11 Compressive and flexural strength and modulus of elasticity of plain and fiber-reinforced NCAS and OPC-based mixes

Mixes	$f_{compressive}$	$f_{flexural}$	**E (MPa)**
NC100	6.9	1.9	9442
NC60	43.5	2.8	11987
LNC100	28.1	2.7	11437
LNC60	44.5	2.1	12516
OPC	55.0	4.1	20804
NC100-PP	8.0	2.0	10469
NC60-PP	44.0	3.2	13340
LNC100-PP	21.3	3.4	12286
LNC60-PP	34.0	3.0	11596
OPC-PP	46.0	4.3	19511
NC100-ST	8.8	4.2	9519
NC60-ST	45.0	4.4	12599
LNC100-ST	26.0	4.3	10665
LNC60-ST	36.3	5.3	10828
OPC-ST	53.0	9.9	19848

Table A.12 Fracture characteristics of plain and fiber-reinforced mixes

Mixes	$a_{eff}(mm)$	K_{Ic}^{ini} $(MPa.m^{1/2})$	K_{Ic}^{un} $(MPa.m^{1/2})$	β	$G_F(N/m)$
NC100	32.3	0.18	0.36	0.51	69
NC60	26.9	0.18	0.41	0.45	48
LNC100	33.0	0.19	0.50	0.37	52
LNC60	36.7	0.16	0.47	0.35	86
OPC	34.1	0.28	0.78	0.36	51
NC100-PP	36.9	0.20	0.48	0.42	542
NC60-PP	36.2	0.26	0.63	0.41	624
LNC100-PP	43.7	0.26	0.98	0.26	672
LNC60-PP	42.3	0.22	0.77	0.29	531
OPC-PP	38.7	0.33	0.99	0.33	835
NC100-ST	49.3	0.24	1.68	0.14	933
NC60-ST	52.7	0.39	2.19	0.18	1138
LNC100-ST	46.4	0.33	1.46	0.23	1027
LNC60-ST	45.0	0.34	1.72	0.20	1210
OPC-ST	49.8	0.49	3.83	0.13	2053

Table A.13 Ultimate drying shrinkage (micro-strain) and ultimate weight reduction (%)

Mixes	Ultimate shrinkage (micro-strain)	Ultimate weight change (%)
NC100-6	2239	6.7
NC80-6	2179	6.2
NC60-6	2249	6.2
LNC100-6	1449	6.0
LNC80-6	1375	6.2
LNC60-6	1549	6.0
NC100-10	2358	5.0
NC80-10	1747	5.0
NC60-10	1635	4.4
LNC100-10	1604	5.6
LNC80-10	1496	5.4
LNC60-10	1304	3.8
OPC	1244	3.6

Table A.14 Average chloride migration coefficient ($\times 10^{-12}$) of NCAS and OPC-based mixes

Mixes	D_{nssm} (m^2/s)
NC100-6	63.7
NC80-6	42.1
NC60-6	33.6
LNC100-6	41.3
LNC80-6	3.1
LNC60-6	1.4
NC100-10	9.6
NC80-10	3.5
NC60-10	1.4
LNC100-10	6.1
LNC80-10	2.3
LNC60-10	1.0
OPC	10.6

B
Figures

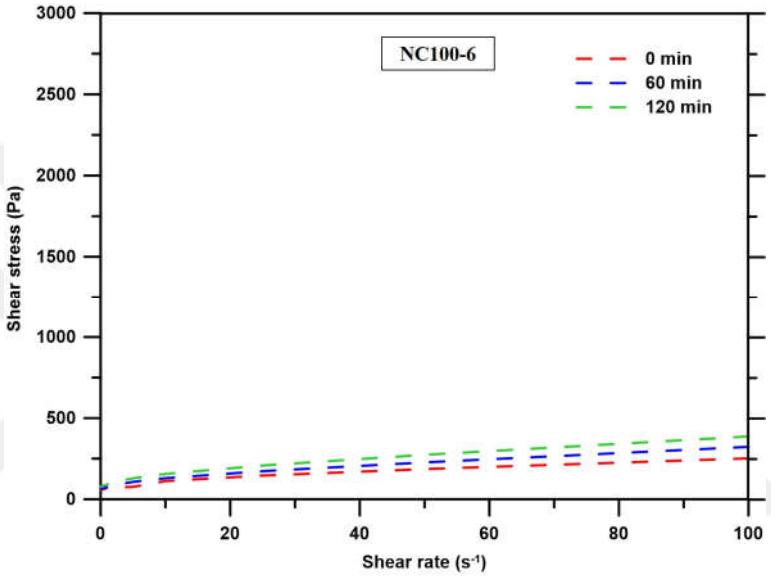

Figure B.1 Flow curves of NC100-6

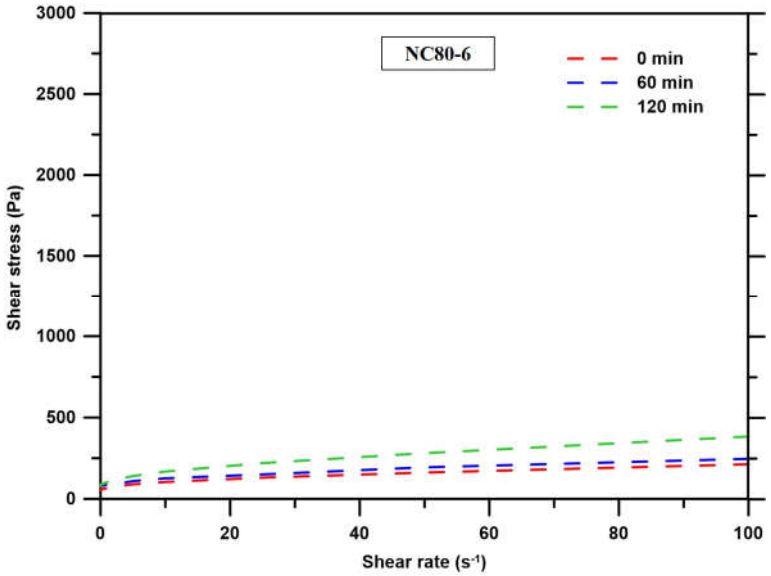

Figure B.2 Flow curves of NC80-6

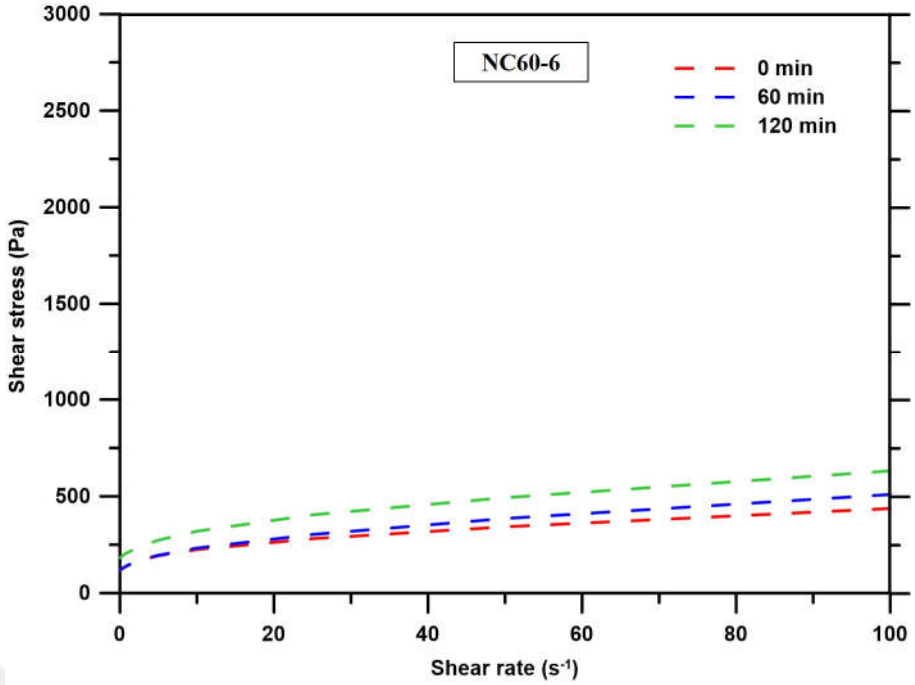

Figure B.3 Flow curves of NC60-6

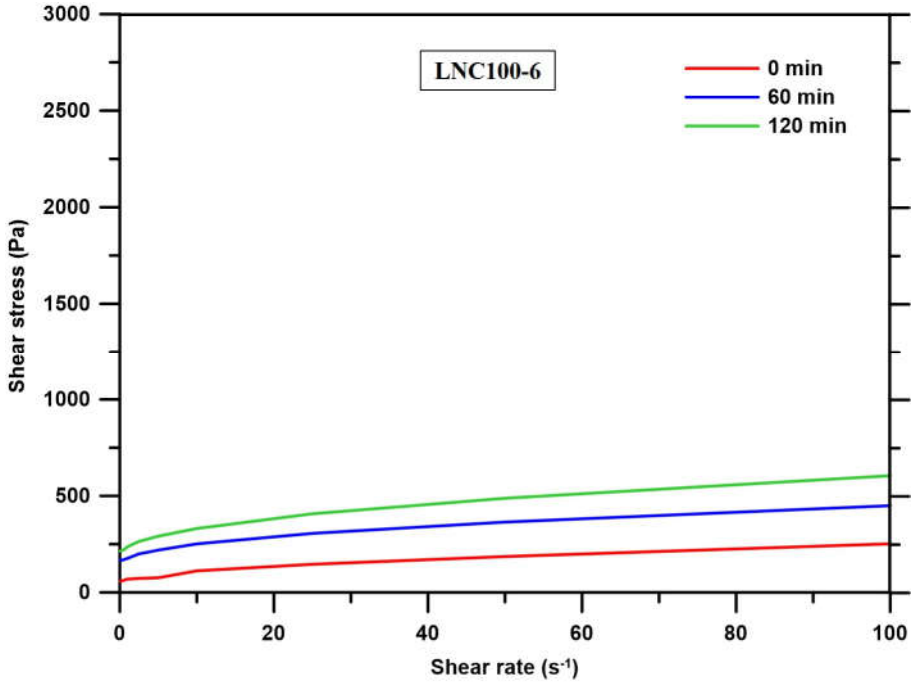

Figure B.4 Flow curves of LNC100-6

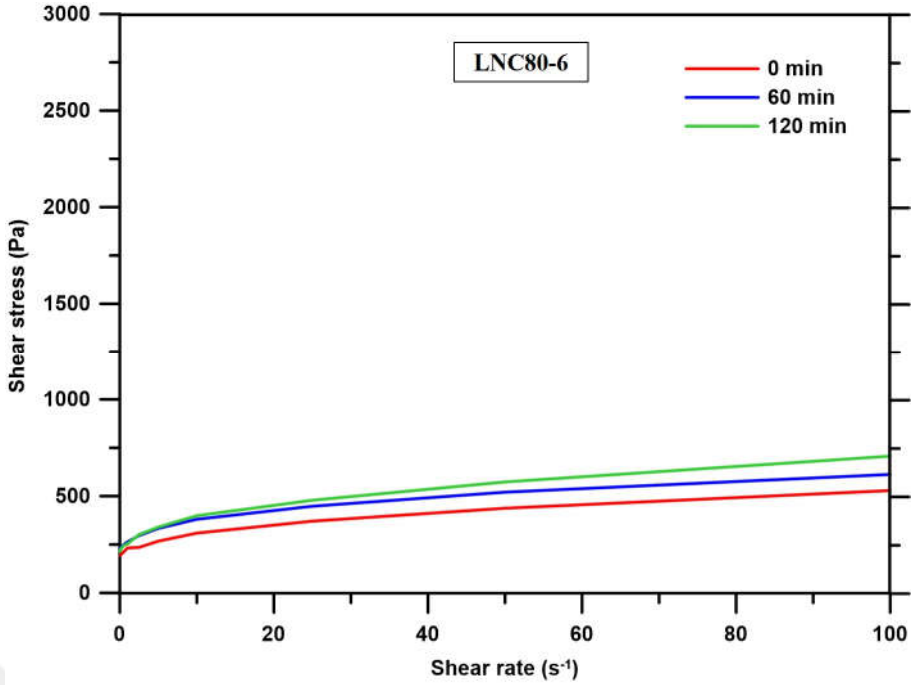

Figure B.5 Flow curves of LNC80-6

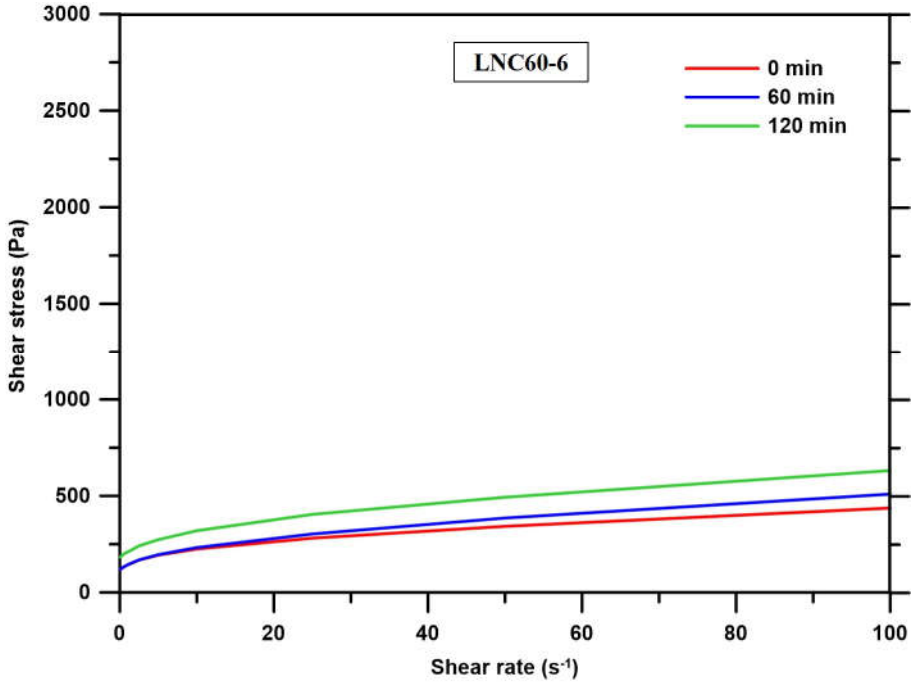

Figure B.6 Flow curves of LNC60-6

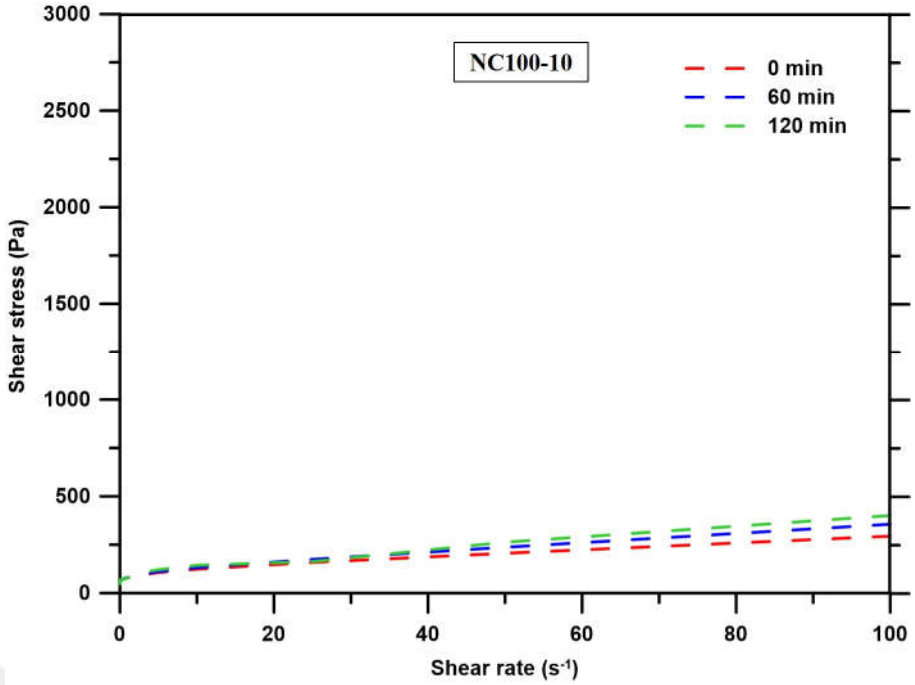

Figure B.7 Flow curves of NC100-10

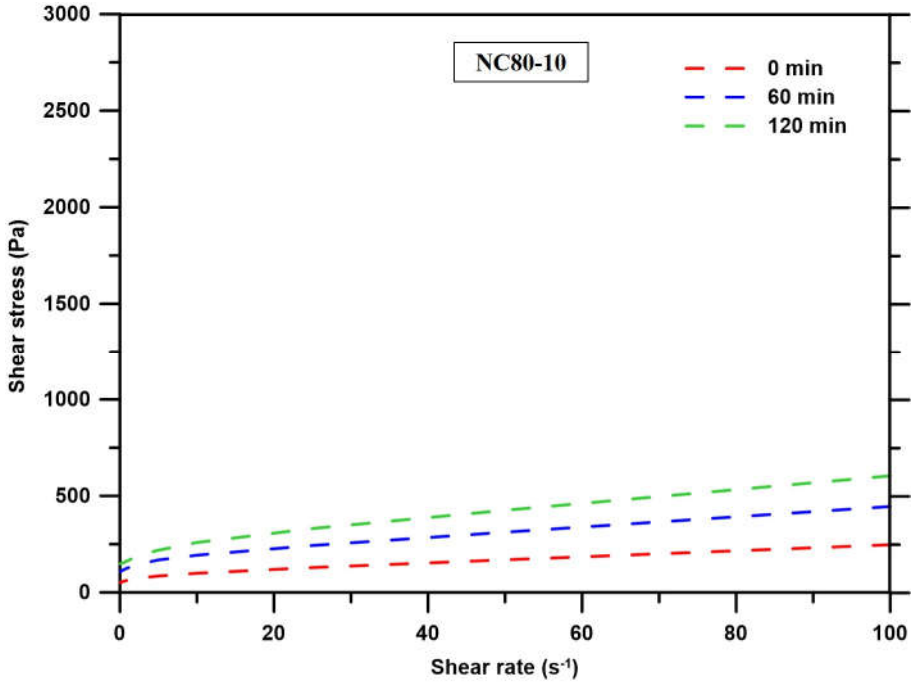

Figure B.8 Flow curves of NC80-10

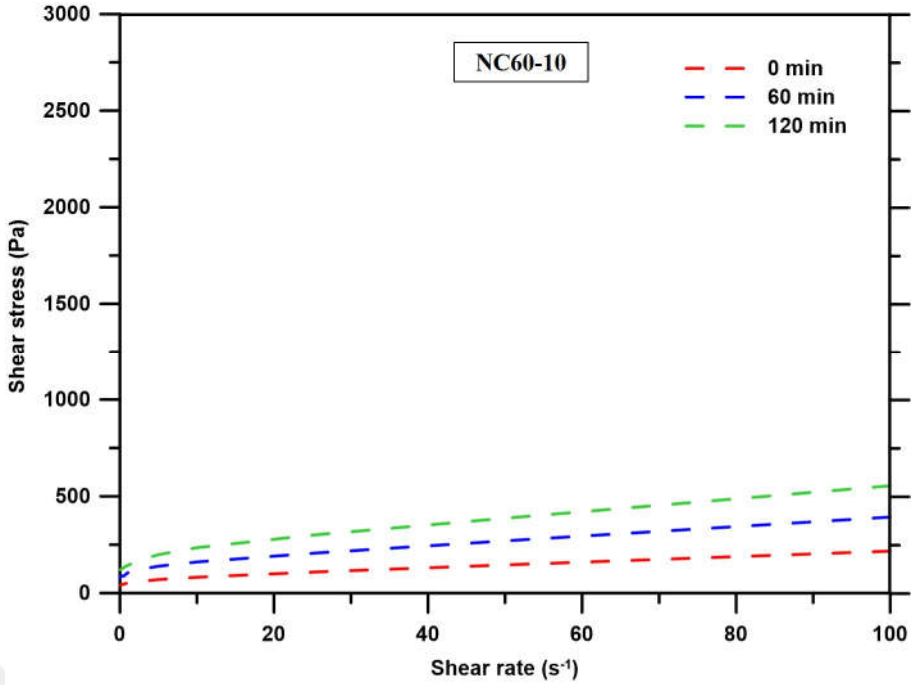

Figure B.9 Flow curves of NC60-10

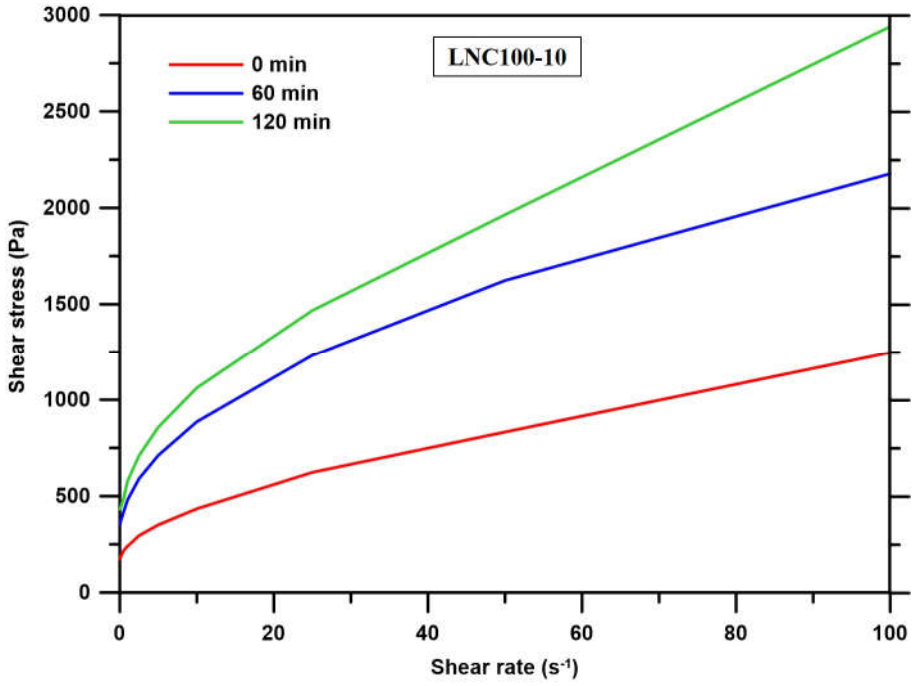

Figure B.10 Flow curves of LNC100-10

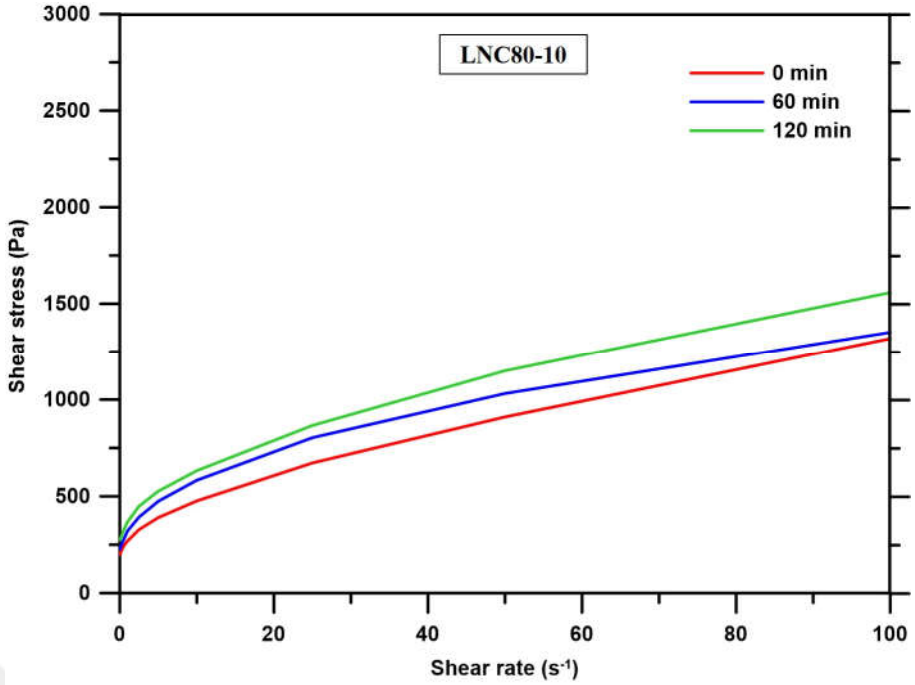

Figure B.11 Flow curves of LNC80-10

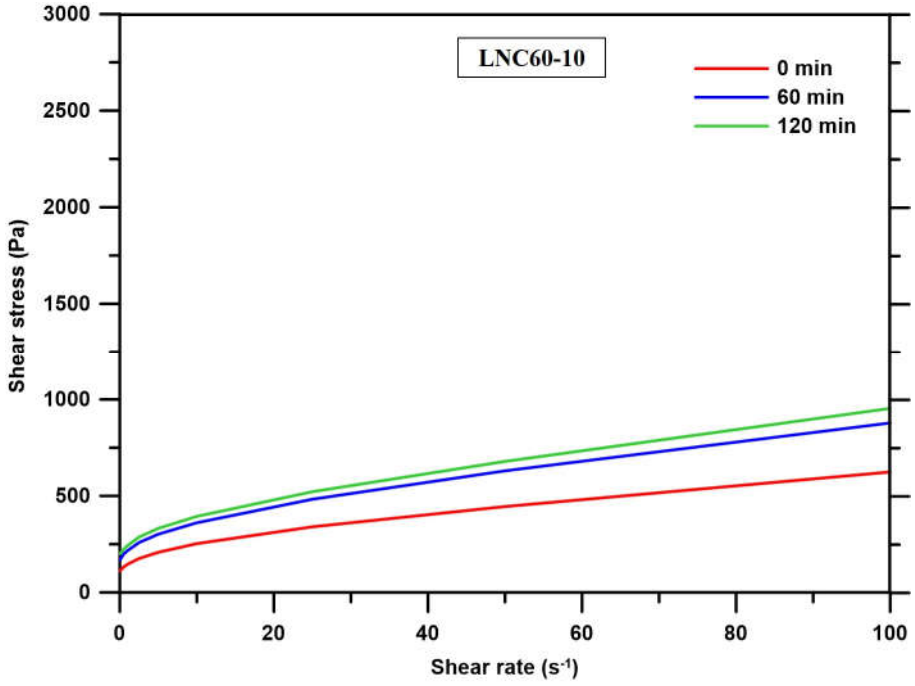

Figure B.12 Flow curves of LNC60-10

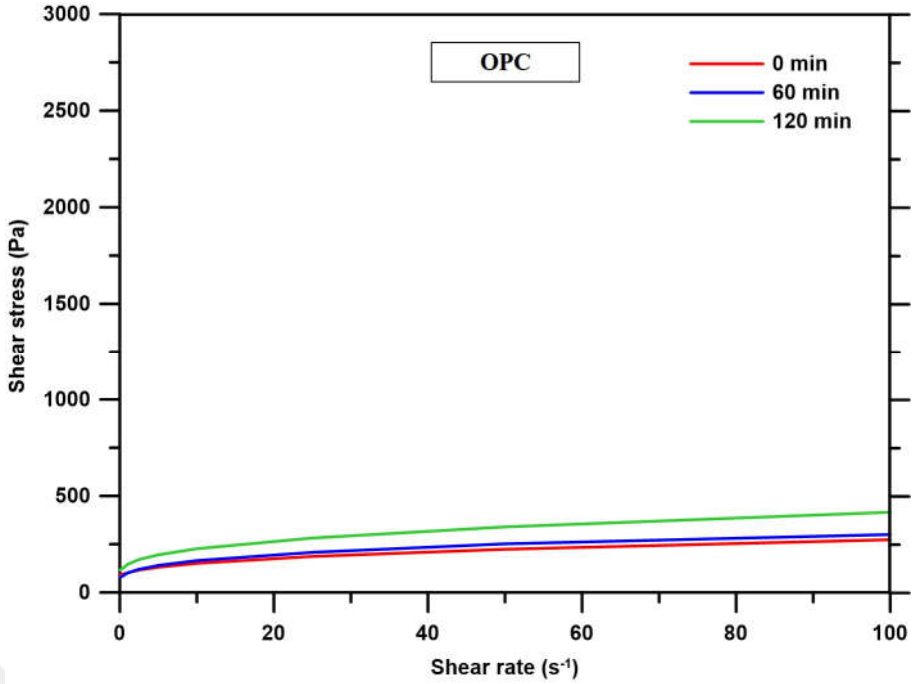

Figure B.13 Flow curves of OPC

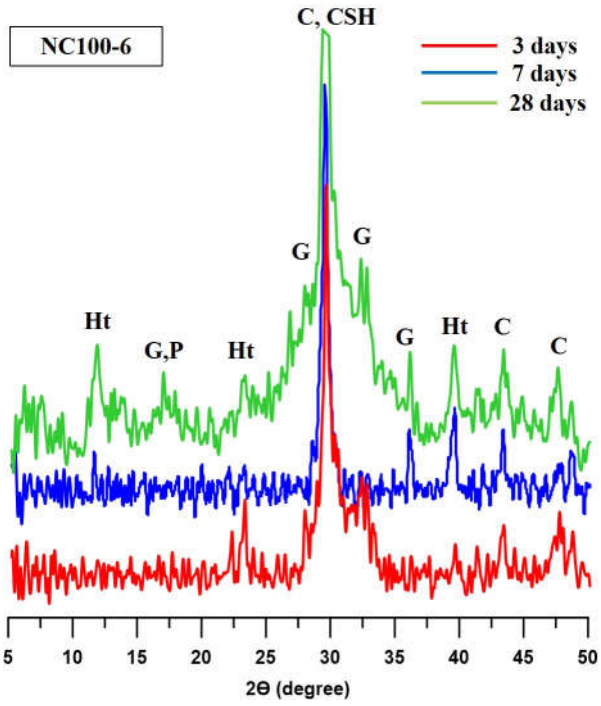

Figure B.14 XRD patterns of NC100-6

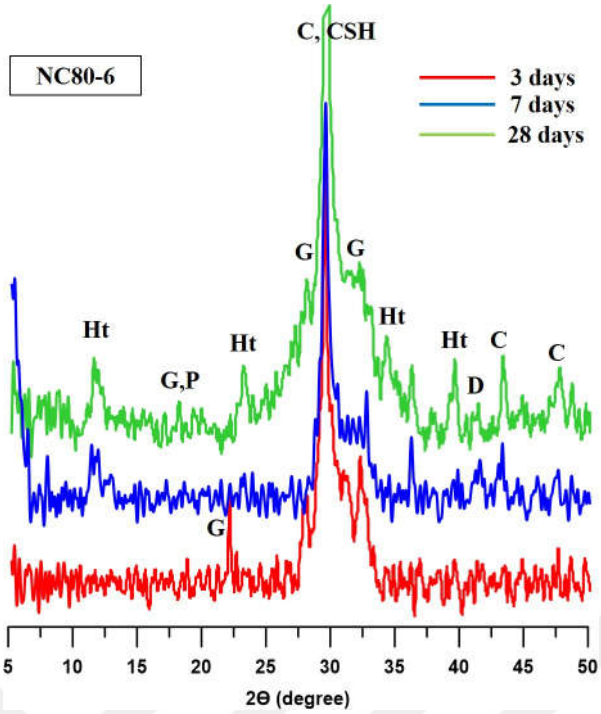

Figure B.15 XRD patterns of NC80-6

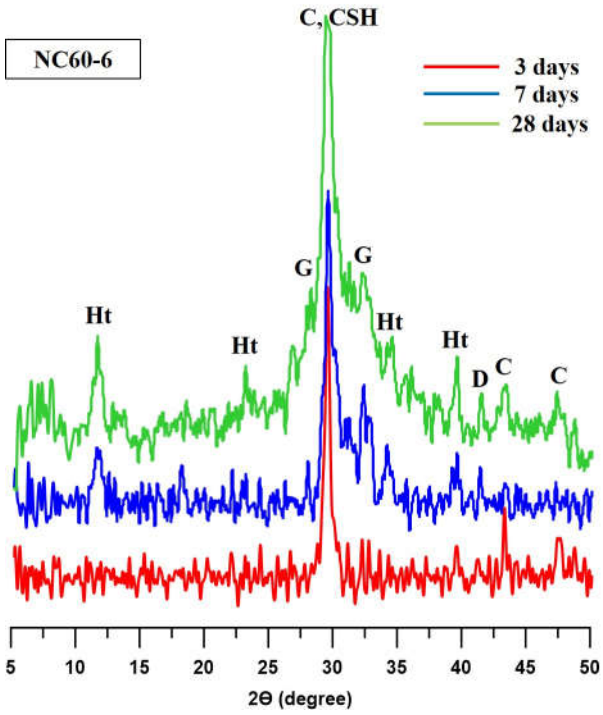

Figure B.16 XRD patterns of NC60-6

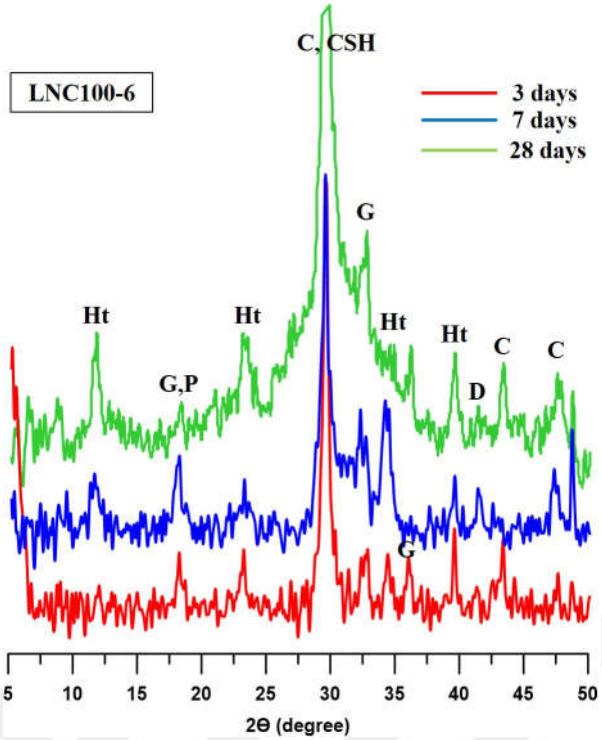

Figure B.17 XRD patterns of LNC100-6

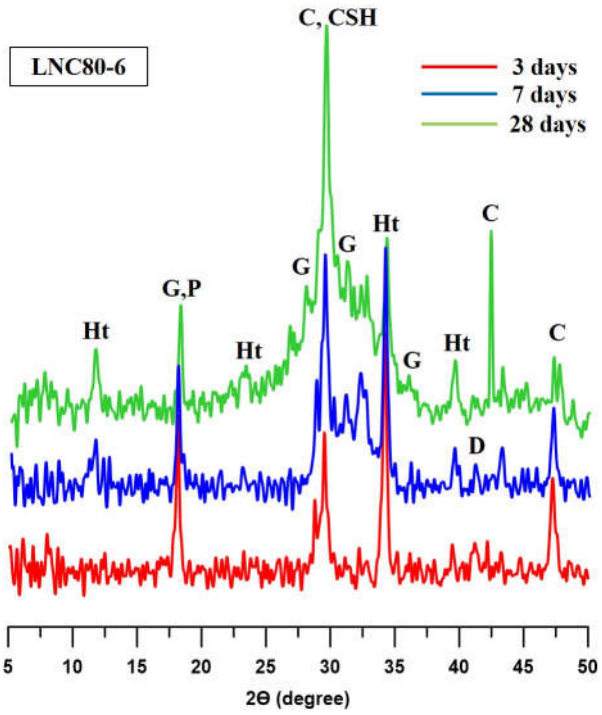

Figure B.18 XRD patterns of LNC80-6

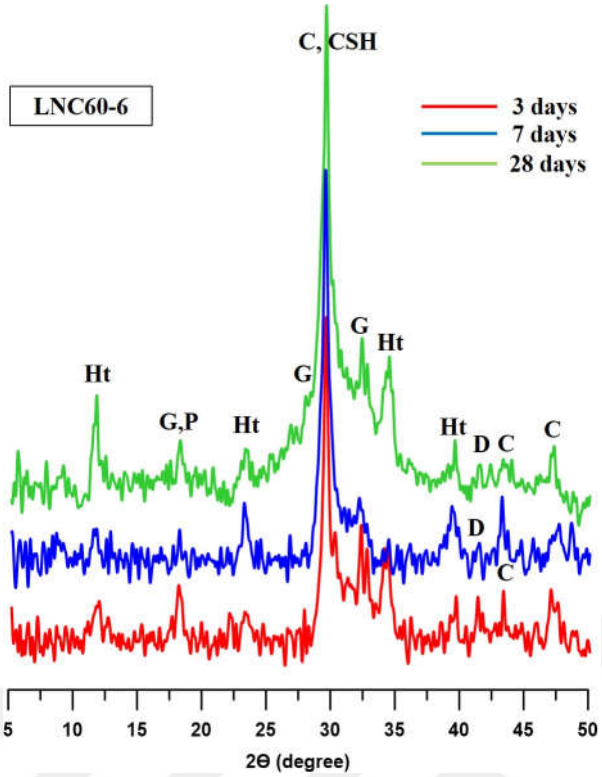

Figure B.19 XRD patterns of LNC60-6

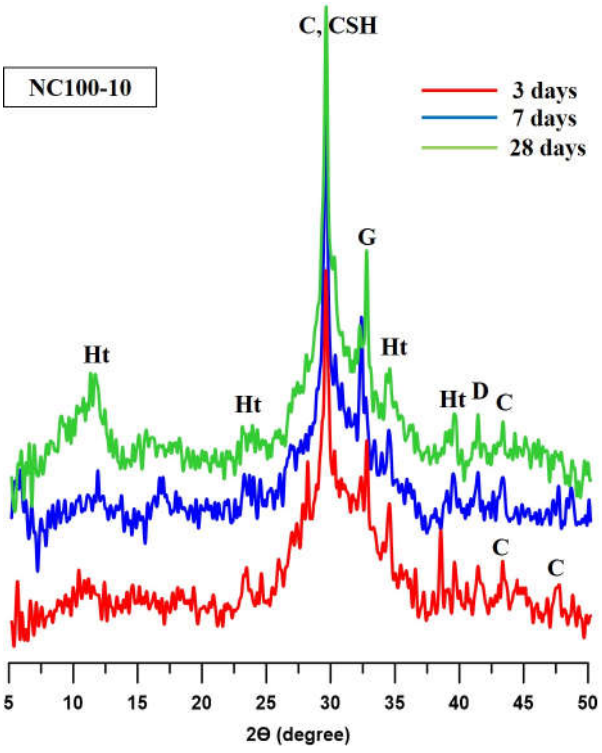

Figure B.20 XRD patterns of NC100-10

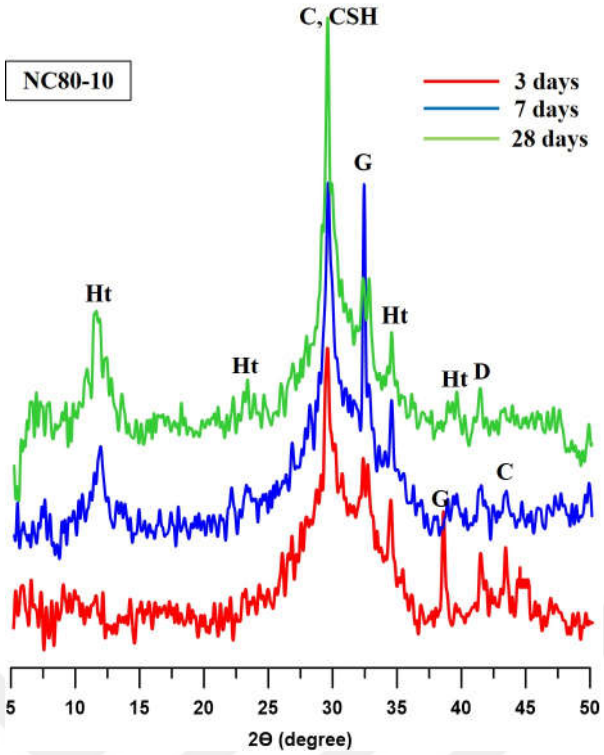

Figure B.21 XRD patterns of NC80-10

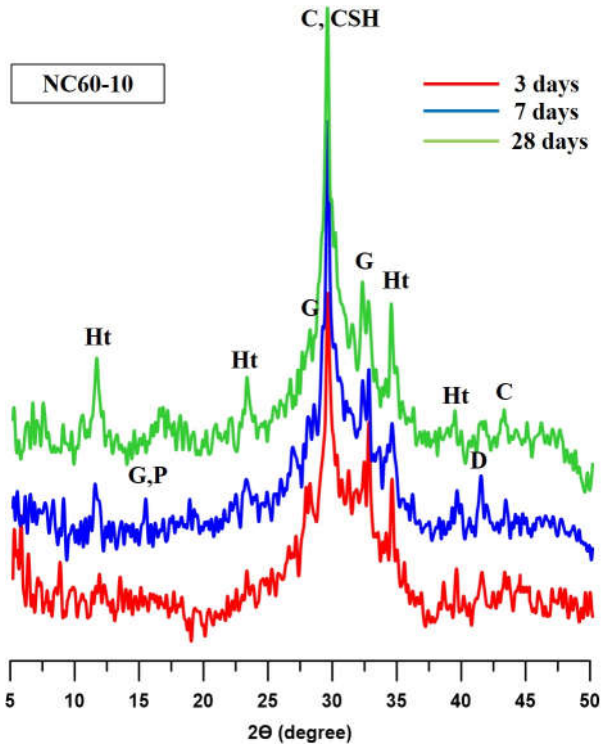

Figure B.22 XRD patterns of NC60-10

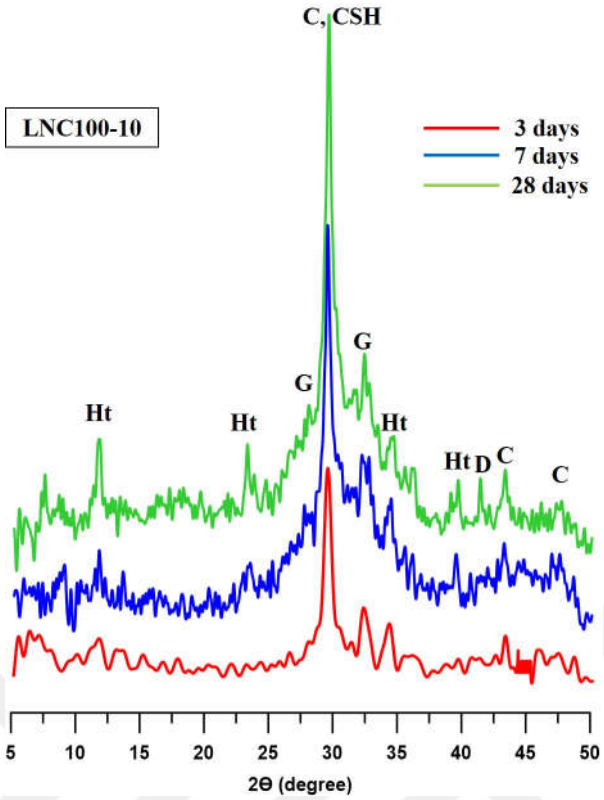

Figure B.23 XRD patterns of LNC100-10

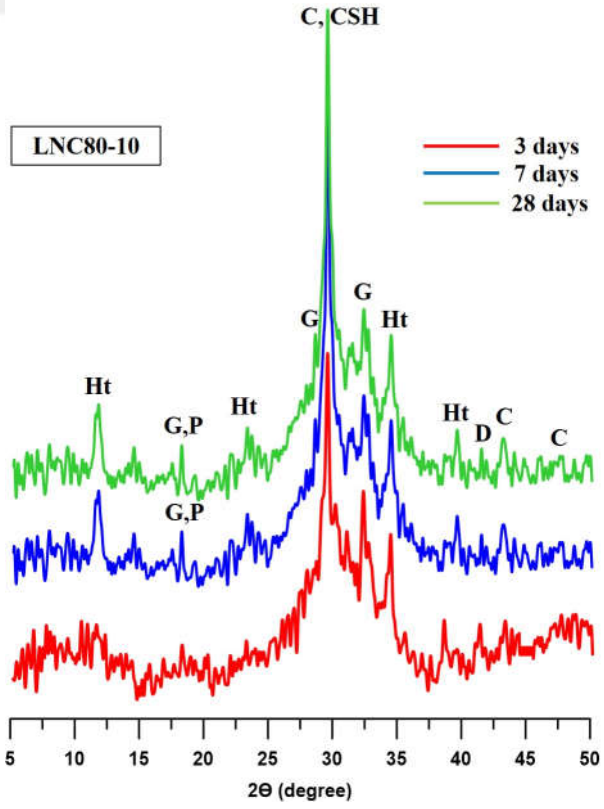

Figure B.24 XRD patterns of LNC80-10

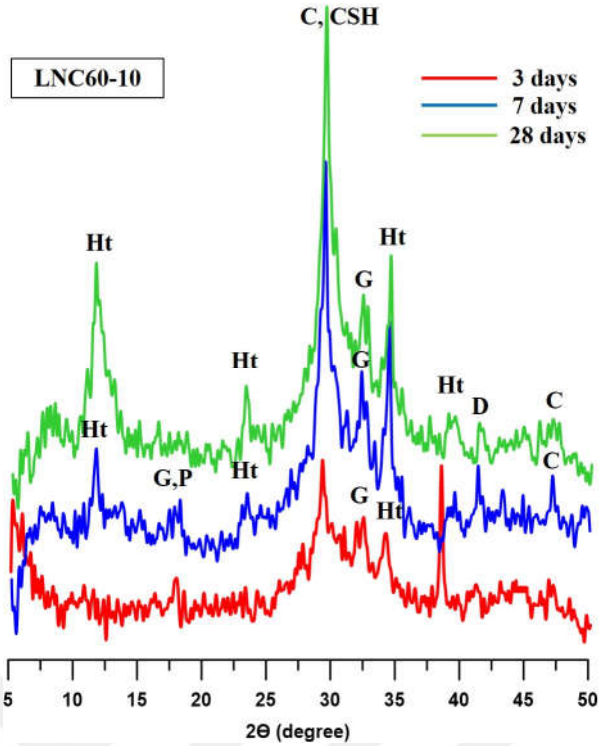

Figure B.25 XRD patterns of LNC60-10

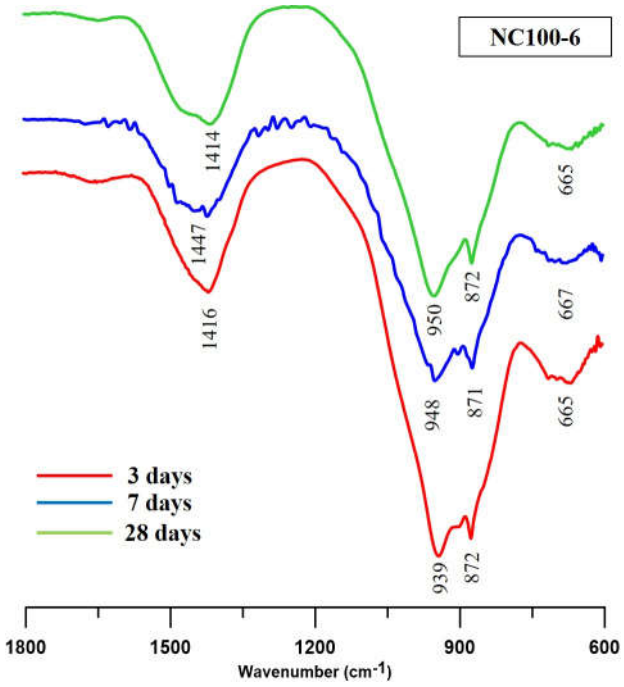

Figure B.26 FTIR spectras of NC100-6

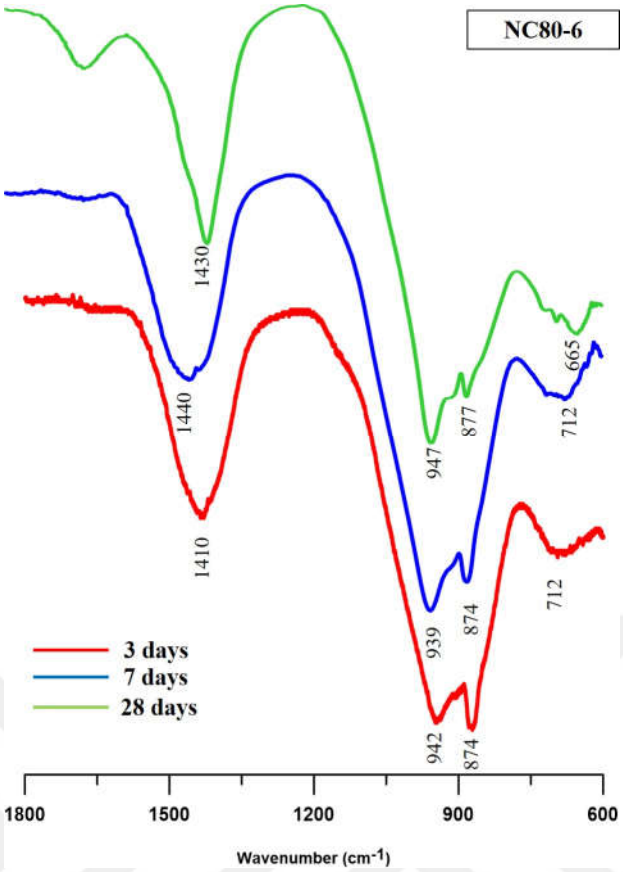

Figure B.27 FTIR spectras of NC80-6

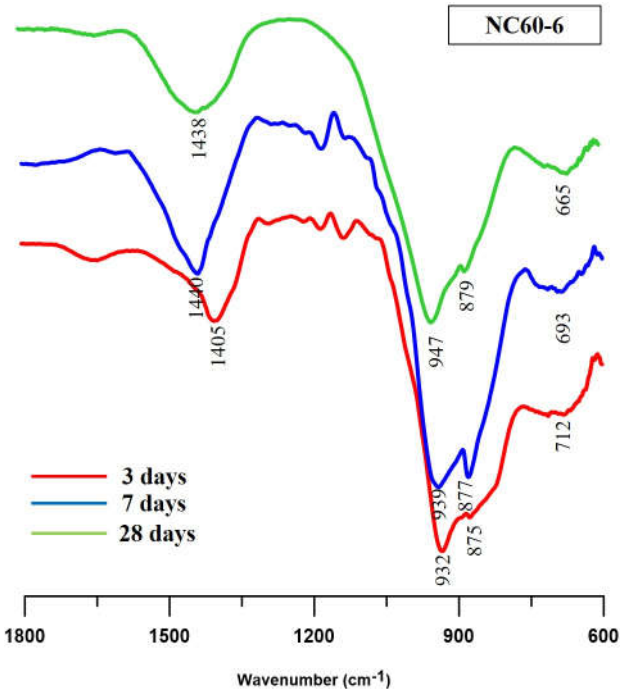

Figure B.28 FTIR spectras of NC60-6

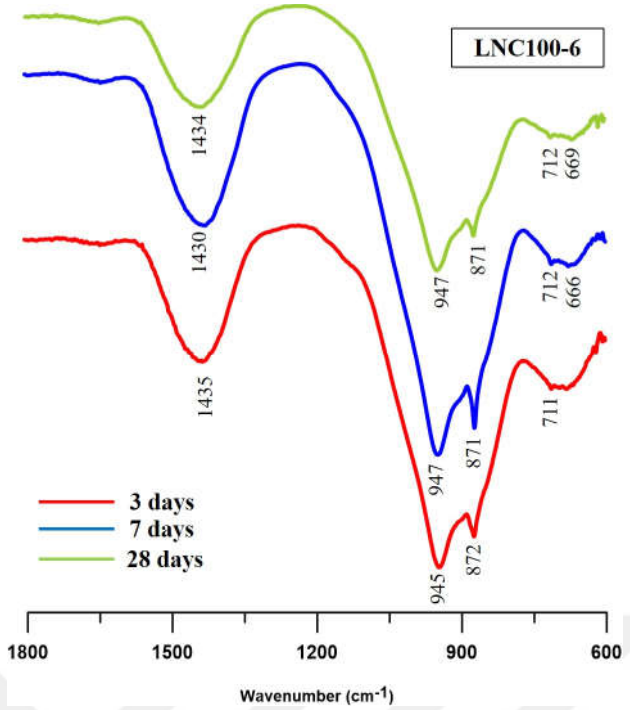

Figure B.29 FTIR spectras of LNC100-6

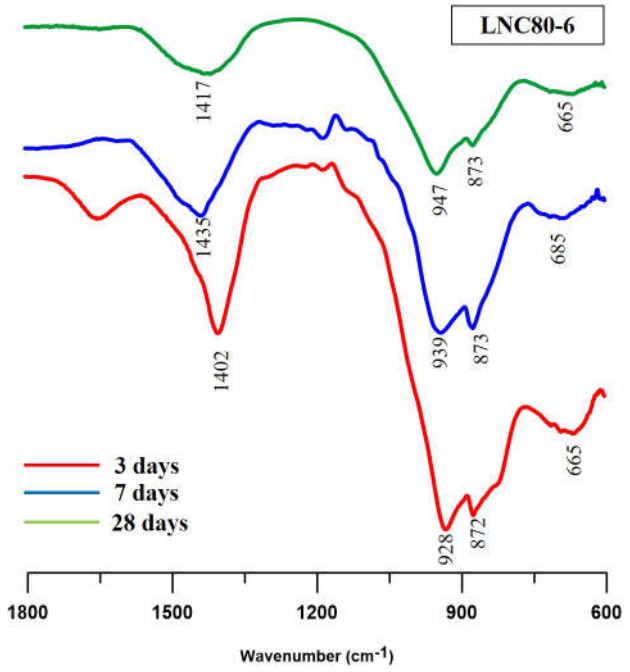

Figure B.30 FTIR spectras of LNC80-6

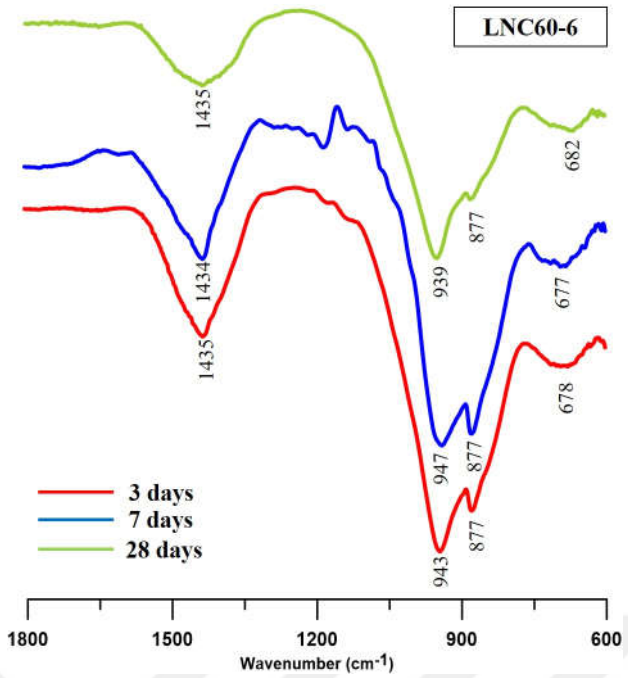

Figure B.31 FTIR spectras of LNC60-6

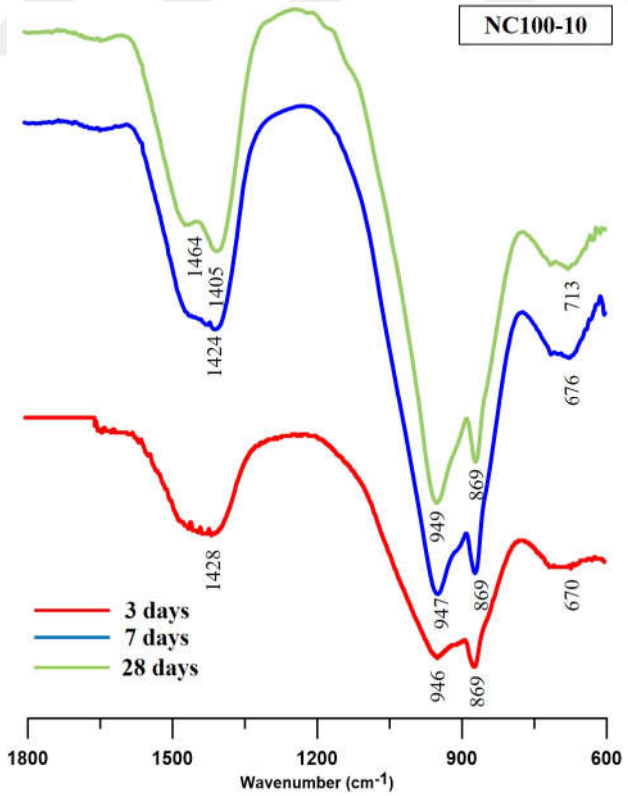

Figure B.32 FTIR spectras of NC100-10

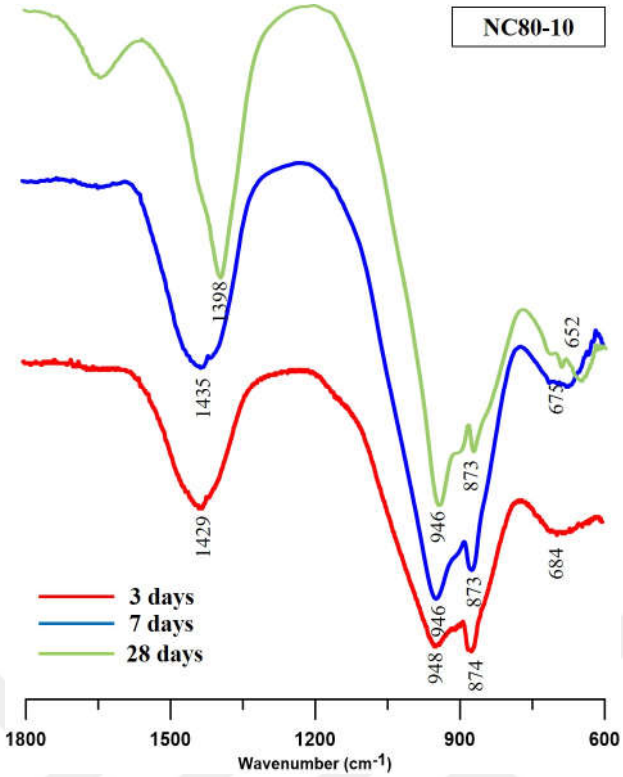

Figure B.33 FTIR spectras of NC80-10

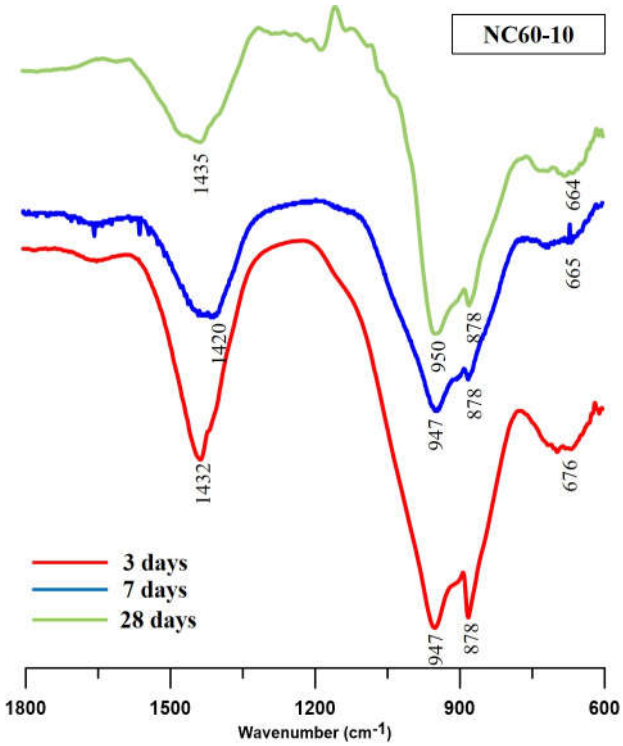

Figure B.34 FTIR spectras of NC60-10

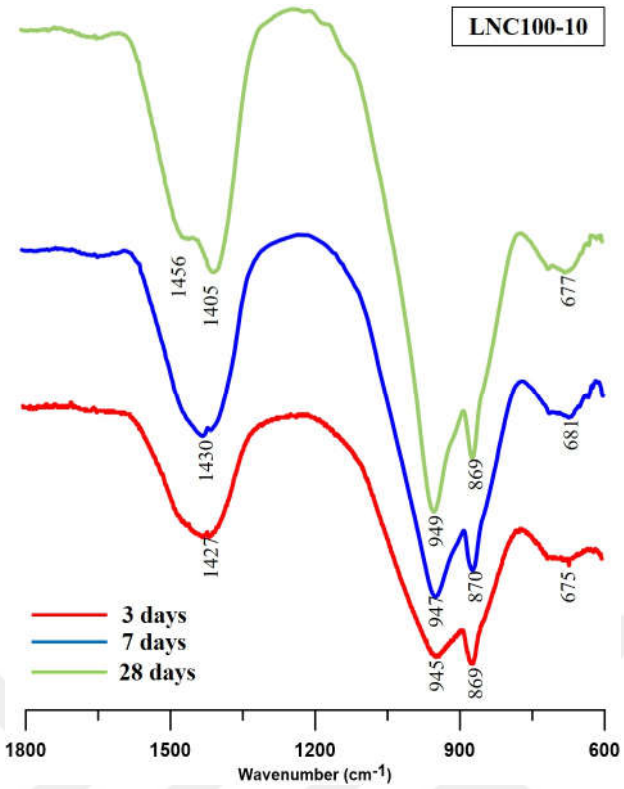

Figure B.35 FTIR spectras of LNC100-10

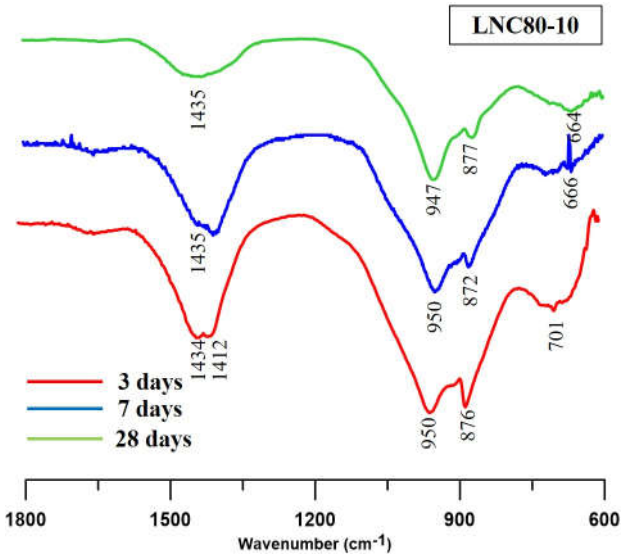

Figure B.36 FTIR spectras of LNC80-10

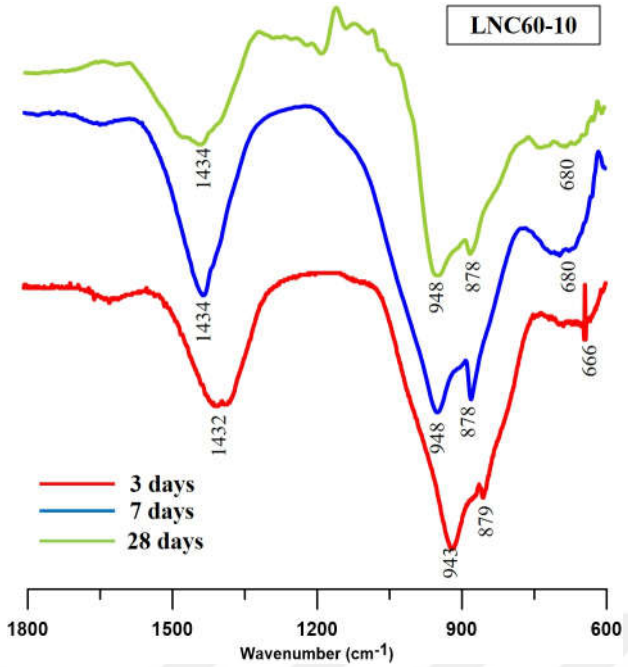

Figure B.37 FTIR spectras of LNC60-10

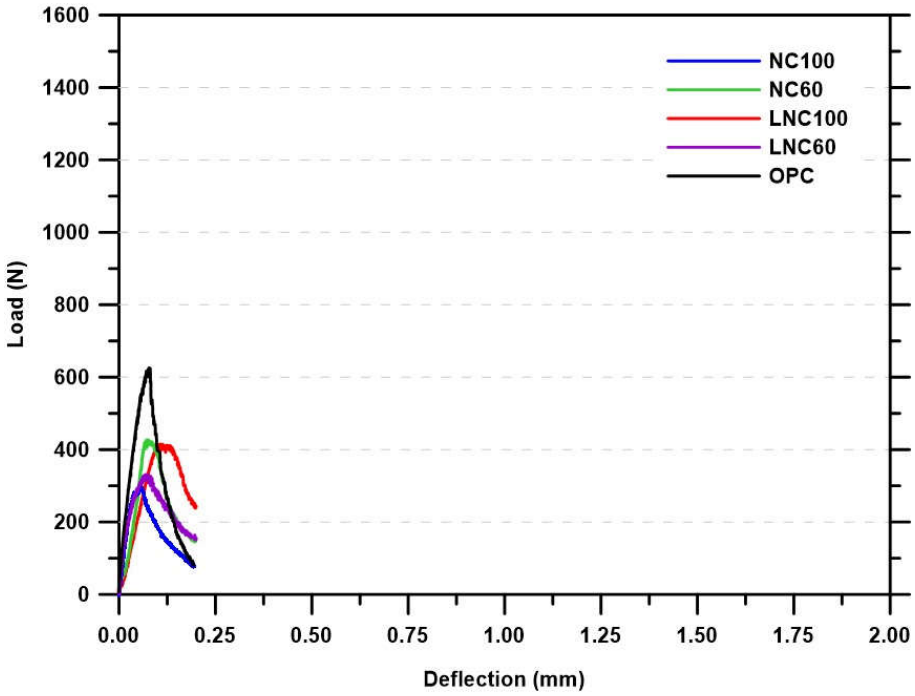

Figure B.38 Load-deflection curves of plain mixes

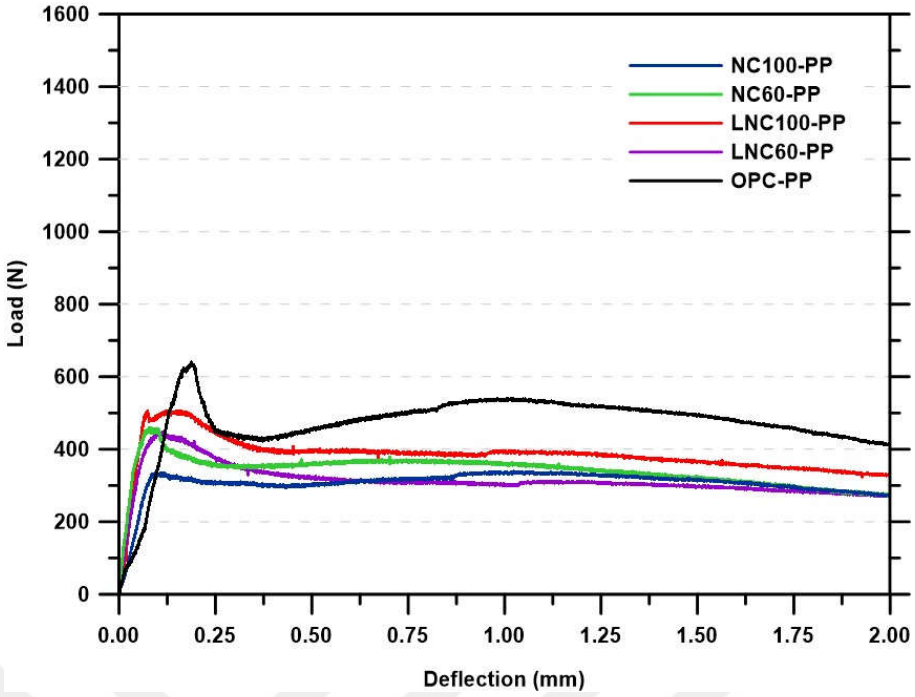

Figure B.39 Load-deflection curves of PP fiber-reinforced mixes

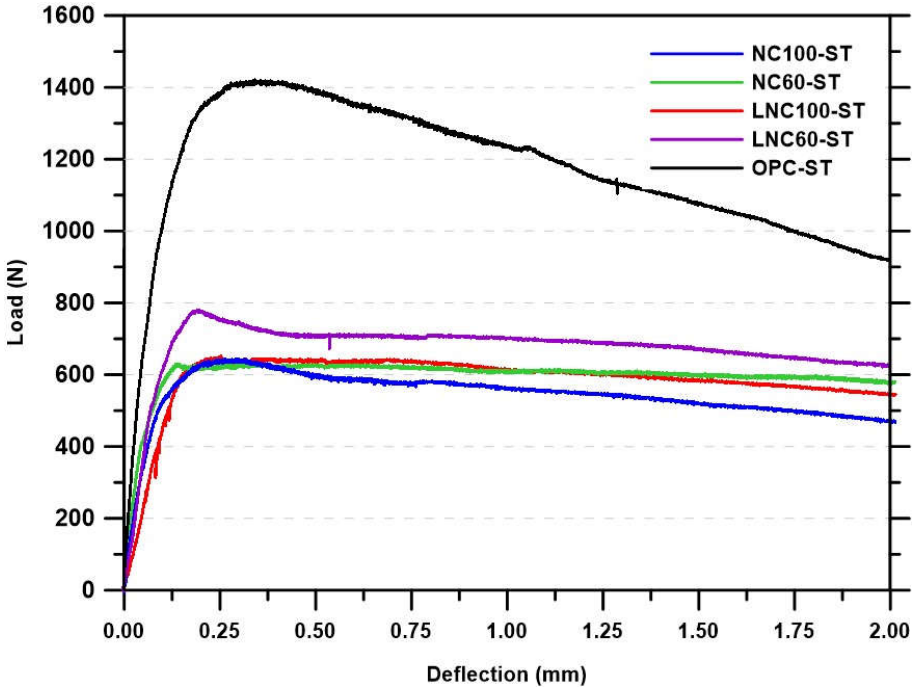

Figure B.40 Load-deflection curves of ST fiber-reinforced mixes

Publications From the Thesis

Contact Information: bucarkosar@gmail.com

Papers

1. **B. Aktürk**, A.B. Kızılkanat, N. Kabay, "Effect of calcium hydroxide on fresh state behavior of sodium carbonate activated blast furnace slag pastes," *Construction and Building Materials*, vol. 212, pp. 388-399, 2019.

2. **B. Aktürk**, S. Nayak, S. Das, A.B. Kızılkanat, "Microstructure and strength development of sodium carbonate activated blast furnace slags," *Journal of Materials in Civil Engineering-ASCE*, vol. 31, pp. 1-11, 2019.

Conference Papers

1. **B. Aktürk**, A.B. Kızılkanat, N. Kabay, "Time-dependent microstructure and compressive strength development of sodium carbonate activated blast furnace slag," in *10th International Concrete Congress*, May 02-04, 2019, Bursa, Turkey.

2. **B. Aktürk**, A.B. Kızılkanat, N. Kabay, "Effect of sodium hydroxide on fresh state properties of sodium carbonate activated blast furnace slag pastes, in *13th International Congress on Advances in Civil Engineering*, September 12-14, İzmir, Turkey.

Projects

1. **Aktürk B.**, Kızılkanat A.B., Investigation of the early age properties of alkali activated binder systems (in Turkish "Alkalilerle aktive edilmiş bağlayıcı sistemlerin erken yaş özelliklerinin Araştırılması"), YTÜ-DOP, Project No: 2016-05-01-DOP03, 2016-2019.